Potential of the Empirical Mode Decomposition to analyze instantaneous flow fields in Direct Injection Spark Ignition engine : Effect of transient regimes

Mehdi Sadeghi

Centre Val de Loire UNIVERSITÉ

UNIVERSITÉ D'ORLÉANS

UNIVERSITE D'ORLEANS

ÉCOLE DOCTORALE
ENERGIE, MATERIAUX, SCIENCES DE LA TERRE ET DE L'UNIVERS

LABORATOIRE PRISME

THÈSE présentée par :

Mehdi SADEGHI

Soutenue le **4 Décembre 2017**

pour obtenir le grade de : **Docteur de l'université d'Orléans**

Discipline/ Spécialité : Energétique

Potential of the Empirical Mode Decomposition to analyze instantaneous flow fields in Direct Injection Spark Ignition engine: Effect of transient regimes

THÈSE dirigée par

Christine MOUNAÏM-ROUSSELLE	Professeur, Université d'Orléans
Fabrice FOUCHER	Professeur, Université d'Orléans
Karim ABED-MERAIM	Professeur, Université d'Orléans

RAPPORTEURS

Jacques BORÉE	Professeur, ISAE-ENSMA Poitiers
Abdel-Ouahab BOUDRAA	HdR, Ecole Navale/Arts & Métiers ParisTech

---

JURY

Jacques BORÉE	Rapporteur, Professeur, ISAE-ENSMA Poitiers
Abdel-Quahab BOUDRAA	Rapporteur, HdR, Ecole Navale/Arts & Métiers ParisTech
Stéphane JAY	Examinateur, HdR, IFP Energies Nouvelles
Luis LE MOYNE	Examinateur, Professeur, ISAT, Université de Bourgogne
Christine MOUNAÏM-ROUSSELLE	Directrice de thèse, Professeur, Université d'Orléans
Fabrice FOUCHER	Directeur de thèse, Professeur, Université d'Orléans
Karim ABED-MERAIM	Encadrant de thèse, Professeur, Université d'Orléans

à mes parents et ma petite sœur

Remerciement

Ce travail a été réalisé dans le cadre d'un projet ANR, ASTRIDE (Aérodynamique et Sprays pour les Transitoires en Injection Directe Essence) au sein de l'axe ECM (Energie, Combustion, Moteur) du laboratoire PRISME (Pluridisciplinaire de recherche en ingénierie des systèmes, mécanique et énergétique). Je remercie Azeddine KOURTA, directeur du laboratoire PRISME, de m'avoir accueilli chaleureusement au sein de ce laboratoire en tant que doctorant.

Je tiens à remercier très sincèrement mes directeurs de thèse Christine MOUNAÏM-ROUSSELLE et Fabrice FOUCHER, professeurs à l'Université d'Orléans, pour la confiance qu'ils m'ont accordé en me donnant l'opportunité d'effectuer cette thèse. Il est difficile d'exprimer tout ce que je dois à ces deux personnes; ce travail n'aurait pas pu voir le jour sans leur direction, leurs conseils scientifiques, leur patience, leur disponibilité et leur soutien dans les moments difficiles.
Je remercie profondément mon encadrant dans la partie de traitement du signal de cette thèse Karim ABED-MERAIM, professeur à l'Université d'Orléans, pour ses conseils scientifiques, sa disponibilité et ses encouragements. Je souhaite à tous d'avoir la chance de travailler avec de tels professeurs, tant pour leurs compétences que pour leurs qualités humaines, leur gentillesse et leur souci d'aider les autres.

J'ai été très honoré que Jacques BORÉE, professeur à ISAE-ENSMA Poitiers, et Abdel-Quahab BOUDRAA, HdR, Ecole Navale/Arts & Métiers ParisTech, aient évalué mes travaux de thèse en tant que rapporteurs. J'exprime ma gratitude à l'examinateur Stéphane JAY, HdR à IFP Energies Nouvelles, et Luis LE MOYNE, professeur à ISAT-Université de Bourgogne, d'avoir accepté de faire partie du jury.

Je suis reconnaissant envers les membres de l'équipe technique du laboratoire PRISME, en particulier Bruno MOREAU, Yahia HAIDOUS et Florian LESPINASSE, sans la contribution desquels la partie expérimentale de cette thèse n'aurait pas été réalisable.

Je souhaite également remercier Nicolas MAZELLIER, Sandrine AUBRUN et Ivan FEDIOUN, enseignants et chercheures à l'université d'Orléans de l'axe ESA (Ecoulements et Systèmes Aérodynamiques) avec lesquelles j'ai eu l'occasion de discuter au sujet de l'aérodynamique et la turbulence.
Un grand merci à Sylvie PLESSARD, secrétaire du laboratoire, qui m'a grandement facilité le travail administratif.
Merci également à Benoit CLAVIER et Pierre AMELOT, du service informatique de Polytech Orléans, pour leur diligence et leur efficacité.

Je termine ces hommages au laboratoire par ceux qui en font le quotidien, mes collègues doctorants, post-docs, stagiaires, enseignants, technicien et ingénieur de recherche : Pierre, J.-B., Antonio, Amine, Charles E, Ricardo, Padipan, Salim, Shadi, Ob, Antoine, Kévin, Audrey, Yann, Annie, Julien, Benoit, Stéphane, Kristan, Nicoletta, Marco S, Ton, Jamale, Nicola, Lam, Anthony, Charles L, Alexandre, Eszter, Marco L , Soufi, Hirokazu, Rajeb, Ida, Hassan, Piettro et toutes les personnes que j'ai pu oublier.

Je tiens à remercier Olivier SIMONIN, professeur à INP-ENSEEIHT de Toulouse, de m'avoir initié à la recherche en mécanique des fluides. J'ai eu la chance de côtoyer ses qualités scientifiques pendant mes études.

Je salue du fond du cœur Richard FOURNIER, professeur à UPS Toulouse, pour son soutien sans faille au cours de mes études en France. Il incarne pour moi un exemple accompli et une source d'inspiration tant dans les valeurs humaines que dans la recherche.

Je remercie mes proches amis Abbas, Milad, Marc, Masoud, Hélène et Daniel pour leur soutien et pour les bons moments passés en leur compagnie.
Enfin, je souhaite par-dessus tout remercier mes parents qui m'ont permis d'en arriver là. Je les remercie pour leur amour sans condition.

Contents

Introduction **1**

1 In-cylinder flow aerodynamic **11**
1.1 The direct-injection spark-ignition engine 11
1.2 In-cylinder flow 12
1.2.1 Turbulence production in GDI engine 14
1.2.2 Mean velocity and turbulence definition 16
1.2.3 Turbulence estimation from in-cylinder velocity field 17

2 The empirical mode decomposition **20**
2.1 The empirical mode decomposition method 21
2.1.1 Stoppage criteria 23
2.1.2 Noise assisted empirical mode decomposition 25
2.2 Multivariate extension of EMD 29
2.2.1 EMD for Bivariate signal 29
2.2.2 EMD for Trivariate signal 31
2.2.3 Multivariate EMD 34
2.2.4 Noise-Assisted Multivariate EMD 36
2.2.5 Adaptive-projection intrinsically transformed MEMD 38

3 Multidimensional extension of EMD **42**
3.1 Monovariate -Two Dimensional EMD 42
3.1.1 Fast and Adaptive bidimensional empirical mode decomposition . . 44
3.1.2 Multi-Dimensional Ensemble Empirical Mode Decomposition 48
3.2 Bivariate (Multivariate)-Two Dimensional EMD 54

4 Validation: Application on homogeneous and isotropic turbulence **59**
4.1 Analysis of decomposition quality via EMD, EEMD, CEEMDAN and CEEMD with different stoppage criteria for sifting process 59
4.2 Application of Bivariate EMD for separating coherent structure from homogeneous and isotropic turbulence 65
4.3 Validation of Bivariate 2D-EMD 73
4.3.1 Influence of the vortex amplitude 74
4.3.2 Influence of the vortex position 85
4.3.3 Influence of the vortex size 90

5 Experimental set up and measurements **100**
5.1 Engine test bench . . . 100
5.2 High and low frequency rate data acquisitions . . . 102
5.3 Engine operating . . . 103
5.3.1 Stationary regime . . . 103
5.3.2 Transient regime . . . 105
5.4 High speed Particle Image Velocimetry in engine . . . 111
5.4.1 Set up . . . 114
5.4.2 Seeding constraints . . . 115
5.4.3 PIV Processing . . . 116

6 Results **118**
6.1 Flow pattern observation . . . 118
6.1.1 Recirculation zone under intake valves . . . 119
6.1.2 At 290 CAD bTDC . . . 121
6.1.3 Appearance of the strong tumble motion . . . 122
6.1.4 At mid-intake stroke . . . 124
6.1.5 At BDC - The generation of a second vortex . . . 125
6.1.6 At mid-compression stroke . . . 129
6.1.7 At 70 CAD bTDC . . . 130
6.2 Tumble center trajectory and Tumble ratio . . . 133
6.2.1 Stationary conditions . . . 135
6.2.2 Slow transient condition . . . 140
6.2.3 Fast transient condition . . . 143
6.2.4 Comparison between stationary and transient conditions . . . 145
6.3 Application of Bivariate 2D-EMD . . . 150
6.3.1 Comparison between EMD and POD . . . 150
6.3.2 Application of Bivariate 2D-EMD on transient in-cylinder velocity fields . . . 160

General conclusion and perspectives **166**

Bibliography **172**

Introduction

As CO2 legislation becomes more and more stringent, it is important to reduce CO2 emissions of all types of vehicles during more realistic driving conditions. For that, a new international procedure more reproducible and in conformity over the world will be adopted by the EU in replacement of New European Drive Cycle (NEDC): the World-Harmonized Light-Duty Vehicles Test Procedure (WLTP) in 2020. The International Council on Clean Transportation [122] evaluated main improvements between NEDC and WLTP: the driving cycle itself, long and more dynamic, the effect of vehicle mass and the cold start conditions.

As underlined, it is well known that "besides the load of the engine, engine speed has a direct impact on CO2 emissions" [122] in addition the CO2 emission is strongly related to specific fuel consumption (SFC).
Therefore if one compares WLTP to NEDC, it can be seen the important number of transitions between low and medium engine regimes and medium to higher ones need to be considered in the impact of acceleration. The new regulatory constraints need to pay more attention to understanding and modeling of physical phenomena during transient engine, for improved technologies, their use or new technology development in order to limit the emission of CO2 as well as CO, HC, NOx and soot.
From previous studies, experimental or modelling, the link between in-cylinder flow, fuel/air mixing and combustion development is clearly demonstrated (Arcoumanis et al. (1998) [5], Lumley et al. (2001) [116], Lee et al. (2007) [105]).

In the case of Spark-Ignition engines, in-cylinder flow affects the first step of combustion development, i.e. the flame kernel (Pajot & Mounaim-Rousselle (2000) [136]), it impacts also misfire or pre-ignition combustion (Yamakawa et al. (2011) [205]). In the majority of cases, these movements are optimized in order to break flow large-scale structures, allowing to generate the turbulence itself, necessary to the combustion development at the engine time scale (Voisine et al. (2011) [188]).
Indeed, the laminar flame velocity is not high enough to burn the fuel/air mixture during available short time for combustion process, while the small-scale turbulent fluctuations cause flame front wrinkling and so increase the flame surface hence promote the rate of mass burn rate and enhance engine efficiency. The breakup of in-cylinder large-scale organized motions are one of the main sources of required turbulence for combustion development. However, its control in order to enhance turbulence level remains an important challenge.

Moreover, as indicated above, in the context of the new WLTP, the evolution of all physical processes that will affect the combustion during transition phases has to be taken into

account in order to predict them by simulation with great accuracy in order to avoid too many real engines tests. Due to the evolution of the optical diagnostics, transient phenomena can be more and more characterized, identified and understood. For example, high speed PIV has now used to analyze for instance cycle-to-cycle variations (Muller et al. (2010) [125]) and also direct interaction between the instantaneous flow and fuel fields on the ignition phase during the same cycle (Peterson et al. (2014) [141], Stiehl et al. (2016) [174]).

Parallel to the development of high speed PIV, large Eddy Simulation (LES) tool demonstrated its capacities to simulate several consecutive cycles (Goryntsev et al. (2009) [66], Hasse et al. (2010) [74], Enaux et al. (2011) [47], Vermorel et al. (2009) [186]). Although several individual cycles can be now simulated, it remains a challenge to identify the cause of in-cylinder flow evolution during one simulated cycle or one experimental.
Therefore, the development of signal processing to extract turbulence, coherent and large-scale structure from measured or computed velocity fields without any use of Reynolds average remains an important challenge. In the paper of Borée & Miles (2014) [18] this problematic is really well introduced and one conclusion is "*removal large-scale, anisotropic turbulent motions by inappropriate filtering will significantly impact the ability of the remaining 'turbulence' to transport mass and momentum.*"

Different tools were developed and improved to accomplish this issue as mainly Proper Orthogonal Decomposition (POD). This method is called Principal Component Analysis (PCA) in signal processing community, developed first by Pearson (1901) [137] and Hotelling (1933) [82] and suggested by Lumley (1967) [114] to extract coherent structures from turbulent flow.
POD is really interesting tools to extract large and smaller scales motions from in-cylinder velocity fields (Baby et al. (2002) [7], Fogleman et al. (2004) [56], Roudnitzky et al. (2006) [164], Foucher et al. (2008) [57], Voisine et al. (2011) [188]). An interesting recent study (Abraham et al. (2014) [1]) compared different decomposition (ensemble averaging and RMS fluctuations, phase-dependent POD modes computed for the LES and PIV samples separately, phase-dependent POD modes of the combined samples, and phase-invariant POD using two different normalization schemes) to improve LES results in comparison to experimental velocity fields. It concluded the phase-invariant POD has a great potential to improve the understanding of cycle development of the in-cylinder flow.

However, the difficulty remains the choice of the mode to be considered for large scale, cyclic variations motion or turbulence energy. In addition POD method is associated with the statistical description of flow that restricts its interest to the non-stationary dynamic phenomena. Also analysis of in-cylinder flow by this approach needs numerous instantaneous velocity fields at a given crank angle, that is not pragmatic when using LES simulations due to the high cost and computational complexity.

More recently, another decomposition method has been also evaluated as a potential tool to analyze both nonlinear and non-stationary data, called Empirical Mode Decomposition (EMD) introduced by Huang et al. (1998) [91]. This method is intuitive, direct and adaptive, with a posteriori-defined decomposition basis driven entirely from the data themselves. EMD meets a great success in various field of science such as seismology

(Zhou et al. (2012) [212]) and geophysics (Feynman & Ruzmaikin (2014) [52]), biology (Liang et al. (2005) [108]), atmospheric physics (Qian et al. (2011) [57], Franzke (2014) [59]) and brain-computer interface (Wu et al. (2011) [198], Hemakom et al.(2016) [79]).
Huang et al. (1999) [90] used EMD and Hilbert transform to assess the evolution of Stokes and nonlinear water waves, they demonstrate the advantages of this approach compare to wavelet decomposition in identification of different events in the velocity field. Huang et al. (2008) [93] applied EMD on homogenous turbulence time series to investigate turbulent scaling intermittency. Benramadan et al. (2007) [11] and Ducoin et al. (2009) [44] applied EMD to analyze temporal evolution of turbulent flow pressure over a transient moving hydrofoil.
Foucher & Ravier (2010) [58] determine turbulence properties on a periodic or random perturbed flow and Mazellier & Foucher (2011) [120] have used EMD to separate coherent structures from random turbulent fluctuations. All these applications are limited to the temporal analysis of the one component of the local velocity vector in flow field.

The EMD was also applied on two-dimensional data during last decade. The Bidimensional EMD meets remarkable success in image processing (Linderhed (2009) [110], Looney & Mandic (2009) [113]) and pattern recognition (Nunes et al. (2005) [131], Guanlei et al. (2009) [70]).

The EMD has two unique properties:

1. It is fully adaptive without any use of basis function in decomposition process so avoids the inflexibility linked to the basis function, contrary to Fourier transform or Wavelet decomposition, and it is suitable to analyze nonlinear and nonstationary phenomena;

2. It provides sparse representation (decomposition) of a given signal i.e. the fewest number of components (modes) in different continuous sub-bands with characteristic frequency. It acts as a dyadic filter bank while decomposed a signal, (Flandrin et al. (2004) [55], Wu & Huang (2004) [199] and (2009) [201]). As a notice the dyadic filter bank decomposes a broad band signal into a collection of successively more band limited components by repeatedly dividing the frequency range.

These interesting properties of EMD and its ability to extract physical information from complex signal can motivated ones to using this approach to analyze in-cylinder unsteady turbulent flow. By using this approach there is no needs to have several velocity fields (snapshots) at a given crank angle and just one velocity field is decomposed to several modes. Then by using an appropriate criterion, the turbulent fluctuations can be separated from the in-cylinder large-scaled organized motion. Such an approach is appeared quiet suitable for study of in-cylinder flow within individual cycle when the engine operates in transient condition.
However, to our knowledge, the EMD analysis has not yet been developed in signal processing community for decomposition of 'bivariate (two component) two-dimensional' data as the two-dimensional velocity field in which the velocity vector has two components i.e. horizontal and vertical velocities.
Therefore, one the main objective of this thesis is to extend the EMD method for decomposition of two component (or multicomponent) two-dimensional signals in order to study the evolution of large-scale structure of in-cylinder flow and to estimate turbulent

fluctuations that have a great influence on flame propagation and so the improvement of combustion process. First, the method is improved by using generated perturbed flow fields, which are a combination between experimental turbulent fields from turbulent spherical vessel and a large scale rotating motion, simulated the Tumble motion in SI engines. In the case of the future WLTP, the evolution of physical processes during transient regime will affect numerical prediction, which suffers at the moment from the lack of experimental data.

The other objective is to provide data for the first time about the flow field evolution in the case of strong regime transition from 1000 to 2000 rpm as function of number of cycles to realize this transition. The velocity fields are obtained within tumble plane in a mono-cylinder DISI engine bench by using a new adapted device and applying high speed 2D-2C PIV system. Flow-fields are also obtained in the case of stable regime in order to provide some statistics comparisons. The purpose is evaluate the change (or not) on the evolution of the Tumble motion during the intake and the compression stroke in transient conditions compared to stable regime.

Overview of the Thesis

Chapter 1 provides a review of in-cylinder flow in SIDI engine. The large-scaled organized motion, its evolution during the cycle and the source of turbulent fluctuations during intake and compression stroke are presented from literature study. Different parts of instantaneous in-cylinder velocity field are explained and the several approach that are commonly used to extract random turbulent fluctuations from velocity field are mentioned.

Chapter 2 describes in details the EMD approach and its algorithm in temporal domain i.e. when it decomposes data time series in a given point. In first section the standard mono variate EMD is investigated and then its extended versions that used an assistant-noise to improved decomposition quality and to reduce mode-mixing problem are discussed. In the second section the EMD analysis appropriate for processing the bivariate signals (like temporal velocity vector with two horizontal and vertical components, U and V in a fixed point), and Trivariate signal i.e. velocity vector with U, V, W components are presented. Afterwards the Multivariate EMD (MEMD) that decompose any temporal signal with several components and Noise-Assisted Multivariate EMD (NA-MEMD) are explained.

Chapter 3 is dedicated to description of Two-dimensional EMD (2D-EMD) that decomposes a given two-dimensional signal in different two-dimensional modes. At first Monovariate 2D-EMD and the developments of such approach is discussed. In the fluid mechanics, it is related with the decomposition of a 2D velocity field in which the velocity vector has one component, either U or V. Then Bivariate 2D-EMD is presented: this method can allow the decomposition of any 2D and 2components signal, as for example, one instantaneous 2D velocity field, containing both U and V components.

Chapter 4 is dedicated to the application of EMD in turbulent flow and the validation of

the proposed Bivariate 2D-EMD. At first perturbed turbulent velocity fields are decomposed by different methods i.e. EMD, EEMD, CEEMD and CEEMDAN. Here the signal under analysis is a temporal series of a one component velocity vector at a fixed point in a turbulent flow. The quality of decomposition via different methods is evaluated in order to find which method is more adapted for decomposition of turbulent velocity field. In the next section for the first time, Bivariate-EMD is applied on the time series turbulent velocity field in order to separate organized motion from Homogeneous and Isotropic Turbulence (HIT) flow. The last section of this chapter is dedicated to the validation of Bivariate-2D EMD when process the 2D turbulent velocity field, the ability of such approach in separation of large-scale organized motion from HIT flow is evaluated.

Chapter 5 presents SIDI engine test bench and High speed PIV set-up used in this thesis work. An overview of the earlier PIV measurements applied on in-cylinder flow is also provided. The conditions of engine operation in transient and stationary regimes are described, especially the intake, in-cylinder and exhaust pressures are compared.

Chapter 6 consists of two parts, the first part provides an analysis of the evolution of in-cylinder organized motion during transient regimes as well as stationary condition. The flow pattern and the characteristic of the Tumble motion, its center trajectory and the evolution of its intensity, during intake and compression strokes are studied for both transient and stationary conditions. In the second part the proposed Bivariate 2D-EMD in Chapter 3, is applied on the experimental in-cylinder velocity field in order to separate flow high frequency part i.e. random turbulent fluctuations from the low frequency part i.e. large-scale organized motion. This separation of different component of in-cylinder flow is carried for the instantaneous velocity fields that are obtained in transient as well as stationary engine operation condition. The results for stationary condition are compared with ones obtained by POD analysis.

Introduction (Version Française)

La législation sur le CO2 devenant de plus en plus stricte, la mesure des émissions de CO2 de tous types de véhicules dans des conditions de conduite plus réalistes est devenue impérative. Une nouvelle procédure internationale plus reproductible du fonctionnement réel a été adoptée par l'Union Européenne en remplacement du cycle européen de conduite (NEDC), the World-Harmonized Light-Duty Vehicles Test Procedure (WLTP), qui sera utilisé dès 2020. The International Council on Clean Transportation [122] a évalué les principales améliorations entre NEDC et WLTP : le cycle de conduite lui-mÃłme, plus long et dynamique, l'effet de la masse du véhicule et les conditions de démarrage à froid.

En effet, comme indiqué, il est bien connu qu' "en plus de la charge du moteur, le régime du moteur a un impact direct sur les émissions de CO2" [122], vu que l'émission de CO2 est fortement liée à la consommation de carburant spécifique. Par conséquent, les différences entre les deux WLTP à NEDC sont aussi visibles sur le nombre important de transitions entre faible et moyen régimes moteur et moyen et fort régimes pour considérer l'impact de l'accélération.
Ces nouvelles contraintes réglementaires nécessitent une modélisation des phénomènes physiques pendant les moteurs en régimes transitoires afin de prédire l'impact de nouvelles technologies et leur utilisation sur les émissions de CO2, CO, HC, NOx et suie. Des études précédentes, expérimentales ou de modélisation ont clairement montré le lien entre l'écoulement dans le cylindre, le mélange combustible/air et le développement de la combustion (Arcoumanis et al. (1998) [5], Lumley et al (2001) [116], Lee et al. (2007) [105]).

Dans le cas des moteurs à allumage commandé comme l'écoulement dans le cylindre affecte la première étape du développement de la combustion, c'est-à-dire le noyau de la flamme (Pajot & Mounaim-Rousselle (2000) [136]), il impacte également les ratés d'allumage ou la combustion de pré-allumage, Yamakawa et al. (2011) [205]). Dans la majorité des cas, ces mouvements sont optimisés pour casser les structures à grande échelle, permettant de générer la turbulence elle-même, nécessaire au développement de la combustion à l'échelle du temps moteur (Voisine et al. (2011) [188]). En effet, la vitesse de la flamme laminaire n'est pas assez élevée pour brûler le mélange air / carburant pendant la courte durée du processus de combustion, tandis que les fluctuations turbulentes à petite échelle provoquent le plissement de la flamme et donc augmentent la vitesse de combustion pour améliorer l'efficacité du moteur. La fragmentation des mouvements organisés à grande échelle dans le cylindre est l'une des principales sources de turbulence requise pour le développement de la combustion. Mais, son contrôle afin d'améliorer le niveau de

turbulence reste un défi important.

De plus, comme indiqué précédemment, dans le contexte du nouveau WLTP, il devient important de prendre en compte de l'évolution de tous les processus physiques qui affectent la combustion pendant les phases de transition, afin de pouvoir comparer et améliorer la simulation et ainsi apporter des outils précis évitant de nombreux tests de moteurs réels. Du fait de l'évolution des diagnostics optiques à haute cadence, les phénomènes transitoires peuvent être désormais caractérisés, identifiés et mieux maitrisés. Par exemple, la PIV à haute cadence a permis d'analyser les variations de cycle à cycle (Muller et al. 2010) [125]) ainsi que les interactions directes entre l'écoulement instantané et les champs combustibles sur la phase d'allumage au cours du même cycle (Peterson et al. (2014) [141], Stiehl et al. (2016) [174]).

Parallèlement au développement de la PIV à haute vitesse, l'outil de simulation à grande échelle (LES) a démontré ses capacités à simuler plusieurs cycles consécutifs (Goryntsev et al. 2009) [66], Hasse et al. (2010) [74], Enaux et al. (2011) [47], Vermorel et al. (2009) [186]). Mais bien que plusieurs cycles individuels puissent maintenant Ãłtre simulés, la comparaison directe avec l'expérience reste délicate. Par conséquent, le développement de traitement du signal sans l'utilisation de la moyenne de Reynolds afin d'extraire la turbulence et les grandes échelles d'écoulement, que ce soit sur des champs de vitesse instantanés mesurés ou calculés reste un défi important. Cette problématique, introduite dans l'article de Borée & Miles (2014) [18] est bien résumée par "l'enlèvement des mouvements turbulents anisotropes à grande échelle par un filtrage inapproprié aura un impact significatif sur la capacité de la turbulence restante à transporter la masse et la quantité de mouvement".

Différents outils ont été développés et améliorés pour répondre à ce problème comme la décomposition en modes propres orthogonaux (POD). Cette méthode est appelée Analyse en Composantes Principales (PCA) dans la communauté de traitement du signal, développée par Pearson (1901) et Hotelling (1933) [82] et suggérée par Lumley (1967) [114] pour extraire des structures cohérentes d'un écoulement turbulent. Le POD est un outil très intéressant pour extraire les mouvements des grandes et des petites échelles à partir des champs de vitesse dans le cylindre (Baby et al. 2002), Fogleman et al (2004) [56], Roudnitzky et al. (2006) [164], Foucher et al. (2008) [57], Voisine et al. (2011) [188]). Une étude récente d'Abraham et al. 2014 a comparé différentes décompositions basées sur la POD en comparant avec les moyennes d'ensemble et fluctuations RMS afin d'améliorer les résultats de LES par rapport aux champs de vitesse expérimentaux. Il a conclu que la POD a un grand potentiel pour améliorer la compréhension de du cycle développement d'écoulement dans le cylindre. Cependant, la difficulté reste le choix du mode à prendre en compte pour la grande échelle, les variations cycliques d'écoulement ou l'énergie de turbulence. De plus, la méthode POD est associée à la description statistique d'écoulement qui restreint son intérêt pour les phénomènes instationnaires. De même, l'analyse d'écoulement dans le cylindre par cette approche nécessite de nombreux champs de vitesse instantanés à un angle de vilebrequin donné, ce qui n'est pas pragmatique lorsqu'on utilise des simulations LES en raison du coût élevé et de la complexité de calcul.

Plus récemment, une autre méthode de décomposition a également été évaluée pour analyser les données instationnaires et non-linéaires, appelée la décomposition modale empirique, ou encore Empirical Mode Decomposition (EMD) en anglais, introduite par Huang et al. (1998) [91]. Cette méthode est intuitive, directe et adaptative, avec une base de décomposition, à postériori, définie entièrement à partir des données elles-mÃłmes. L'EMD rencontre un grand succès dans divers domaines scientifiques tels que la sismologie (Zhou et al (2012) [212]), la géophysique (Feynman & Ruzmaikin (2014) [52]), la biologie (Liang et al (2005) [108]), la physique atmosphérique (Qian et al (2011) [146], Franzke (2014) [59]) et l'interface cerveau-ordinateur (Wu et al (2011) [198], Hemakom et al. (2016) [79]).
Huang et al. (1999) [90] ont utilisé l'EMD et la transformation Hilbert pour évaluer les vagues non-linéaires d'eau, ils démontrent les avantages de cette approche par rapport à la décomposition par ondelettes dans l'identification de différents événements dans le champ de vitesse d'écoulement. Huang et al. (2008) [93] ont appliqué l'EMD sur des séries temporelles homogènes de turbulence pour étudier l'intermittence de l'échelle turbulente. Benramadan et al. (2007) [11] et Ducoin et al. (2009) [44] ont appliqué l'EMD pour analyser l'évolution temporelle de la pression d'écoulement turbulent sur un hydrofoil en mouvement transitoire. Foucher & Ravier (2010) [58] ont déterminé les propriétés de turbulence sur un écoulement perturbé périodique ou aléatoire et Mazellier & Foucher (2011) [120] ont utilisé EMD pour séparer des structures cohérentes à fluctuations turbulente aléatoire. Toutes ces applications sont limitées à l'analyse temporelle de l'une des composantes du vecteur de vitesse locale dans le champ d'écoulement.
L'EMD a également été appliqué à des données bidimensionnelles récemment. L'EMD bidimensionnelle rencontre un succès remarquable dans le traitement de l'image (Linderhed (2009) [110], Looney & Mandic (2009) [113] et la reconnaissance de motifs (Nunes et al. 2005) [131], Guanglei et al. (2009) [70]).

L'EMD a deux propriétés uniques:

1. Il est entièrement adaptatif sans aucune utilisation de la fonction de base dans le processus de décomposition ce qui évite l'inflexibilité, contrairement à la transformée de Fourier ou décomposition en ondelettes. Elle convient donc pour analyser des phénomènes qui sont instationnaires et non-linéaires.

2. Il fournit une représentation, soit une décomposition, clairsemée d'un signal donné, c'est-à-dire le moins nombre de composants (modes) dans différentes sous-bandes continues avec une caractéristique de fréquence. Il se comporte comme une banque de filtres dyadiques lors de la décomposition d'un signal (Flandrin et al. (2004) [55], Wu & Huang (2004) [199] et (2009) [201]).

Ces propriétés intéressantes de l'EMD et sa capacité à extraire des informations physiques d'un signal complexe peuvent motiver à utiliser cette approche pour analyser l'écoulement turbulent instationnaire dans le cylindre. En utilisant cette approche, il n'est pas nécessaire d'avoir plusieurs champs de vitesse (instantanés) à un angle de vilebrequin donné et un seul champ de vitesse est décomposé en plusieurs modes. Puis en utilisant un critère approprié, les fluctuations turbulentes peuvent être séparées du mouvement organisé à grande échelle dans le cylindre. Une telle approche est apparue tout à fait approprié pour l'étude de l'écoulement dans le cylindre dans un cycle individuel quand le moteur fonctionne en état transitoire.

Cependant, à notre connaissance, l'EMD n'a pas encore été développée par la communauté de traitement du signal pour la décomposition des données bivariées (deux composantes) en espace bidimensionnel comme un champ de vitesse bidimensionnel dans lequel le vecteur de vitesse a deux composantes.
Par conséquent, l'un des principaux objectifs de cette thèse est d'optimiser et de valider la méthode EMD pour la décomposition de signaux bidimensionnels à deux composantes (ou multicomposants) afin d'identifier l'évolution des structures à grande échelle dans le cylindre. La méthode est dans un premier temps améliorée en utilisant des champs d'écoulement perturbés synthétiquement en combinant les champs turbulents expérimentaux obtenus dans une enceinte sphérique turbulente et un mouvement de rotation à grande échelle qui simule le mouvement Tumble dans les moteurs GDI.

Le second objectif est de fournir les premières données de l'évolution de l'écoulement dans un cylindre moteur dans le cas de transition de régime moteur passant de 1000 à 2000 tr/min dans un temps plus moins long soit en plus ou moins de cycles. Les champs de vitesse sont obtenus dans le plan vertical centré de Tumble sur un moteur mono-cylindre GDI par PIV 2D2C à haute cadence. Des champs d'écoulement sont également obtenus dans le cas d'un régime stable afin de fournir des comparaisons statistiques. Le but est d'évaluer le changement (ou non) sur l'évolution du mouvement de Tumble pendant l'admission et la compression dans des conditions transitoires par rapport au régime stable. Enfin, une première décomposition par l'EMD 2D sur un exemple est proposée en comparaison en stationnaire avec la POD.

Plan du mémoire

Le chapitre 1 présente une étude bibliographique sur les différentes études, réalisées sur les écoulements dans le cylindre dans le moteur GDI. Le mouvement organisé à grande échelle, son évolution au cours du cycle et la source des fluctuations turbulentes pendant l'admission et de compression y sont rappelés. Différentes parties du champ de vitesse instantané dans le cylindre sont expliquées et les diverses approches couramment utilisées pour extraire la fluctuation turbulente aléatoire du champ de vitesse sont mentionnées.

Le chapitre 2 décrit en détail l'approche EMD et son algorithme dans le domaine temporel, c'est-à-dire lorsqu'il décompose des séries temporelles de données en un point donné. Dans la première section, le standard EMD mono variée est étudiée, puis ses versions étendues avec l'ajout d'un bruit pour améliorer la qualité de décomposition et réduire le problème de mélange de mode (Mode-mixing) y sont discutées. Dans la deuxième section, l'analyse EMD appropriée pour le traitement des signaux bivariés (comme un vecteur de vitesse temporel avec deux composantes horizontales et verticales, U et V dans un point fixe), et un signal trivarié, c'est-à-dire un vecteur de vitesse avec des composantes U, V, W est présentée. Ensuite, l'EMD multivariable (MEMD) qui décompose tout signal temporel avec plusieurs composants et EMD multivariable assisté par bruit (NAMED) sont expliqués.

Le chapitre 3 est dédié à la description de l'EMD bidimensionnel (2D-EMD) qui décompose un signal bidimensionnel donné dans différents modes bidimensionnels. Dans

un premier temps l'EMD 2D monovariate et les développements d'une telle approche est discutée. Dans la mécanique des fluides, elle est liée à la décomposition d'un champ de vitesse 2D dans lequel le vecteur de vitesse a une composante, U ou V. Puis Bivariate 2D-EMD est présenté: cette méthode peut permettre la décomposition de tout signal 2D et 2 composantes, comme par exemple un champ de vitesse 2D instantané, contenant à la fois des composantes U et V.

Le chapitre 4 est consacré à l'application de l'EMD en écoulement turbulent et à la validation de Bivariate 2D-EMD. Dans un premier temps, les champs de vitesse turbulents perturbés sont décomposés par différentes méthodes: EMD, EEMD, EEMD, CEEMD et CEEMDAN. Ici, le signal analysé est une série temporelle d'un vecteur de vitesse à une composante à un point fixe dans un écoulement turbulent. La qualité de la décomposition par différentes méthodes est évaluée afin de trouver quelle méthode est la plus adaptée à la décomposition du champ de vitesse turbulente. Dans la section suivante pour la première fois, l'EMD bivariate est appliqué sur le champ de vitesse turbulent de la série temporelle afin de séparer le mouvement organisé de l'écoulement turbulence homogène et isotrope (THI). La dernière section de ce chapitre est dédiée à la validation de Bivariate 2D-EMD lors du traitement du champ de vitesse turbulente 2D, la capacité d'une telle approche dans la séparation du mouvement organisé à grande échelle de l'écoulement THI est évaluée.

Le chapitre 5 présente le dispositif expérimental : le moteur à accès optiques à injection directe ainsi que le système PIV à haute cadence utilisé dans cette thèse. Une vue d'ensemble des mesures de PIV antérieures appliquées à l'écoulement dans le cylindre est également fournie. Les conditions de fonctionnement du moteur dans des régimes transitoires et stationnaires sont décrites, en particulier les pressions d'admission, de cylindre et d'échappement sont comparées.

Chapitre 6 se compose de deux parties, la première partie fournit une analyse de l'évolution de mouvement organisé dans le cylindre pendant les régimes transitoires ainsi que l'état stationnaire. La configuration d'écoulement et la caractéristique du mouvement organisé (Tumble), la trajectoire de sa centre et l'évolution de son intensité, pendant les courses d'admission et de compression sont étudiées pour les conditions transitoires et stationnaires.

Dans la seconde partie, le Bivariate 2D-EMD proposé dans le chapitre 3 est appliqué sur le champ de vitesse expérimental dans le cylindre afin de séparer la partie de haute fréquence d'écoulement, c'est-à-dire les fluctuations turbulentes aléatoires à la partie basse fréquence, c'est-à-dire mouvement organisé. Cette séparation des différentes composantes de l'écoulement dans le cylindre est réalisée pour les champs de vitesse instantanée qui sont obtenus en condition de fonctionnement du moteur à la fois transitoire et stationnaire. Les résultats pour l'état stationnaire sont comparés à ceux obtenus par analyse POD.

Chapter 1

In-cylinder flow aerodynamic

1.1 The direct-injection spark-ignition engine

The Direct-Injection Spark-Ignition (DISI) (or Gasoline Direct Injection (GDI) technology was first developed in France in V8 engine configuration by Leon Levavasseur in 1902 and commonly used for farm tractors during the 30's (Lumley (1999) [115]) and also for aircrafts during the second world war. In the early 1950s this technology was used in two-stroke engine due to low fuel consumption however the first car with a four-stroke GDI engine was developed in 1955 (Mercedes-Benz, 300 SL). The interests of GDI engine around the world for many automotive car manufacturers were reinitiated when Mitsubishi in 1997 announced the difference fuel strategies and the fuel consumption gain reached (Queiroz & Tomanik (1997) [147]).
The DISI engines have great advantages: as the charge can be more stratified than in the case of port-fuel injection engines, the fuel efficiency can be improved. The evaporation of injected fuel droplet cools the entire in-cylinder charge hence increases the volumetric efficiency. Therefore, the fuel consumption can be reduced up to 35% (Zhao et al. (1999) [211]). As the stratification strategy can be optimized to avoid knock, they can operate with low octane number fuels. In addition in transient modes these engines are efficient, fast starting with less cold enrichment reducing cold-start hydrocarbon emission as well as CO2 emissions, (Lumley (1999) [115]).
The DISI engine provides an easier and wider air-flow control compared to compression-ignition (CI) engines, although as in CI engines, multiple injections during compression stroke can also be optimized to provide efficient air-fuel mixing. In the other hand, as in diesel engines, large fuel droplets can need more time to evaporate, involving incomplete combustion and exhaust pollutants emissions increase. Furthermore even in partial loads, due to the high temperature in the reaction zone, DISI engines can produce considerable amount of NOx.
At low loads the fuel is injected late during the compression stroke (usually called 'stratified mode') and as the load increases in order to give sufficient time to the fuel to be mixed with in-cylinder air, the start of injection is advanced, closer to the intake stroke (usually called 'homogeneous mode'). According to how the spray fuel is transported near the spark plug to form an ignitable mixture, three different systems have been developed during several years.

1) Wall-guided systems: is the first one, used in GDI engines to stratify the charge, in which the spark plug remains in the central position and the direct injector is located on one side of combustion chamber, Figure 1.1a. The stratification is based on the interaction between the fuel spray at piston head. For this purpose, the piston head has a special design (a kind of non-symmetrical double bowl or cavity shape) to guide the fuel spray near the spark plug. But while the fuel spray impacts the piston head some fuels remain on the bowl surface and wet it which does not favor complete vaporization. Therefore, the consequences are fuel consumption increase as well as CO and HC emissions.

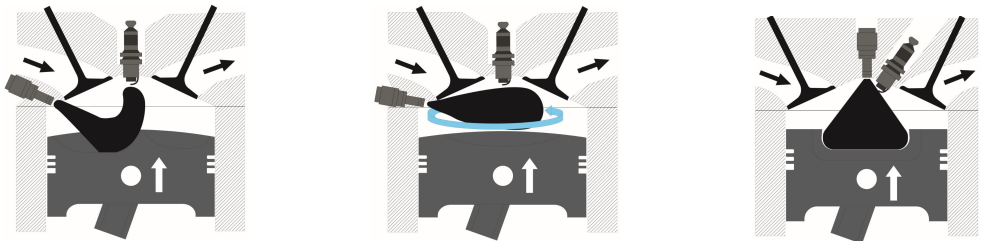

(a) Wall-guided (b) Air-quided (c) Spray-quided

Figure 1.1: Simplified schematics of the different combustion systems for GDI engine in stratified mode, from Stefan (2004) [173].

2) Air-guided systems: both spark plug and injector are located in the same position than in wall-guided system as in Figure 1.1b, but the piston head has a special shape to compress fuel spray and governs it near the spark plug (Baumgarten, 2006) [10]). In this system there is less pollution due to fuel wetting on piston surfaces but it is very sensible to the in-cylinder air motion and its cycle to cycle variations.

3) Spray-guided system: injector is placed closed to the spark plug, near the cylinder head center, as shown in Figure 1.1c. The stratification process is then based on the spray dynamics and its characteristics however the shape of piston head and air motion have less influence. This technology provides a higher efficiency compared to the other ones but needs advanced injector device as piezo injector. This stratification process is less sensible to in-cylinder flow variation and piston head wetting itself. Symmetrical injection of fuel promotes fuel-air mixing process and increases stratified operation range. But such a method is more affected by the injection. The cyclic variations of the ignition and of spray vaporization reduce the engine performance. Therefore, it can be said that the effects of the in-cylinder flow in the case of DISI engine are the causes of the lower performance of this kind of engine and need to be well understand, experimentally and numerically to be optimized to design high efficiency engines. In the following part, more details about the in-cylinder flow specification will be given.

1.2 In-cylinder flow

The in-cylinder flow plays a major role in the performance of Internal Combustion Engine (SI, CI, HCCI engine). The resistance to auto-ignition, misfire, heat transfer, filling-emptying efficiency and post-combustion are all affected by air motion. Air-fuel mixing

process is accomplished by both the mean flow structure and turbulent eddies (Rothrock & Spencer (1939) [163], Lumley (1999) [115], Petersen & Miles (2011) [138]). The in-cylinder flow is the result of numerous parameters such as intake manifold and geometry (Haworth et al. (1990) [75], Stiehl et al. (2016) [174]), the position and number of inlet valves, valves schedule, fuel injection system, cylinder head geometry (Freudenhammer et al. (2015) [61]) the shape of the combustion chamber (Fujimoto et al.(2002) [62]) or of the piston head (Krishna & Malikarjuna (2010) [103]). The engine designers investigate and modify these parameters to optimize the in-cylinder flow for improving engine efficiency as well as reducing air pollution.

Large-scale motion

The generic Large-scale organized motions in the cylinder scale of IC engines are separated in two types:

- The *Swirl* motion, a rotational motion about the axis parallel to cylinder axis, Figure 1.2a, generated when air jet enters to the cylinder by some angular momentum.

- The *Tumble* motion (sometimes called the 'vertical swirl'), a bulk fluid motion about axis perpendicular to the cylinder axis and to the symmetric plane Figure 1.2b. The air rotation at the plan perpendicular to tumble plane is called cross-tumble. These two motions are responsible for the air macro mass transport inside the engine cylinder.

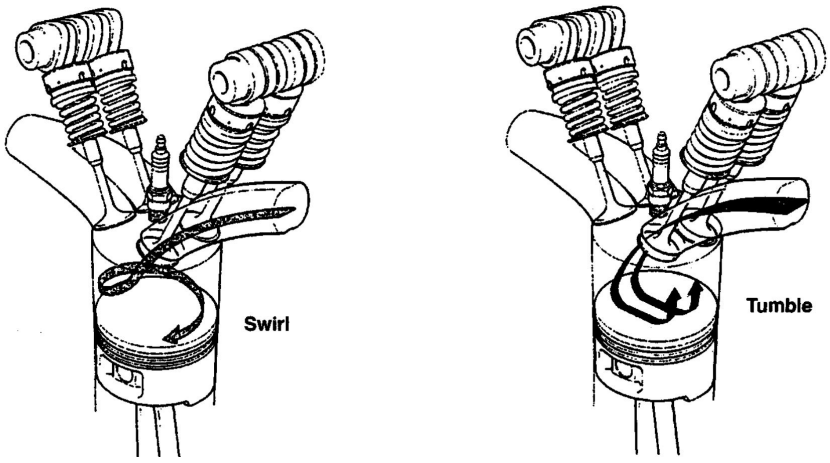

(a) (b)

Figure 1.2: Two kinds of large-scale organized motions within engine cylinder, from Lumley (1999) [115].

Due to the shape of the combustion chamber and the combustion processes, Tumble is more adequate for SI engines and Swirl for Classical Diesel engines. However, some DISI engines were designed with some swirl motions. Tumble and Swirl motions are generated by mass flow through the inlet valves or can be controlled by the throttle plates installed at the intake ports. Moreover in the case of CI engines, some additional motions as Squish

one, can be developed.

Inducing and manipulating of large-scale organized motions have a considerable importance for ICE combustion development. The momentum and energy of the intake flow through the valves are stored in these motions, due to the large scale feature they are less dissipative compared to turbulent energy. This energy is then used for mixing the injected fuel and air charge, and then to affect combustion itself and also post-combustion process. Both Tumble and swirl are characterized by non-dimensional number so-called tumble or swirl ratio, defined as the ratio between the tumble (resp. swirl) angular velocity to the crankshaft angular velocity, $R_t = \omega_t/(2\pi N)$, where N is the engine rotation rate (revolutions per second). The tumble (or swirl) angular velocity, ω_t is taken as one for the solid-body rotating flow that has the same averaged angular momentum as the real tumble (or respectively swirl), Lumley (1999) [115]). It is easier to determine in steady flow the swirl ratio (Reuss et al. (1995) [160] and Petersen & Miles (2011) [138]) than the tumble ratio, usually computed in transient flow experiments since the piston motion has a significant impact on tumble structure (Khalighi et al. (1991) [101]).

The intensity of organized motions, the location of the motion center and the evolution of their structures during intake and compression strokes have a great influence on the combustion, especially near TDC (Kent et al. (1989) [99], Hill & Zhang (1994) [81]). In SI engines the local flame speed depends on the turbulence front of the flame, the turbulence reduces the combustion duration. Hadded & Denbratt (1991) [72] investigated the correlations between the turbulent properties in a tumble flow and flame propagation rate as well as combustion duration in a SI engine. Hu et al. (1992) [85] and Pajot & Mounaim Rousselle (2000) [136] studied the effect of turbulent mixture motion just before the spark, on flame propagation and combustion characteristics in a SI engine. When the engine operates under partially load, in which lean mixture burns slowly, or at high speed that needs complete oxidation in shorter time, the turbulent fluctuating velocity improves combustion propagation and so increase engine performance. It is worthwhile to mention that Ricardo and Clerk are the first, at the early of 1900s, to observe the influence of turbulent flow on the quality of combustion process in engine cylinder, Lumley (2001) [116].

1.2.1 Turbulence production in GDI engine

As, inside the cylinder different scales of turbulence are generated from the largest turbulence scale in the order of the size of the flow boundaries to the smallest-scale of random fluctuations. The inlet air jet is unsteady, inhomogeneous and strongly turbulent due to the shear stress, further when the intake air encounters inlet valves or the solid boundary near this area, the flow separation can be generated some recirculation zones (ring-vortex) under inlet valves (Ekchian & Hoult (1979) [45]) enforcing turbulent fluctuations as shown in Figure 1.3b.

Dannemann et al. (2011) [37] investigated the 3D structure of velocity field in a four-valve research engine and observed the generation of two ring-vortices during intake stroke in the plan perpendicular to tumble plane as Foucher et al. (2008) [57]. They demonstrated these vortices have a more significant role than the tumble motion itself in the in-cylinder

mixing process.
Bücker et al. (2012) [20] by applying stereoscopic PIV in a DISI engine observed these structures at about 60 CAD after intake TDC as represented in the example Figure 1.3b The center of ring-vortices remains in the half way between the piston and cylinder head during intake stroke.

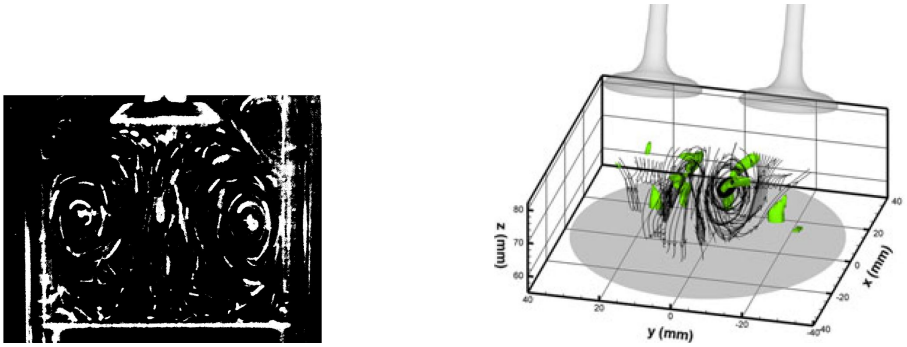

(a) (b)

Figure 1.3: Two mean ring-vortices generated under inlet valves; (a) by hydraulic analogous in a IC engine, from Ekchian & Hoult (1979) [45], (b) by Stereoscopic PIV in a DISI engine, from Bücker et al. (2012) [20].

When the inlet valves are closed, most of the mean flow energy of inlet jet is also converted into the turbulent energy. A large amount of intake Turbulent Kinetic Energy (TKE) is decayed during intake stroke due to the viscous dissipation. Around the Bottom Dead Center (BDC) for a few number of CAD, the mean flow pattern experiences some relaxations. It should be mentioned the jet-piston interaction during intake stroke causes the flow pattern becomes more complex, it is one of the origins of the flow large-scale variability cycle to cycle (Voisine (2010) [187]).

Contrary to intake stroke in which the flow is divergent free, during the compression stroke, the work done by piston increases the mean flow energy via tumble motion. In fact conservation of angular momentum when the density change induces the intensification of tumble vortex whereas the tumble vortex length is fixed during compression stroke, called Spin-up process. The increase in rotation rate is proportional to the ratio of fluid density at BDC and at TDC, i.e. to the compression ratio. Tumble motion has two major roles: First, it encapsulates the mean flow momentum and energy, and gives them back as a turbulent kinetic energy when it is locally needed for combustion process. Second, it can increase the mean flow energy due to the compression process hence more turbulent kinetic energy will be generated near TDC by tumble breakdown.

During compression stroke as the piston approaches to TDC, the rotation axis of the tumble (ellipsoidal rotation flow) changes and becomes unstable (Obukhov (1976) [133] and (2000) [132], Gledzer & Ponomarev (1992) [65], Lundgren & Mansour (1996) [117], Lumley (2001) [116]). The perturbations, even tiny, develop this instability and the tumble breaks up into strong small-scale motions. Further instabilities produce multiple small vorticities and generate high turbulence kinetic energy. Several authors report the beginning of tumble breakup mechanism at about 60 CAD before TDC (Arcoumanis et al.

(1990) [6], Borée et al. (2002) [17]).
Voisine et al. (2011) [188] studied the evolution of tumble motion during the end-half of compression stroke, they show the transfer of mean flow energy to turbulent fluctuations starts at about 60 CAD bTDC even though cyclic variations of in-cylinder mean flow has about 30% contribution in the fluctuating kinetic energy near TDC. Muller et al. (2010) [125]) compared the evolution of flow spatial averaged kinetic energy and turbulent one during compression at different engine speed. They observed by increasing the engine speed, the transfer of energy from mean flow to turbulence occurs earlier in the compression stroke.

In the case of DISI engine, the interaction of fuel spray with the large flow motion has a great influence on turbulent kinetic energy. Spray can reinforce tumble vortex and modifies its evolution (Yamakawa et al. (2011) [205], Chen et al. (2011) [29]) and consequently impacts turbulence generation process near TDC. Moreau et al. (2004) [123] analyzed the tumble vortex in a compression chamber that mimics engine cylinder. They observed early breakdown of tumble in the presence of direct injection jet, which provides more time for dissipation of turbulent kinetic energy due to tumble-jet interaction and so results in reduction of total turbulent kinetic energy.

1.2.2 Mean velocity and turbulence definition

The in-cylinder turbulent velocity field is unsteady since flow pattern changes during individual cycle and the mean flow varies from one cycle to another one. Turbulence is defined as a fluctuations about an average velocity so the instantaneous flow velocity at a given position within the cylinder can be written in general form as:

$$\mathrm{U}(\theta, i) = \overline{\mathrm{U}}(\theta, i) + \mathrm{u}(\theta, i) \tag{1.1}$$

Where U is the velocity vector at crank-angle of θ during cycle i , $\overline{\mathrm{U}}$ is the average velocity in this cycle and u is the velocity fluctuations about this average.

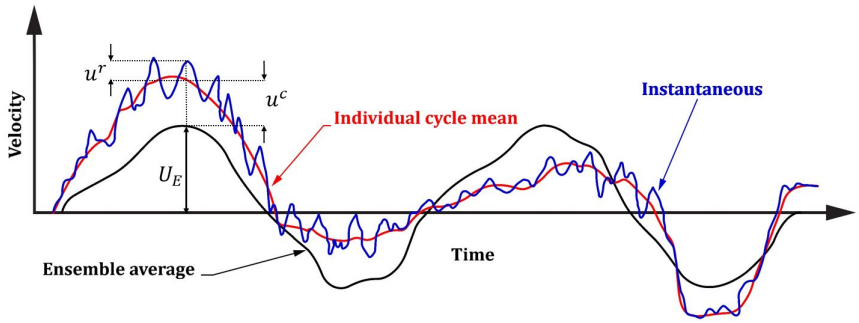

Figure 1.4: Decomposition of instantaneous flow velocity at a given point inside the engine cylinder, from Heywood (1988)[80].

If there is no change in the mean flow velocity for different cycles (quasi-periodic flow), the average velocity can be replaced by ensemble-averaged (phase-averaged) velocity $\mathrm{U}_{EA}(\theta)$, therefore instantaneous velocity field becomes:

$$\mathrm{U}(\theta, i) = \mathrm{U}_{EA}(\theta) + \mathrm{u}(\theta, i) \tag{1.2}$$

with $U_{EA}(\theta) = \frac{1}{N}\sum_{i=1}^{N} U(\theta, i)$ that is computed at each crank-angle, θ from a large number of N independent cycles. Whereas in unsteady turbulent flow, as the main motion varies a lot cycle to cycle due to large-scale variation in flow structures, the average velocity for one cycle i, can be defined as:

$$\overline{U}(\theta, i) = U_{EA}(\theta) + u^c(\theta, i) \tag{1.3}$$

Where $u^c(\theta, i)$ is the coherent fluctuations associated with cycle-to-cycle variation (CCV) (or cyclic variability) of the mean flow.
So the instantaneous velocity is defined as follows:

$$U(\theta, i) = U_{EA}(\theta) + u^c(\theta, i) + u^r(\theta, i) \tag{1.4}$$

$u^r(\theta, i)$ is the random turbulent fluctuations from the individual-cycle average as schematized in Figure 1.4. Therefore by using Eq (1.3), the term u includes two types of fluctuations: coherent fluctuations and random turbulent fluctuations, $u = u^c + u^r$.
This definition is associated with statistical description of turbulent flow, Reynolds Averaged Navier-Stokes (RANS) equations. By this approach the global characteristic of flow can be quite well predicted however since the small-scale structures of flow are eliminated, the understanding of turbulence in detail is infeasible.

The in-cylinder flow cyclic variation, associated with u^c, is due to the large-scale variation of flow structures from several origins (Lumley (1999) [115], Reuss (2000) [157]). During the intake stroke, the perturbations of air through the intake manifold and inlet valves, the fluctuations of turbulent air jet, the turbulent dissipation due to the interaction between the jet and the piston and the residual fluctuations from the previous cycle are responsible of the change in the large-scale flow pattern. The CCV generated during intake stroke can be amplified during compression stroke. Moreover, the tumble instability and the evolution of turbulence itself are some sources of this phenomenon during compression stroke. At the end, cyclic variability of the flow has a negative effect on combustion process (Ozdor et al. (1994) [134]) as it can cause misfire or non-controlled auto-ignition.

The other part of fluctuations i.e. random fluctuations u^r due to turbulent flow motion has also an important influence on flame development. For example, a high level of TKE at the vicinity of the ignition point accelerates the combustion and affects engine efficiency and pollutant emissions themselves.

1.2.3 Turbulence estimation from in-cylinder velocity field

Several approaches have been proposed to extract turbulent fluctuations from in-cylinder velocity field or to separate turbulent fluctuations from the large-scale coherent fluctuations, as presented in next sections:

- Filtering approaches
In these kinds of approaches the instantaneous velocity field is decomposed into low frequency part (mean) and high frequency part (turbulence). So the in-cylinder velocity field can be described as:

$$U(\theta, i) = U_{Lf}(\theta, i) + U_{Hf}(\theta, i) \tag{1.5}$$

Where $U_{Lf}(\theta, i)$ is the low frequency part, includes ensemble-averaged velocity and cyclic variability, $U_{Hf}(\theta, i)$ the high frequency part that corresponds to turbulent fluctuations.

$$U_{Lf}(\theta, i) = U_{EA}(\theta) + u^c(\theta, i) \quad , \quad U_{Hf}(\theta, i) = u^r(\theta, i) \tag{1.6}$$

Several tools (Fansler & French (1988) [50] and Catania & Mittica (1989) [25]) as moving average or cyclic averaging can do this kind of separation to decompose the flow into mean and turbulent components. Reuss et al. (1990) [159] applied a Gaussian spatial filter to instantaneous velocity to separate turbulence and Pajot (2000) [135] applied Fourier transform and Hamming filter on in-cylinder instantaneous velocity field.
Wavelet filtering was also used in different studies to extract turbulent fluctuations within engine flow (Wiktorsson et al. (1996) [195] , Sullivan et al. (1996) [177] and (1999) [178], Soderberg & Johansson (1998) [170]). These methods are reliable if there exist a clear distinct scale, in time or space, between the mean and turbulent flows. As most of the turbulent flows, in the case of engine flow (Enotiadis et al. (1990) [48]) the choice of a cut-off frequency (filtering criterion) remains a complex subject. The characteristics of estimated turbulence depend on how this threshold is selected, an inappropriate filter can remove the flow structures responsible for the mass and momentum transport but moreover no universal criterion has been defined.
Furthermore several modeling approaches have been used to evaluate the large-scale variability of in-cylinder flow and so to estimate random turbulent velocity field by large-eddy simulation (LES) (Haworth (1999) [76], Vermorel et al. (2009) [186], Granet et al. (2012) [68]) or by hybrid modeling like URANS (Unsteady RANS)/LES (Hass et al. (2010) [74]). The models are based on spatial low-pass filtering corresponds to Fourier decomposition in which a random small scale motions (more universal) are filtered out, these flow structures are then resolved by a closure model. Hence these methods also involve the size of filter that affects certainly the energy of predicted turbulent velocity field.

- POD

Proper orthogonal decomposition (POD), proposed by Lumley (1967) [114] in turbulence context, is a linear procedure that decomposes the velocity field into a set of orthogonal basis functions or modes in which flow structures containing most of the energy are reconstructed by a few modes, as coherent structures should be the structures that have the largest mean square projection on the velocity field. Unlike wavelet and Fourier transform in which the data are decomposed in a prior basis functions, POD modes are computed from the own properties of the data. POD has been applied to in-cylinder flow in several studies: as for example, Baby et al. (2002) [7] which used this method for separating turbulent fluctuations from cycle-to-cycle variations or Roudnitzky et al. (2006) [164] to recognized three parts in flow structure within the tumble plane through POD modes (mean, coherent and a random Gaussian fluctuation); Cosadia et al. (2006) [32] used this this method to investigate the evolution of swirl flow in different cycles during the compression stroke in a CI engine. Also Kapitza et al. (2010) [98] applied this method on intake valve flow in a DISI engine to analyze the flow structures and to study their influences on the in-cylinder flow fluctuations. Chen et al. (2012) [27] applied POD on a synthetic 2D velocity field for better understanding the properties of POD modes obtained from in-cylinder flow. Fogleman et al. (2004) [56] introduced phase-invariant POD that provides a suitable basis for low-order description of the velocity field. Voisine et al. (2011) [188] studied the breakdown and cycle-to-cycle variation of tumble flow in a

research engine by means of this method. However in the POD approach the separation between the contributions of the coherent and random fluctuations (incoherent) in turbulent velocity field is performed by truncating the series of the modes, this needs to define an objective criterion (Druault et al. (2005) [43], Roudnitzky et al. (2006) [164], Foucher et al. (2008) [57]). Therefore the difficulty is the same as in any filtering approaches and is due the fact that there is no clear separate scale between coherent and background turbulent velocity fields. It should be mentioned the POD filtering is a statistical approach associated with a convergence criterion, therefore when applying on unsteady flow it must satisfy the statistical convergence (Hekmati et al. (2011) [77], Druault et al. (2012) [42]), this feature restricts its applications to the flows intrinsically transient.

- Lagrangian finite time techniques
This approaches introduced by Haller (2002) [73] and Shadden et al. (2006) [168] for separation flow spatial coherence structure in the unsteady conditions. It was used to investigate the flow separation from in-cylinder wall (Voisine et al. (2011) [188] and Ruiz et al. (2010) [166]). This method also can be suggested for extracting turbulent fluctuations at the end of compression stroke.

- Cluster-based analysis
It was proposed by Cao et al. (2014) [24] for identification of cycle-to-cycle variation of in-cylinder flow. Cluster analysis is usually used in pattern reorganization, however in fluid mechanics extends the POD analysis and can be applied on any periodically driven flow at large Reynolds number.

From the highlights about, the way to get most accurate processing of the velocity fields, this study is focused on the potential of a new approach, based on Empirical Mode Decomposition, but for 2D and called Bivariate 2D-EMD to decompose in-cylinder instantaneous velocity fields. This approach is well adapted to the nonstationary and nonlinear phenomena. Moreover, one advantage of this method is only one unique velocity field is required, it is not a statistical method.
Therefore, especially in the case of transient engine mode, turbulent fluctuations could be extracted from one unique in-cylinder velocity field. During this work the proposed Bivariate 2D-EMD will be validated and tested in instantaneous velocity fields in engine with as objective to provide a better understanding of the evolution of the in-cylinder large-scale organized motion during the cycle itself.

Chapter 2

The empirical mode decomposition

Data are the main link we have with the real-life, hence data analysis is a critical issue in the scientific research. In most physical phenomena, the data is both nonlinear and nonstationary whilst standard data analysis methods are either for linear but nonstationary, or nonlinear but stationary or deterministic processes.

Traditional Fourier-based analysis (invented 1807 and fully developed by Plancherel (1933) [145]), can only give meaningful interpretation to linear and stationary processes and its application to nonlinear and nonstationary processes is problematic. Wavelet transforms (Strang (1989) [176], Haar (1910) [71], Daubechies (1992) [38]) and the Time-Frequency distribution (Flandrin (1998) [53], Gröchenig (2001) [69]) were design for nonstationary but linear data.

A drawback of such analysis method is that they represent the signal in terms of prior basis functions (harmonic, mother wavelet or sum of sinusoids with fixed frequency) hence the performance of the analysis is closely tied to how well the morphology of signals under study is represented by these selected basis elements.

There is various time series analysis method that are suitable for nonlinear dynamic but stationary or deterministic processes see, (Tong (1990) [181], Kantz & Schreiber (1999) [97], Diks (1999) [41]).

However presenting the signal in a well-established paradigm is mathematically rigorous but the final purpose is to find out the physical mechanism and to extract the information hidden in the observed process. A necessary condition to represent nonlinear and nonstationary data is to have an adaptive basis, in other words to let the data speak for themselves.
A few adaptive methods are available for signal analysis, as summarized by Windrows & Stearns (1985)[197] which relies mostly on feedback loops but not on an adaptive basis hence such methods are not convenient for nonstationary processes.

For the analysis of nonstationary and nonlinear data Huang et al. (1996) [89] and (1998) [91] introduce the method referred to as Empirical Mode Decomposition (EMD). In contrast to almost all of the previous methods, this new approach is intuitive, direct, and adaptive, with a posteriori defined basis derived from data.

The combination of the EMD and Hilbert spectral analysis (HSA) designated as the Hilbert-Huang Transform (HHT) by NASA, is a potentially tool for nonlinear and non-stationary data analysis, especially for time-frequency-energy representation. The EMD decomposes any complicated data set into a finite and often small number of simple intrinsic oscillatory modes, also called intrinsic mode functions (IMFs). An IMF is a counterpart to the simple harmonic function but instead of constant amplitude and frequency, it has both variable amplitude and frequency as function of time. After obtaining intrinsic mode components, one can compute instantaneous frequency by applying Hilbert transform on each component. The modes resulting from Empirical Mode Decomposition have the following properties:

- Adaptivity: The EMD bases are amplitude/frequency modulated (AM-FM) locally (Huang et al. (1998) [91] and Daubechies et al. (2011) [39]), data-adaptive, and sparse (Hou & Shi (2011) [83] and (2013) [84]) hence helping to find out intrinsic patterns at multiple scales. Therefore there is no need to rigid mathematical assumption linked to harmonic function or stationary data structures.

- Enhanced accuracy: Through a model free identification of the multiple within- and cross-channel scales in data, EMD promises the time-frequency accuracy at the instantaneous frequency level, and a natural account of inter- and intrawave modulations (nonlinearity).

- Integrity: Coherent instantaneous treatment of multi-channel information ensures the integrity of multivariate bases, thus facilitating synchrony, causality and data fusion studies, while allowing for intrinsic, 'scale-dependent', data association metrics, Chen et al. (2010) [31].

The EMD has been tested and validated exhaustively (Huang & Attoh-Okine (2005) [88], Huang & Shen (2005) [87]), in almost all the studies, the results of HHT method are much sharper than most of traditional ones and its ability to reveal physical insight of data buried under non desired processes has been proven.

2.1 The empirical mode decomposition method

In contrast to almost any method the EMD works in temporal space directly rather than in the corresponding frequency space.
The decomposition is based on the simple assumption: at any given time, the data may have many different coexisting mode of oscillation, with significantly different frequencies, one superimposing on the others. Each of these oscillatory modes is defined as an intrinsic mode function (IMF) with the following conditions, Huang et al. (1998) [91]:

(a) In the whole data set the number of extrema and zero-crossing are either equal or differ by exactly one (i.e. almost equivalent to have all local maxima positive and all local minima negative).
(b) At any point, the mean value of the envelope defined by the local maxima and the envelope defined by the local minima is zero (symmetric upper/lower envelop).
It is interesting to point out contrary to a harmonic function an IMF can have variable frequency and amplitude i.e. Multiscale function.

The EMD algorithm to decompose a signal $x(t)$ into IMFs is presented as follows:

1. Identify all local extrema of the variable $x(t)$.
2. Interpolate (using local spline interpolation) between all the minima (resp. maxima) to obtain the signal envelope passing through the minima, emin(t) (resp. emax(t)).
3. Compute the local mean m(t) = (emin(t)+emax(t))/2, shown in Figure 2.1a.
4. Subtract the local mean from the signal to obtain the modulated oscillation, detail $h(t) = x(t) - m(t)$, Figure 2.1b.
5. The component $h(t)$ is then examined to check if it satisfies the condition to be an IMF (Stoppage criteria, given below). If yes it is considered as the first IMF and denoted $IMF_1 = h(t)$, else set $x(t) = h(t)$ and go to step 1.
6. Subtract the so derived IMF from the variable x(t) so that the residual; $r(t) = x(t) - IMF(t)$, see Figure 2.1c, is taken as the new data series in step 1.
7. Stop the process when the residual from step 6 becomes a monotonic function from which no more IMFs can be extracted.

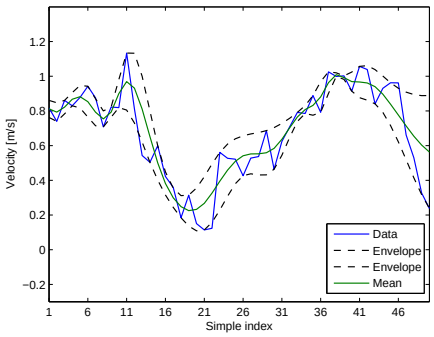

(a)

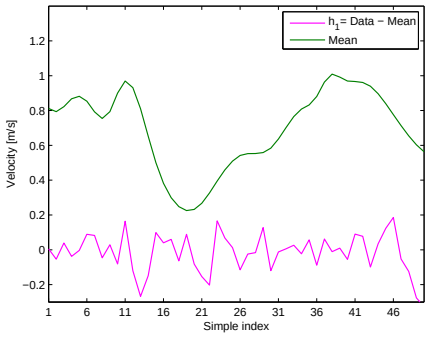

(b)

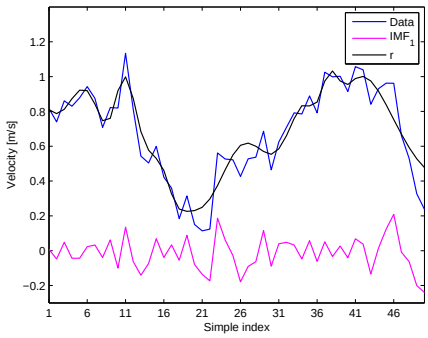

(c)

Figure 2.1: (a) The data (blue), upper and lower envelopes (black dash) and the mean value (green) of upper and lower envelopes.(b) First detail (violet) and its residue; Mean (green). (c) The data (blue), First IMF(violet) which obtained after 10 iteration and the residue r (black) that treated as a new data in next step.

So the original signal is expressed as follows: $x(t) = \sum_{k=1}^{N} IMF_k(t) + r_N(t)$. By construction the number of extrema decreases going from one residual to next, thus guaranteeing the number of IMFs to be finite for a complete decomposition, typically the complexity of total number of IMFs is $O(\log_2 n)$ for n data point (Flandrin & Goncalves (2004) [54]). In the manner now being indicated, EMD decomposes gradually any arbitrary signal from the finest scale of the shortest period to longer period as displayed in Figure 2.2.

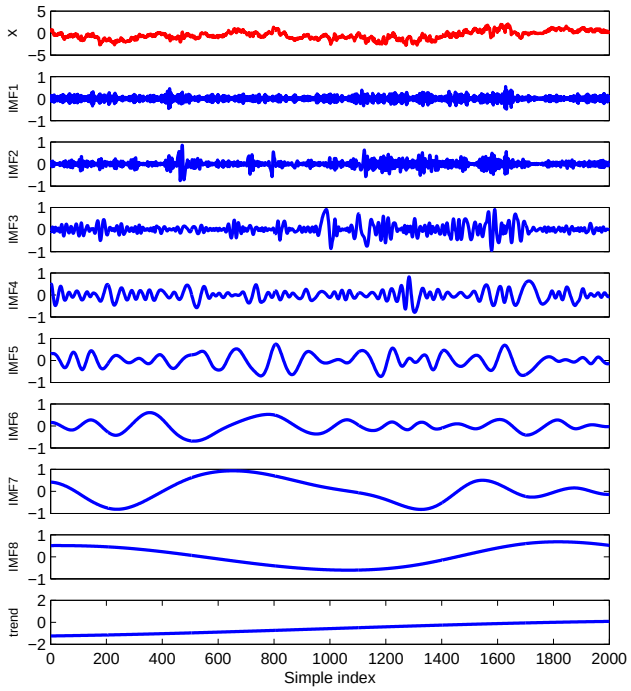

Figure 2.2: EMD analysis of a given signal in first panel and the corresponding IMFs (modes).

2.1.1 Stoppage criteria

In EMD procedure step 1 to step 5 is called Sifting processes that iterates until the detail $h(t)$ encounters both enumerated conditions of IMF. Several stoppage criteria, specifying the number of iteration for sifting process, were proposed by different studies that all can be classified as follow:

(a) The Cauchy type criterion

The first stoppage criterion was introduced by Huang et al. (1998) [91] using a Cauchy type of convergence test between two successive proto-IMF defined as

$$SD = \sum_{t=0}^{T} \frac{[h_{k-1}(t) - h_k(t)]^2}{h_{k-1}^2} \tag{2.1}$$

The sifting process will stop when this square difference SD is smaller than a predetermined value, this criterion is rigorous mathematically but does not depend on the

definition of IMF (cannot guarantee the same number of zero-crossing and exterma for the IMFs functions). In practice the choice of threshold is difficult, if it is too high the different modes in decomposition are not separated and if it is too small the signal over-decomposing problem will occur. Huang et al. (1998) [91] were proposed to keep typically SD between 0.2 and 0.3. The other version of this stoppage criterion is given in Shen et al. (2005) [169].

(b) The S-number criterion

To overcome the shortage of the previous criterion Huang et al. (2003) [92] proposed a second criterion based on the agreement of the number of zero-crossing and exterma. The sifting process stop only after the numbers of zero crossings and exterma are equal or at most differ by one and stay the same for S-number consecutive times. They suggest for the optimal decomposition the range of S-number should be set between 4 and 8, typically the value of 5 has been used the most. It should be noted this is a global criterion and could leads to undesirable mode mixing effects.

(c) The Mean-value criterion

This stoppage criterion was proposed by Rilling & Flandrin (2004) [55], it is concerned with the evaluation of the following function:

$$\sigma(t) = \frac{m(t)}{a(t)} \tag{2.2}$$

where $m(t)$ and $a(t)$ are the local mean of the minimum and maximum envelopes and the amplitude of corresponding mode respectively:

$$m(t) = \frac{e_{max}(t) + e_{min}(t)}{2} \quad , \quad a(t) = \frac{e_{max}(t) - e_{min}(t)}{2} \tag{2.3}$$

The sifting is iterated until $\sigma(t) < \theta_1$ during some prescribe fraction $(1 - \alpha)$ of the total duration, while $\sigma(t) < \theta_2$ for the remaining fraction. The authors suggested setting $\alpha \approx 0.05$, $\theta_1 \approx 0.05$ and $\theta_2 \approx 10\theta_1$.
This is a combined global-local stoppage criterion and as it forces the envelopes minima/maxima coming symmetric, it satisfies one of the IMF condition.

(d) The Fixed sifting time criterion

The fact that the EMD acts like a dyadic filter bank has been revealed by Flandrin et al. (2004) [55] and Wu & Huang (2004) [199] and (2005) [200]).
Later with a systematic study, Wu & Huang (2010) [203] showed the dyadic filter property is valid only if one imposes a small sifting number; fixed to 10 and so the EMD behaves like a cubic spline wavelet transform with a scale factor of 2. In addition in this case there are maximum separation and minimum leakage between the IMFs functions resulting from EMD.

2.1.2 Noise assisted empirical mode decomposition

EMD despite the several advantages suffers from the mode mixing problem which is defined as a single mode either consists widely disparate scales (oscillations) or a single scale appears in different modes. The mode mixing could be often occurred when the process contains intermittent high frequency oscillation and/or variation of instantaneous amplitude and frequency of the modes, Wu & Huang (2009) [201] and Rehman & Mandic (2011) [154]. The intermittence can cause two major undesirable effects: Aliasing in time-frequency distribution and losing the physical meaning of IMFs. Figure 2.3 displays four synthetic components of simulated signal, the first panel is intermittent turbulent signal and the three others are sinusoidal waves. The simulated signal (assumption of

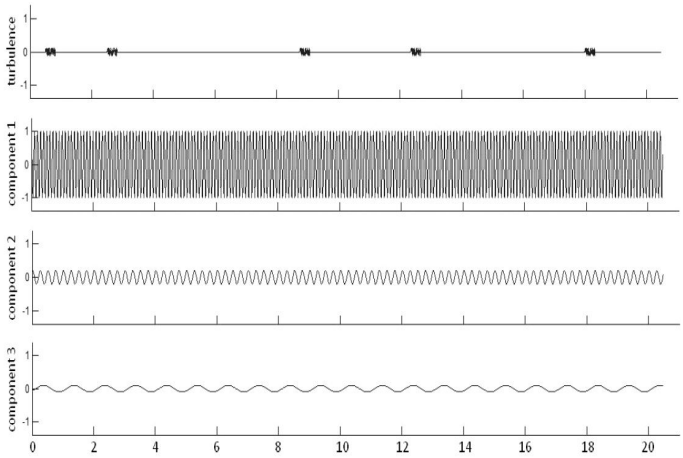

Figure 2.3: Four component of synthetic signal, from Yeh et al. (2010) [207].

four components) was decomposed by EMD and the results are presented in Figure 2.4. The mode-mixing problem is clear in IMF 1 and IMF 2. In fact while the intermittent turbulent signal appears; parts of IMF 1 were shifted to IMF 2. To overcome these drawbacks the new noise-assisted data analysis methods (NADA) using the dyadic filter bank property of EMD when applied to white noise has been developed.

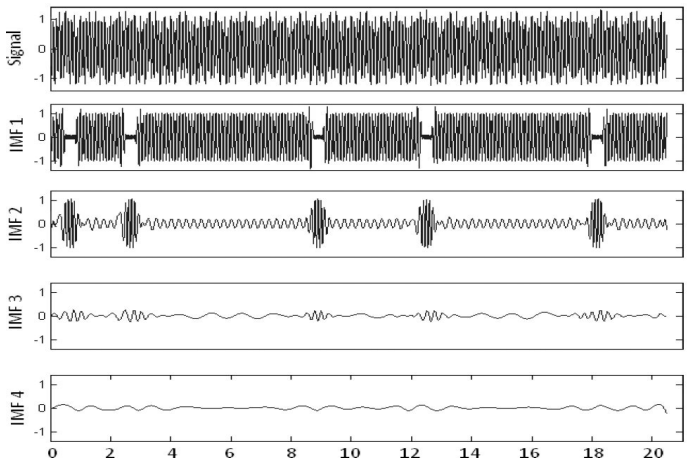

Figure 2.4: The simulated signal in first panel and its components result from EMD.

2.1.2.1 EEMD

Ensemble Empirical Mode Decomposition (EEMD) was proposed by Wu & Huang (2009) [201] to overcome the problem of scale-mixing. EEMD defines the true IMF components as the mean value of an ensemble trial. In each trial a random white noise of finite amplitude is added to the signal then the basic EMD is applied on the polluted signal resulting in series of IMF components.
Obtaining the (ensemble) mean of corresponding IMFs of the different decomposition leads to final results. A collection of white noise neutralizes itself in a time space ensemble mean of enough trials; therefore only the signal can persist in the final mean result. The principle of EEMD is: the added white noise could provide a uniformly distributed scale in time-frequency space. The intrinsic oscillations in the signal with different scales would automatically project onto similar scales of reference established by the white noise. Therefore, the intrinsic local oscillation can be filtered adaptively to proper scales via the natural filter bank of EMD associated to the added white noise.

The EEMD algorithm is described as:

1. Initialize the number of trials NE and the amplitude of the white noise ε .
2. Generate the white noise and add it to the signal: $\mathbf{X}_i(t) = x(t) + \varepsilon w_i(t)$.
3. Decompose $\mathbf{X}_i(t)$ into K IMFs by using EMD; $IMF_k^i(t)$ where $(k = 1, \ldots, K)$ indicates the k^{th} mode and i denotes the trial number.
4. Repeat step 2 and step 3 but with different additive white noise for each trial up to pre-initialized NE trials.
5. Compute the average of the corresponding $IMF_k^i(t)$ for the NE trials:

$$\overline{IMF}_k(t) = \frac{1}{NE} \sum_{i=1}^{NE} IMF_k^i(t)$$

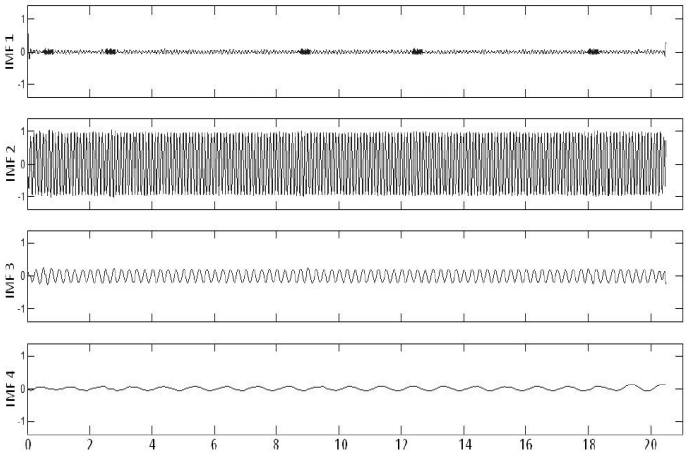

Figure 2.5: The IMFs of simulated signal by EEMD.

The same simulated signal as in Figure 2.4 is decomposed by EEMD and the results are provided in Figure 2.5, as one can see the first mode is more representative of intermittent signal and the three following IMFs are almost similar to the three original sinusoidal waves in simulated signal.

The amplitude of white noise is defined as $\varepsilon = \varepsilon_0.std\,(x\,(t))$, where ε_0 is the input noise level and in practice is chosen as $0.1 < \varepsilon_0 < 0.4$, (Wu & Huang (2009) [201] and Wang et al. (2014) [189]). It should be noted while the data is dominated by high-frequency signals; the amplitude of noise must be set to a small value and vice versa, Wu & Huang (2009) [201].
Also the number of the ensemble trials NE should be of the order of 100 which produces a satisfactory result and the remaining noise in the IMFs would cause less than a fraction of 1% of the IMF estimated error, (Wang et al. (2014) [189]).

2.1.2.2 CEEMD

The EEMD reduces significantly mode mixing problem however there is a difference between reconstructed signal via IMFs results of decomposition and the original input signal. Indeed some traces of added whit noise (residues) are remained in the resulted modes, this issue can be suppressed by increasing the number of ensemble realizations of white noise but it is computationally expensive.
To eliminate this draw back Yeh et al. (2010) [207] proposed complementary ensemble empirical mode decomposition (CEEMD) in which the white noise is added in pairs of positive and negative to the original data. The ensemble IMFs obtained from positive (resp. negative) mixture contribute to a set of IMFs with positive (resp. negative) residues of added white noises. The final IMF is the ensemble of both the IMFs with positive and negative noises.

2.1.2.3 CEEMDAN

As shown above the EEMD can significantly alleviate the problem of mode-mixing, however it has some drawbacks. In fact, some trace of white noise could be left in the IMFs and different realization of signal plus noise could lead to different number of modes in decompositions. To overcome these problems Torres et al. (2011) [182] developed a new strategy; complete ensemble empirical mode decomposition with adaptive noise (CEEMDAN).

The CEEMDAN algorithm is described as below:

1. Initialize the number of trial NE and the amplitude of the white noise ε.

2. The first mode is computed like in EEMD; $\widetilde{IMF_1}(t)$.

3. Calculate the first residue as $r_1(t) = x(t) - \widetilde{IMF_1}(t)$.

4. Decompose realizations $r_1(t)+\varepsilon_1 E_1\,[w_i(t)]$, i=1,. . . , NE until their first EMD mode.Operator $E_j[.]$ produces j-th mode using EMD and $w_i(t)$ is the standard normal white noise, $N(0,1)$. Thus the second mode is defined:

$$\widetilde{IMF_2}(t) = \frac{1}{NE}\sum_{i=1}^{NE} E_1[r_1(t) + \varepsilon_1 E_1[w_i(t)]] \tag{2.4}$$

5. For k=2,...,K , where K is the total number of IMF, calculate the k-th residue:

$$r_k(t) = r_{k-1}(t) - \widetilde{IMF_k}(t) \tag{2.5}$$

6. Decompose realizations $r_1(t) + \varepsilon_1 E_1[w_i(t)]$, *i=1,...,NE* until their first mode and define the *(k+1)*-th mode as:

$$\widetilde{IMF}_{k+1}(t) = \frac{1}{NE}\sum_{i=1}^{NE} E_1[r_k(t) + \varepsilon_k E_k[w_i(t)]] \tag{2.6}$$

7. Go to step 5 for next k.

8. Repeat step 5 to 7 until the residue becoming mono component, the final residue satisfies

$$R(t) = x(t) - \sum_{k=1}^{K} \widetilde{IMF}_k(t) \tag{2.7}$$

Therefore the given signal $x(t)$ can be expressed as follows:

$$x(t) = \sum_{k=1}^{K} \widetilde{IMF}_k(t) + R(t) \tag{2.8}$$

As an example an ECG signal (Electrocardiography) was decomposed by EEMD and CEEMD, and the result of this comparison is illustrated in Figure 2.6.

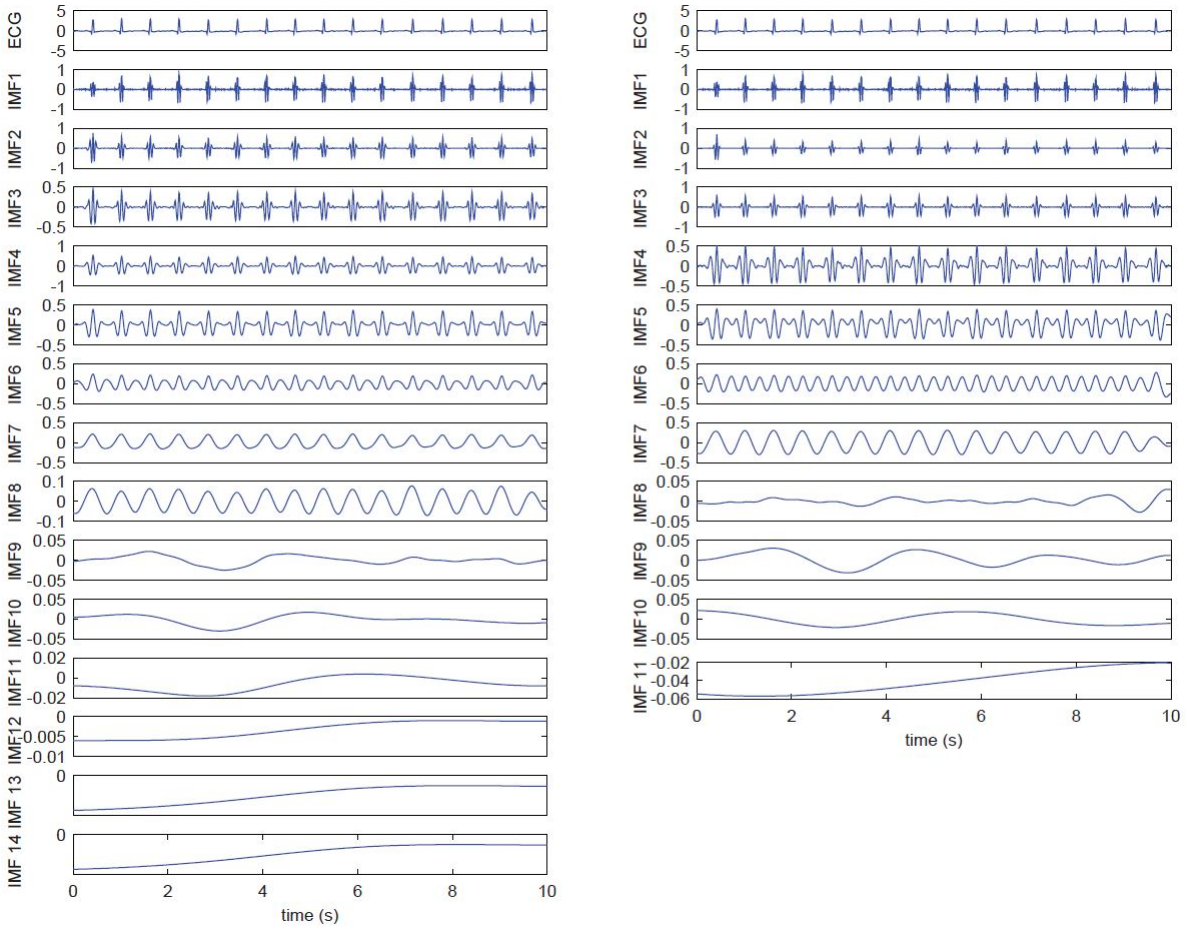

Figure 2.6: Decomposition of ECG signal with a length of 10 second by EEMD (left) and CEEMD (right), from Torres et al. (2011) [182].

2.2 Multivariate extension of EMD

2.2.1 EMD for Bivariate signal

• Complex EMD

The first complex extension of EMD was proposed by Tanaka & Mandic (2006) [179]. They use the fact that EMD behaves as a dyadic sub-band decomposition structure and the concept of analytical signal. The complex signal is divided into its positive and negative frequency parts then basic real-valued EMD is applied to each part. This approach cannot guarantee the same number of IMFs for the real and imaginary parts and so the physical interpretation of the IMFs becomes difficult. Also this method cannot be extended to dimensions higher than two.

• Rotation-Invariant EMD

Rotation-Invariant EMD (RI-EMD) unlike the complex EMD works fully in complex domain, This approach was first developed by Altaf et al. (2007) [4]. The extrema detection of complex/bivariate signal is not straightforward and they will be defined based on a

change in the signal phase corresponding to the points where the first derivative of complex signal becomes zero. The signal envelopes are then produced by using component-wise spline interpolation and then the local maxima minima are averaged to obtain the local mean, the rest of procedure is like the basic EMD. Unlike the complex EMD the IMFs resulting from RI-EMD have the appropriate physical meaning as shown in [4]. Also the problem of different number of IMFs for real and imaginary part of signal, that is encountered in complex EMD, does not exist in this approach. In addition, as the definition of extrema in this approach does not depend on the date dimension and the interpolation techniques for high dimensional data already exist, this method could be extended to higher dimension.

• **Bivariate EMD**

The basic idea of bivariate EMD (BEMD) is: "The bivariate signal = fast rotations superimposed on slower rotations" as introduced by Rilling & Flandrin (2007) [162].
In order to separate the more rapidly rotating components from slower ones, the idea is once again to define the slowly rotating component as the mean of some envelope, yet the envelope is now a 3-dimensional tube that tightly encloses the signal, Figure 2.7 , thus the slowly rotating portion of the signal at any point in time can then be defined as the center of the enclosing tube.

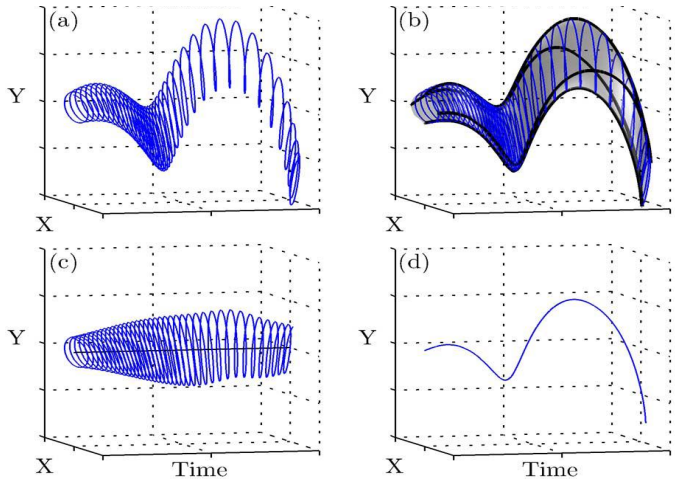

Figure 2.7: (a) The bivariate signal, (b) The signal enclosed in its 3D envelope (tube) (c) The fast rotating component corresponding to residue (proto-IMF) (d) The slowly rotating component corresponding to the mean of the tube in(b), from Rilling & Flandrin (2007) [162].

To define the envelope, the signal should be projected in a given set of directions: $\varphi_k = 2k\pi/N$, $1 \leq k \leq N$, the periphery of the envelope then is the signal extrema in each direction. For example in the case of k=4 directions, the top point of envelope is defined when the signal reaches a local maximum in the vertical direction and is therefore tangent of the envelope. Interpolation (cubic spline) of extrema ending up with the envelope associated with the upward direction. (cf the black lines in Figure 2.7.b)

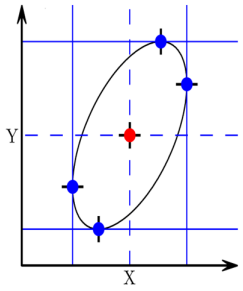

Figure 2.8

The mean of envelope is define as the intersection of two straight lines, one being halfway between the two horizontal tangents, the other one halfway between the vertical ones (see Figure 2.8) The bivariate extension is defined by the same algorithm as the basic EMD, just with a new sifting operator defined as follows :

1. for $1 \leq k \leq N$
2. Project the complex-valued signal $x(t)$ on direction φ_k: $p_{\varphi_k}(t) = Re(e^{-i\varphi_k})$, where $e^{-i\varphi_k}$ is a unit complex number.
3. Extract the maxima of $p_{\varphi_k}(t)$: $\{t_i^k, p_i^k\}$ with t_i^k the location and p_i^k the value of maxima at projected signal in direction k for signal sample i.
4. Interpolate the set $\{t_i^k, e^{i\varphi_k}), p_i^k\}$ to obtain the partial envelope curve in direction $\varphi_k : e'_{\varphi_k}(t)$.
5. Compute the mean of all tangents: $m(t) = \dfrac{2}{N} \sum_k e'_{\varphi_k}(t)$.

The rest of procedure is like the basic EMD. The RI-EMD and BEMD algorithms are equivalent for $N = 4$ directions.

2.2.2 EMD for Trivariate signal

As described in the previous section in BEMD extrema envelopes are generated by projection of an input signal on the uniformly distributed directions in the complex plane. Inspired this idea, the Trivariate EMD was developed by Rehman & Mandic (2010) [153]. In this method the extrema are found by projecting the input signal in multiple directions in 3D space using quaternion rotation framework, Dam et al. (1998) [34], in which a unite quaternion vector is written as :

$$q = cos\theta + \mathbf{u}sin\theta = e^{\mathbf{u}\theta/2} \tag{2.9}$$

where $\mathbf{u}$ is a 3D vector of unit length. So B' the rotation of a 3D vector B about $\mathbf{u}$ by angle 2θ is defined by using

$$B' = qBq^* = e^{\mathbf{u}\theta/2} B \left(e^{\mathbf{u}\theta/2}\right)^* \tag{2.10}$$

where the symbol "$*$" denotes the quaternion conjugate. Therefore to obtain the signal rotations in 3D space, it needs generating a set of values of $\mathbf{u}$ and θ (multiple direction vectors). Each direction vector can be represented by a point on the surface of unit sphere

(that is the end point of the unit vector drawn from the sphere center) as illustrated in Figure 2.9a, So a set of direction vectors that represents the rotation axis u and the rotation angles 2θ is represented by several points at one longitudinal line of a unit sphere Figure 2.9b. To project a signal on the whole 3D space, different equi-distance longitu-

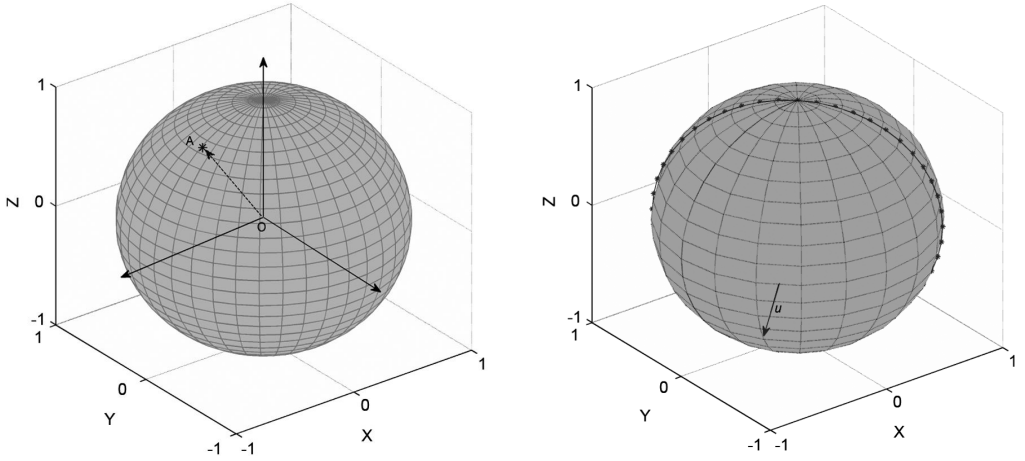

(a) (b)

Figure 2.9: (a) $\overrightarrow{OA}$ direction vector can be represented by a point on the surface, (b) Multiple direction vectors on a single longitudinal line, corresponding to rotation axis **u**, from Rehman & Mandic (2010) [153].

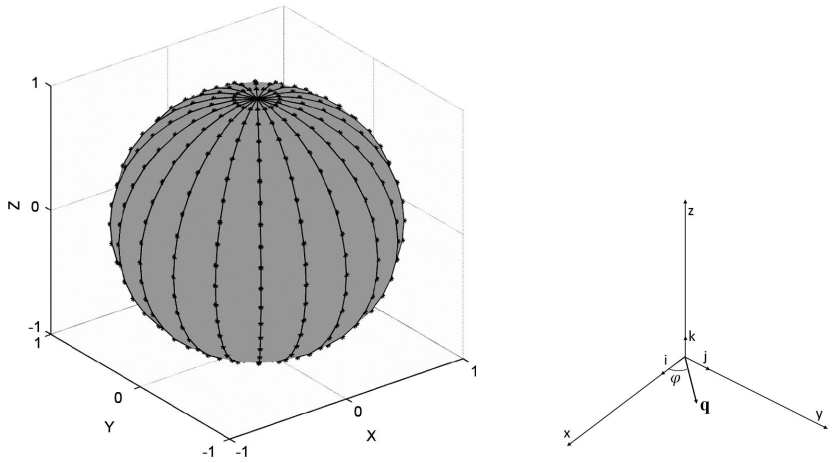

(a) (b)

Figure 2.10: (a) a set of multiple directions vector spanning the whole 3D space, (b) quaternion vector **q** as a rotation axis that represent with series of $\phi \, \epsilon[0, \pi]$, all rotation axes of a set multiple directions vector in (a), from Rehman & Mandic (2010) [153].

dinal lines on the sphere should be considered, see Figure 2.10a, each one corresponds to one 3D rotation axis. So the projection of the input signal along multiple direction vectors can be calculated by rotating the input signal about a set of vectors q, rotation axes, that also can be presented by a set of unit quaternion so $\mathbf{q} = 0 + \cos(\phi)\vec{i} + \sin(\phi)\vec{j} + 0\vec{k}$, by ϕ an angle to the x-axis, Figure 2.10b. By using Eq 2.9 and taking its projection along the z-axis ($\vec{k}$):

$$P_\theta^\phi = e^{\mathbf{q}\theta} x\,(t)\left(e^{\mathbf{q}\theta}\right)^* .\vec{k} \tag{2.11}$$

with $x(t)$ is the trivariate input signal that can be represented as a pure quaternion signal:

$$x(t) = 0 + X(t)\,\vec{i} + Y(t)\,\vec{j} + Z(t)\,\vec{k} \tag{2.12}$$

where X, Y and Z are real numbers and $\vec{i}$, $\vec{j}$ and $\vec{k}$ are the unit vectors along the three vector dimensions.

The algorithm of Trivariate EMD is given as follows:

1. Obtain projections of trivariate quaternion input signal $x(t)$; $P_{\theta_k}^{\phi_n}(t)$ by using Eq 2.11, where $\theta_k = k\pi/K$ for k=1,...,K, and $\varphi_n = n\pi/N$ for n=1,..., N.
2. Find the time instants $\{(t_k^n)_i\}$ corresponding to the maxima of $P_{\theta_k}^{\varphi_n}(t)$, for all k and n.
3. Interpolate $[(t_k^n)_i, x((t_k^n))_i]$ by using a component-wise spline interpolation, to obtain quaternion envelop curves $e_{\theta_k}^{\phi_n}$, for all values of k and n.
4. Compute the mean of all the envelopes: $m(t) = \dfrac{1}{KN}\sum_{k=1}^{K}\sum_{n=1}^{N} e_{\theta_k}^{\phi_n}$.
5. Subtract the mean from the signal to obtain rapidly oscillatory component, dominant mode, (proto-IMF): $h(t) = x(t) - m(t)$, If $h(t)$ satisfies the stopping criterion for a quaternion-valued IMF, then $h(t)$ becomes an IMF and the above procedure is applied to $x(t) - h(t)$; otherwise it is applied to $h(t)$.

To illustrate the potency of Trivariate EMD, the results of the decomposition of a trivariate signal that comes from hand movement, are displayed in Figure 2.11.

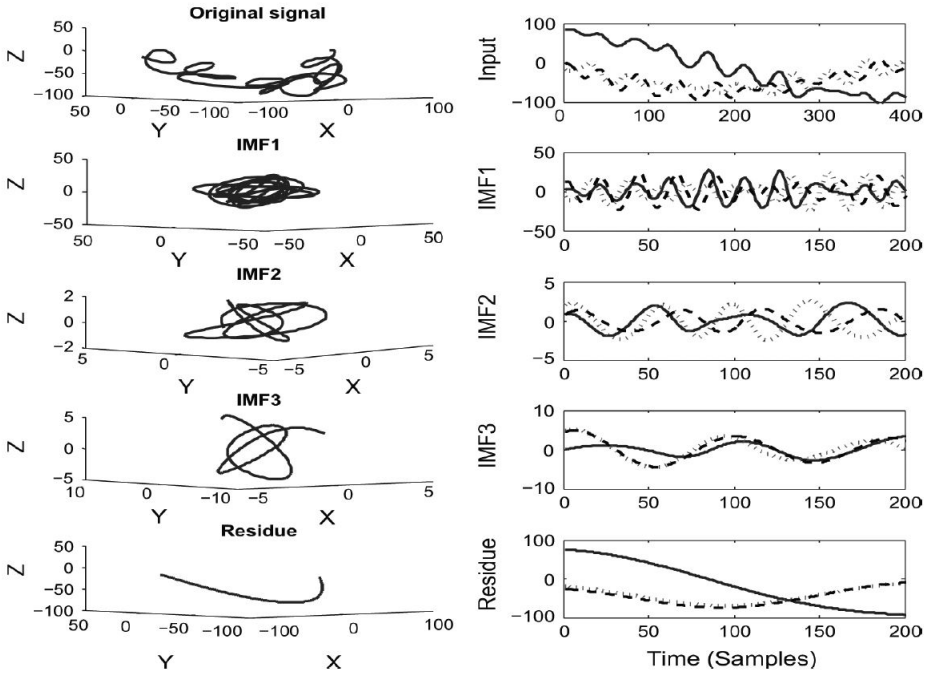

Figure 2.11: Decomposition of trivariate signal by proposed method, from Rehman & Mandic (2010) [153].

2.2.3 Multivariate EMD

The multivariate empirical mode decomposition (MEMD) has been recently developed to operate for an arbitrary number of input variables (channels), Rehman & Mandic (2009) [152]. A crucial issue for extending standard EMD to multivariate signals is the definition of local mean since the definition of extrema for multivariate signals is not obvious. Multivariate EMD is the generalization of Bivariate EMD and Trivariate EMD in which the extrema envelopes are calculated by projecting the input signal along " multiple directions in n-dimensional spaces ".
To represent direction vectors in an n-dimensional space, the points on the surface of corresponding unit $(n-1)$ spheres are considered, Rehman & Mandic (2009) [152]. Indeed an n sphere (extension of the ordinary sphere to an arbitrary dimension) resides in an $(n+1)$-dimensional Euclidean coordinate system. The accuracy of the envelopes estimation is coupled to how uniformly these points are selected. (Each point on the sphere surface corresponds to one direction vector from the center of sphere).
There are two methods for points sampling: (a) Conventional uniform angular sampling Figure 2.12a, (b) Low-discrepancy point sets based sampling Figure 2.12b. As was demonstrated in Cui & Freeden (1997) [33] the second approach yields to more uniform sampling whereas it is based on Halton and Hammersly sequence over quasi-Monte Carlo methods, Niederreiter (1992) [127]. Moreover this approach is more pertinent than uniform sampling in higher dimensional spaces.

Once the multiple direction vectors in n-dimensional space are defined, the input signal is projected on these directions resulting in multiple real-valued projected signals. Then the extrema of such single-dimensional projections are interpolated via cubic spline interpolation to obtain multi-dimensional signal envelopes.

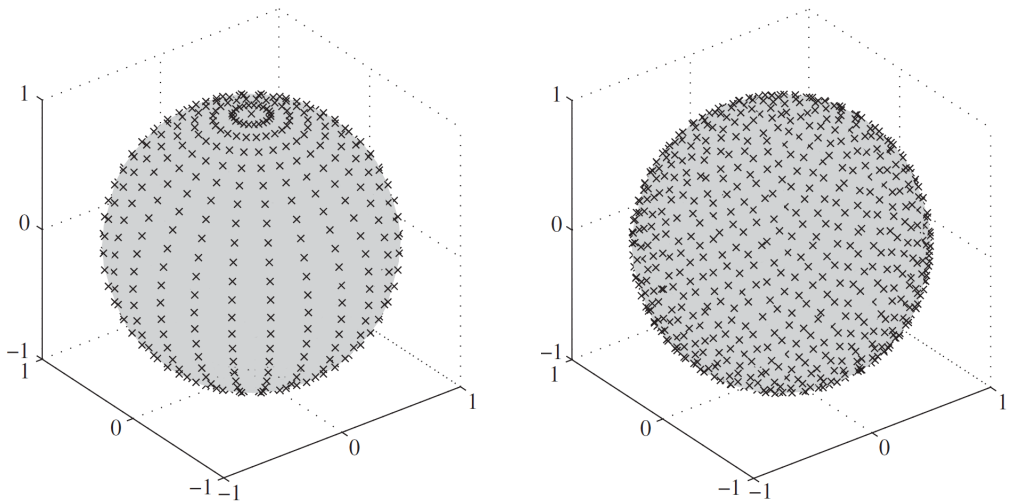

Figure 2.12: Direction vectors for taking projections of trivariate signal on a two-sphere generated by using (a) spherical coordinate system and (b) low-discrepancy Hammersley sequence, from Rehman & Mandic (2009) [152].

Consider a multivariate signal $\mathbf{s}(t)$ with n-variate (components) that are represented by a sequence of n-dimensional vectors:

$$\{\mathbf{s}(t)\}_{t=1}^{T} = \{s_1(t), s_2(t), s_3(t)..., s_n(t)\} \tag{2.13}$$

and a set of direction vectors along the directions given by angles $\theta^k = \{\theta_1^k, \theta_2^k, \theta_3^k, ..., \theta_n^k, \}$ on an $(n-1)$sphere are given by:

$$\mathbf{x}^{\theta_k} = \{x_1^k, x_2^k, x_3^k, ..., x_n^k, \} \tag{2.14}$$

Then the procedure of MEMD for the decomposition of $\mathbf{s}(t)$ is summarized in following steps:

1. Generate a suitable point set based on the Hammersley sequence for sampling on $(n-1)$ sphere.

2. Calculate a projection, denoted by $\{P^{\theta_k}(t)\}_{t=1}^{T}$, of the input signal $\{\mathbf{s}(t)\}_{t=1}^{T}$ along the direction vectors $\mathbf{x}^{\theta_k}$, for k=1,...,K (the whole set of direction vectors), giving $\{P^{\theta_k}(t)\}_{k=1}^{K}$ as the set of projections.

3. Find the time instant$\{t_i^{\theta_k}\}$ corresponding to the maxima of the set of projected signal $\{P^{\theta_k}(t)\}_{k=1}^{K}$.

4. Interpolate $\left[t_i^{\theta_k}, \mathbf{s}(t_i^{\theta_k})\right]$ for all values of k, to obtain multivariate envelope curves $\{\mathbf{e}^{\theta_k}(t)\}_{k=1}^{K}$.

5. Calculate the mean of the K multidimensional envelope curves as $\mathbf{m}(t) = \frac{1}{K}\sum_{k=1}^{K}\mathbf{e}^{\theta_k}(t)$.

6. Extract the detail $\mathbf{h}(t) = \mathbf{s}(t) - \mathbf{m}(t)$, if $\mathbf{h}(t)$ fulfills the stoppage criterion for multivariate IMF (see below), apply the above procedure to $\mathbf{s}(t) - \mathbf{h}(t)$, otherwise apply it to $\mathbf{h}(t)$.

The stoppage criteria adopted for standard EMD can be used also for multivariate EMD. However since the extrema cannot be properly defined for multivariate signals, the condition for equality of the number of extrema and zero crossing is not impose. It should be emphasized for the multivariate IMF, the sifting process can be stopped when *all the projected signals fulfill the stoppage criteria.*
An important aspect of MEMD is the number of direction vectors in which the input signal is projected. In order to extract the meaningful modes (IMFs), it should be considerably greater than the dimensionality of the signal (Rehman & Mandic (2009) [152]), as a rule of thumb the minimum number of directions should be twice the number of data channels.

An interesting property of EMD is its behavior as a dyadic filter bank when applied to any white or fractional Gaussian noise series, (Flandrin (2004) [55] and Wu & Huang (2004 [199], 2005 [200]). The MEMD has also this characteristic when applied on white noise as demonstrated by Rehman & Mandic (2011) [154]. They applied MEMD on eight-channel white Gaussian noise and compare the results of this decomposition with those of EMD

processed separately on the same eight noise channels. This study reveals two important issues; Firstly, as illustrated in Figure 2.13, in the case of MEMD the overlapping of frequency bands of same-index IMFs associated with different channels is much more prominent compared to standard EMD.

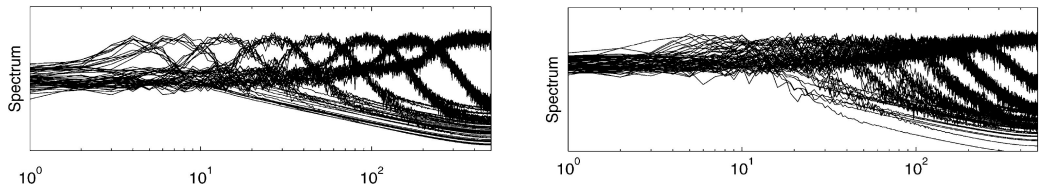

(a) (b)

Figure 2.13: (a) Spectra of the same index IMFs associated with different channels of eight-channel white Gaussian noise result from MEMD, (b) Spectra of the IMFs for same eight noise channels were separately decomposed by standard EMD, from Rehman & Mandic (2011) [154].

Secondly, for a given number of white noise realizations, MEMD can successfully separates a set of common scales across different components, (variates) Figure 2.14a, whereas the EMD failed to properly align the bandpass filters associated with the corresponding IMFs for different channels Figure 2.14b.

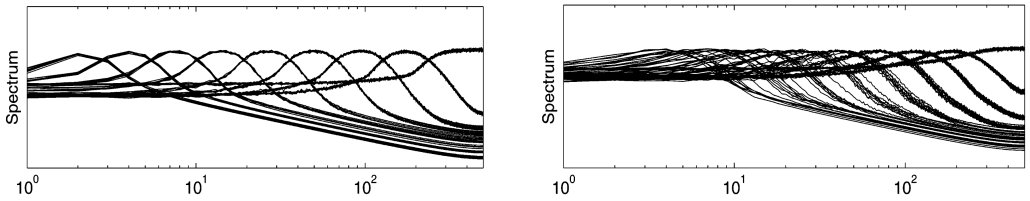

(a) (b)

Figure 2.14: Average spectra of IMFs obtained from 500 realization of eight-channels white Gaussian noise via (a) MEMD, (b) the standard EMD, from Rehman & Mandic (2011) [154].

2.2.4 Noise-Assisted Multivariate EMD

EEMD and its extend version CEEMD can significantly reduce mode-mixing effect while that occurs in standard EMD. However, despite this success they suffer from some drawbacks. Adding noise to data not only may increase the residual error but also could produce different number of modes for different realizations besides this an ensemble average of different IMFs may not strictly conform to the IMF definition.

To overcome these disadvantages the noise-assisted multivariate empirical mode decomposition (NA-MEMD) was introduced by Rehman & Mandic (2011) [154], inspired by EEMD, this method is based on the dyadic filter bank structure of MEMD on white noise. Unlike the EEMD, the white Gaussian noise (WGN) is not directly added to the channels of the multivariate signal, but they are all considered as an adjacent subspace. Then such a composite signal is processed by MEMD. The resulting IMFs channels corresponding to white noise are then discarded thus leading to a set of IMFs associated with only original input.

The added white noise would populate the whole time-frequency space uniformly with the constituting components of different scales. MEMD aligns its different components (IMFs) in accordance with the quasi-dyadic filter bank structure, as was described in previous section (i.e. each IMF contains a separate scale of the input signal). By doing this consequently, the IMFs of the original signal also align themselves in accordance with the structure of a quasi-dyadic filter bank.

The NA-MEMD algorithm is described as follows:

1. Create an uncorrelated Gaussian white noise time-series (l-channels) of the same length as the input signal, $l \geqslant 1$.
2. Add the noise channels created in step 1 to the input multivariate signal (n-channels), obtaining an $(n+l)$-channels multivariate signal.
3. Decompose the resulting $(n+l)$-channels by MEMD to obtain multivariate IMFs.
4. From the resulting $(n+l)$-variate IMFs, discard the l channels corresponding to the noise, giving a set of n-channels IMFs corresponding to the original input signal.

Similaire to EEMD, the amplitude of WGN is defined as $\varepsilon = \varepsilon_0.std\left(x\left(t\right)\right)$, where ε_0 is the input noise level, depending on the target SNR. In practice the power (variance) of noise should be within 2-10 % of the power of the input signal, Rehman et al. (2013) [155], so $0.1 < \varepsilon_0 < 0.4$ and increasing the noise power (reducing SNR) enforce filterbank structure within the IMFs. The powers in each of the noise channels are identical and the total perturbation is a linear mixture of the noise channels.
By increasing the number of uncorrelated noise channels, the correlation between the perturbations decreases hence it optimizes the noise-assisted performance in which the perturbations should ideally be as independent as possible. Indeed the higher the number of noise channels, the faster the roll-of a filterbank structure, Looney et al. (2014) [112]. This feature is required for the decomposition of the narrow band signals to ensure such signals are contained in a single IMF. Whereas for a wider bandwith signals which are composed of several oscillatory components, lower number of adjacent WGN is needed i.e. slower roll-off of a filterbank structure in order to contain those oscillations within the same IMF, Hemakom et al. (2016) [79].
It should be pointed out the noise-assisted extensions of EMD, (EEMD, CEEMD and NA-MEMD) benefits the dyadic filter bank structure of EMD hence they can significantly reduce mode-mixing for a class of signals in which the dyadic sub-band filter is relevant, otherwise these method may spread the desired signal across multiple IMFs.

NA-MEMD uses a single realization of one or l-channels Gaussian white noise for decomposition of a multivariate signal so may be lead to slightly different results for different realization of l-channels white noise therefore uniqueness of the decomposition is questionable. To overcome this shortcoming an ensemble approach inspired by EEMD was adopted by Rehman et al. (2013)[155], Ensemble-NA-MEMD whereby an input multivariate signal was decomposed several times by MEMD, each time by different set of l-channels noise then the set of multivariate IMFs obtained from MEMD are ensemble averaged to obtain the output.

2.2.5 Adaptive-projection intrinsically transformed MEMD

In order to compute the local mean, MEMD (or Ensemble-NA-MEMD) projects the input multivariate signal a long multiple uniformly sampled direction vectors in multidimensional spaces i.e. fix distribution of direction vectors. Such a method is quite suitable for circular data with equal channel powers. However in the real-world there are a power discrepancy and/or inherent correlation between data channels so the density of projections should match the signal dynamics and uniformly projection of the signal leads to the sub-optimal estimation of the local mean.

To overcome this problem Nonuniformly Sampled BEMD (NS-BEMD) was proposed by Ahrabian et al. (2013) [3] to process bivariate signal and also NS-TEMD by Hemakom et al. (2015) [78] for trivariate signal decomposition. The principle of both method is the same, in the first step the directions of principal importance in the scatter data are determined in terms of interchannel power imbalances and correlations. In NS-BEMD it is obtained by the first estimating of the circularity quotient i.e. complex variable circularity based on second-order moments. Its modulus gives the degree of correlation (power imbalance) between two data channels and the phase of its square-root is the direction along which such correlation exist, Ahrabian et al. (2013) [3].

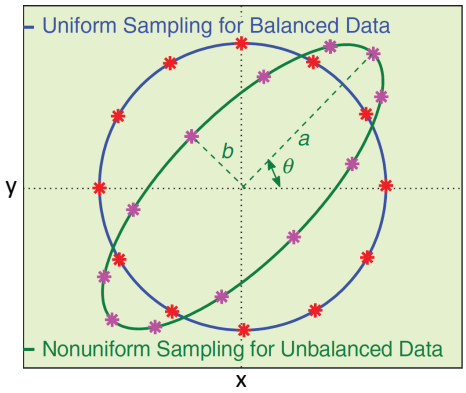

Figure 2.15: Uniform sampling in BEMD versus Nonuniform sampling in NS-BEMD that is 12 elliptically distributed projections with higher density of sample along the major axis a, from Mandic et al. (2013) [118].

In NS-TEMD the directions of principal importance are defined by an eigendecomposition of the signal covariance matrix. The eigenvector matrix captures the directions of principal importance and the eigenvalues determine the relative power of the resulting directions. For more detailed one can refer to Hemakom et al. (2015) [78].
Afterwards the directions of principal importance and the interchannels power imbalance are used to map uniformly sampled direction set to nonuniform sampling i.e. elliptically distributed points along the directions of principal importance. This issue for a bivariate signal in 2D space is illustrated in Figure 2.15, as one can see for noncircular bivariate signal in the nonuniform sampling the density of the points for signal projections is higher along the ellipse major axis .

The noise assisted NS-BEMD was already used to analyze the Doppler radar signal of a moving object (Ahrabian et al. (2013) [3]) and it was demonstrated this method gave more accurate information, object speed and its localization, compared with wavelet and Fourier based analysis,(Mandic et al. (2013) [118]). Also it was shown in the analysis of EEG data (Electroencephalography) the noise-assisted NS-TEMD provides more accurate decomposition compared with NA-MEMD, (Hemakom et al. (2015) [78]).
However in several applications as cooperative BCIs (Brain-computer interfaces), the signal contains multiple channels and collects correlated information from different sources. The analysis of such signal in order to find intrinsic correlated inter-channel information and so revealing its physical characteristics require a moral general approaches than NS-TEMD which is limited to analysis of trivariate signal.

The NS-TEMD used all eigenvectors and eigenvalues of the trivariate signal covariance matrix in order to determine the directions and inter-channels imbalance for mapping the pre-generated n-dimensional uniform projection vectors on their new position in an n-dimensional ellipsoid.
Applying same method in the case of multivariate signal is quite difficult task, it is mainly because of "*the direction of global highest curvature of the original input signal may not always align with the direction of local first principal component of each sifting input, resulting in a suboptimal estimate of the local mean.*" (Hemakom et al. (2016) [79]).

To overcome this complexity a new approaches is so called Adaptive-projection intrinsically transformed MEMD (APIT-MEMD) is introduced by Hemakom et al. (2016) [79] in which the direction of the first principal components that reflects the largest power imbalance and/or correlation in the channels of the multivariate signal is determined adaptively. Indeed in each sifting processes the vectors that are used to relocate uniform pre-generated direction vectors are defined locally.

Consider a n-variate signal $\mathbf{s}(t)$ as an input for *each sifting process*, the procedure of APIT-MEMD is described as follows :

1. Determine the first principal component of $\mathbf{s}(t)$;
   Perform the eigendecomposition of the covariance matrix given by, $\mathbf{C} = E\{\mathbf{s}\mathbf{s}^T\} = \mathbf{V}\mathbf{\Lambda}\mathbf{V}^T$, (with $E\{.\}$ is the statistical exception operator and $(.)^T$ is the transpose operator). Where $\mathbf{V} = [\mathbf{v}_1, \mathbf{v}_2, ..., \mathbf{v}_n]$ is the eigenvector matrix and $\mathbf{\Lambda} = \text{diag}\ \{\lambda_\mathbf{1}, \lambda_\mathbf{2}, ..., \lambda_\mathbf{n}\}$ is the eignevalue matrix, with the largest eigenvalue $\lambda_\mathbf{1}$ corresponding to eigenvector $\mathbf{v}_1$ i.e. First principal component.

2. Construct a vector pointing in the diametrically opposite direction to the first principal component vector in n-dimensional space; $\mathbf{v}_{01} = -\mathbf{v}_1$, see Figure 2.16a.

3. Uniformly sample an $(n-1)$ sphere using the Hammerseley sequence, (Rehman & Mandic (2009) [152]), to generate a set of K direction vectors $\left\{x^{\theta_k}\right\}_{k=1}^{K}$.

4. Compute the Euclidean distances from each of the uniform direction vectors to $\mathbf{v}_1$.

   Relocating of uniform direction vectors: *Step 5 and Step 6.*

5. Half of all the uniform projection vectors, $\mathbf{x}_{\mathbf{v}_1}^{\theta_k}$, nearest to $\mathbf{v}_1$, are relocated using $\hat{\mathbf{x}}_{\mathbf{v}_1}^{\theta_k} = \dfrac{\mathbf{x}_{\mathbf{v}_1}^{\theta_k} + \alpha\mathbf{v}_1}{|\mathbf{x}_{\mathbf{v}_1}^{\theta_k} + \alpha\mathbf{v}_1|}$, where $0 \leqslant \alpha \leqslant 1$ controls the densities of the projection vectors around the first principal component.

6. The other half of all the uniform projection vectors, $\mathbf{x}_{\mathbf{v}_{01}}^{\theta_k}$, nearest to $\mathbf{v}_{01}$, are relocated using $\hat{\mathbf{x}}_{\mathbf{v}_{01}}^{\theta_k} = \dfrac{\mathbf{x}_{\mathbf{v}_{01}}^{\theta_k} + \alpha\mathbf{v}_{01}}{|\mathbf{x}_{\mathbf{v}_{01}}^{\theta_k} + \alpha\mathbf{v}_{01}|}$.

7. Perform local mean estimation according to MEMD algorithm by using the adaptive direction vectors $\hat{\mathbf{x}}_{\mathbf{v}_1}^{\theta_k}$ and $\hat{\mathbf{x}}_{\mathbf{v}_{01}}^{\theta_k}$.

The α value reflects the degree of power imbalances across the data channels, when $\alpha = 0$ it means there exists no power imbalance or not accounted in the decomposition so APIT-MEMD acts as MEMD, Figure 2.16b. By increasing α the direction vectors will be more clustered around the first principal component of multivariate signal so that $\alpha = 1$ in the case of higher unbalance data, Figure 2.16d. Further developments are required for adaptive selection of this parameter.

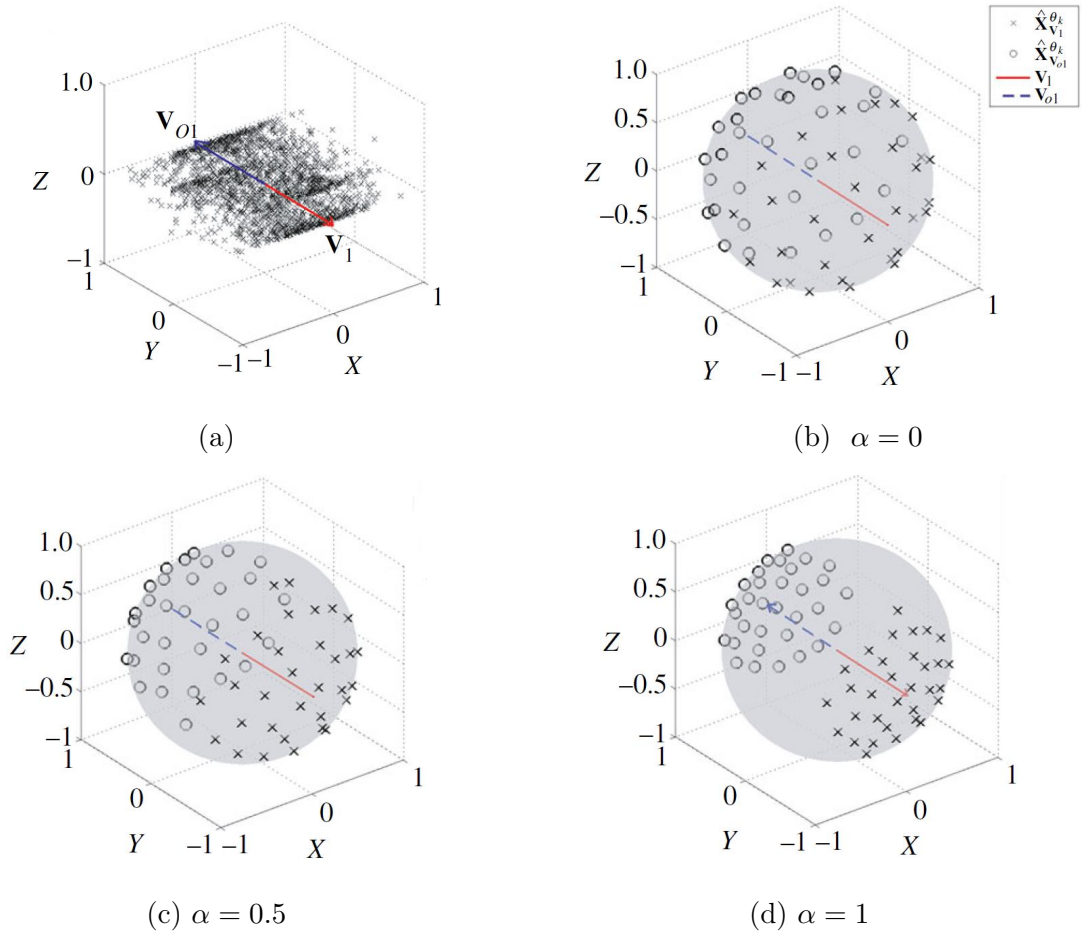

(a) (b) $\alpha = 0$

(c) $\alpha = 0.5$ (d) $\alpha = 1$

Figure 2.16: (a) Scatter plot of the trivariate data. (b), (c) and (d) projection vectors addapted to different α values, from Hemakom et al. (2016) [79].

The APIT-MEMD can operates in the noise-assisted mode i.e. NA-APIT-MEMD, in such case the noise powers should be close to those of the input signal channels, such that the WGN processes themselves do not cause power imbalance. One can choose the noise power as a mean of input signal channels powers.
It should be remind having a noise channel would enforce the dyadic filterbank property and also that increasing the number of WGN would further reduce the degree of overlap (mode-mixing) between the IMFs. If signal resides in multiple dyadic subband, using any noise-assisted APIT/-MEMD algorithms may spread the desired signal across multiple IMFs. Finally in MEMD the number of projection should be 5-6 times more than the number of data channels in order to generate meaningful IMFs however using APIT-MEMD since the direction vectors are more clustered around the first principal component, a fewer direction vectors are required.

Chapter 3

Multidimensional extension of EMD

The EMD has been generally developed to analyze nonlinear and nonstationary one-dimensional (1D) signals. It is a multiresolution decomposition technique which is intuitive, direct and adaptive (data driven) without any pre-defined basis functions that considered any complicate data set into different simple oscillatory modes (IMF) based on local time scales. The combination of EMD with Hilbert spectral analysis creates a paradigm shift in nonlinear-nonstationary data analysis methodology which helps scientist to better understand the physical meaning of different processes. All these properties of EMD have motivated its development for analyzing two or higher dimensional data.

3.1 Monovariate -Two Dimensional EMD

There are two major steps in the sifting process of EMD: definition of signal extrema and subsequent interpolation of those extrema for obtaining max/min envelopes, these issues make the development of EMD for higher dimensions more complicated. Generally there are three types of bidimensional-EMD for analyzing univariate data in 2D space:

(i) In the first type the two-dimensional signal is treated as a collection of one dimensional signals: every row and/or column of 2D-signal is processed by one-dimensional-EMD (standard EMD or EEMD) separately. Such an approach, is called the Pseudo-BEMD, was introduced by Huang et al. (2001) [86]. This method was used for processing the carrier wave data and produced a satisfactory results (Long (2005) [111]). Since in this approach the correlation between horizontal (cf. vertical) structures of the two dimensional signal is not considered, it can be used reliably in the case of existence of a dominant direction in data.

(ii) The second type of 2D EMD, namely the Conventional BEMD, is based on surface fitting. It means the identification of the extrema of the 2D scatter data (two dimensional signal) and then interpolation of those points to generate min/max envelope, i.e. surfaces. There are several versions of this type of two dimensional EMD that differ from each other in the way the surface fitting is achieved.

- Nunes et al. (2003) [129] , (2005) [131] and (2009) [130] used morphological reconstruction or neighboring windows for finding the extrema of two dimensional signal. Then they used radial basis functions or multilevel bi-splines to

compute the surface interpolation. Also they replaced Hilbert transform by Riesz transform to compute the instantaneous frequency of the signal.

- Linderhed (2005) [109] & (2009) [110] introduced the image empirical mode decomposition (IEMD) in which natural extension of the cubic spline to 2D, thin-plate splines (TPS)[16], was used for surface interpolations. In addition, by adding extra data points at the borders of image, the interpolation quality was improved significantly and led to more accurate results comparing to wavelet basis analysis.
- In other studies, Song et al. (2001) [171], Damerval et al. (2005) [35], (2007) [36] and Yuan et al. (2008) [208] proposed two dimensional EMD based on a Delaunay triangulation of the subset of the extrema points and then piecewise cubic interpolation on triangles. As describe by Yang (1986) [206], these types of implementations are computationally effective.
- Hui et al. (2012) [190] proposed empirical mode decomposition on surface in which interpolation was performed by solving a bi-harmonic field with Dirichlet boundary condition, this method behaves like a thin-plate spline interpolation in Euclidean space.
- Niang et al. (2012) [126] proposed Bidimensional-EMD through a mathematical frame work. Nonlinear diffusion filtering as a coupled parabolic partial differential equation is used to estimate the upper and lower envelopes. However this method leads to extrema envelopes like those computed by the cubic interpolation in standard EMD.
- Also there are methods in which the local means of the two dimensional signal are calculated with only one approximation of data and there is no need to interpolation of exrema points. Xu et al. (2006) [204] used the finite-element basis functions to define the local means directly without resorting to envelope interpolation. In this method the local mean of the two dimensional signal is represented as a linear combination of non-oscillated basis functions, the method is rather efficient but cannot correctly analyze the border of the two dimensional signal.
  Jager et al. (2010) [94] combined the method based on local means, inspired by the idea of Chen et al. (2006) [30], with an adaptive wavelet data fitting to extend standard EMD to n-dimensional space.
  Fast-Adaptive Bidimensionel EMD (FABEMD) was introduce by Bhuiyan et al. (2008) [12], (2010) [13] and its improved version, Chen et al. (2014) [26] which replace extrema interpolation for generating envelopes by a direct envelope estimation method. The fact that using no surface interpolation privileges this approach to all before mentioned implementation of bidimensional EMD, this approach is explicitly described in section 3.1.1.

(iii) There is an effective and well-organized approach, so called Multi-Dimensional Ensemble Empirical Mode Decomposition that uses the local spatial filtering feature of EEMD, Wu et al. (2009) [202]. In this method the EEMD is applied to both orthogonal direction of bi-dimensional signal and the final decomposition is obtain by using a new strategy of combining of appropriate components. This method is investigated in section 3.1.2.

The generic algorithm of all Conventional BEMD can be summarized as follows: Let the input two dimensional signal be $I(x, y)$,

1. Obtain the local maxima and minima map of $I(x, y)$, by means of various morphological operations or sliding windows, denoted as $Maxmap(x, y)$ and $Minmap(x, y)$ respectively.

2. Calculate the local mean envelope $M(x, y)$ by:

   (a) Surface interpolation of $Maxmap(x, y)$ (resp. $Minmap(x, y)$), using various type of radial basis function, thin-plate splines, Delunay triangulation, finite-element method and so construction of upper envelope $U_e(x, y)$ (resp. lower envelope $L_e(x, y)$) and then $M(x, y) = [U_e(x, y) + L_e(x, y)]/2$.

   (b) Direct approximation as described in Xu et al. (2006) [204] and Jager et al. (2010) [94].

   (c) Order statistic filter (FABEMD), introduced by Bhuiyan et al. (2008) [12].

3. Subtract the local mean from the two dimensional signal to obtain the detail $h(x, y) = I(x, y) - M(x, y)$.

4. if $h(x, y)$ fulfills the conditions of Stoppage criterion for Bidimensional IMF (BIMF) , as described in the sequel, then $IMF(x, y) = h(x, y)$ otherwise set $I(x, y) = h(x, y)$ and go to step 1.

5. Subtract $IMF(x, y)$ from the $I(x, y)$, so that the residual $r(x, y) = I(x, y) - IMF(x, y)$ is set as the new data series in step 1.

6. Stop the process when the residual $r(x, y)$ from step 5 has less than three extrema at it is considered as a trend component of the considered two dimensional signal.

3.1.1 Fast and Adaptive bidimensional empirical mode decomposition

There are some major problems in the interpolation of 2D scattered data used in classical bidimensional EMD, sometimes at the boundary region of the two dimensional signal there are no extremum point i.e. interpolation center and so cause incorrect upper end lower estimations in this region. This error propagates into the mid region of the signal from iteration to iteration in the sifting process which leads to spurious BIMFs. This shortcoming is more crucial in the last modes.
The second serious problem associated with interpolation is over/under shooting of the estimate envelopes that cause incorrect BIMFs. The third difficulty is linked with the inadequate extrema points which are irregularly placed in the latest modes of decomposition which is another source of error in the decomposition process.

Besides these drawbacks the surface interpolation is a time consuming process since it is an iterative procedure utilizing the extrema points of scatter data to fit a surface to those points so that in some cases decomposition of one two dimensional signal takes hours. Therefor this time complexity restricts its application to real images of only low

resolution per size; (Bhuiyan et al. (2010) [13]) in which different type of surface interpolation in bidimensional EMD were investigated.

To eliminate the need for surface interpolation Bhuiyan et al. (2008) [12] proposed a new approach so-called fast and adaptive bidimensional EMD (FABEMD) in which the upper and lower envelope are computed by mean of some order statistic filter which size is derived from local feature of data itself. The procedure for the generation of upper and lower envelopes in FABEMD is presented in detail as follows:

1. **Extrema detection:** The local extrema are obtained by use of neighboring windows method. A data point is considered as a local extrema if its value is strictly higher (lower) than all of its neighbors. Generally a 3×3 window size result in optimum extrema map for a given two-dimensional signal. In some applications the windows size may be set larger but can lead to the envelopes that do not contain the whole of signal. For finding extrema points at the boundary or corner, the neighboring points beyond the signal are neglected.
   Once the local maxima and minima of the signal are detected, they are stored in the arrays with the same size of input signal, called maxima map; $Maxmap(x, y)$ and minima map; $Minmap(x, y)$, if one point is not neither maximum nor minimum it is replaced by zero in these arrays.

2. **Order statistic filter and windows size determination:** In FABEMD the upper and lower envelopes will be obtained directly by applying two order statistic filters, MAX filter for generating upper envelope and MIN filter for lower envelope, on original data in which the size of filters are obtained by using maxima and minima maps. Order statistic filters are spatial filters whose response is based on ordering the elements contained within the data area that encompassed by the filter, the response of the filter at any point is determined by the ranking result.

   The major issue in FABEMD is the determination of the filter size. For each local maximum point in maxima map $Maxmap(x, y)$, the Euclidean distance to the nearest other maxima points is calculated. This distance is stored in the so-called adjacent maxima distance array $d_{adj-max}$, similarly the adjacent minima distance array $d_{adj-min}$ is calculated by using minima map $Minmap(x, y)$.

   It is evident that the number of elements in each adjacent distance array is the same as the number of maximum or minimum points in the corresponding map, both $d_{adj-max}$ and $d_{adj-min}$ are set in descending order for convenient selection of distances from these arrays. Considering square window, the order statistic filter width (OSFW) w_{en} can be determined as follows:

$$\begin{aligned} w_{en-1} &= min\left\{min\left\{d_{adj-max}\right\}, min\left\{d_{adj-min}\right\}\right\} \\ w_{en-2} &= max\left\{min\left\{d_{adj-max}\right\}, min\left\{d_{adj-min}\right\}\right\} \\ w_{en-3} &= min\left\{max\left\{d_{adj-max}\right\}, max\left\{d_{adj-min}\right\}\right\} \\ w_{en-4} &= max\left\{max\left\{d_{adj-max}\right\}, max\left\{d_{adj-min}\right\}\right\} \end{aligned} \tag{3.1}$$

   where max and min denote the maximum and minimum values of the elements in the array { }. These four candidates for the filtering operation are rounded to the

nearest odd integer. Let the order statistic filter widths w_{en-1}, w_{en-2}, w_{en-3} and w_{en-4} be denoted as Type-1, Type-2, Type-3 and Type-4 respectively, it is obvious that type-4 is the highest OSFW and type-1 is the lowest OSFW; Type-1 $<$ Type-2 $<$ Type-3 $<$ Type-4.

If using Type-3 and Type-4, the w_{en} required for $i+1th$ BIMF generally appears larger than that for the ith BIMF hence ensure the local spatial scales of the bidimensional mode hierarchically increase by going to the later modes (Bhuiyan et al. (2008) [12]) and also it is in such case that the extraction of the modes becoming data driven, however, using type-1 and type-2 for determination of w_{en} may not lead to larger w_{en} for $ith+1$ BIMF than that for the ith BIMF.
Once the w_{en} was obtained it is used for both MAX and MIN filter, in fact employing the same filter size for generating upper and lower envelope enforces extraction of the similar spatial scales into the BIMFs. It should be mentioned different types of order statistic filter are suitable for difference applications.

3. **Applying OSF and smoothing for envelop generation:** Once the filter size is defined, MAX and MIN filter are applied to obtain upper and lower envelopes, $U_e(x,y)$and $L_e(x,y)$, specified as

$$U_e(x,y) = MAX\left\{S(s,t)\right\} \quad , \quad (s,t) \in Z_{xy} \tag{3.2}$$

$$L_e(x,y) = MIN\left\{S(s,t)\right\} \quad , \quad (s,t) \in Z_{xy} \tag{3.3}$$

In Eq(3.2) the value of the upper envelope $U_e(x,y)$, at any point (x,y) is simply the maximum value of the elements in $S(s,t)$ in the region defined by Z_{xy}, where Z_{xy} is the square region of size $w_{en} \times w_{en}$ centered at any point (x,y) of $S(s,t)$. Similarly the value of lower envelope $L_e(x,y)$ at any point (x,y) in Eq(3.3) is the minimum value of the elements $S(s,t)$ in the region defined by Z_{xy}.
Subsequently an averaging smoothing operation is carried out on $U_e(x,y)$ and $L_e(x,y)$ employing the same window size used for corresponding order statistic filter, which may be expressed as:

$$U_e(x,y) = \frac{1}{w_s \times w_s} \sum_{(s,t)\in Z_{xy}} U_e\left(s,t\right) \tag{3.4}$$

$$L_e(x,y) = \frac{1}{w_s \times w_s} \sum_{(s,t)\in Z_{xy}} L_e\left(s,t\right) \tag{3.5}$$

where w_s is the window size of averaging smoothing filter and $w_s = w_{en}$, Z_{xy} is the square region of size $w_s \times w_s$ centered at any point (x,y) of $U_e(x,y)$ and $L_e(x,y)$.

After determination of smoothed envelopes, the mean envelope is calculated like conventional BEMD; $M(x,y) = \left[U_e(x,y) + L_e(x,y)\right]/2$.

In FABEMD, the number of Sifting processes (i.e. extrema detection, determination of upper and lower envelopes, computation of mean envelope and finally subtraction of that envelope from the 2D signal) for finding a bidimensional IMF is restricted to one, in fact one iteration per BIMF in FABEMD produces similar or better results than can be achieved by conventional BEMD with more than one iteration (Bhuiyan

et al. (2008) [12]). So FABEMD can decompose fastly two-dimensional signal of any size or resolution while conventional BEMD is unable.

Another and also the major interest of this method is the elimination of over/under shoot in the data boundaries, in Figures 3.1 the efficiency of FABEMD to estimate the signal envelopes is compared with cubic spline interpolation.

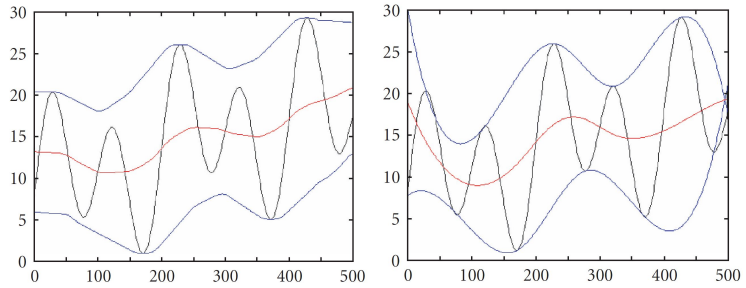

Figure 3.1: Envelope estimation; (a) Using FABEMD, (b) Using cubic spline interpolation, [12].

3.1.2 Multi-Dimensional Ensemble Empirical Mode Decomposition

The major drawback of Pseudo-BEMD, as mentioned at the first of this chapter, is the inter-slice discontinuity while two dimensional signals is treated as a collection of one-dimensional signals. But when two-dimensional signal has coherente structures associated with the spatial scale in a particular direction, this problem can be solved by replacing EMD with EEMD. In this case Pseudo-BEMD benefits from the spatial-temporally local filtering feature of EEMD, Wu & Huang (2009) [201].

However in most cases the spatial two-dimensional data do not have preferred direction so they should be equally treated in any given orthogonal directions, for this purpose the Multi-dimensional Ensemble Empirical Mode Decomposition was introduce by Wu et al. (2009) [202]. In this method EEMD is applied to spatial data in one dimension similar to pseudo-BEMD, followed EEMD is applied in the second dimension to the results of decomposition in first dimension, then by applying the combination strategy so called the comparable minimal scale principle, the appropriate components are fused and the decomposition of signal will be obtained. The procedure is as following: suppose $f(m,n)$ represents *gridded* spatially two-dimensional data of a function $f(x,y)$

$$f(m,n) = \begin{bmatrix} f_{1,1} & f_{2,1} & \dots & f_{M,1} \\ f_{1,2} & f_{2,2} & \dots & f_{M,2} \\ \dots & \dots & \dots & \dots \\ f_{1,N} & f_{2,N} & \dots & f_{M,N} \end{bmatrix} \tag{3.6}$$

mth column of the data can be written as

$$f(m,\sim) = \begin{bmatrix} f_{m,1} \\ f_{m,1} \\ \dots \\ f_{m,N} \end{bmatrix} \tag{3.7}$$

and its decomposition using EEMD is

$$f(m,\sim) = \sum_{j=1}^{J} C_j(m,\sim) = \sum_{j=1}^{J} \begin{bmatrix} C_{m,1,j} \\ C_{m,2,j} \\ \dots \\ C_{m,N,j} \end{bmatrix} \tag{3.8}$$

so to decompose $f(m,n)$ in one direction, here y-direction, all columns of $f(m,n)$ are decomposed and the outputs are rearranged into J number of matrices, with jth matrix being

$$g_j(m,n) = \begin{bmatrix} C_{1,1,j} & C_{2,1,j} & \dots & C_{M,1,j} \\ C_{1,2,j} & C_{2,2,j} & \dots & C_{M,2,j} \\ \dots & \dots & \dots & \dots \\ C_{1,N,j} & C_{2,N,j} & \dots & C_{M,N,j} \end{bmatrix} \tag{3.9}$$

Henceforth each component $g_j(m,n)$ is decomposed in horizontal direction, i.e. applying EEMD on each row of $g_j(m,n)$ as done in previous step. The nth row of jth component $g_j(\sim,n)$ of $f(m,n)$ is

$$g_j(\sim, n) = \begin{bmatrix} C_{1,n,j} & C_{2,n,j} & \dots & C_{M,n,j} \end{bmatrix} \tag{3.10}$$

and its EEMD decomposition is

$$g_j(\sim, n) = \sum_{k=1}^{K} D_{j,k}(\sim, n) = \sum_{k=1}^{K} \begin{bmatrix} d_{1,n,j,k} & d_{2,n,j,k} & \dots & d_{M,n,j,k} \end{bmatrix} \tag{3.11}$$

So the kth component in x-direction while applying EEMD on jth components (result from decomposition in y-direction) is

$$h_{j,k}(m, n) = \begin{bmatrix} d_{1,1,j,k} & d_{2,1,j,k} & \dots & d_{M,1,j,k} \\ d_{1,2,j,k} & d_{2,2,j,k} & \dots & d_{M,2,j,k} \\ \dots & \dots & \dots & \dots \\ d_{1,N,j,k} & d_{2,1,j,k} & \dots & d_{M,N,j,k} \end{bmatrix} \tag{3.12}$$

Finaly two-dimensional input data is represented as

$$f(m, n) = \sum_{k=1}^{K} \sum_{j=1}^{J} h_{j,k}(m, n) \tag{3.13}$$

Figure 3.2 represents a horizontal component of in-cylinder velocity filed at 212 CAD bTDC for 1400 rpm engine speed. This filed as an original data (45×61 data length) is decomposed by above procedure and the results is displayed in Figure 3.3. The top row represents the decomposition in the horizontal direction, each two-dimensional component (horizontal direction components) is decomposed in the vertical direction with their results illustrated in the vertical columns.

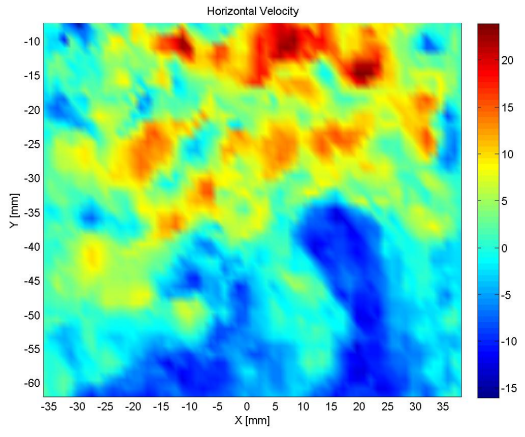

Figure 3.2: Original data; horizontal velocity of an in-cylinder flow field at 212 CAD bTDC for 1400 rpm engine speed, the unit is $[m.s^{-1}]$.

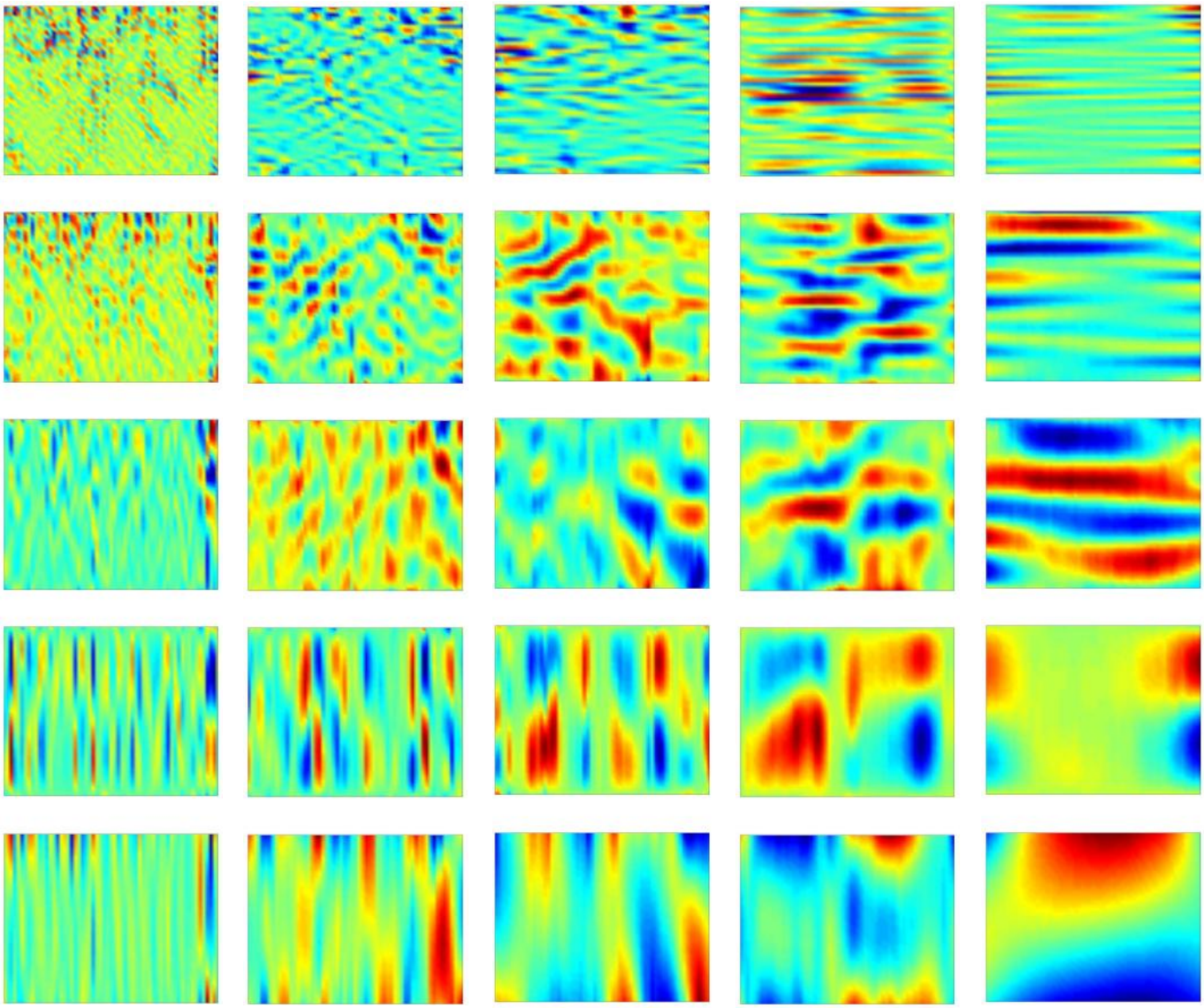

Figure 3.3: The components result from applying EEMD in two orthogonal directions of original data (Figure 3.2). The scale in each panel is different, Blue color correspond to zero magnitude.

By careful consideration the results in Figure 3.3 reveal some oriented scale of the original data and also some similar characteristics in different components can be observed. The horizontal velocity oscillation for different row (resp. column) components along the central column i.e. $31th$ of 61 columns (resp. row i.e. $23th$ of 45 rows) are displayed in Figure 3.4 (resp. Figure 3.5).
As one can see the components of each row have approximately the same vertical scale and the components of each column have approximately the same horizontal scale. Also the horizontal (vertical) scales of the each row (column) increase as k (j) increase, this feature for the first row and column is presented in Figures 3.6a and 3.6b respectively.

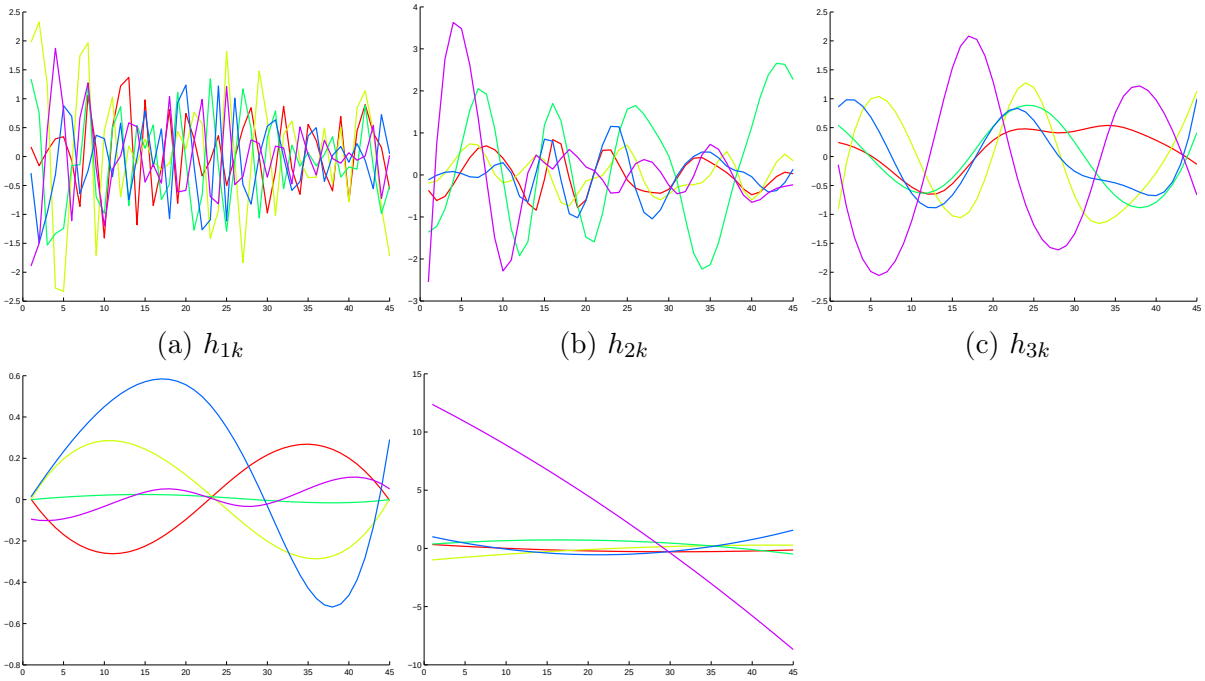

(a) h_{1k} (b) h_{2k} (c) h_{3k}

(d) h_{4k} (e) h_{5k}

Figure 3.4: Vertical scales of the row components. There are five row components $(h_{1k}, h_{2k}, ..., h_{5k})$ and each row consists of five components $(k = 1, 2, .., 5)$. For each row component the horizontal velocity oscillation along the central column (the $31th$ column along 45 data points in vertical direction) are displayed. In each figure the different colors correspond to different components: red lines; $k = 1$, light green lines; $k = 2$, green lines; $k = 3$, blue lines; $k = 4$, magenta lines; $k = 5$.

Another important property of the components displayed in Figure 3.3 is to have approximately the same minimal scales for the first row h_{1k} components in vertical direction and for the first column h_{j1} component in horizontal direction.

The final components of the original data are obtained by applying the comparable minimal scale principle: "*among all the components resulted from applying EEMD in two orthogonal directions, the combination of the components having comparable minimal scales would give the most meaningful results. This combination will give a single IMF component revealing the true two-dimensional feature of the data.*" Wu et al. (2009) [202]. Using this combination principle the final i*th* BIMF can be obtained by

$$BIMF_i = \sum_{k=i}^{K} h_{i,k} + \sum_{j=i+1}^{J} h_{j,i} \tag{3.14}$$

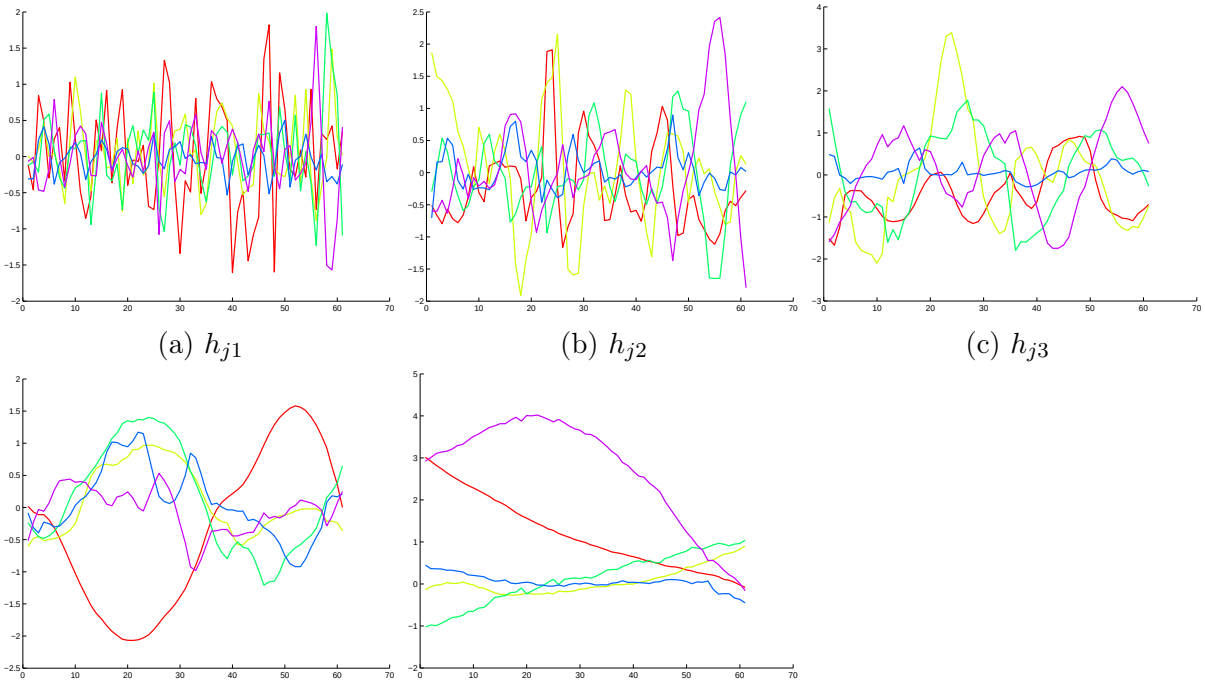

(a) h_{j1} (b) h_{j2} (c) h_{j3}

(d) h_{j4} (e) h_{j5}

Figure 3.5: Horizontal scales of the column components. There are five column components $(h_{j1}, h_{j2}, ..., h_{j5})$ and each column consists of five components $(j = 1, 2, .., 5)$. For each column component the horizontal velocity oscillation along the central row (the $23th$ row along 61 data points in horizontal direction) are displayed. In each figure the different colors correspond to different components: red lines; $j = 1$, light green lines; $j = 2$, green lines; $j = 3$, blue lines; $j = 4$, magenta lines; $j = 5$.

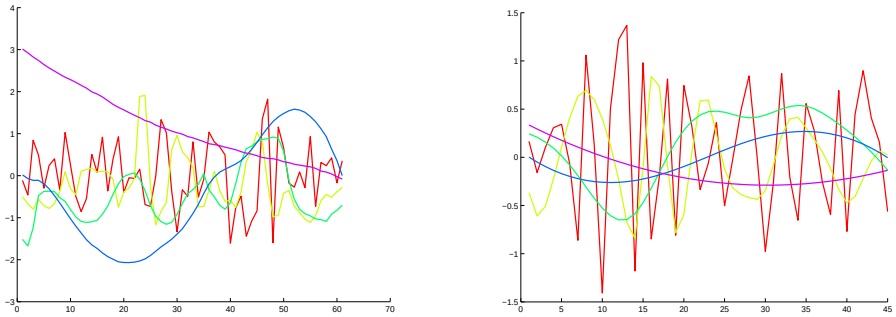

(a) h_{1k} (b) h_{j1}

Figure 3.6: (a) Horizontal scales of the first row components, (b) Vertical scale of the first column components. In each figure the different colors correspond to different components: red lines; k or $j = 1$, light green lines; k or $j = 2$, green lines; k or $j = 3$, blue lines; k or $j = 4$, magenta lines; k or $j = 5$.

The schema of Eq(3.14) is presented in Figure 3.7, the neighbor components with the same shade are summed to construct a final mode.

$h_{1,1}$	$h_{1,2}$	...	$h_{1,k}$
$h_{2,1}$	$h_{2,2}$	...	$h_{2,K}$
...	...	...	...
$h_{K,1}$	$h_{K,2}$	...	$h_{K,K}$

Figure 3.7: Combination strategy for different components resulted from applying EEMD in two orthogonal directions, in presented schema the component numbers for both horizontal and vertical direction are the same, otherwise the Eq(3.14) is yet valid.

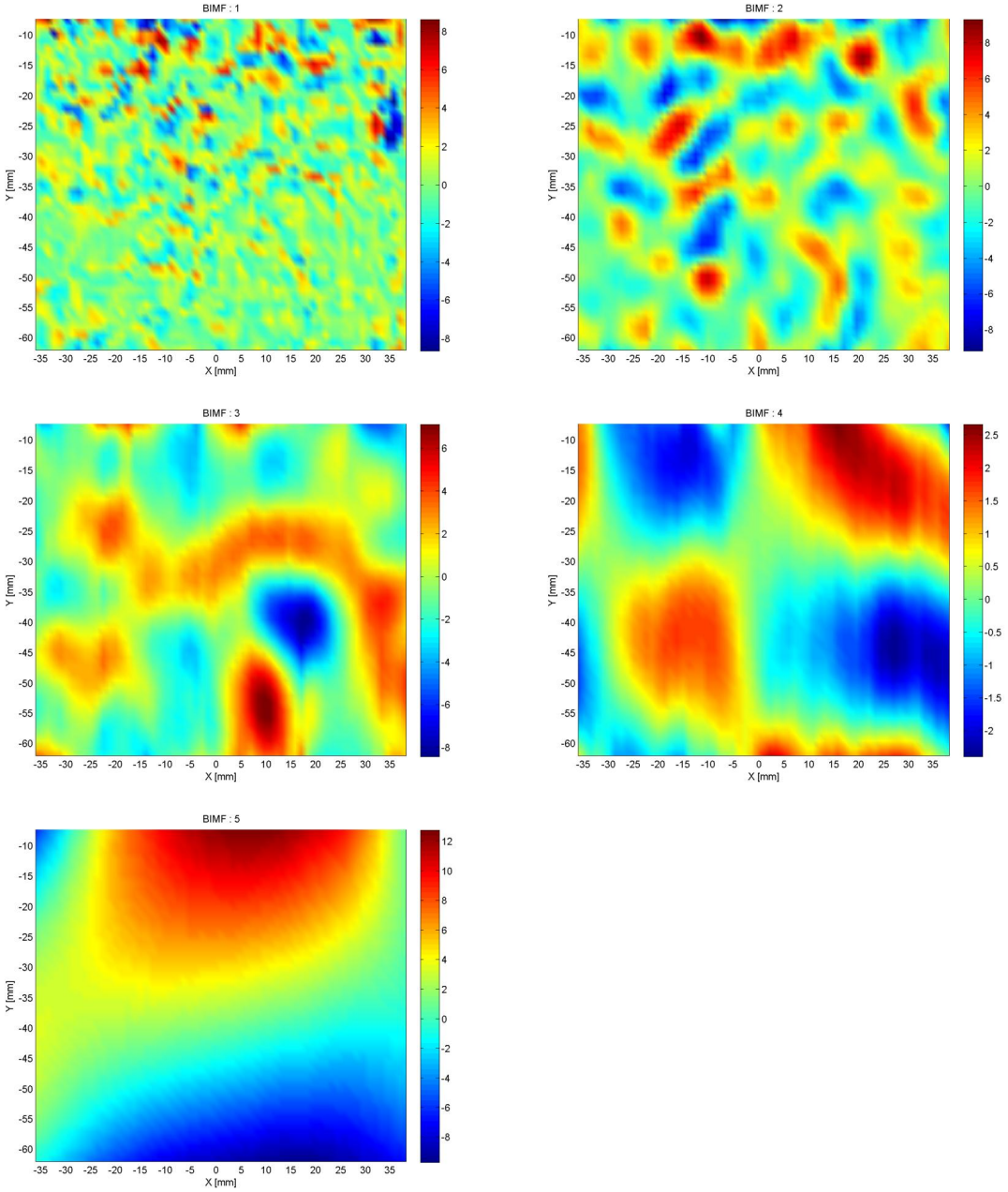

Figure 3.8: The final BIMFs of the original data presented in Figure 3.2.

The final modes of the original data (horizontal component of in-cylinder velocity field at 212 CAD bTDC for 1400 rpm engine speed) are displayed in Figure 3.8. It should be mentioned the decomposition is independent of the selection of the orthogonal reference frame so the results are not sensitive to the choice of direction(first horizontal and then vertical or vice versa) for applying EEMD.

3.2 Bivariate (Multivariate)-Two Dimensional EMD

The potentiel of Bivariate EMD (BEMD) in fusion of two images i.e. data multiscale fusion was already investigated by Looney & Mandic (2009) [113] and Rehman et al. (2009) [151]. In such approach the same index rows (or column) of two images, A and B, are considered as two components of a complex signal then using bivariate EMD it is decomposed into M complex IMFs. Separating the IMFs into their real and imaginary components and reconverting each into their original 2D form gives a set of M scale images for both A and B, Figures 3.9. The final image is obtained by applying a fusion methodology based on local variance for each scale, same-index IMFs, at each location. This study is not concerned with the image fusion algorithms and for detailed explication see above mentioned references.

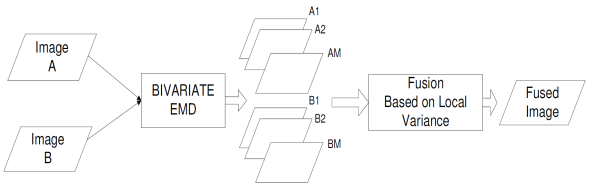

Figure 3.9: Image fusion methodology by bivariate EMD, from Rehman et al. (2009) [151].

Also in other investigation MEMD was used to combine any number of input images but via different multi-scale fusion methodology, Rehman et al. (2015). Different studies reported significantly better performance of MEMD-based fusion schemes compared with those based on discrete wavelet transform (DWT) or principal components analysis (PCA) as so-called POD in fluid mechanics community, (Mandic et al. (2013)[118], Rehman et al. (2015) [156]). In fact by insightful viewpoint these results reveal the ability of EMD approach to ***relate*** *multiple components (i.e. IMFs) of a multichannel signal which its variates are laid in two-dimensional space.*

In this study we propose the use of Ensemble NA-APIT-MEMD for analysis (processing) of two-dimensional velocity field. The instantaneous two dimensional velocity field is considered as a two dimensional trivariate signal $\mathbf{U}(x, y) = U(x, y) + V(x, y) + W(x, y)$, where U, V and W are the velocity components in x, y and z direction respectively.
In first step the Ensemble NA-APIT-MEMD is applied to each row (or column) of the two dimensional signal i.e. decomposition in first dimension.
Subsequently in the second step it is applied to each column (or row) of the results of the decompositions in the first step i.e. decomposition in second dimension. In the last step using comparable minimal scale combination principle (Wu et al. (2009) [202]), the appropriate components are merged together in order to construct different two dimensional

trivariate IMFs (modes). The algorithm of decomposition is similar to that in Multidimensional EEMD, which was explained in Section 3.1.2.

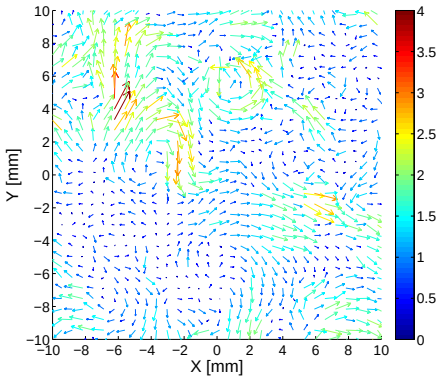

Figure 3.10: Experimental homogeneous and isotropic turbulent velocity field.

Figure 3.10 displays a single experimental homogeneous and isotropic turbulent velocity field, this signal is decomposed by proposed Bivariate 2D- EMD and the results of decomposition are presented in Figure 3.11. The first panel presents the two components U and V of this signal and the different IMFs resulted from decomposition are presented in following below them.

For Bivariate 2D-EMD analysis, one adjacent white Gaussian noise channel is used. In order to not modify the degree of power imbalance between data channels the noise variance is equal to the mean variance of the two principal input signals i.e. U and V velocity components. To compute the mean envelope, input multi-components signal is projected on 64 directions with the projection density defined by $\alpha = 0.3$.
For Sifting process the Mean-value stoppage criterion with $(0.05, 0.5, 0.05)$ is used and the number of ensemble realizations NE is set to 100.

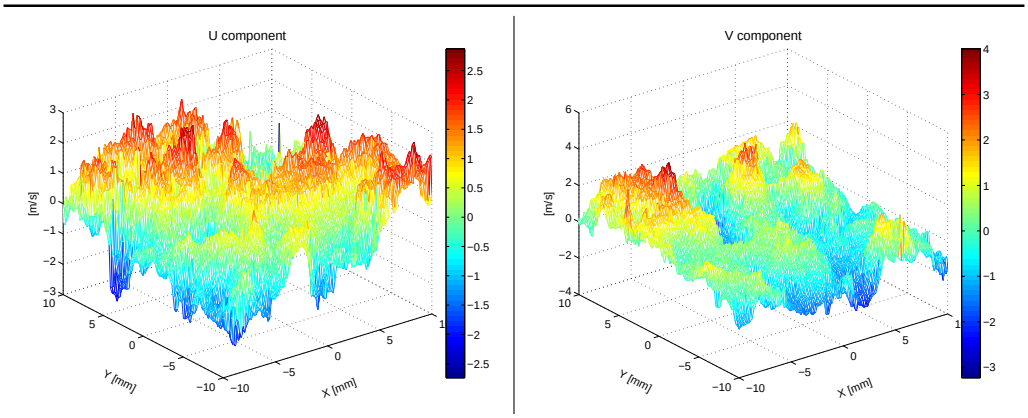

Figure 3.11 *Cont.*

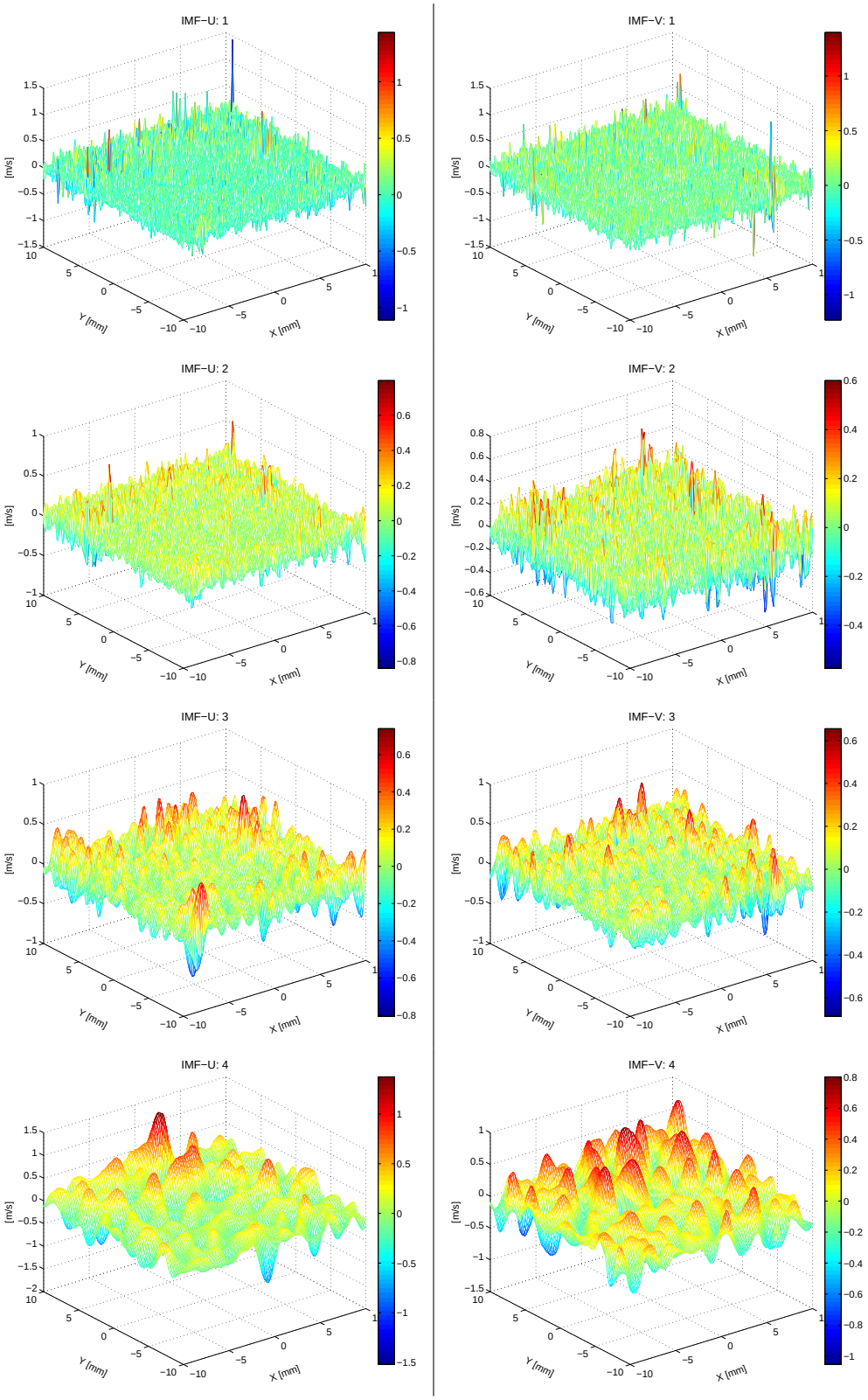
IMF−U: 1
IMF−V: 1
IMF−U: 2
IMF−V: 2
IMF−U: 3
IMF−V: 3
IMF−U: 4
IMF−V: 4
[m/s]
Y [mm]
X [mm]

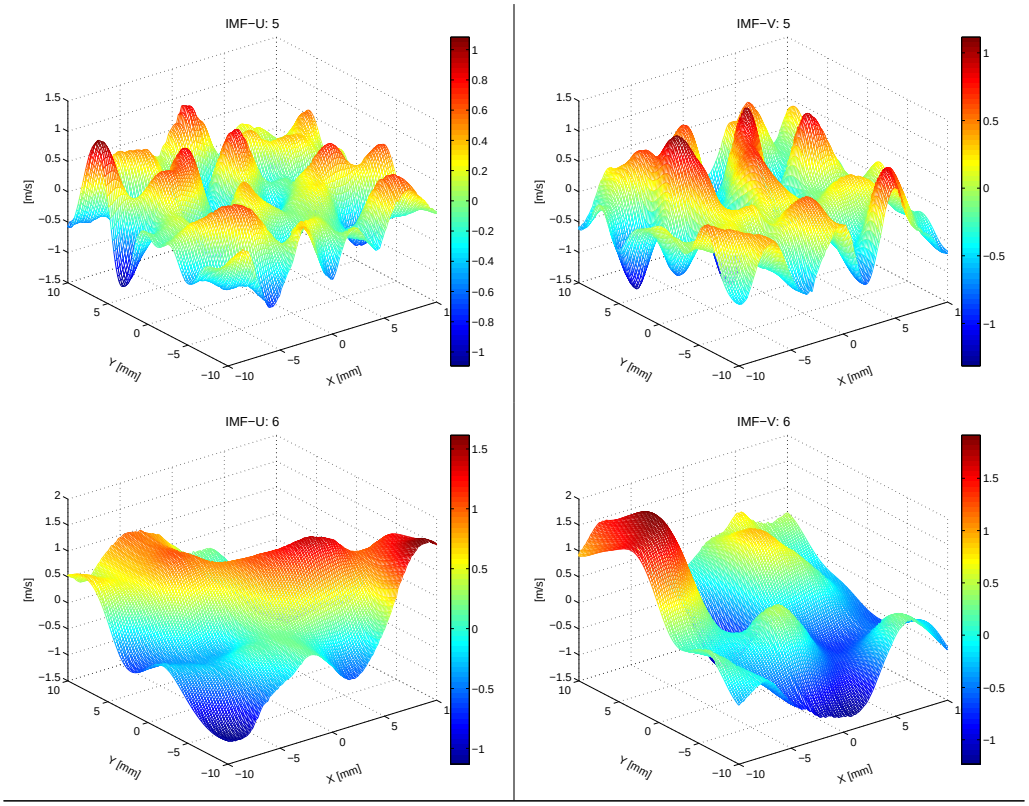

Figure 3.11: The horizontal and vertical components of velocity field presented in Figure 3.10 and different modes resulted from Bivariate 2D-EMD analysis.

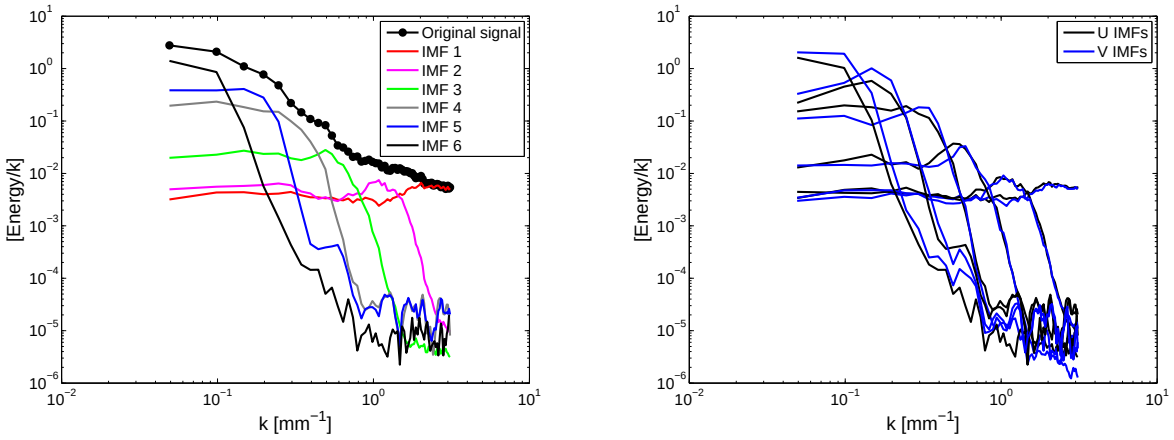

(a) (b)

Figure 3.12: (a) Power spectra of different bivariate IMFs, (b) Overlapping of the frequency band for the same-index modes corresponding to components, U and V of the input velocity field.

As one can see in Figure 3.11 the first mode of each components U and V contains the highest order of fluctuations that are associated with the smallest scale of the velocity field. When the decomposition progresses, the spatial frequency of the fluctuations in the modes decreases and the last mode of each components represents the tendency of

the input signal that are associated with the large-scale structure of velocity fields. This property of Bivariate 2D-EMD decomposition can be verified by computing the spatial power spectral density of each bivariate IMFs, Figure 3.12a. Also it is observed the energy of different modes are concentrated in different wavenumbers (scales) that ensure a very low degree of mode-mixing in the decomposition.
In addition different components of input velocity field are match in the number of modes and also the same-index modes across data channels contains common scales i.e. Mode alignment. The power spectrum of all IMFs associated with two velocity components are presented in Figure 3.12b and as one can see the frequency-bands of the same-index modes are quite overlapped.
It is worth noticing that the Mono dimensional APIT-MEMD algorithm is provided by Rehman & Mandic (2010) [152] and Hemakom et al. (2016) [79], is available in
http://www.commsp.ee.ic.ac.uk/~mandic/research/emd.htm .

Chapter 4

Validation: Application on homogeneous and isotropic turbulence

This chapter is dedicated to applications of EMD on a turbulent velocity field in order to evaluate the performance of this approach to decompose this type of signals. An experimental homogeneous isotropic turbulent (HIT) flow is used as an initial (original) velocity signal, $\mathrm{U}_i(x, y, t)$, including U and V components in x and y directions respectively. This flow was obtained in a spherical combustion chamber where 6 fans generated turbulence with zero average velocity. The velocity field of 127×127 vectors was provided by means of High Speed-PIV at 3.5 kHz frequency with a spatial resolution 0.16 mm mesh size, so field of view of 20.32×20.32 mm^2. This homogeneous isotropic turbulent velocity field was previously characterized in terms of Integral length and time scales and energy spectra by Galmiche et al. (2014) [64].

4.1 Analysis of decomposition quality via EMD, EEMD, CEEMDAN and CEEMD with different stoppage criteria for sifting process

In this section the performance of EMD, EEMD, CEEMDAN, CEEMD in the decomposition of perturbed turbulent velocity signal is evaluated, the velocity signal under analysis is temporal (One point-different times) and mono component U. To achieve this objective the methodology is as fallow:

The initial HIT velocity field is perturbed by a known synthetic signal, so-called interference or perturbation signal, then the velocity signal at "each point" of the outcome perturbed flow field is decomposed by different versions of EMD using different stoppage criteria for sifting process. Afterwards the correlations between perturbation signal and different IMFs results from decomposition are computed and then the maximum correlation is normalized by others correlation values as following:

$$C_{Max} = \frac{max(c_i)}{\frac{\sum_{i \neq I}^{c_i}}{n-1}} \tag{4.1}$$

Where c_i is the correlation between i^{th} IMF of perturbed signal and perturbation one with $i = 1, 2, ..., n$ and n is the total number of the modes. max denotes the maximum value of the elements in the array and I the index of the IMF that has the maximum correlation with perturbation signal.
The key point is: a high value for C_{Max} indicates the feature of perturbation is buried rather in one IMF of perturbed velocity signal. By this way C_{Max} is computed at each point of the perturbed velocity field (127×127 position points) and then average over all points, which results in $C_{Max-mean}$ indicator.
The perturbed velocity field is also decomposed by EEMD, CEEMDAN and CEEMD, therefore the $C_{Max-mean}$ associated to each one is computed. Among different methods the one that leads to the highest value of $C_{Max-mean}$ is considered as the most effective method to decompose this type of perturbed velocity signal.

The homogeneous isotropic turbulent flow field U_i is perturbed by a part of synthetic Lamb-Ossen vortex velocity field P, this perturbation signal could almost mimics in-cylinder large scale motion. The maximum magnitude of the perturbation is 9 $m.s^{-1}$ and the frequency of the vortex center fluctuations is set to 25 Hz that corresponds to the 1500 rpm engine speed. Then the perturbed signal is $U_p = U_i + P$, see Figure 4.1.

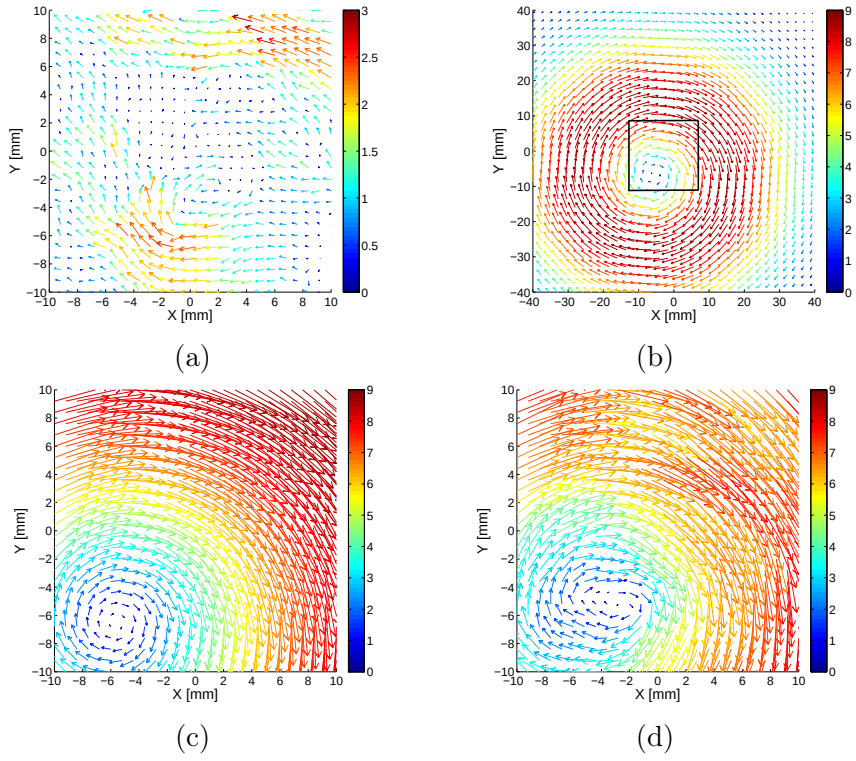

Figure 4.1: (a) U_i initial experimental flow-field (HIT) every five vectors were displayed, (b) Complete Lamb-Ossen generated vortex, (c) P arbitrary part of Lamb-Ossen vortex, same size of initial signal that corresponds to the black square in (a) and (d) U_p perturbed signal, considered as input signal for EMD analysis.

Once applying different versions of EMD on this type of perturbation itself P, just two IMF will be obtain, as an example this issue for three points on perturbation field is presented in Figure 4.2. The second IMF is always a trend of perturbation so to compute

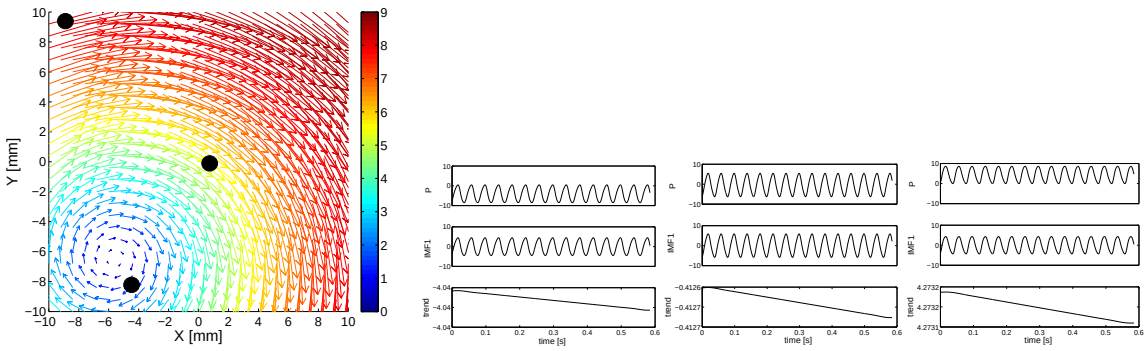

(a) (b) (c) (d)

Figure 4.2: (a)Positions of 3 different points in the perturbation velocity filed and their EMD decomposition in (b), (c) and (d).

C_{Max} in Eq (4.1), the correlation between the first IMF of perturbation signal and different IMFs of perturbed signal are considered.
To understand better this methodology, the EMD was applied to one point of perturbed flow field and also to the perturbation on this point and then the correlation between the first IMF of perturbation and the different IMFs of perturbed signal are computed and the results is shown in Figure 4.3. As one can see the perturbed signal has 7 IMFs and the 4^{th} IMF has the maximum correlation of $c_I = 0.92$ with the perturbation signal and when it was normalized by others correlations using Eq (4.1) the $C_{Max} = 19$ for this point.

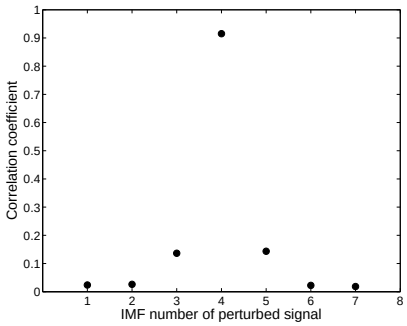

Figure 4.3: Correlation coefficient between the first IMF of perturbation and different IMFs of perturbed velocity signal.

In this investigation, the Cauchy type and the S-number stoppage criteria for the sifting process are not considered since the first is based on mathematical convergence condition and does not depend on the definition of IMF as described by Huang et al. (1998) [91] and the second leads to mode mixing problem as underlined Wu & Huang (2009) [201]. So two other types, Mean value criterion and Fixed sifting time criterion i.e. 10 iterations, are used in Sifting process.

It must be noted the choice of interpolation for generating extrema envelopes has an important effect on resulting IMF components, the linear or polynomial interpolation increases the number of sifting process or causes the over decomposition of signal while the cubic spline interpolation preserves the decomposition quality (Huang et al (1998) [91] and Rilling et al. (2003) [161]). Using this type of interpolation each interval between data

points is represented by a different Third-order spline function as described by Bojanov et al. (1993) [15].

Application of EMD

Different test cases including different stoppage criteria and signal end processing are summarized in Table 4.1. By applying standard EMD with fixed sifting time stoppage criterion and modification of linear extrapolation for signal end processing, $C_{Max-mean}$ reaches the maximum value of 24.05.

Test case	Stoppage criterion	Boundary condition for signal end	$C_{Max-mean}$
a	Mean value	Mirror symmetry	17.67
b	Fixed sifting time	Mirror symmetry	15.22
c	Mean value	Modified linear extrapolation	24.05

Table 4.1: Different test conditions and the results obtained by EMD.

Application of EEMD

When applying EEMD, CEEMD and Complete EEMD the ensemble number of trial is set to the order of 100 as proposed by Wang et al. (2014) [189] and the noise level ε_0 of added white Gaussian noise is selected to 0.1, 0.2 and 0.4 in all different test cases.
In this study the application of EEMD is divided in two categories with respect to the stoppage criterion. In the first category, the Mean value stoppage criterion for sifting process and Mirror symmetry boundary condition for signal-end effect treatment, are used, the different test cases are presented in Table 4.2. The values of $C_{Max-mean}$ drop drastically with replacing standard EMD by EEMD under these conditions, also the variations of noise amplitude have not considerable influence in decomposition quality.

Test case	ε_0	$C_{Max-mean}$
a	0.1	7.97
b	0.2	9.11
c	0.4	8.77

Table 4.2: Effect of noise level for the application of EEMD, with the Mean-value stoppage criterion.

In the second category, fixed sifting time stoppage criterion is chosen for sifting process, and in addition to the Mirror symmetry boundary condition for extending the interpolation to the signal edge, the Modified linear extrapolation is tested with also the different noise levels. All tested conditions are summarized in Table 4.3.

Test case	Boundary condition for signal end	ε_0	$C_{Max-mean}$
a	Mirror symmetry	0.1	10.22
b	Modified linear extrapolation	0.1	9.75
c	Mirror symmetry	0.2	9.80
d	Modified linear extrapolation	0.2	9.57
e	Mirror symmetry	0.4	17.36
f	Modified linear extrapolation	0.4	12.57

Table 4.3: Effect of noise level for the application of EEMD, with the Fixed sifting time stoppage criterion.

When signal boundary is treated by Modified linear extrapolation technique the values of $C_{Max-mean}$ are low without real effect of added noise level. In the case of use Mirror symmetry for handling signal end, the high value of noise level, $\varepsilon_0 = 0.4$, increases the decomposition quality. It is also important to notice that in this study the initial signal with maximum amplitude of 3 $m.s^{-1}$ is dominated by the perturbation with 9 $m.s^{-1}$ maximum amplitude hence adding a noise with high amplitude leads to amelioration of decomposition.

Application of CEEMDAN

As previous parts, the performance of CEEMDAN is evaluated in two categories : first, by using Mean value stoppage criterion for sifting process and then Fixed sifting time stoppage criterion. It should be noticed this approach is introduced by Torres et al (2011) [182] and they proposed use of Mirror symmetry boundary for signal-end handling. The conditions for the first and second categories and associated results are presented in Table 4.4.

Test case	ε_0	$C_{Max-mean}$
a	0.1	8.65
b	0.2	8.14
c	0.4	7.85

(a)

Test case	ε_0	$C_{Max-mean}$
a	0.1	8.43
b	0.2	8.00
c	0.4	7.54

(b)

Table 4.4: Conditions for CEEMDAN.(a) The Mean-value and (b) The Fixed sifting time stoppage criterion.

There is no significant difference between these two categories of tests, small values of $C_{Max-mean}$ are obtained, representing the inefficiency of this approach to decompose the input velocity signal.

Application of CEEMD

This approach was introduced by Yeh et al. (2010) [207]. They proposed the use of the

Fixed sifting time stoppage criterion for sifting process, whereas the signal boundary is treated by both Mirror symmetry and Modified linear extrapolation technique. The test cases and results are summarized in Table 4.5, the values are significantly similar to ones obtained when applying EEMD with Fixed sifting time stoppage criterion.

Test case	Boundary condition for signal end	ε_0	$C_{Max-mean}$
a	Mirror symmetry	0.1	10.22
b	Modified linear extrapolation	0.1	9.71
c	Mirror symmetry	0.2	9.80
d	Modified linear extrapolation	0.2	9.95
e	Mirror symmetry	0.4	17.39
f	Modified linear extrapolation	0.4	12.30

Table 4.5: Effect of noise level for the application of EEMD, with Mean-value stoppage criterion.

The quality of decomposition is lower than standard EMD, in the case of Modified linear extrapolation but while the signal boundary is handled by Mirror symmetry technique the quality of decomposition is quite good for high amplitude of added noise i.e. $\varepsilon_0 = 0.4$ same as application of EEMD with Fixed sifting time stoppage criterion.

As a conclusion, in this part of study the different types of EMD were used to decompose a synthetic-perturbed HIT flow, with a perturbation signal representing the large scale motion generated in the cylinder of engine. The input velocity field was analyzed as a mono-component signal with temporal evolution.
The results demonstrate by using standard EMD with Fixed sifting time stoppage criterion, the feature of monotone perturbation appears almost in one mode after decomposition and does not diffuse over several modes. By using an adapted approach, the perturbation can separated from the initial signal. Application of some other methods to decompose this type of signal did not improve the decomposition quality and sometimes leads to drastic mode-mixing phenomena, as in the case of CEEMDAN.
The interesting issue reveals once using EEMD with Fixed sifting time stoppage criterion. In this case the decomposition is sensible to the amplitude of added white Gaussian noise, in which by increasing $\varepsilon_0 = 0.4$ the quality of decomposition is improved significantly.

The Matlab codes used in this study are available in:
EMD, http://perso.ens-lyon.fr/patrick.flandrin/emd.html
EEMD and CEEMD, http://rcada.ncu.edu.tw/
CEEMDAN, http://bioingenieria.edu.ar/grupos/ldnlys/metorres/re_inter.htm

4.2 Application of Bivariate EMD for separating coherent structure from homogeneous and isotropic turbulence

In this part, the initial(called also original) signal $U_i(t)$, i.e. the homogeneous isotropic turbulent (HIT) flow field, is perturbed by a monotone signal as a synthetic fluctuation $P(t) = A.sin(2f.t)$, with A and f the amplitude and frequency of the perturbation respectively. This perturbation that could simulate a coherent structure is added to each component of velocity, U and V in every points of the initial field (127×127 points), so the perturbed velocity vector used for the analysis is $U_p(t) = U_i(t) + P(t)$.

The methodology was as follows: by applying Bivariate EMD, the input velocity field is decomposed to different modes (IMFs), it is simultaneous decomposition of the two coupled velocity components U and V afterwards recovered signal $U_r(t)$, is obtained thanks to the resemblance criterion. If the turbulent properties in the recovered velocity field are the same as ones in the initial signal, it means the synthetic perturbation was separated from the original flow field.

The Bivariate EMD considers the bivariate signal as a fast rotation superimposed on slower ones, Rilling et al.(2007) [162]. It assorts the different modes (bivariate IMFs) of a velocity signal from high frequency to the lowest one.

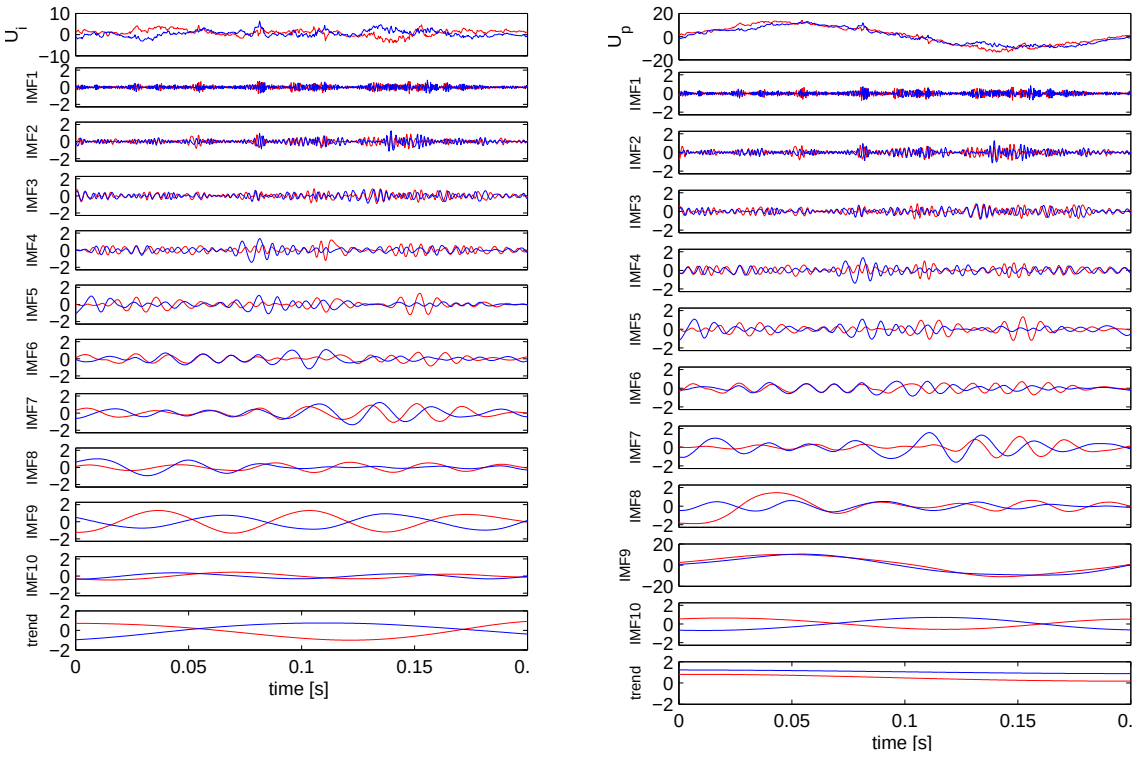

(a) (b)

Figure 4.4: Decomposition of velocity field by mean of Bivariate EMD. (a) Initial HIT signal, (b) Perturbed signal. the red line: horizontal velocity U and and blue line: vertical velocity V. The unit of signals is $m.s^{-1}$.

The first IMF is the representation of the highest frequency part, i.e. smallest scale, of the flow and while decomposition progresses the IMFs are more and more representative of the global velocity tendency i.e. the large scale. Bivariate EMD analysis of the initial and perturbed signals at one point of velocity field is illustrated in Figure 4.4.
Here the perturbation amplitude was set to $A = 10\ m.s^{-1}$ with a frequency 1 Hz. One can see that the feature of perturbation appears in 9^{th} IMF of perturbed velocity field. To separate perturbation from the initial signal, Mazellier & Foucher (2011) [120] introduced the resemblance criterion based on the statistical dependence between the reconstructed signals resulting from two successive steps. This criterion for two components signal becomes :

$$R(n) = \frac{\langle U_n(t)U_{n-1}(t)\rangle + \langle V_n(t)V_{n-1}(t)\rangle}{\sqrt{\langle U_n(t)^2\rangle + \langle V_n(t)^2\rangle}\sqrt{\langle U_{n-1}(t)^2\rangle + \langle V_{n-1}(t)^2\rangle}} \qquad if \quad 1 < n < N,$$
$$R(n) = 0 \qquad if \quad n = 1 \tag{4.2}$$

Where the two components of reconstructed signal; $U_n(t)$ and V_n are defined as follows:

$$U_n(t) = \sum_{k=1}^{n} IMF_{Uk}(t) \quad , \quad V_n(t) = \sum_{k=1}^{n} IMF_{Vk}(t) \qquad if \quad n < N,$$
$$U_n(t) = \sum_{k=1}^{n} IMF_{Uk}(t) + r_{UN}(t) \quad , \quad V_n(t) = \sum_{k=1}^{n} IMF_{Vk}(t) + r_{VN}(t) \qquad if \quad n = N \tag{4.3}$$

With n the reconstruction number and N the total number of the modes. IMF_{Uk} and IMF_{Vk} denote the horizontal and vertical components of k^{th} bivariate IMF, respectively. In this way the resemblance criterion $R(n)$ is computed by adding consecutive IMF in each step.
When original HIT signal is not polluted by perturbation, the value of $R(n)$ increases in each step as a function of n and leads to 1 by adding the signal trend i.e. last IMF, otherwise the sudden drop occurs while the perturbation feature appears. In this methodology the main idea for separating undesirable modes is based on the poor statistical dependency between perturbed and original flow fields.

To illustrate this issue, the evolution of the resemblance criterion $R(n)$ as a function of the reconstruction number n is plotted in Figure 4.5. It is observed that $R(n)$ drops while adding the 9^{th} IMF to the reconstructed signal. This is in agreement with the shape of this mode seen in Figure 4.4b. To compute the recovered signal, the number of IMFs for which the fall of k_n is occurred, is considered like a cut-off frequency. So the IMF_k for which $k \geq k_c$ are rejected and the recovered signal is defined as:

$$U_r(t) = \sum_{k=1}^{k_c-1} IMF_{Uk} \quad , \quad V_r(t) = \sum_{k=1}^{k_c-1} IMF_{Vk} \tag{4.4}$$

so for the perturbed signal in Figure 4.4b, k_c is set to 9 and in the recovering procedure three last modes are rejected.
To assess the quality of recovering algorithm the temporal energy spectra of initial velocity

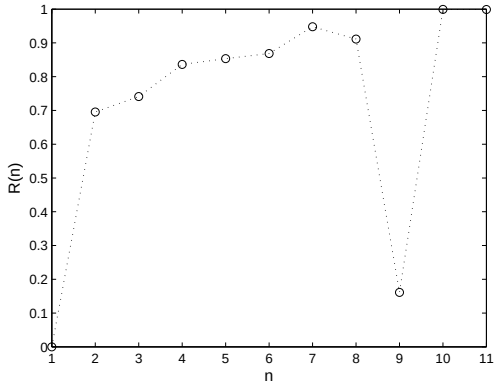

Figure 4.5: Evolution of resemblance criterion as a function of the reconstruction number.

field are compared to recovered velocity signal. The one dimensional energy spectra is defined as $\langle u^2 \rangle = \int_0^\infty E(f)\,.df$ with u instantaneous velocity fluctuations; $u = U - \langle U \rangle$ and f the spectral frequency, similarly for V component of the velocity field. The signal length at each point is 2^{13} and the Welch method (1967) [191] with 50 % overlap is used for computing power spectra.

The temporal energy spectrum is computed at each point of the velocity field then the mean of spectra over all points is represented as the flow field energy spectra. In Figure 4.6a and Figure 4.6b the energy spectra of the two components, U and V of the initial velocity field and perturbed ones are displayed, the amplitude of perturbation is the same in all cases and its maximum is 2 $m.s^{-1}$ but its frequency varies from 0.1 to 15 Hz. As one can see the feature of perturbation appears clearly as a sharp peak in the corresponding perturbed velocity energy spectrum.

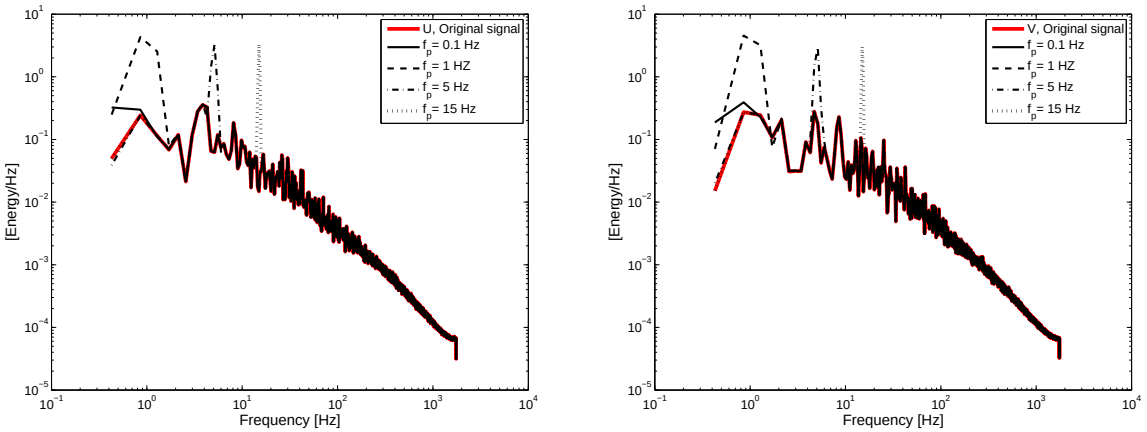

(a) (b)

Figure 4.6: The mean temporal energy spectrum of the initial velocity field and perturbed ones, (a) U and (b) V velocity component.

The energy spectra for corresponding recovered velocity fields (U and V components) are also plotted in Figure 4.7a and Figure 4.7b. As one can see in all cases the high-frequency dynamics are perfectly recovered but by increasing the perturbation frequency, the Fourier spectrum of recovered signal differs more and more from the initial one. When

perturbation frequency $f = 0.1$ Hz, there is a good agreement between both spectra and the spectra of recovered flow superimpose the spectra of HIT original flow. As one can see in the inertial region of both flow, the energy spectra exhibit a $-5/3$ decay, following Kolmogorov-Obukhov scaling laws.

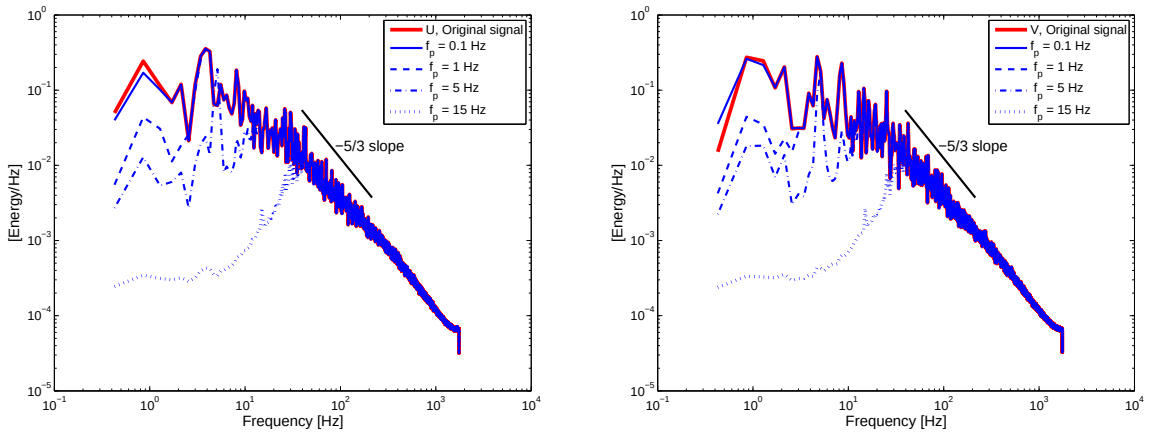

(a) (b)

Figure 4.7: The mean temporal energy spectrum of the initial velocity field and recovered ones, (a) U and (b) V velocity component.

The difference between the energy spectra of the recovered and initial signal occurs in the region $f \leq f_p$, this issue becomes from the feature of recovering procedure in which by using resemblance criterion the high-order polluted IMF are rejected, see Figure 4.5. The energy of these modes as illustrated in Figure 4.8 for a HIT velocity signal is concentrated in the low frequency so once they filter out, the energy of recovered signal drops at such frequency band.

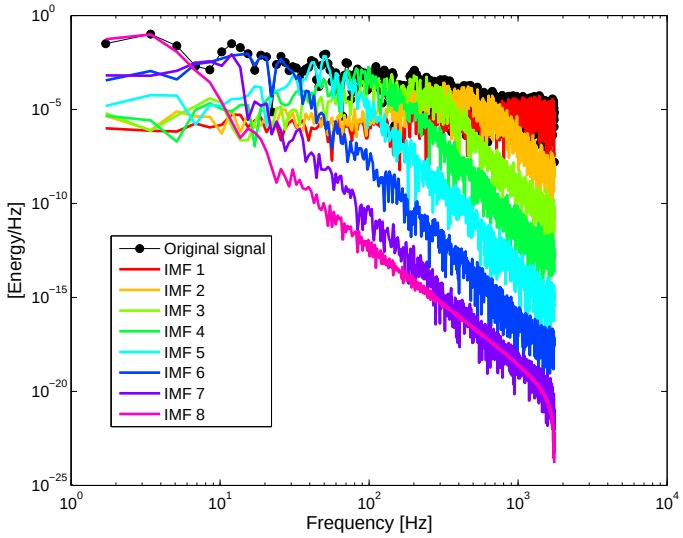

Figure 4.8: Power spectrum of a temporal HIT velocity field and its different IMFs (modes).

Hence by proposed recovering procedure just in the case the perturbation frequency is much lower than the typical frequency of the integral length-scale (here 1 Hz), the low

frequency scale of the initial HIT can be recovered.

The mean power spectral density of the two components of the recovered velocity field (U_r and V_r) is computed for different perturbations generated with variation of the amplitude, A and the frequency, f. The correlation between these spectra and the corresponding ones from the original HIT flow is determined and represents as a quality indicator. The contour of the average value of this coefficient is presented as function of A and f in Figure 4.9.

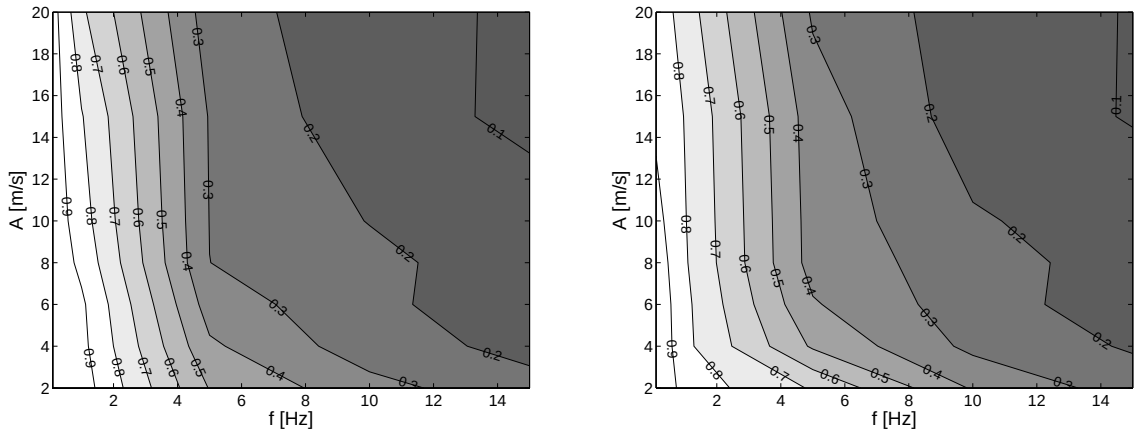

(a) (b)

Figure 4.9: Contour plot of the recovering quality indicator computed between the mean power spectral density of the recovered and initial flow with respect to the parameters of the signal tone perturbation, (a) U and (b) V velocity component.

This illustration indicates the recovering algorithm is not sensitive to the amplitude of perturbation for one given frequency but decreases significantly with perturbation frequency increase. For frequency lower than 1 Hz, a good agreement is obtained between recovered turbulent velocity field and initial HIT flow.

To compare large scale of recovered turbulent flow field and initial one, the integral time and length scales of both flow fields are computed. The integral time scale is defined as $T = \int_0^\infty R(\tau).d\tau$, with $R(\tau)$ the auto-correlation coefficient (one point-two times) and the time lag τ. The auto-correlation coefficient for U and V components of velocity in given point (x, y) is described as

$$R_{Ut}(\tau) = \frac{\langle u\,(t)\,u(t+\tau)\rangle}{\langle u^2(t)\rangle^{1/2}\langle u^2(t+\tau)\rangle^{1/2}} \qquad R_{Vt}(\tau) = \frac{\langle v\,(t)\,v(t+\tau)\rangle}{\langle v^2(t)\rangle^{1/2}\langle v^2(t+\tau)\rangle^{1/2}} \tag{4.5}$$

Where u and v are the instantaneous velocity fluctuations in X and Y directions respectively; $u = U - \langle U\rangle$, $v = V - \langle V\rangle$ and $\langle\cdot\rangle$ represents time average. $R_{Ut}(\tau)$ and $R_{Vt}(\tau)$ are computed at each point then they are averaged over all the velocity field.
The auto-correlation coefficient of initial velocity signal and recovered ones in the case that maximum perturbation amplitude is 2 $m.s^{-1}$ with different perturbation frequencies are illustrated in Figure 4.10. For the case of perturbation frequency of 0.1 Hz, the mean integral time scale of the recovered velocity field and original one is compared in Table 4.6, as one can see in such case there is an excellent agreement between the two scales.

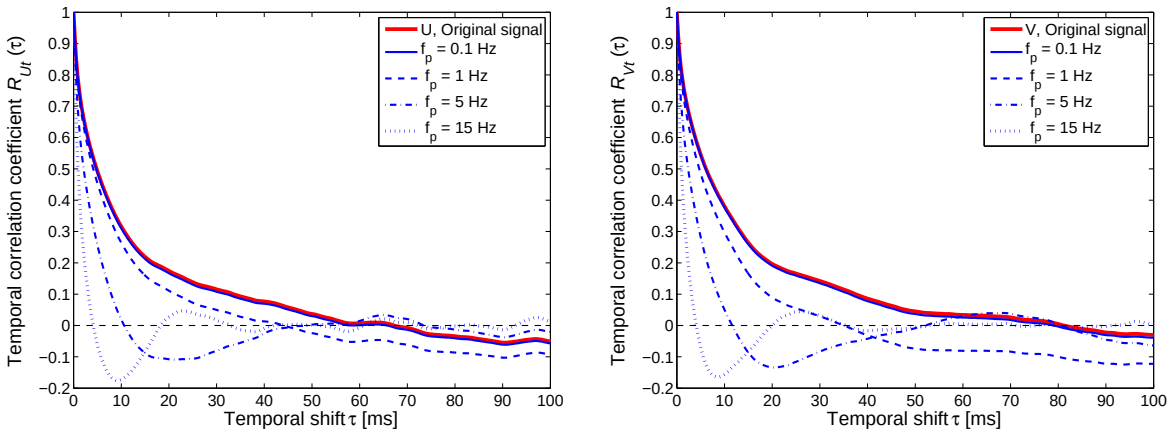

(a) (b)

Figure 4.10: Temporal correlation of recovered velocity fields and original one. (a) U and (b) V velocity components.

Integral time scale $[ms]$	Initial HIT	Recovered velocity
T_{Ut}	10.68	10.22
T_{Vt}	12.82	12.23

Table 4.6: Mean integral time scale of the original (initial) HIT flow and the recovered velocity in the case of perturbation with $f = 0.1$ Hz and $A = 2$ $[m.s^{-1}]$.

The integral length scale is defined as $L_E = \int_0^\infty R(\xi).d\xi$, where $R(\xi)$ is the inter correlation coefficient (two points-one time) with the spatial lag ξ. The longitudinal correlations coefficient for U and V components of velocity field in X and Y directions respectively, at one given instant are defined as:

$$R_{Ux}(\xi) = \frac{\langle u\,(x,y)\,u(x+\xi,y)\rangle}{\langle u^2(x,y)\rangle^{1/2}\langle u^2(x+\xi,y)\rangle^{1/2}} \qquad R_{Vy}(\xi) = \frac{\langle v\,(x,y)\,v(x,y+\xi)\rangle}{\langle v^2(x,y)\rangle^{1/2}\langle v^2(x,y+\xi)\rangle^{1/2}} \tag{4.6}$$

where $\langle\cdot\rangle$ represents spatial average from each velocity field, in this case u and $v$are determined from all the velocities U and V in instantaneous velocity field.

Also the lateral correlation coefficients for U and V velocity components in Y and X directions respectively are

$$R_{Uy}(\xi) = \frac{\langle u\,(x,y)\,u(x,y+\xi)\rangle}{\langle u^2(x,y)\rangle^{1/2}\langle u^2(x,y+\xi)\rangle^{1/2}} \qquad R_{Vx}(\xi) = \frac{\langle v\,(x,y)\,v(x+\xi,y)\rangle}{\langle v^2(x,y)\rangle^{1/2}\langle v^2(x+\xi,y)\rangle^{1/2}} \tag{4.7}$$

The correlation coefficients computed from Eq (4.6) and Eq (4.7) are then averaged over all velocity fields. As shown in Figure 4.11 and Figure 4.12 by decreasing perturbation frequency the both longitudinal and lateral correlation coefficient of the recovered velocity field accede to the ones for initial HIT flow field.

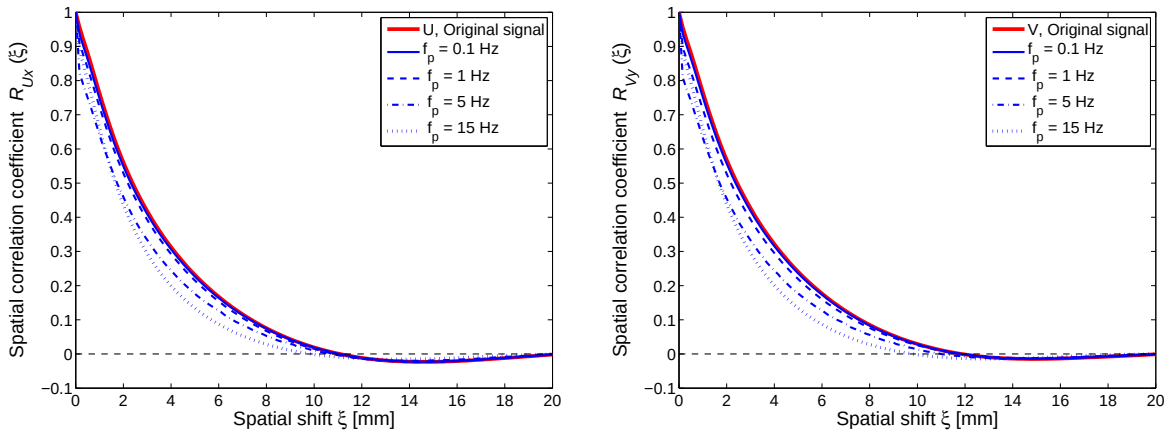

(a) (b)

Figure 4.11: Evolution of longitudinal correlation coefficients for recovered velocity fields and original one.(a) U and (b) V velocity components.

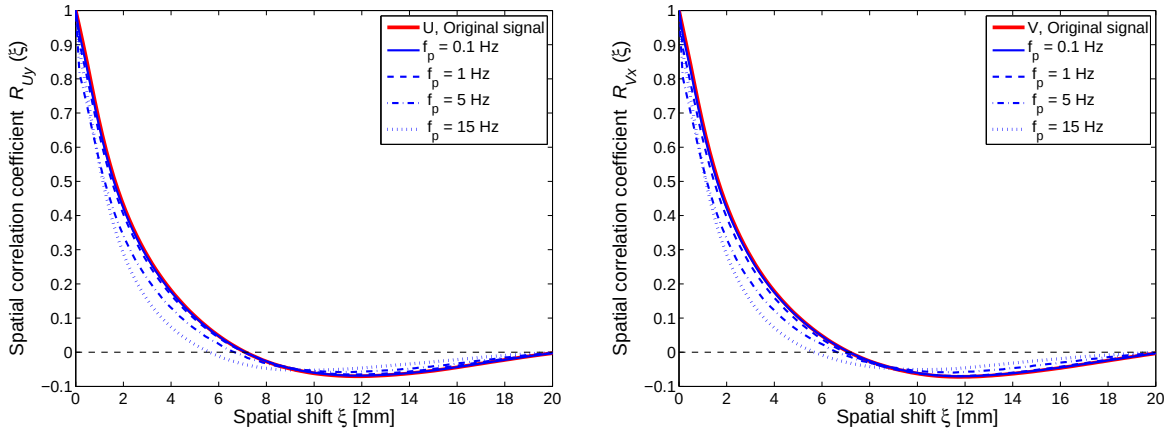

(a) (b)

Figure 4.12: Evolution of lateral correlation coefficients for recovered velocity fields and original one.(a) U and (b) V velocity components.

The integral length scales of both flow fields are compared in Table 4.7, in the case of $f = 0.1$ Hz as perturbation frequency. For this frequency the agreements between the longitudinal and lateral integral scale of the recovered turbulent field and original HIT flow field are very good. The initial turbulent flow is homogeneous and isotropic hence $L_{Ux} = 2L_{Uy}$ and $L_{Vy} = 2L_{Vx}$, this property is also revealed in recovered flow filed.

To evaluate the quality of recovering algorithm, the correlation coefficient between the recovered signal and initial one can also be computed as below:

$$C = \frac{\langle U_i(t)U_r(t)\rangle + \langle V_i(t)V_r(t)\rangle}{\sqrt{\langle U_i(t)^2\rangle + \langle V_i(t)^2\rangle}\sqrt{\langle U_r(t)^2\rangle + \langle V_r(t)^2\rangle}} \tag{4.8}$$

where U and V are the components of velocity field, index i and r represent respectively the initial HIT flow and recovered one. The contour of the average correlation coefficient,

Longitudinal integral scale $[mm]$	Initial HIT	Recovered velocity
L_{Ux}	3.05	2.99
L_{Vy}	3.20	3.14

(a)

Lateral integral scale $[mm]$	Initial HIT	Recovered velocity
L_{Uy}	1.62	1.59
L_{Vx}	1.60	1.57

(b)

Table 4.7: Mean integral length scale of the initial HIT flow and the recovered velocity filed in the case of perturbation with $f = 0.1$ Hz and $A = 2$ $[m.s^{-1}]$. (a) Longitudinal integral scale, (b) Lateral integral scale.

represents recovering quality, as function of the amplitude, A and the frequency, f of perturbation is plotted in Figure 4.13.

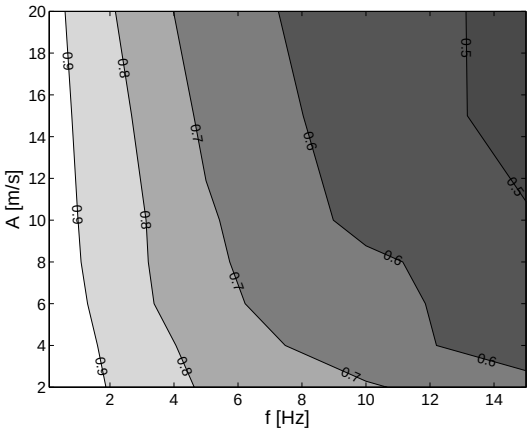

Figure 4.13: Contour plot of the recovering quality indicator with respect to the parameters of the signal tone perturbation.

It is observed that, the recovering procedure is less sensitive to the perturbation amplitude than its frequency. When the perturbation frequency is low, there is a good agreement between two flow fields, the initial HIT is perfectly recovered from perturbed velocity field. This recovering procedure becomes less effective by increasing the perturbation frequency.

In this study the Bivariate EMD is applied on the perturbed turbulent velocity field, by this approach two inter-coupled components of the velocity filed U and V are decomposed simultaneously as a single two components vector. By using the recovering procedure introduced by Mazellier & Foucher (2011) [120], a posterior perturbation is separated. The influence of amplitude and frequency of the perturbation on the recovering signal was studied. This investigation indicates in the case where the perturbation frequency is in a range lower than the frequency of integral scale of turbulent flow, the initial HIT flow can be perfectly recovered otherwise just the fast dynamic of flow is detectable. As a notice, the Bivariate EMD code used in this investigation can be downloaded from http://perso.ens-lyon.fr/patrick.flandrin/emd.html.

4.3 Validation of Bivariate 2D-EMD

To assess the ability of the proposed Bivariate 2D-EMD in the decomposition of turbulent velocity field to separate large-scale organized motions from HIT flow field, the following methodology was designated, improved and tested.
The initial HIT flow fields $\mathrm{U}_i(x, y)$, is the same as used in previous section. As a reminder they were obtained from HS-PIV with the frequency of 3500 Hz within 127×127 windows points with 0.16 mm mesh size so 20.32×20.32 mm^2. Then they are perturbed by a synthetic Lamb-Ossen vortex $\mathrm{P}(x, y)$ to represent the flow large-scale organized structure. The two-dimensional perturbed velocity field $\mathrm{U}_p(x, y) = \mathrm{U}_i(x, y) + \mathrm{P}(x, y)$ is decomposed by Bivariate 2D-EMD into different modes (IMFs).
Based on an energy criterion the original (initial) turbulence flow can be recovered within the modes. To evaluate the quality of separation, the turbulent properties of original HIT flow are compared to ones in recovered turbulent velocity field.
The amplitude A, scale l and the position of the added vortex (perturbation signal), are varied regarding to the initial HIT. The different test cases are summarized in following Tables:

Test case	A
a	10.TKE
b	5.TKE
c	2.TKE
d	1.TKE

Table 4.8: Position: center, $l = 5.L_x$

Test case	l
a	$10.L_{Ux}$
b	$2.L_{Ux}$
c	$1.L_{Ux}$

Table 4.9: Position: center, A=5.TKE

Test case	Position
a	mid-distance
b	corner

Table 4.10: A=5.TKE, $l = 5.L_x$

To seek a demonstration, in first step the procedure is applied only for three instantaneous different velocity fields, called in the following as HIT Field 1 , 2 and 3. These fields were generated from the same "physical conditions" but some discrepancies can be seen between them; presence of more or less small structures, more or less highest vectors values, as shown in Figure 4.14. In the second step a purturbation vortex is added to 200 HIT velocity fields and the mean turbulent properties of recovered velocity fields are compared to ones for initial HIT fields.

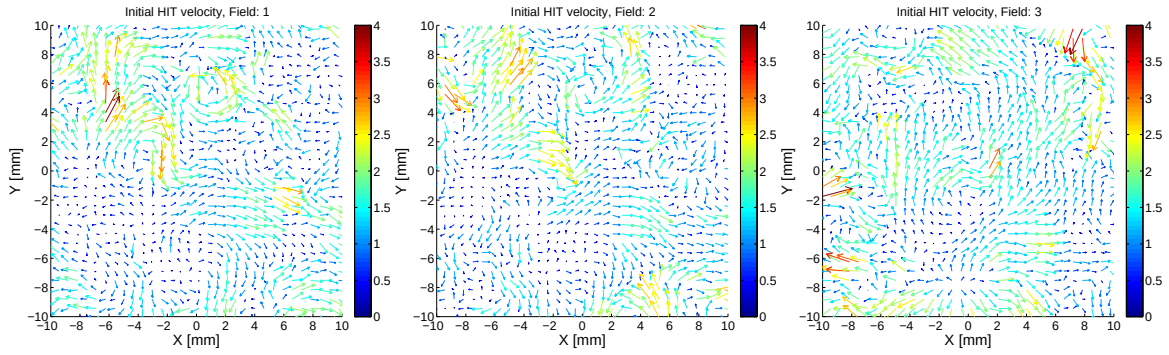

(a) HIT Field 1 (b) HIT Field 2 (c) HIT Field 3

Figure 4.14: Three experimental instantaneous HIT velocity fields.

As a notice in Bivariate 2D-EMD approach, one adjacent white Gaussian noise channel is used and the input multi-components signal is projected on 64 directions with the projection density defined by $\alpha = 0.3$. For Sifting process the Mean-value stoppage criterion with $(0.05, 0.5, 0.05)$ is used and the number of ensemble realizations NE is set to 100.

4.3.1 Influence of the vortex amplitude

The amplitude A of the added vortex , representing the organized motion, was varied as a 10, 5, 2, 1 times of the input HIT turbulent kinetic energy, TKE $\simeq 1\ m^2s^{-2}$. The scale (size) of the vortex was fixed to the five times of longitudinal integral scale of the HIT flow, $l = 5.L_{(Ux,Vy)}$ with $L_{(Ux,Vy)} \simeq 3.2\ mm$ and the center of the vortex was positioned at the $(0, 0)$ center of the HIT velocity field, as shown in Figure 4.15.

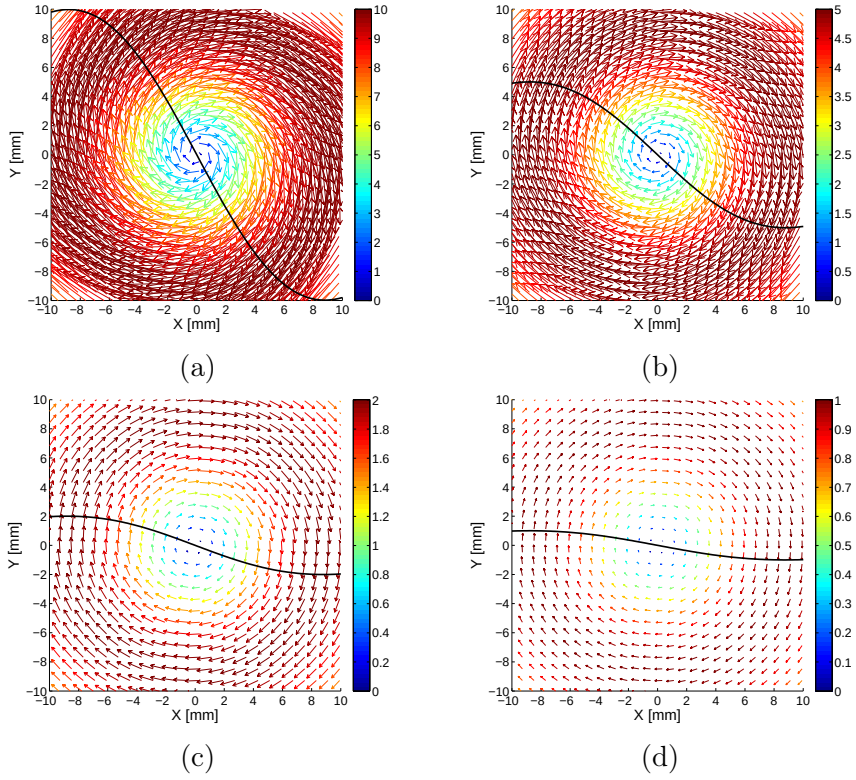

Figure 4.15: Velocity field of the generated vortex centered in the middle, $l = 5.L_{(Ux,Vy)} = 16$ mm size, for 4 different amplitudes. (a) $A = 10$, (b) $A = 5$, (c) $A = 2$ and (d) $A = 1\ m.s^{-1}$.

- **Test case a:** $A = 10\ m.s^{-1}$

In Figure 4.16 the first initial HIT and the 2D perturbed velocity fields obtained from the addition of the vortex in Figure 4.15a, are presented.The Bivariate 2D-EMD is applied on this perturbed velocity field, and the different modes results of the decomposition are illustrated in Figure 4.17. The first row displays the two components U and V of the input perturbed velocity field.

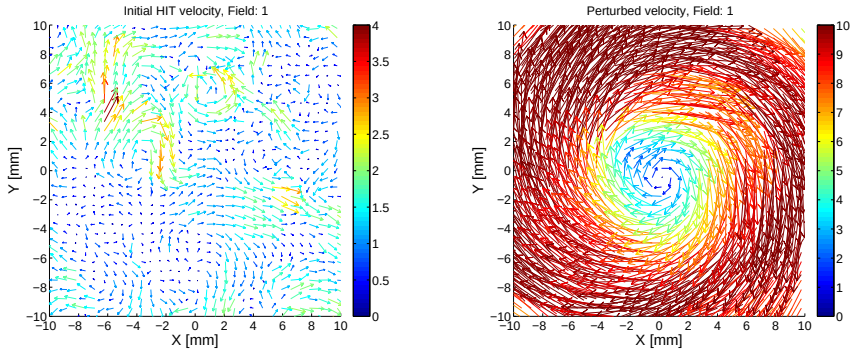

(a) (b)

Figure 4.16: (a) HIT Field 1 and (b) associated perturbed flow field with a centered vortex of 10 $m.s^{-1}$ amplitude and a length scale of 16 mm.

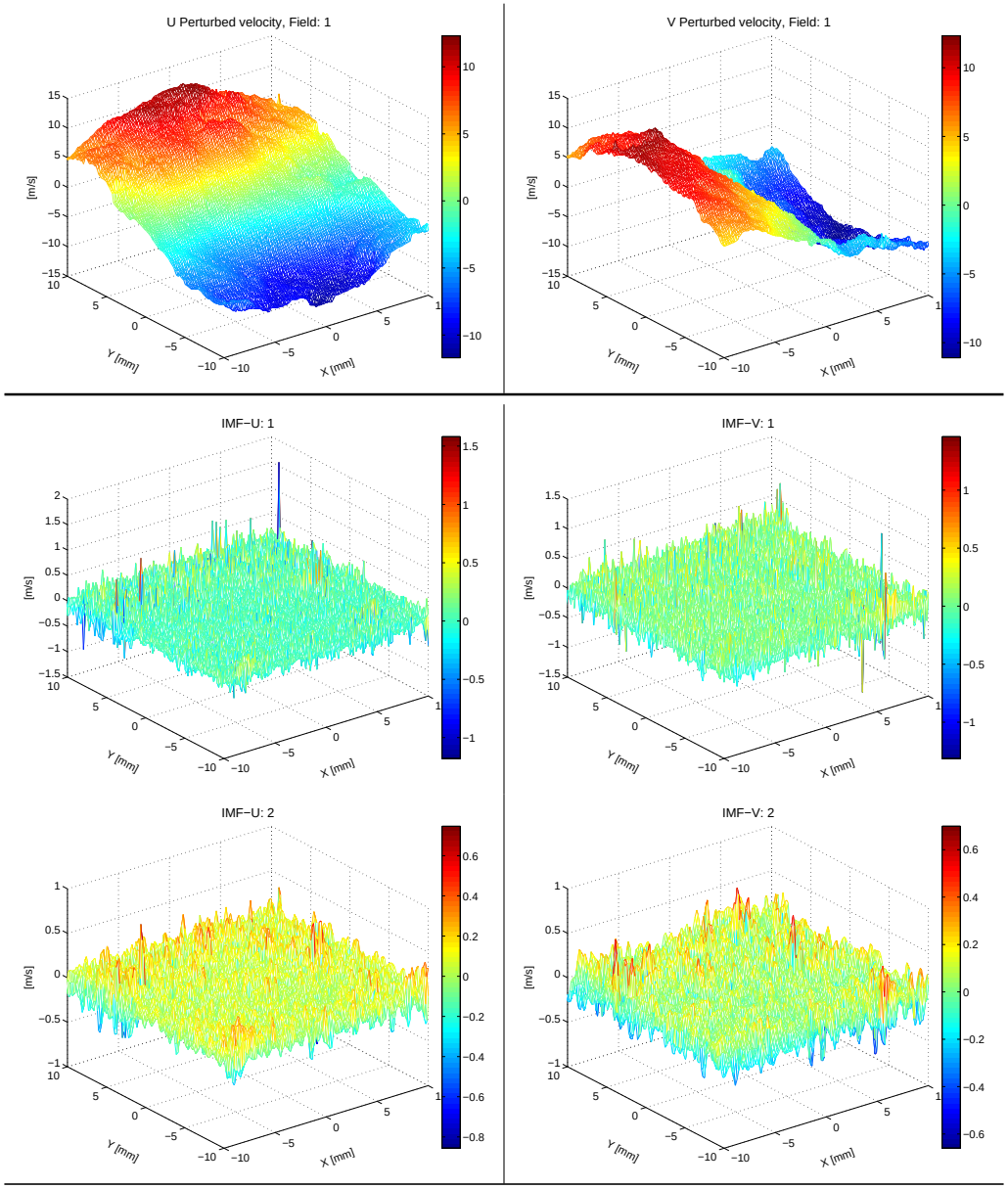

Figure 4.17 *Cont.*

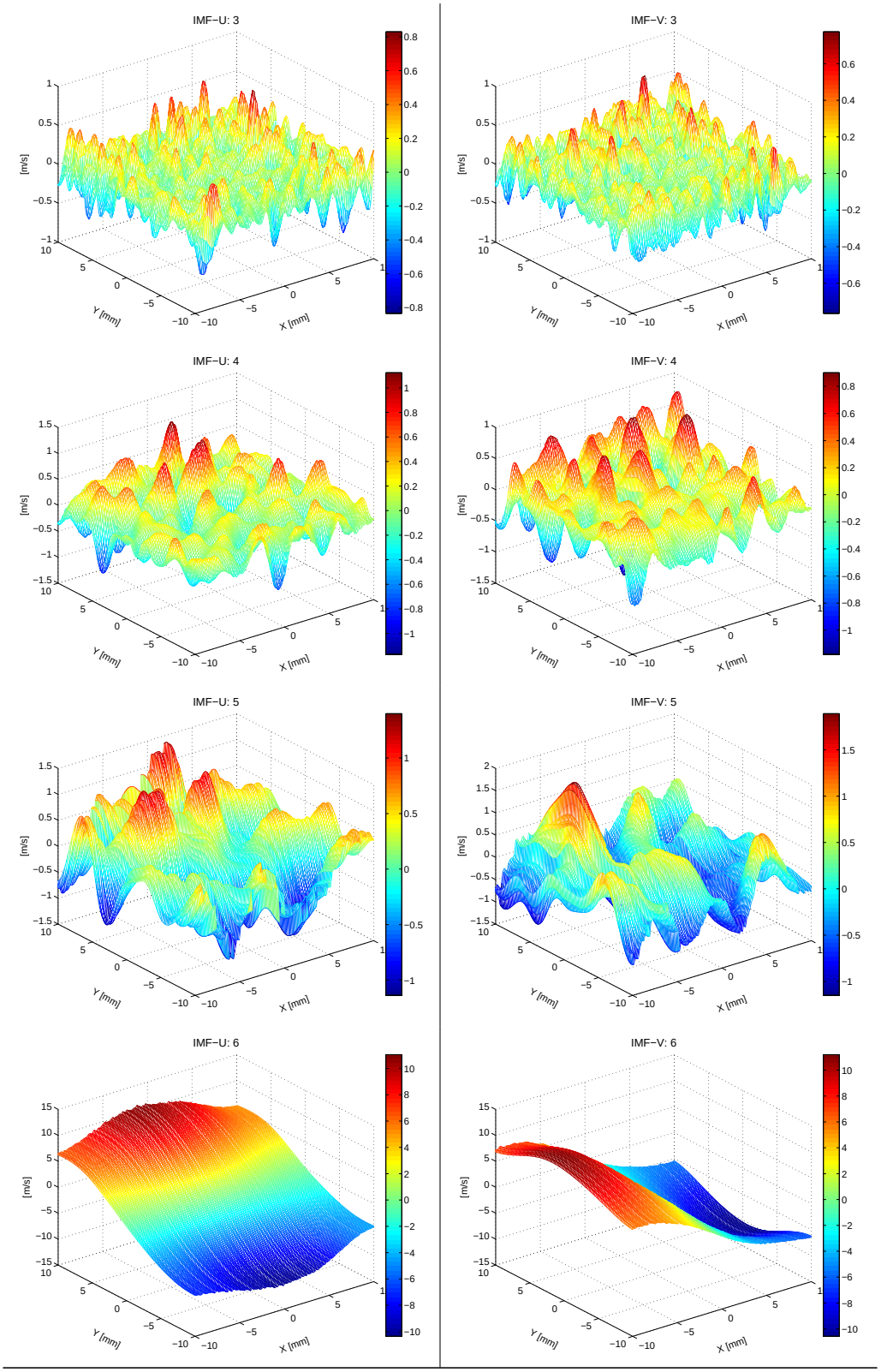

Figure 4.17: Spatial evolution of the horizontal U and vertical V component of the perturbed velocity field in the first panel and the 6 different modes obtained by Bivariate 2D-EMD.

It is observed by increasing the order of the modes, the frequency of the fluctuations decrease and the last mode of each component U and V represents the tendency of the

perturbed velocity field. Moreover the same-index modes across velocity two components, contains the same scales of fluctuations i.e. scales-alignment.

Separation between turbulence and organized motion

In order to recover the initial HIT velocity field within the different modes the energy criterion related with signal intensity is used. It is defined as $E_n = 0.5\left(\langle U_n^2\rangle + \langle V_n^2\rangle\right)$ where n index is the mode number and the symbol $\langle\cdot\rangle$ denotes to the total spatial average, so when applying on two dimensional signal it becomes:

$$E_n = \frac{0.5}{n_x n_y}\sum_{i=1}^{n_x}\sum_{j=1}^{n_y}\left(U_n^2(x_i, y_j) + V_n^2(x_i, y_j)\right) \tag{4.9}$$

Where n_x and n_y are the total numbers of the points in 2D-signal in x and y direction respectively, here $n_x = n_y = 127$. It should be mentioned the resemblance criterion as defined in Eq (4.2) can be easily adopted for 2D-velocity field but such a criterion is highly sensible to the signal perturbation in two dimensional space, hence it is not recommended in such cases. The energy criterion is computed for each mode, and plotted in Figure 4.18a. As one can see there is sudden jump in the 6th mode energy hence the recovered velocity field that ideally should represent the initial HIT velocity field is defined as a sum of the first five modes, Figure 4.18b and the 6^{th} mode is considered as a flow large-scale structure i.e. low frequency part, Figure 4.18c.

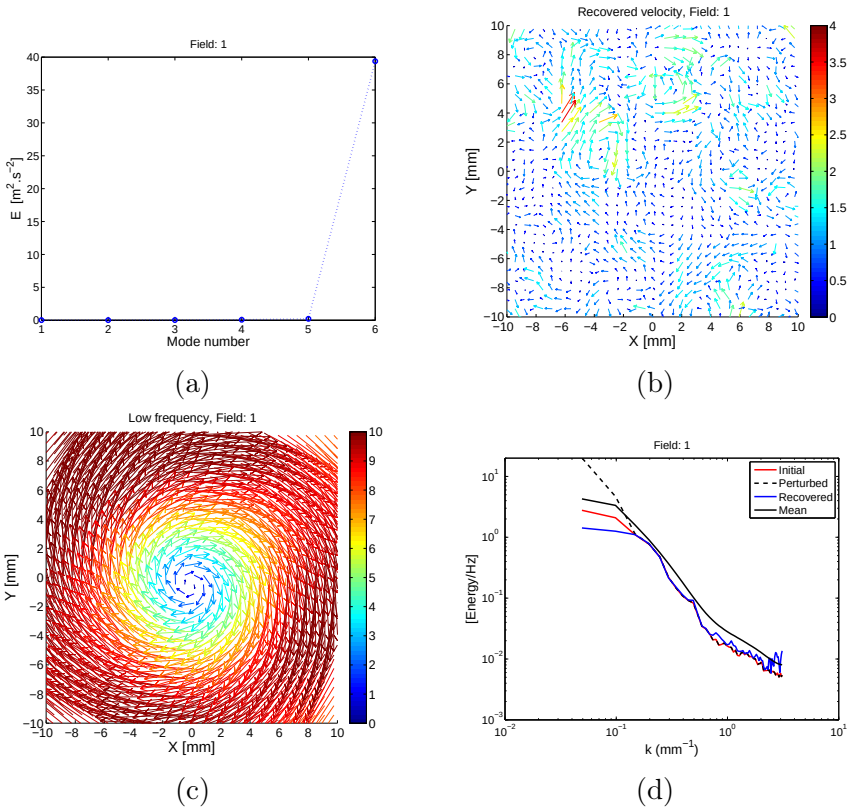

Figure 4.18: Test case a, (a) Energy contents as function of mode number, (b)recovered velocity field with 5 first IMF, (c) low frequency part (IMF6) and (d) Power spectrum density for the initial HIT, perturbed and recovered and mean experimental velocity fields.

The spatial power spectra of the initial HIT, perturbed and recovered velocity fields are presented in Figure 4.18d, also as an indicator, the mean spatial power spectra of the initial 8000 experimental instantaneous HIT flow fields is depicted. The same procedure was applied for HIT fields 2 and 3. The energy contents presents for both also the strong jump from 5^{th} to 6^{th} mode, Figure 4.19 summarizes all results.

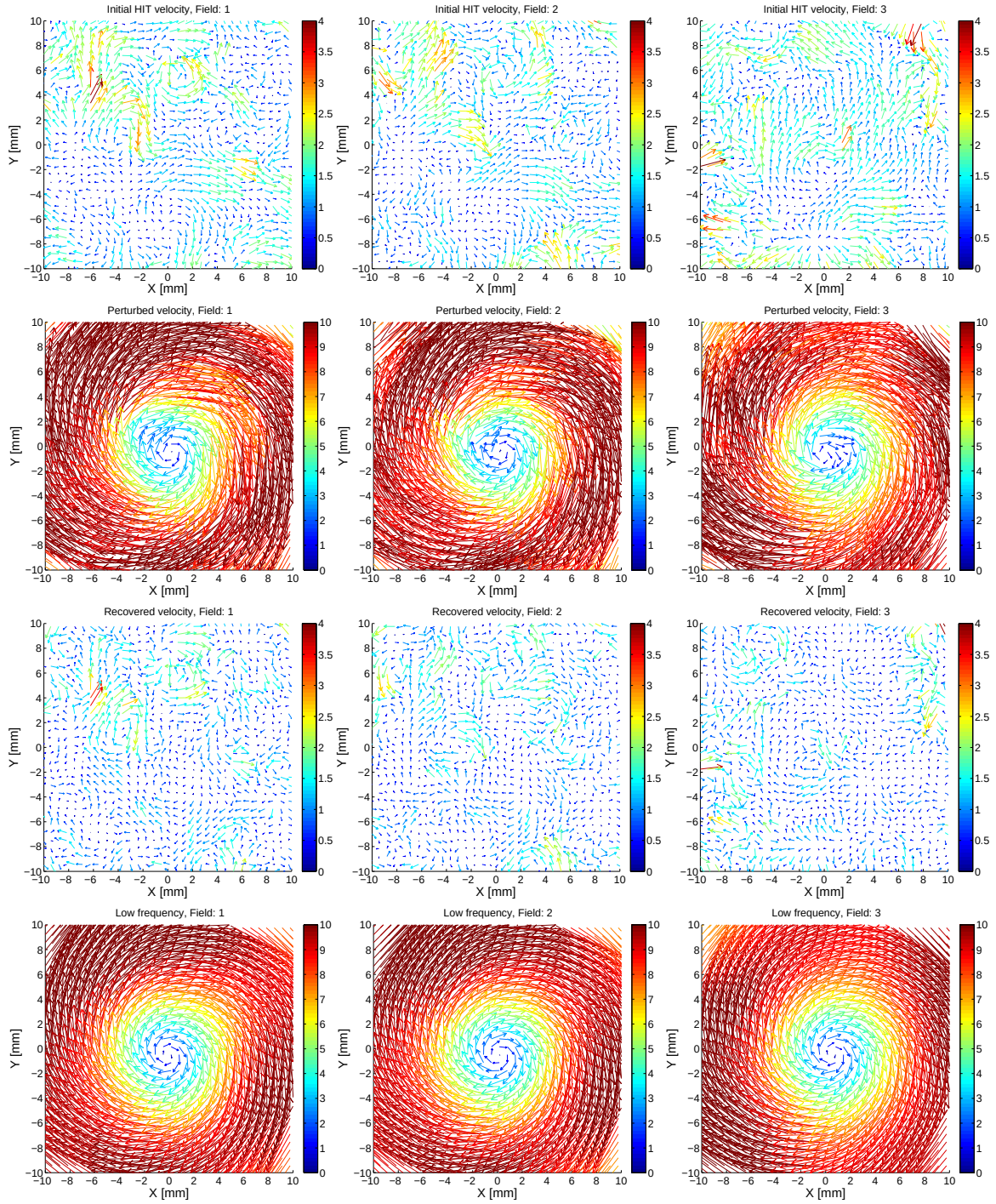

Figure 4.19: Comparative results from Bivariate 2D-EMD analysis for three arbitrary experimental instantaneous HIT flow fields perturbed with a centered vortex of 10 $m.s^{-1}$ amplitude and the length scale of 16 mm.

The spatial power spectra of the initial HIT, perturbed and recovered velocity fields are presented in Figure 4.20, also as an indicator, the mean spatial power spectra of the initial 8000 experimental instantaneous HIT flow fields is depicted . It is observed the

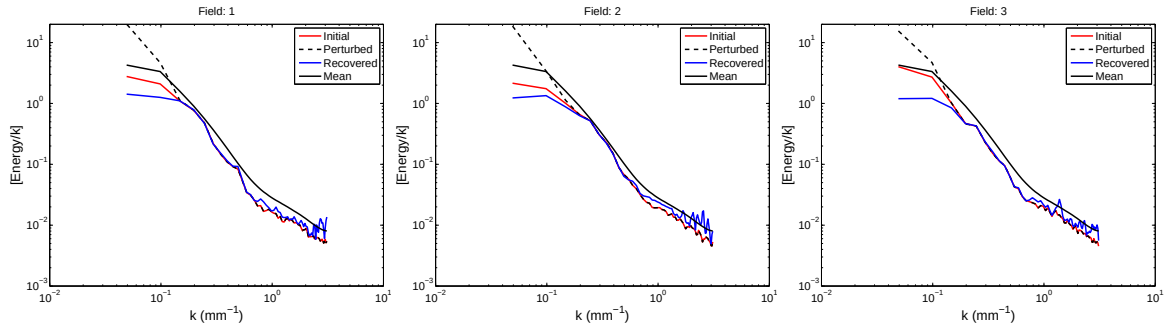

(a) (b) (c)

Figure 4.20: The spatial power spectra of the initial HIT, perturbed and recovered velocity fields, (a) HIT field 1, (b) HIT field 2, (c) HIT field 3.

spatial power spectral density of the recovered turbulent velocity field is underestimated in the region associated with the flow large-scale structure for three velocity fields but it is superimposed to the initial HIT flow in inertial subrange and there are some fluctuations in the energy spectrum of the recovered field at smallest scale.

- **Test case b:** $A = 5\ m.s^{-1}$

In this case the perturbation vortex has a maximum amplitude of 5 $m.s^{-1}$, and a size of $l = 5.L_{(Ux,Vy)} = 16\ mm$ and positioned at the center of initial HIT. It is added to three HIT velocity fields. For all cases also, the jump in energy contents remains from the 5^{th} mode. The results are summarized in Figure 4.21.

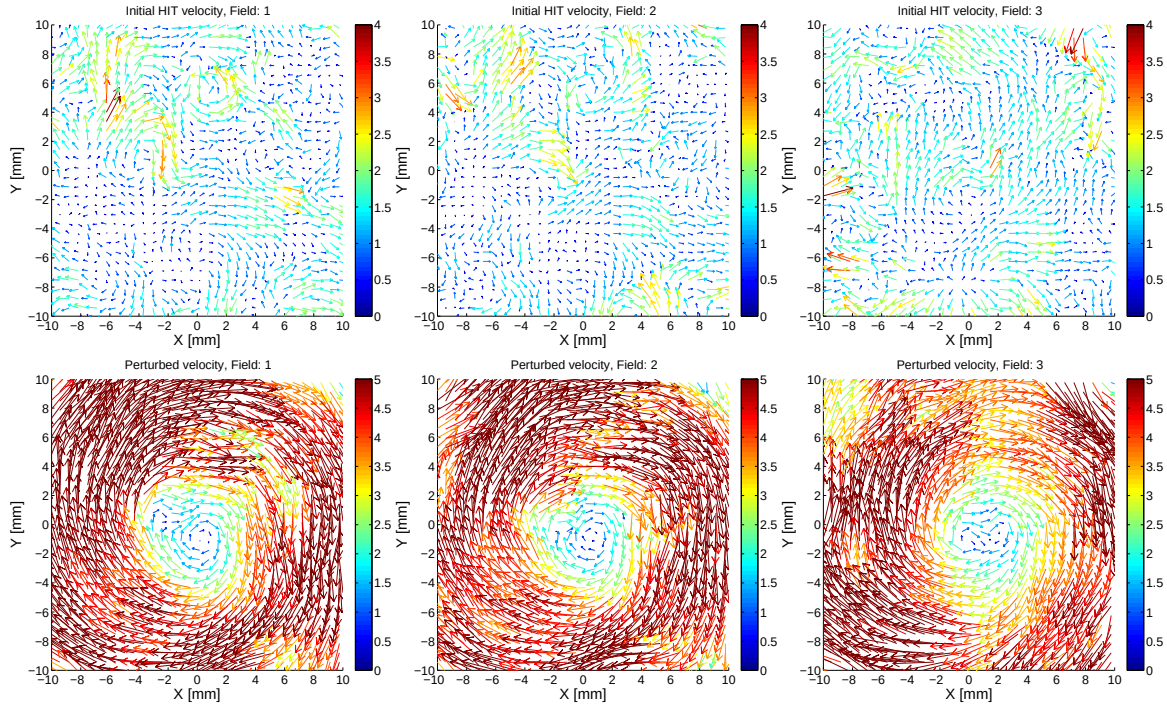

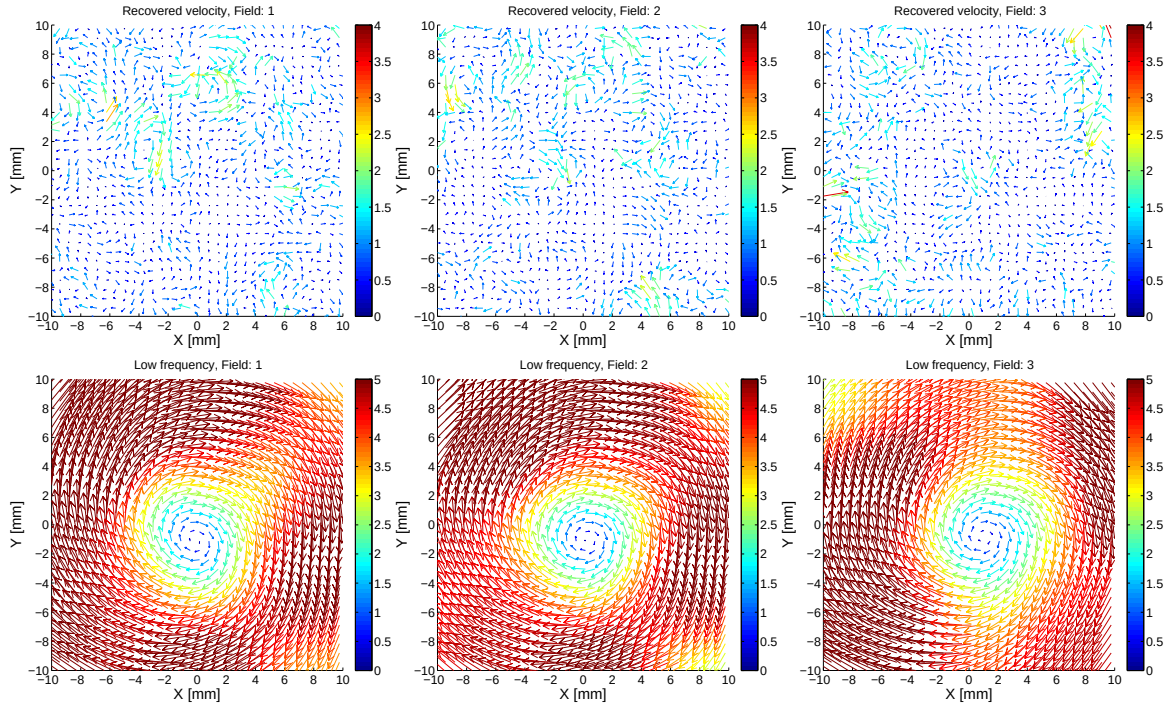

Figure 4.21: Comparative results from Bivariate 2D-EMD analysis for three arbitrary experimental instantaneous HIT flow fields perturbed with a centered vortex of 5 $m.s^{-1}$ amplitude and the length scale of 16 mm.

The spatial power spectra of the initial HIT, perturbed and recovered velocity fields are presented in Figure 4.22. As one can see when the amplitude of perturbation velocity field decreases, the energy spectrum of the recovered velocity field at smallest scale also superimposed on that in initial HIT, however in the region associated with flow large-scale structure the energy of all recovered fields are under estimated.

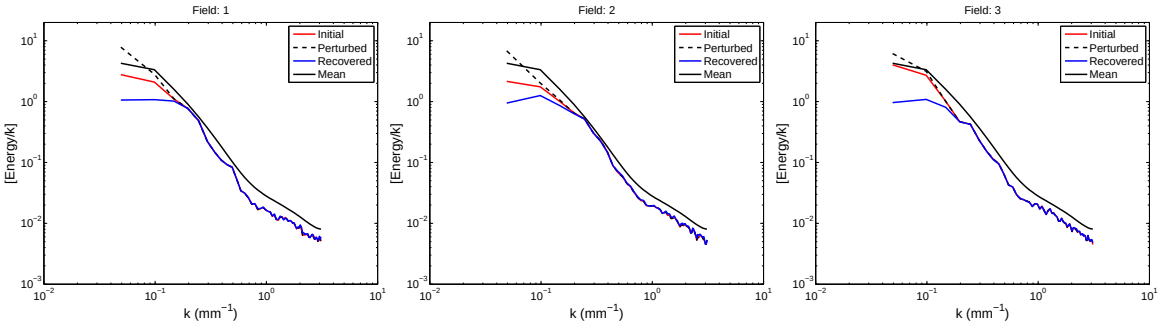

(a) (b) (c)

Figure 4.22: The spatial power spectra of the initial HIT, perturbed and recovered velocity fields, (a) HIT field 1, (b) HIT field 2, (c) HIT field 3.

- **Test case c:** $A = 2\ m.s^{-1}$

In this case the perturbation vortex has a maximum amplitude of 2 $m.s^{-1}$, and a size of $l = 5.L_{(Ux,Vy)} = 16\ mm$ and positioned at the center of initial HIT. It is added to three HIT velocity fields. For all cases also, the jump in energy contents remains from the 5^{th} mode. The results are summarized in Figure 4.23.

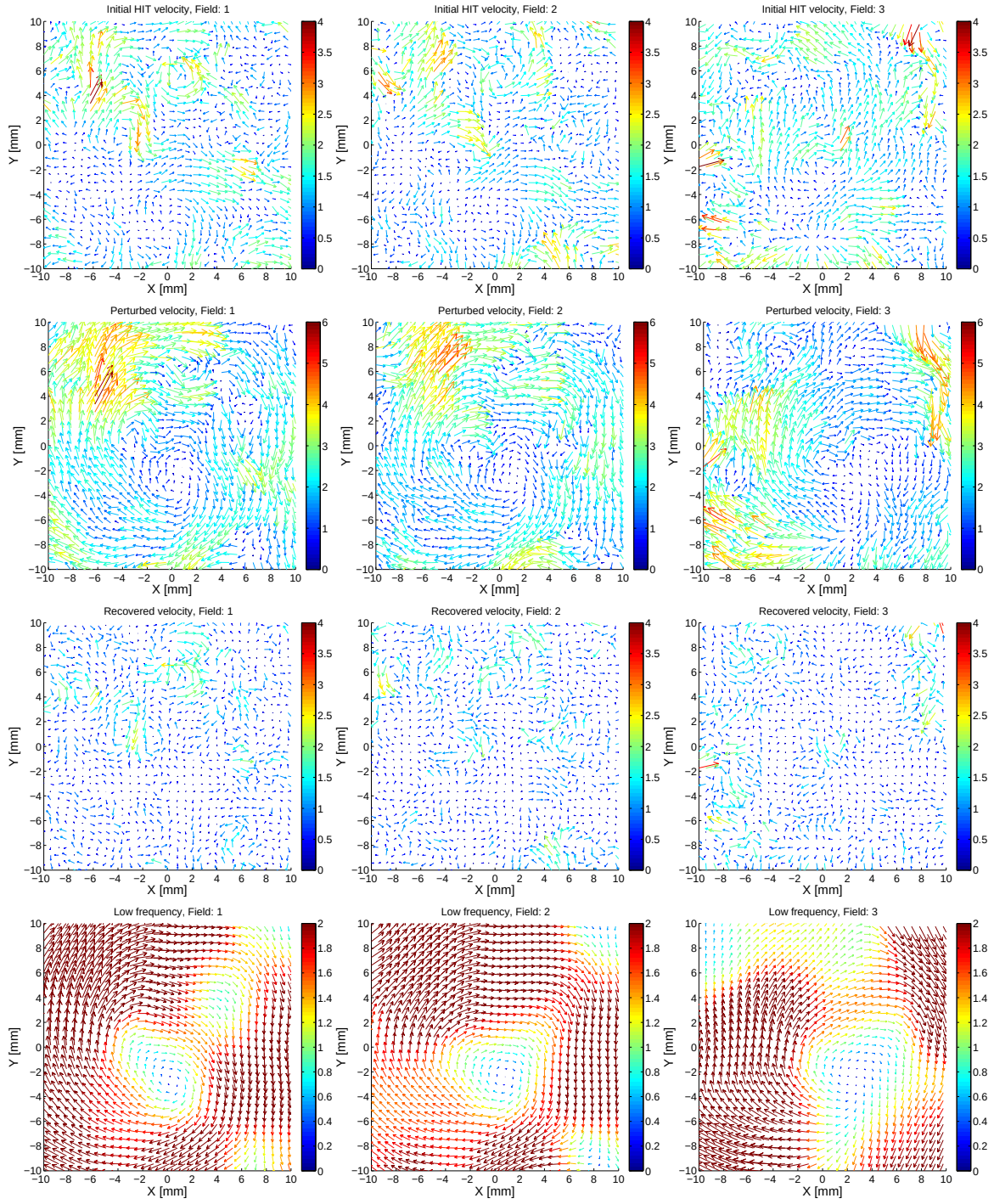

Figure 4.23: Comparative results from Bivariate 2D-EMD analysis for three arbitrary experimental instantaneous HIT flow fields perturbed with a centered vortex of 2 $m.s^{-1}$ amplitude and the length scale of 16 mm.

The spatial power spectra of the initial HIT, perturbed and recovered velocity fields are presented in Figure 4.24, the results are similar as the previous ones.

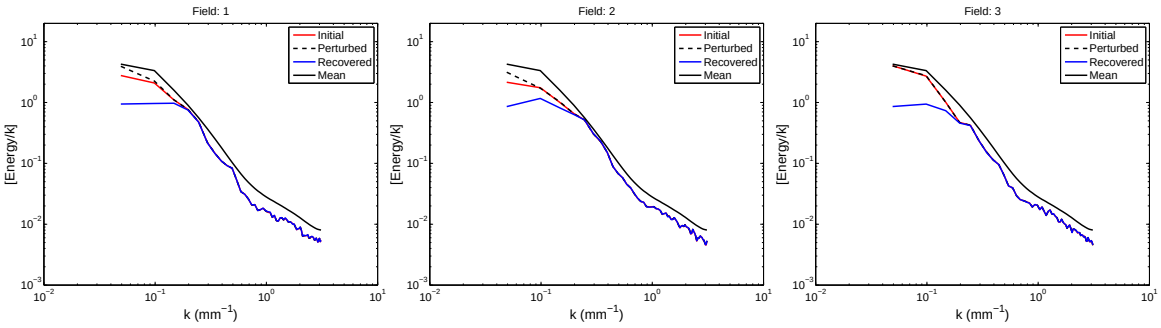

(a) (b) (c)

Figure 4.24: The spatial power spectra of the initial HIT, perturbed and recovered velocity fields, (a) HIT field 1, (b) HIT field 2, (c) HIT field 3.

- **Test case d:** $A = 1\ m.s^{-1}$

In this case the perturbation vortex has a maximum amplitude of 1 $m.s^{-1}$, and a size of $l = 5.L_{(Ux,Vy)} = 16\ mm$ and positioned at the center of initial HIT. It is added to three HIT velocity fields. For all cases also, the jump in energy contents remains from the 5^{th} mode. The results are summarized in Figure 4.25.

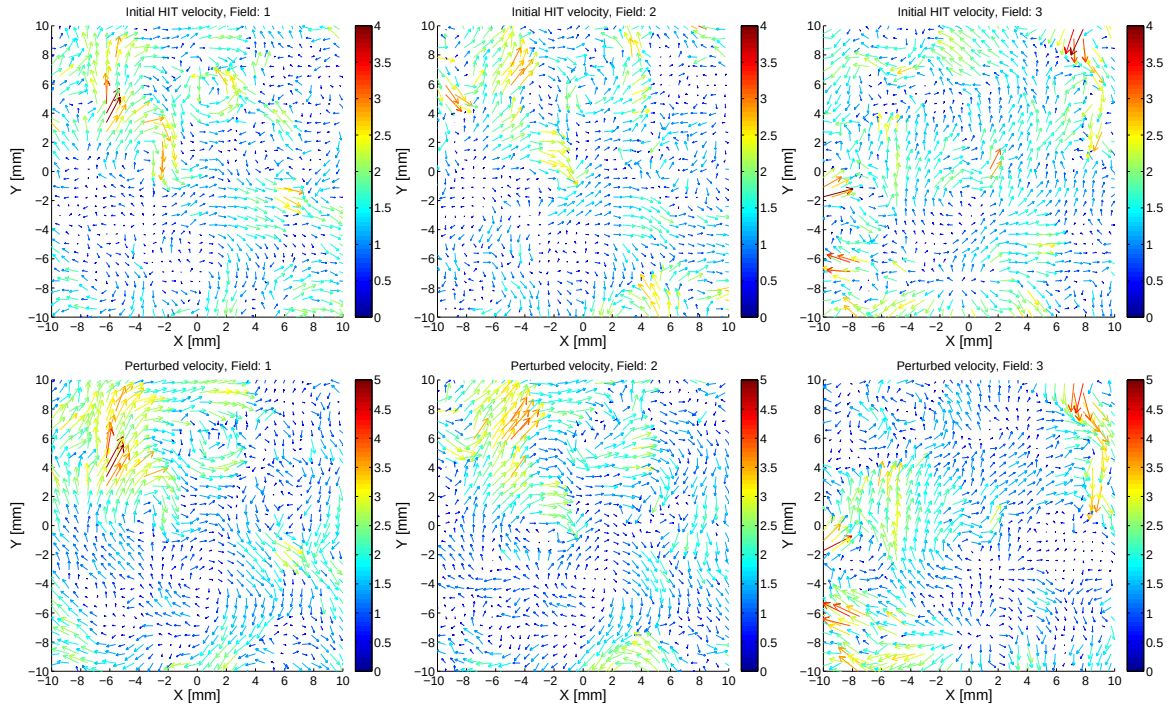

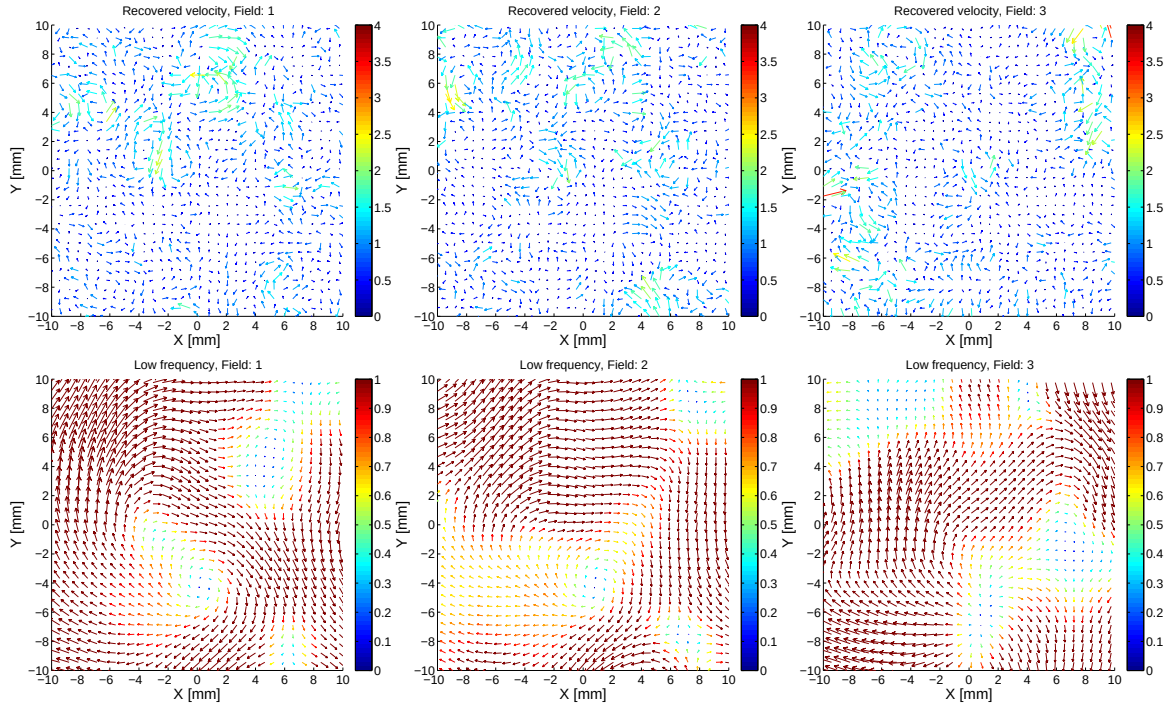

Figure 4.25: Comparative results from Bivariate 2D-EMD analysis for three arbitrary experimental instantaneous HIT flow fields perturbed with a centered vortex of 1 $m.s^{-1}$ amplitude and the length scale of 16 mm.

The spatial power spectra of the initial HIT, perturbed and recovered velocity fields are presented in Figure 4.26, the results are coherent with ones for previous cases.

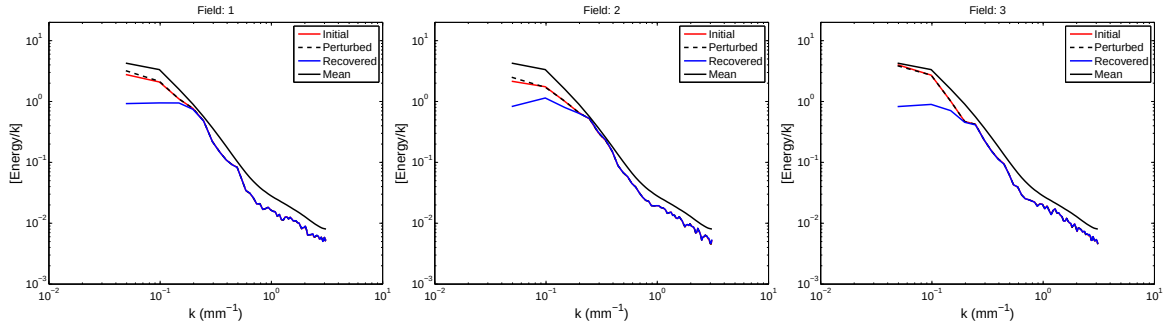

(a) (b) (c)

Figure 4.26: The spatial power spectra of the initial HIT, perturbed and recovered velocity fields, (a) HIT field 1, (b) HIT field 2, (c) HIT field 3.

- ***Discussion***

For the HIT field 1, the following figure presents the difference of energy contents as a function of the amplitude of the vortex.
In all cases the spatial power spectrum of the recovered turbulent velocity field is underestimated in the region associated with the flow large-scale structure. It is due to the

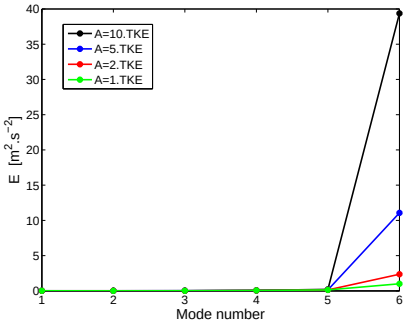

Figure 4.27: Effect of the vortex amplitude on the Energy contents as a function of the mode number - HIT field 1.

presence of the convection flow i.e. large-scale structures in the initial HIT velocity field, this issue is observed in each initial HIT velocity field, see the first panel of Figure 4.25. These structures have a low spatial frequency hence when the perturbed velocity field is decomposed by Bivariate 2D-EMD their feature appears in the same mode with the perturbation vortex that also has a low spatial frequency.

When the amplitude of the added vortex is 1, 2, 5 times of TKE of the initial HIT flow, the power spectrum of the recovered velocity field is superimposed to the initial one in turbulence inertial subrange and smallest scale regions however in the case in which the amplitude of added vortex is 10 times of the TKE there are some fluctuations in the energy spectrum of the recovered field at smallest scale. As an example in Figure 4.28 the spatial power spectrum of the first and second initial HIT velocity fields and their recovered ones that obtained from the perturbed velocity fields with different amplitudes are shown together. The perturbations are positioned at the center of the initial HIT velocity fields and have a size of $l = 5.L_{(Ux,Vy)} = 16\ mm$. There is a good agreement between the spatial power spectrum of the different recovered velocity fields.

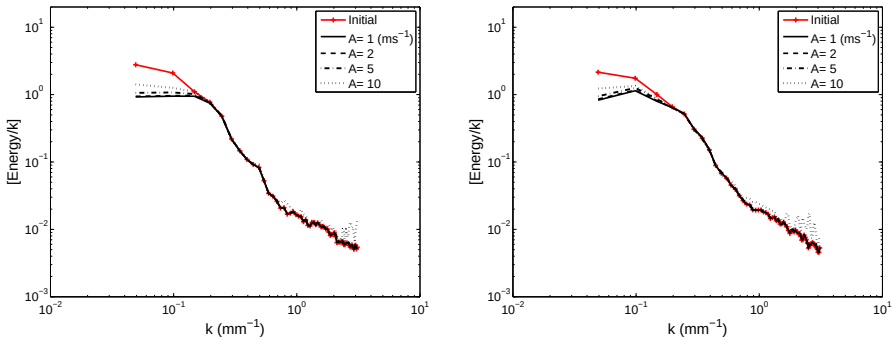

(a) (b)

Figure 4.28: Spatial power spectrum of the initial HIT velocity field and the recovered ones, obtained from the perturbed velocity fields with different vortex amplitudes. For (a) First and (b) Second HIT velocity field.

Also to help the observation, the first initial HIT velocity field and its recovered ones from different perturbed velocity fields are again represented together in Figure 4.29. As one can see the similar structure can be obviously detected in different recovered velocity fields, such a structures are observed in the initial HIT flow field. The initial HIT velocity

field, see Figure 4.29a, contains some large-scale structure and they are disappeared in recovered turbulent velocity fields.

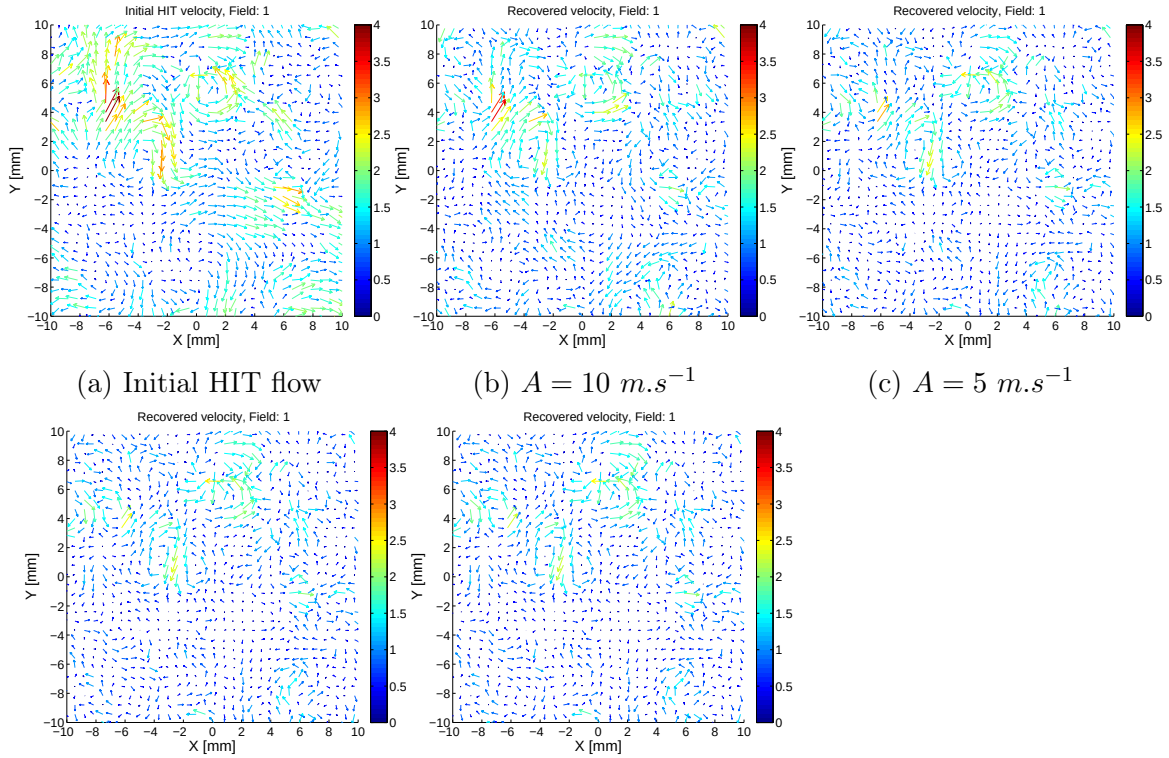

(a) Initial HIT flow (b) $A = 10\ m.s^{-1}$ (c) $A = 5\ m.s^{-1}$

(d) $A = 2\ m.s^{-1}$ (e) $A = 1\ m.s^{-1}$

Figure 4.29: Initial HIT velocity field 1 versus to the recovered ones from those perturbed with different vortex amplitudes, A.

4.3.2 Influence of the vortex position

In this part of study, the position of the vortex center (perturbation signal) get varied compared to initial HIT velocity field. The objective is to assess if the developed Bivariate 2D-EMD suffers the end-effect problems i.e. decomposition of signal at the velocity field boundary. The vortex maximum amplitude is fixed to 5 $m.s^{-1}$ and its scale of 16 mm but the location of its center gets varied.

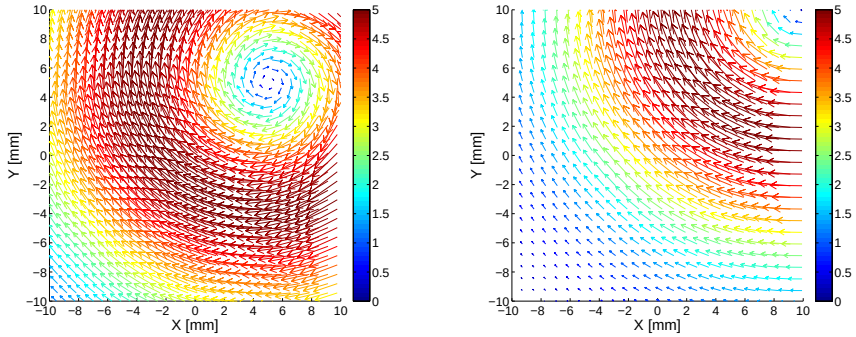

(a) (b)

Figure 4.30: Different vortex locations, maximum amplitude of 5 $m.s^{-1}$ and size of 16 mm.

In addition to the case in which the vortex centered in the middle, two other cases are considered : the center located at mid-distance between the center and one corner (up-right) of the initial HIT field, and at the corner of the initial HIT field, as plotted in Figure 4.30a and Figure 4.30b, respectively.

• **Perturbation vortex positioned at the mid-distance between center and corner of the initial HIT velocity field**

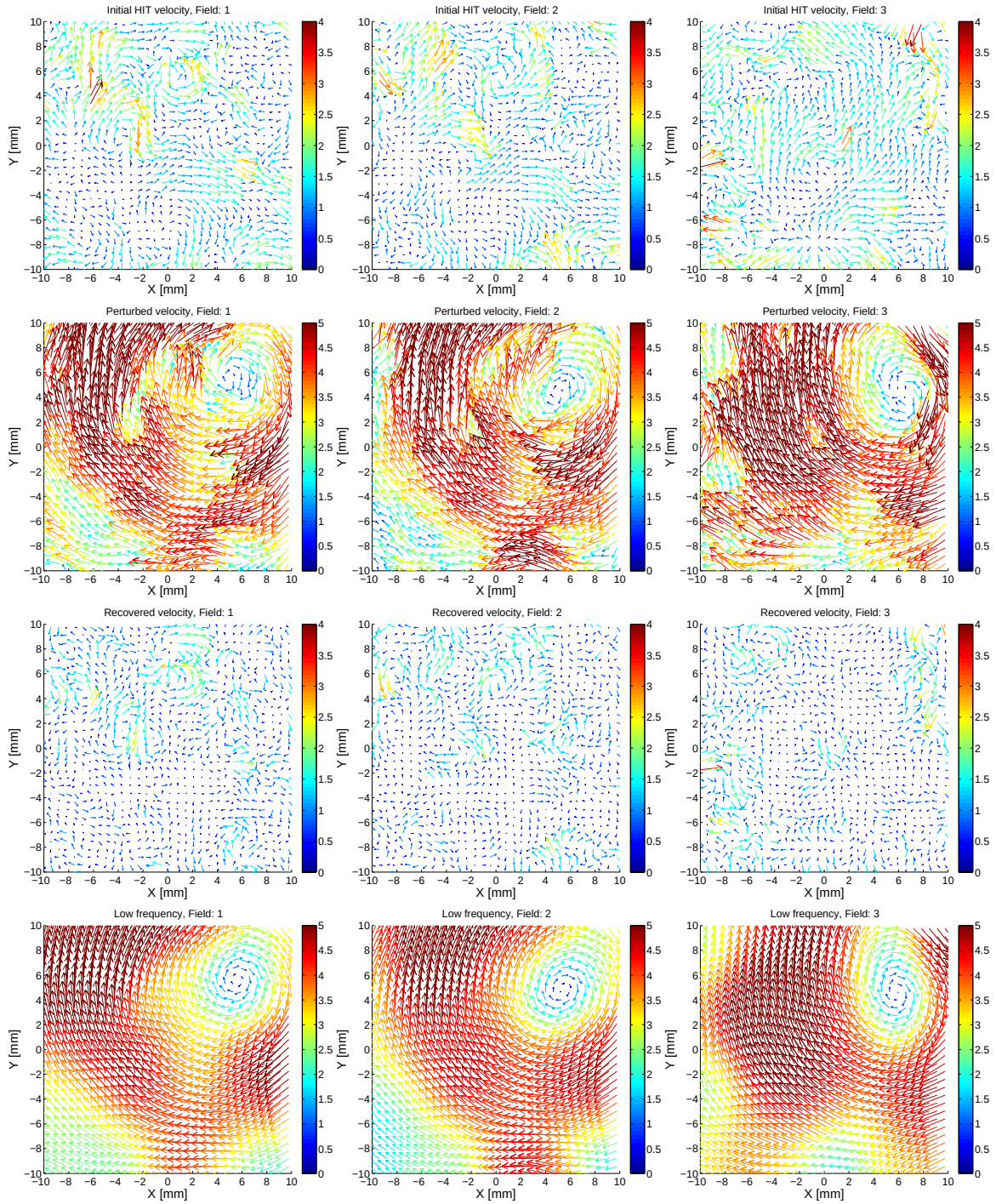

Figure 4.31: Comparative results from Bivariate 2D-EMD analysis for three arbitrary experimental instantaneous HIT flow fields perturbed with a vortex positioned at the mid-distance.

The spatial power spectra of the initial HIT, perturbed and recovered velocity fields are presented in Figure 4.32. As one can see the results are not affected by the change in the position of vortex.

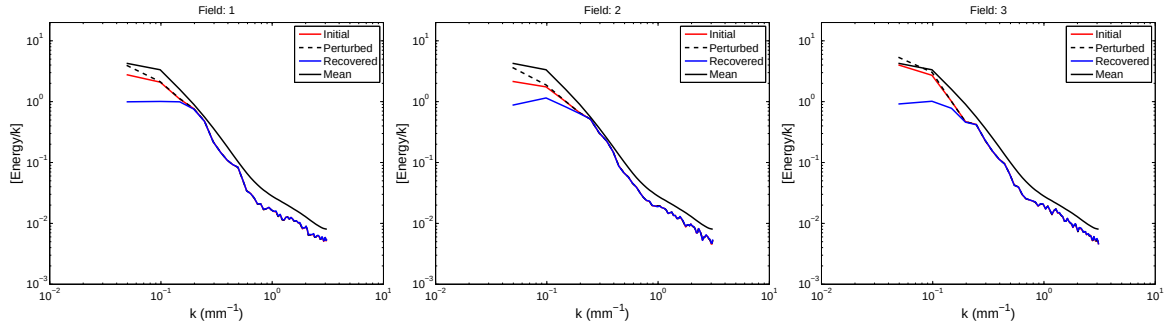

(a) (b) (c)

Figure 4.32: The spatial power spectra of the initial HIT, perturbed and recovered velocity fields, (a) HIT field 1, (b) HIT field 2, (c) HIT field 3.

- **Perturbation vortex positioned at the corner of the initial HIT velocity field.**

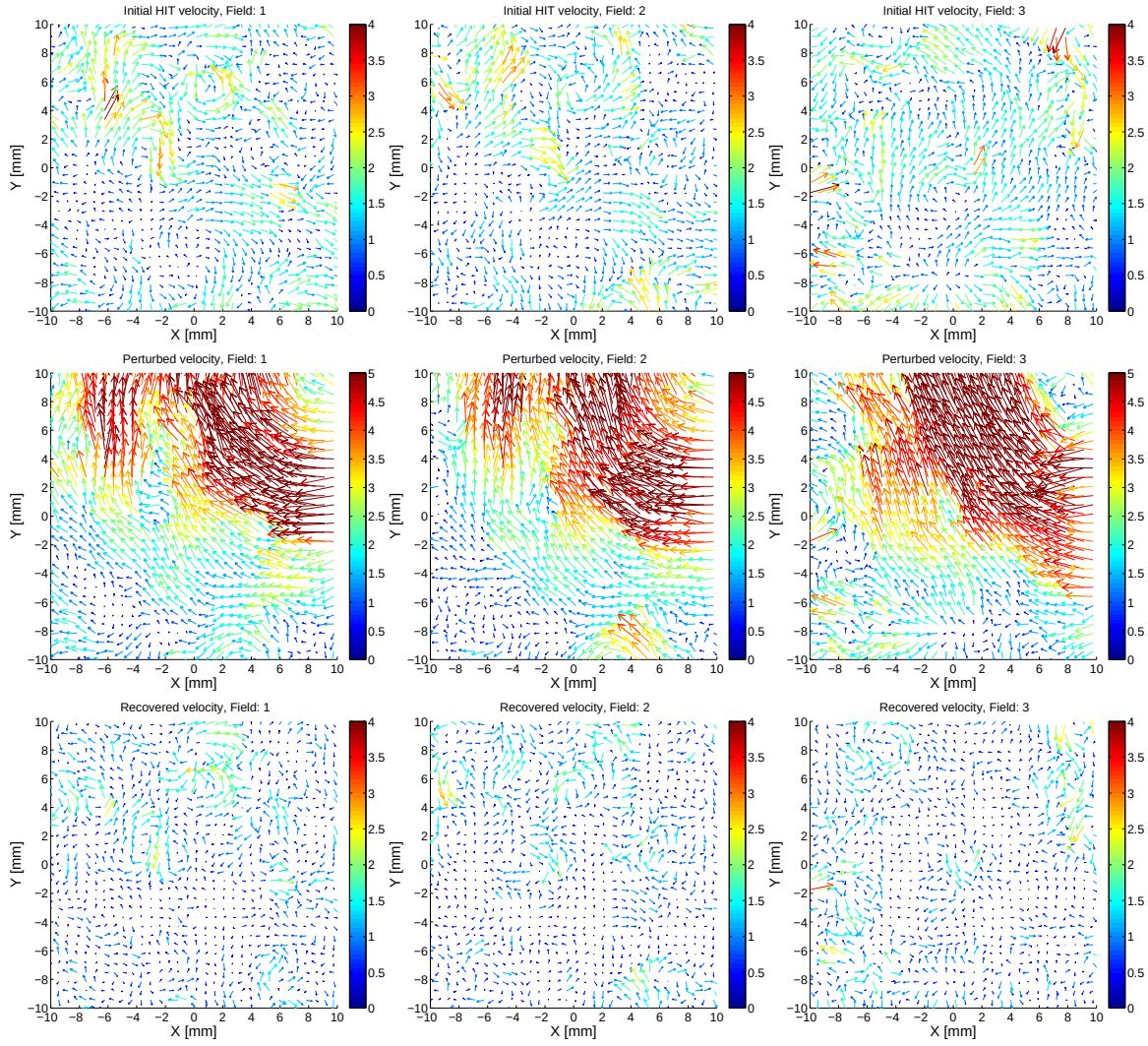

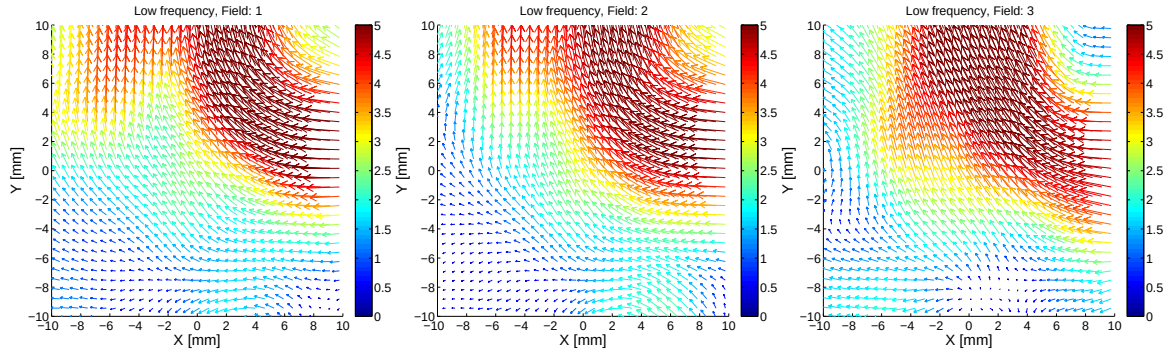

Figure 4.33: Comparative results from Bivariate 2D-EMD analysis for three arbitrary experimental instantaneous HIT flow fields perturbed with a vortex with a vortex positioned at the corner.

The spatial power spectra of the initial HIT, perturbed and recovered velocity fields are presented in Figure 4.34. It is observed even when the perturbation vortex is placed at the boundary of initial HIT, there is good agreement between the power spectra of the recovered velocity fields and the ones for iniale HIT velocity fields.

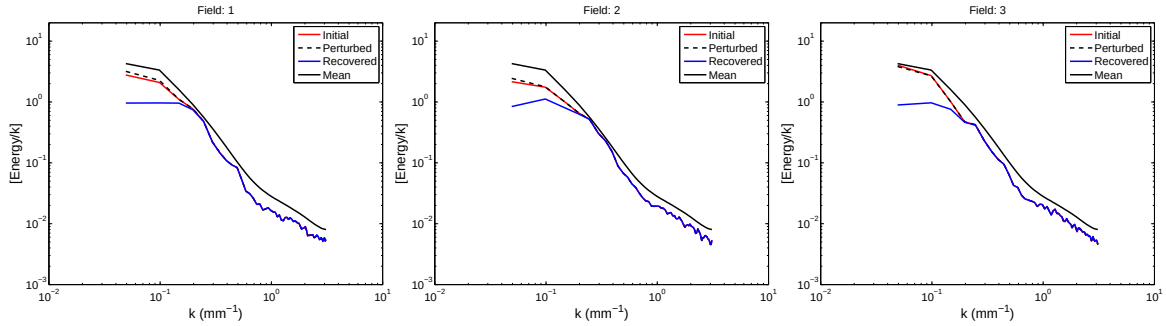

(a) (b) (c)

Figure 4.34: The spatial power spectra of the initial HIT, perturbed and recovered velocity fields, (a) HIT field 1, (b) HIT field 2, (c) HIT field 3.

- ***Discussion***

For the HIT field 1, the Figure 4.35 presents the difference of energy contents as a function of the different vortex locations. This etude proves that the decomposition of the velocity field by Bivariate 2D-EMD and so the properties of recovered turbulent field are not sensible to the position of the perturbation vortex.

In Figure 4.36 the spatial power spectrum of the first and third HIT velocity fields and their recovered ones are presented. The recovered velocity fields have been obtained from the perturbed velocity fields in which the center of the perturbation vortex is located at the center, mid distance between the center and corner and the corner of the initial HIT velocity fields. As one can see in each case, the power spectra of the different recovered velocity fields are superimposed together however they are underestimated at the small wave number i.e. large structures.

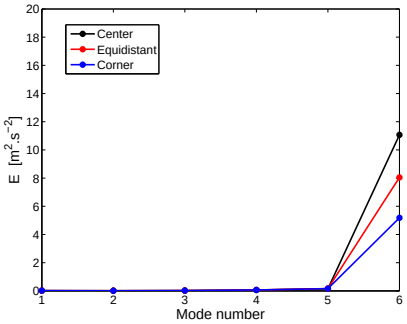

Figure 4.35: Effect of the vortex position on the Energy contents as a function of the mode number, HIT field 1.

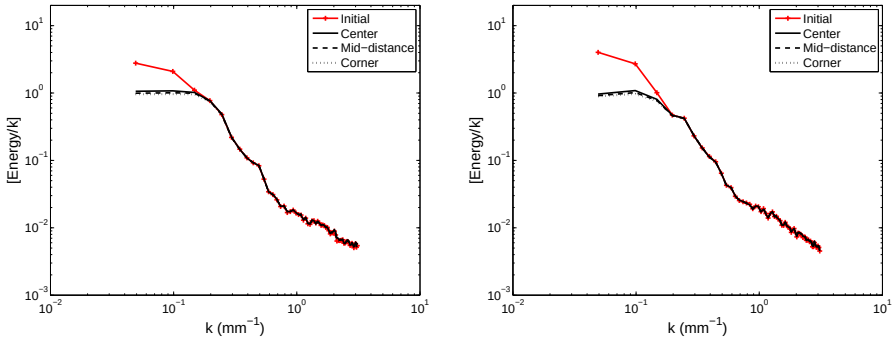

(a) HIT Field 1 (b) HIT Field 3

Figure 4.36: Spatial power spectrum of the initial HIT velocity field versus the recovered turbulent velocity field. The perturbation vortex was added at the center, mid-distance between center and corner and at the corner of initial velocity fields. For (a) First and (b) Third HIT velocity field.

As an example, the third initial HIT velocity field and its recovered ones from different perturbed velocity fields are shown together in Figure 4.37. The initial HIT velocity field includes the convection motions, Figure 4.37a, they are suppressed in recovered turbulent velocity fields. Indeed the large-scales of the initial HIT velocity fields and the perturbation vortex are lumped together through the decomposition process by Bivariate 2D-EMD. The traces of such scales can be perceived in all the low frequency part of the perturbed velocity field, as the last row of Figure 4.33. One can see the different recovered velocity fields are really similar: whatever the location of the perturbation vortex (that simulate large-scale motion) in HIT velocity field, the velocity field is really well recovered from perturbed flow field buy using Bivariate 2D-EMD.

In addition even when the center of the perturbation vortex is located at the boundary of initial HIT velocity field, Figure 4.33, there exist no over/under shoot effects at the border of the resulted recovered velocity fields as well as at the border of the low frequency parts hence this method of decomposition does not suffer from the signal end-effect problem.

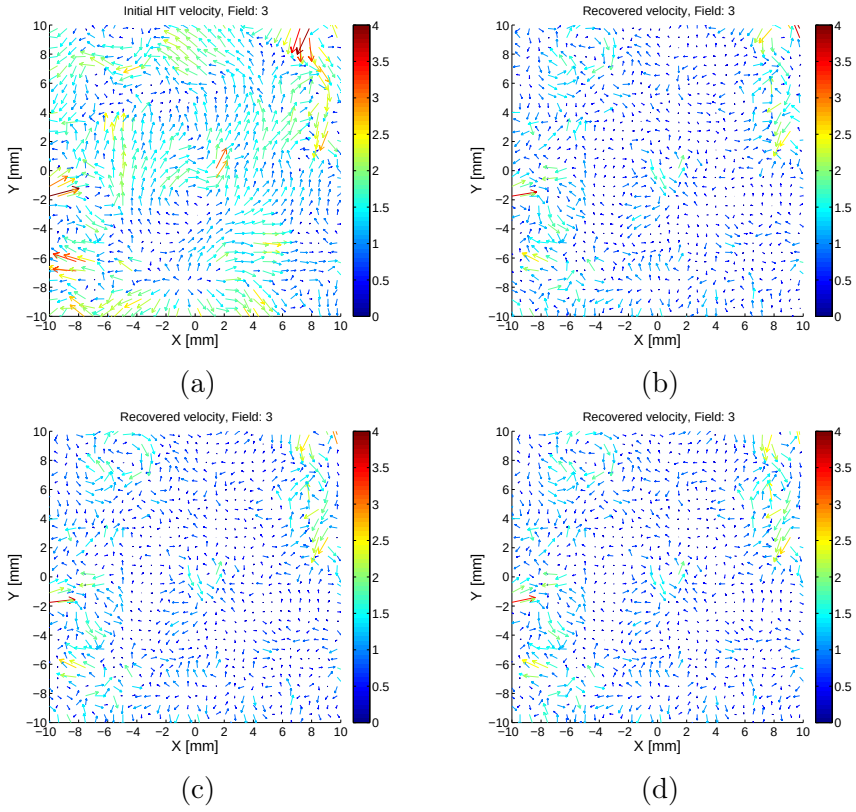

Figure 4.37: Initial HIT velocity field compared to the recovered ones. The perturbation vortex was added at the (b) Center, (c) Mid-distance between the center and corner and (d) Corner of the initial velocity field.

4.3.3 Influence of the vortex size

The influence of the perturbation size i.e. the characteristic length scale of the vortex, on the decomposition and the quality of recovered signal is then investigated. For that, a vortex of 5 $m.s^{-1}$ amplitude, positioned at the center of initial HIT velocity field is generated but with a size l varying as a function of longitudinal integral length scale of the initial HIT flow; $l = \alpha.L_{(Ux,Vy)}$ with $L_{(Ux,Vy)} \simeq 3.2\ mm$ and $\alpha = 1,\ 2,\ 5,\ 10$. The perturbation signals generated with $\alpha = 2$ and $\alpha = 1$ are shown in Figure 4.38.

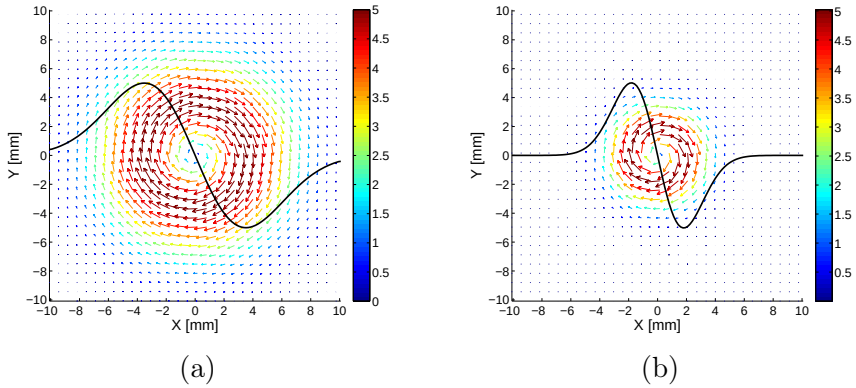

Figure 4.38: Centered perturbation vortices with size of (a) $l = 2.L_{(Ux,Vy)}$ and (b) $l = L_{(Ux,Vy)}$ - amplitude 5 $m.s^{-1}$.

The case in which $\alpha = 5$ was already investigated in subsection 4.3.1 on p. 79. The perturbation signal with $\alpha = 10$ is presented in Figure 4.39b but it has to be mentioned that due to the properties of perturbation signal, the maximum amplitude of the perturbation leads to 6 $m.s^{-1}$.

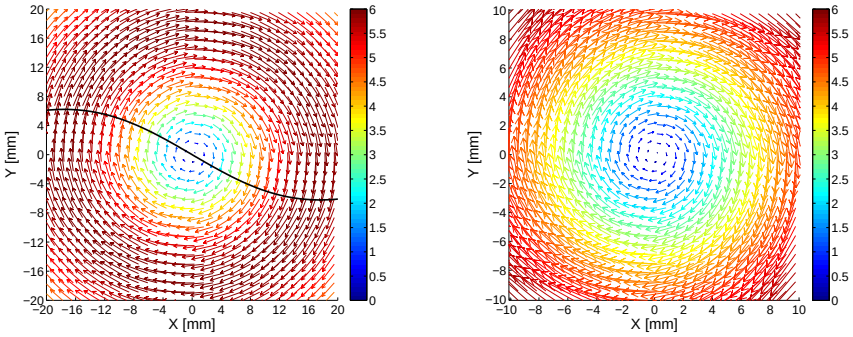

(a) (b)

Figure 4.39: Perturbation vortices with size of $l = 10.L_{(Ux,Vy)}$ and maximum amplitude of 6 $m.s^{-1}$. (a) In the region of $40.64 \times 40.64\ mm^2$, (b) Zoom of the same vortex in $20.32 \times 20.32\ mm^2$.

- **Test case a:** $l = 10.L_{(Ux,Vy)}$

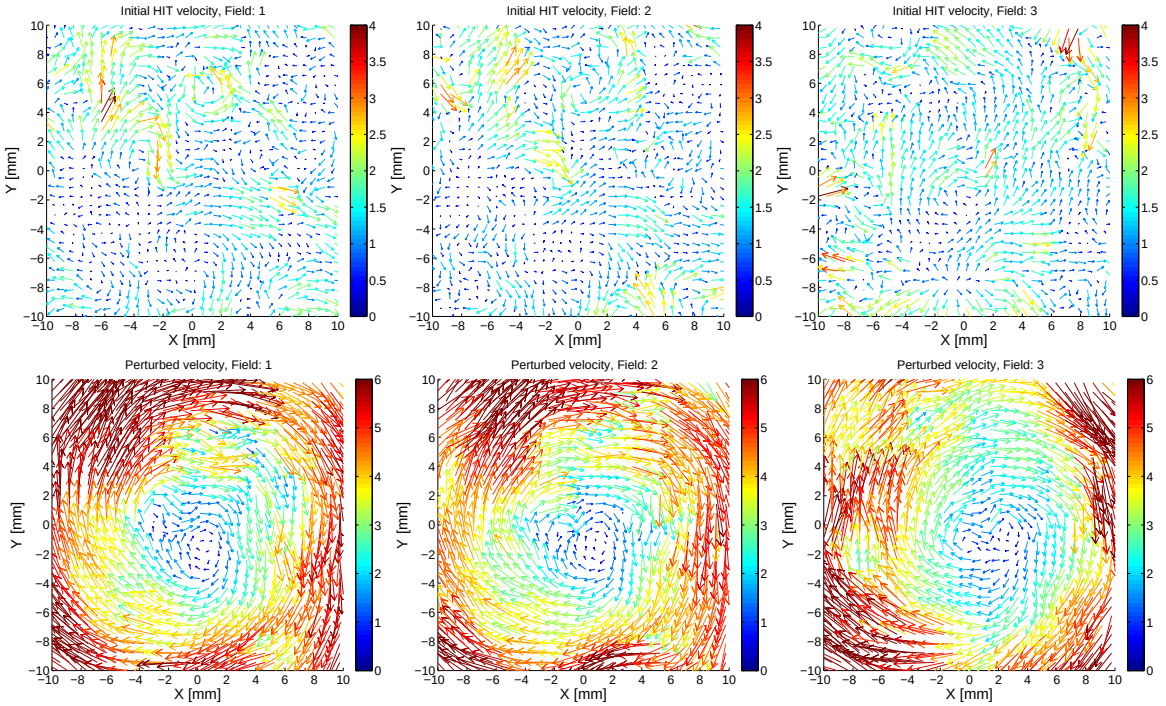

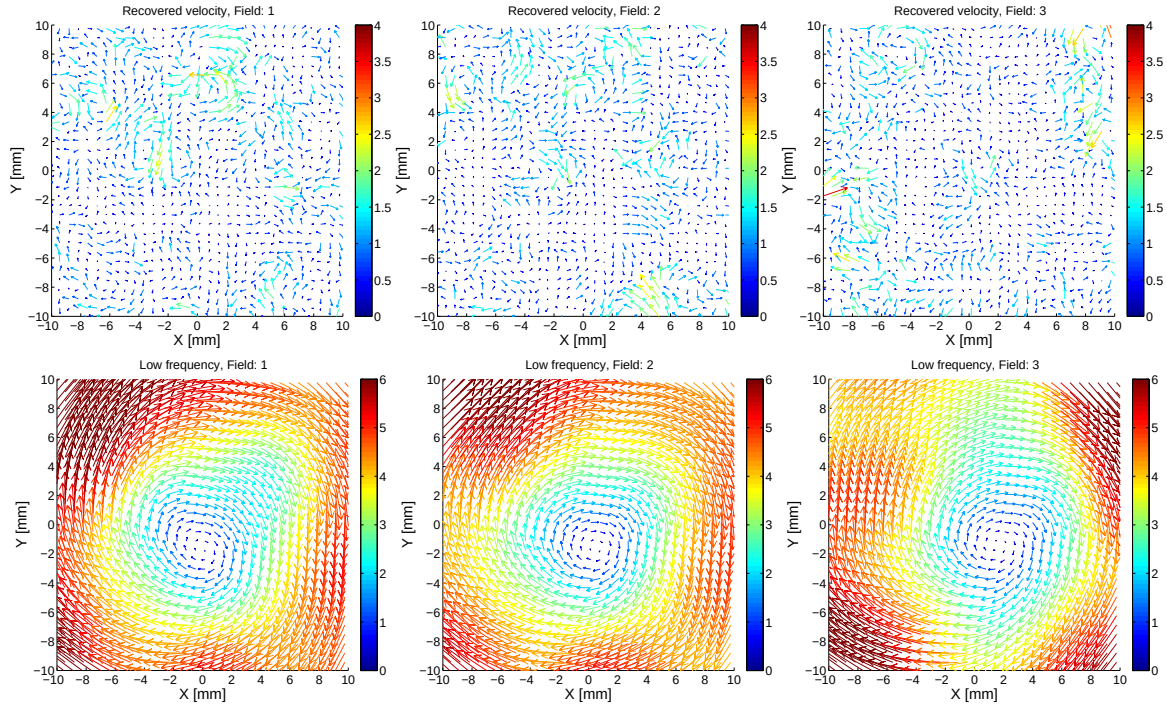

Figure 4.40: Comparative results from Bivariate 2D-EMD analysis for three arbitrary experimental instantaneous HIT flow fields perturbed with a centered vortex of 6 $m.s^{-1}$ maximum amplitude and a length scale of $l = 10.L_{(Ux,Vy)}$.

The spatial power spectra of the initial HIT, perturbed and recovered velocity fields are presented in Figure 4.41. It is observed the quality of recovered velocity fields do not decrease in the case in which the scale of perturbation vortex, that mimics the large-scale organized motion, is much higher than integral length scales of the initial HIT flows.

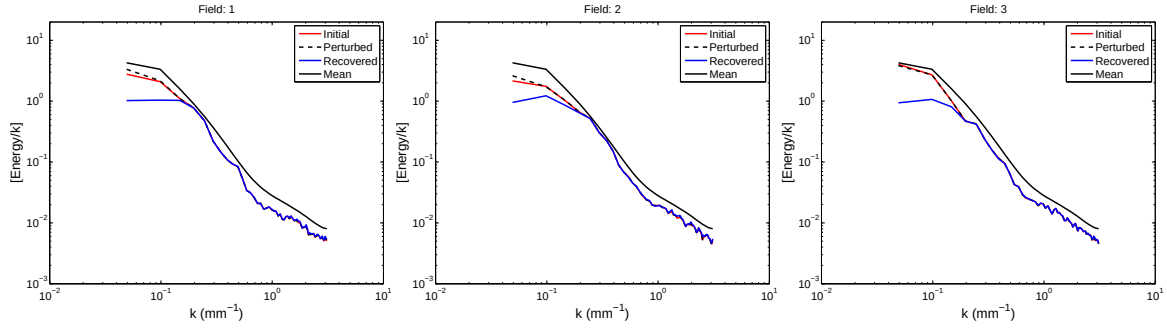

(a) (b) (c)

Figure 4.41: The spatial power spectra of the initial HIT, perturbed and recovered velocity fields, (a) HIT field 1, (b) HIT field 2, (c) HIT field 3.

- **Test case b:** $l = 2.L_{(Ux,Vy)}$

The perturbation vortex in Figure 4.38a was added to the same HIT velocity fields and the same procedure as previous study cases is used to extract the HIT flow from the perturbed velocity field. Here, only results for HIT field 1 are presented, exactly same tendencies and conclusions could be accomplished for the two others. Figures 4.42a and 4.42b present initial HIT flow field 1 and its associate perturbed velocity field respectively.

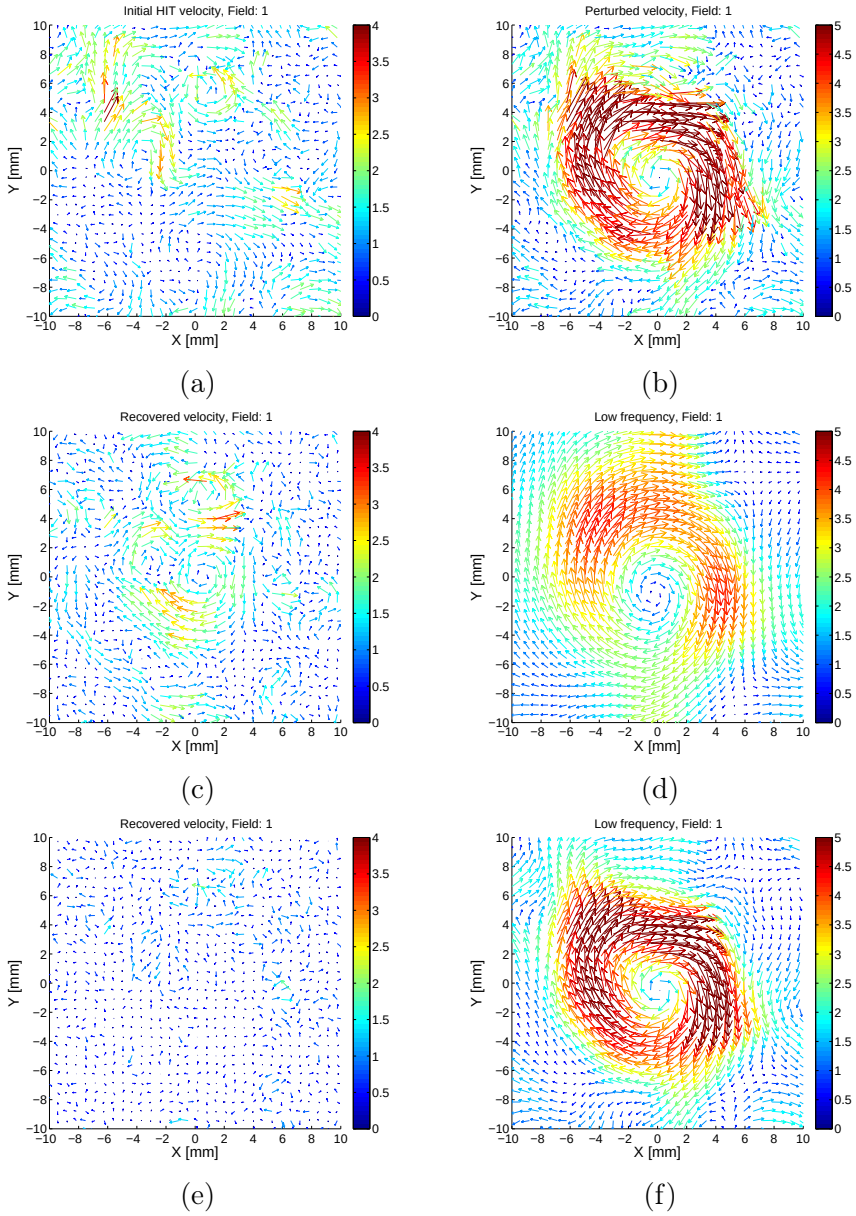

Figure 4.42: $l = 2.L_{Ux,Vy}$, HIT field 1. (a) Initial, (b) Perturbed velocity field. (c) Recovered from the first 5 modes and (d) Low frequency field: 6^{th} mode. (e) Recovered from the first 4 modes and (f) Low frequency field: $5^{th} + 6^{th}$ mode.

As above, this velocity field was decomposed by Bivariate 2D-EMD and the energy criterion for the result modes is plotted in Figure 4.43. It is observed the energy content does not strongly jump from 5^{th} to 6^{th} but starts to evolve from the 4^{th} one.
In Figure 4.42c the recovered turbulent flow is computed from the sum of the first five modes and so the 6^{th} mode is considered as an organized motion Figure 4.42d. As one can see some signatures of the perturbation vortex appear in the center of the recovered turbulent velocity field, this feature is also revealed as an increase in the energy of the recovered velocity field compared to the initial HIT flow in the region of small wave numbers, see Figure 4.44a.
To avoid some large scales component on the recovered velocities field, a test was done by estimated it as the sum of the first four modes as is illustrated in Figure 4.42e.

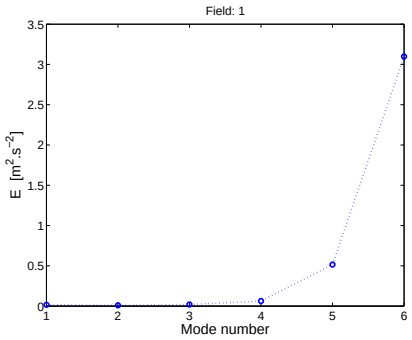

Figure 4.43: Energy contents as function of mode number, $l = 2.L_{(Ux,Vy)}$, HIT field 1.

The corresponding low frequency field, Figure 4.42f, is also more representative of the generated one. However the sever shoot in the power spectral density of the recovered turbulent velocity field is observed, as shown in 4.44b .

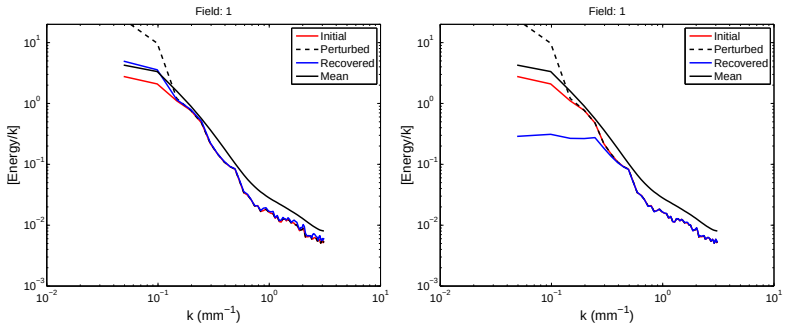

(a) (b)

Figure 4.44: Spatial energy spectral density for Initial HIT field 1, Perturbed by a centered vortex of size 6.4 mm and Recovered from EMD, (a) Low frequency component: 6^{th} mode, (b) low frequency component: $5^{th} + 6^{th}$ modes.

- **Test case c:** $l = L_{(Ux,Vy)}$

Here the size of perturbation vortex, Figure 4.38b is equal to the longitudinal integral length scale of the initial HIT velocity field that is 3.2 mm. It is added to the first initial HIT and the outcome perturbed signal, Figure 4.45b is decomposed by Bivariate 2D-EMD. As shown in Figure 4.46 the energy criterion computed for each mode arise progressively and no distinct threshold, sudden jump in mode energy, can be notified. Same study as the previous case is performed, Figure 4.45c represents the recovered velocity field when the sum of the first fives modes are considered as a turbulent part and the last mode as the perturbation, Figure 4.45d. it is observed that some part of perturbation signal remains in the recovered velocity field and so the energy spectrum of this field is overestimated, Figure 4.47a .
One can consider the sum of the first four modes as a turbulent part i.e. recovered flow, Figure 4.45e, and the remained modes ($5^{th} + 6^{th}$) as a perturbation vortex, as shown in Figure 4.45f.In this case the large-scales of initial HIT flow is entirely filtered out and the power spectrum of the turbulent recovered velocity field is drastically underestimated for

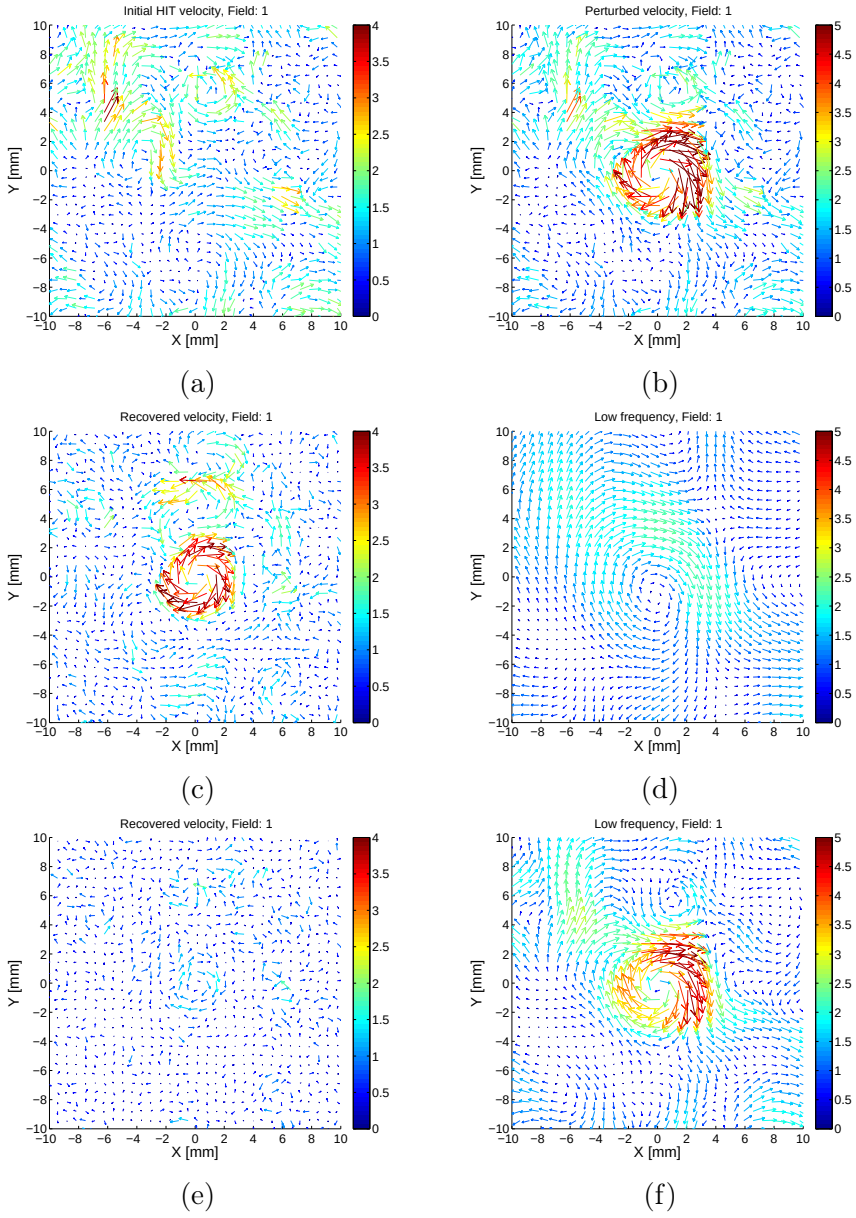

Figure 4.45: $l = L_{(Ux,Vy)}$, HIT field 1. (a) Initial, (b) Perturbed velocity field. (c) Recovered from the first 5 modes and (d) Low frequency field: 6^{th} mode. (e) Recovered from the first 4 modes and (f) Low frequency field: $5^{th} + 6^{th}$ mode.

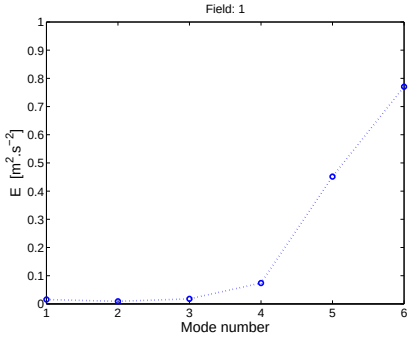

Figure 4.46: Energy contents as function of mode number, $l = L_{(Ux,Vy)}$, HIT field 1.

these scales, Figure 4.47b. Furthermore some traces of perturbation signal can be observed in the center of recovered velocity field.

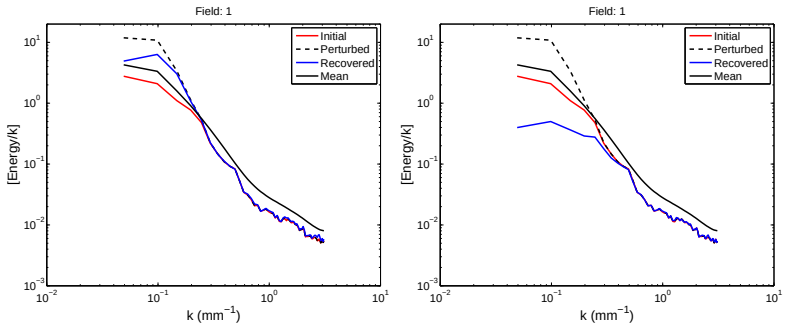

(a) (b)

Figure 4.47: Spatial energy spectral density for Initial HIT field 1, Perturbed by a centered vortex of size 3.2 mm and Recovered from EMD, (a) Low frequency component: 6^{th} mode, (b) low frequency component: $5^{th} + 6^{th}$ modes.

• ***Discussion***

This investigation attests when the size of perturbation vortex is much larger than the integral length scale of the initial HIT flow (5 or 10 times of $L_{(Ux,Vy)}$, which can be really considered as a large-scale organized motion, the initial turbulent velocity field can be recovered using Bivariate 2D-EMD method with energy criterion. But when the size of perturbation vortex approaches to the turbulent length scale of HIT flow, the quality of recovered turbulent field reduces drastically. In the case in which the size of perturbation vortex is equal to the integral scale of initial velocity field $L_{(Ux,Vy)}$, they have both same feature and so they are not separable.

From the matrix of tests in order to evaluate the potential of the proposed Bivariate 2D-EMD in estimation of turbulent velocity field, in the next step the synthetic Lamb-Ossen vortex that simulate the large-scale organized motion generated in SI engine, is added to the 200 experimental instantaneous HIT velocity fields. The vortex has a maximum amplitude of 5 $m.s^{-1}$ and the size of 16 mm (corresponding to $5.L_{Ux,Vy}$), as shown in Figure 4.48, is positioned at the center of the velocity fields.

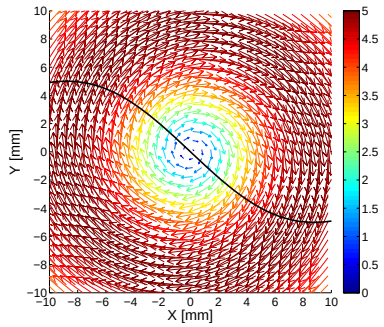

Figure 4.48: Perturbation vortex that mimics large-scale organized motion with the size of $5.L_{(Ux,Vy)} = 16$ mm and maximum amplitude of $A = 5$ $m.s^{-1}$.

It should be mentioned the time interval between initial HIT flow is 2.8571×10^{-4}, so in order to eliminate the statistical correlation between the velocity fields, every 40 field are sampled to regroup 200 velocity fields that are under process. Some of these velocity fields are randomly selected and displayed in Figure 4.49.

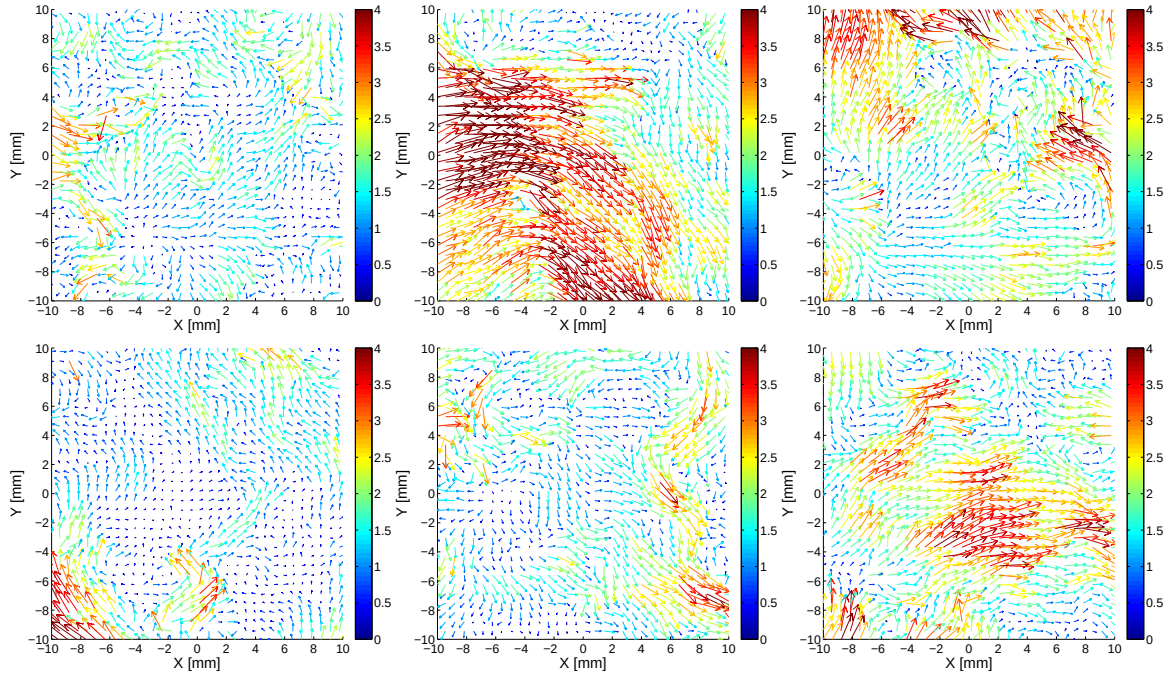

Figure 4.49: Examples of instantaneous HIT velocity fields.

Each perturbed velocity field is decomposed by developed Bivariate 2D-EMD approached and using the energy criterion, the initial HIT velocity field is recovered. The mean spatial power spectra for recovered velocity fields that corresponds to the average of the spectrum computed for each velocity field, is compared to ones for the initial HIT and perturbed velocity fields in Figure 4.50.

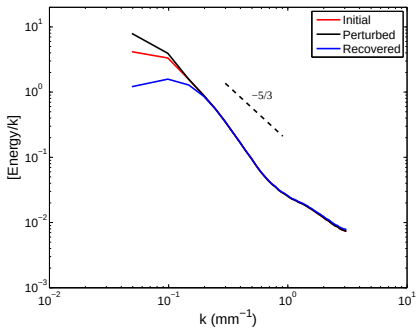

Figure 4.50: Mean spatial energy density spectra for experimental initial HIT, perturbed and recovered from EMD velocity fields.

There is a good agreement between the power spectrum of the initial HIT flow and the recovered turbulent flow in the inertial sub-range and smallest scale region however for the small wave number corresponding to larger scales, the energy of the recovered turbulent flow remains underestimated.
As a notice in computation of the power spectrum only the fluctuations of the instantaneous velocity are taken into account and the spatial mean of the velocity is subtracted. Also the power spectral density is computed by using Welch's method with the length 127 (i.e. size of velocity field) of the FFT with 50% overlapping segments and Hann window function.

The longitudinal and lateral correlation coefficients of the initial, perturbed and recovered velocity fields are compared in Figure 4.51. They are computed from the fluctuating components for each instantaneous velocity field, and then averaged over all the velocity fields. The evolution are different and as expected, in perturbed flow as large vortex is added, the correlation coefficient crosses the length axis at larger value. In the case of recovered field, the correlation functions present more usual evolution of turbulent flow field.

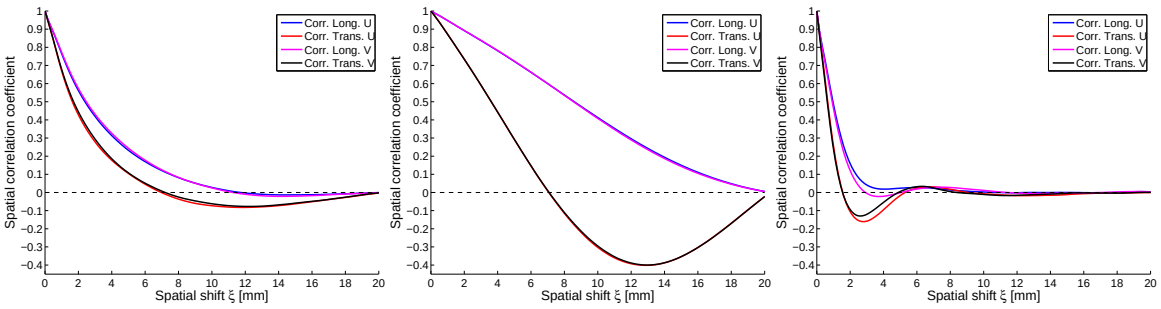

Figure 4.51: Evolution of the mean longitudinal and lateral spatial correlation coefficients for initial HIT, perturbed and recovered velocity field for both velocity components.

Longitudinal integral scale $[mm]$	Initial HIT	Recovered velocity
L_{Ux}	3.1580	1.2504
L_{Vy}	3.1763	1.0977

(a)

Lateral integral scale $[mm]$	Initial HIT	Recovered velocity
L_{Uy}	1.4974	0.3003
L_{Vx}	1.6299	0.3908

(b)

Table 4.12: Mean longitudinal (a) and lateral (b) integral length scales estimated from the experimental initial HIT and recovered velocity fields, averaged based on 200 fields.

Turbulent integral length scale are obtained by integrating the spatial correlation functions until the first passage of the functions by zero, these turbulent flow properties

are computed for the three different velocity fields and the result are presented in Table 4.12. It is observed that the integral scales of the recovered velocity fields are not similar for both components of velocity U and V. Moreover, in initial HIT flow the longitudinal integral scales are two times of the lateral ones, $L_{Ux} = 2.L_{Uy}$ and $L_{Vy} = 2.L_{Vx}$, but not in the case of recovered flow fields.
As illustrated in Figure 4.49 the initial HIT velocity fields are not "absolute" HIT flow fields and contains the large-scale convection structure. Therefor when the perturbed velocity fields decomposed by Bivariate 2D-EMD method, the large-scale of the initial filed and the perturbation vortex appear in the same mode.
Indeed *if after decomposition the large-scales of the initial HIT flow and the large-scale perturbation vortex reside in two different modes, it means identical scale in different modes and it is the definition of Mode-mixing.*

In conclusion, these steps of validation attest the efficiency of proposed Bivariate 2D-EMD to separate large-scale organized motion i.e. flow low frequency part from random turbulent fluctuations i.e. high frequency part in an instantaneous 2D velocity field.
In the case in which the scale of perturbation vortex accedes to the turbulent integral length scale of the initial velocity field, it cannot be still considered as a flow large-scale organized motion so physically it is not separable from flow turbulent contribution, in the other words such a distinction is exactly undesirable. The proposed approach does not suffer from over/under effects at the velocity field boundary. It should be noted when the velocity magnitude of organized motion is much higher than the TKE of initial HIT flow, there exists some small fluctuations in the power spectral density of recovered velocity field in the regions that are associated with very small wavelengths.

Chapter 5

Experimental set up and measurements

5.1 Engine test bench

The experiments were performed in a research optical single cylinder Direct-Injection Spark-Ignition (DISI) engine, PSA Peugeot Citroën Group, (Ref: EP6N34). It is a twin-cam, 4 overhead-valves cylinder with a pent-roof spray guide combustion chamber. Engine characteristics are summarized in Table 5.1.

Displacement volume$[c.m^3]$	399.54
Stroke $[mm]$	85.8
Bore $[mm]$	77
Compression ratio	10.5:1
Connecting Rod Length $[mm]$	138.5
Number of Valves	4

Table 5.1: Engine geometry.

A transparent cylinder made of quartz-glass (15.04 mm thickness and an optical piston, especially designed for DISI, with a non-symmetrical pentroof central dish crown, were used to provide optical accesses to perform PIV as it can be seen in Figure 5.1. The sealing set of two double graphite rings with 5 mm inter-distance and 5 mm from piston head to avoid air leakage.

(a) (b)

Figure 5.1: (a) Transparent quartz cylinder, (b) Piston crown.

In this work, the convention reference point, CAD= 0 is taken at the Top Dead Center of combustion (TDC). Intake and exhaust valve timings are presented in Figure 5.2 and more detailed in Table 5.2 aTDC and bTDC denote after TDC and before TDC respectively.

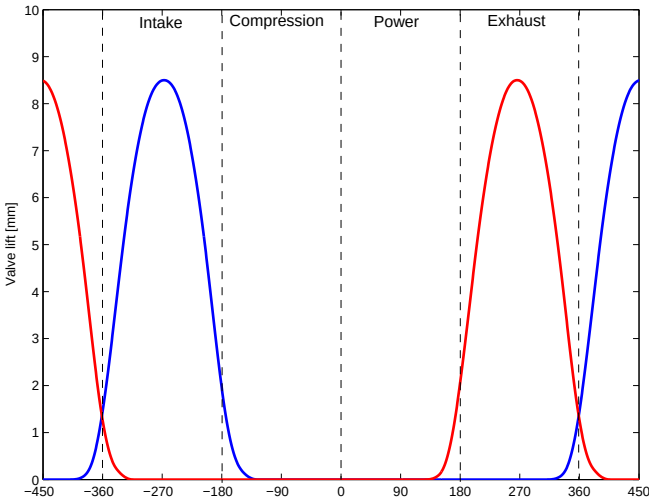

Figure 5.2: Valves lift profiles.

Intake Valve Opening	337° aTDC
Intake Valve Peak Lift	267° bTDC
Intake Valve Closing	147° bTDC
Exhaust Valve Opening	151° aTDC
Exhaust Valve Peak Lift	266° aTDC
Exhaust Valve Closing	334° bTDC

Table 5.2

The engine intake port is connected to a manifold of 0.4 l volume. A 60 l plenum is added to limit the variations of the intake pressure for both operating modes, stationary and transient ones. The intake line between electronic throttle control and plenum has 1 m length and 43 mm internal diameter. A global view of the engine can be seen in Figure 5.3.

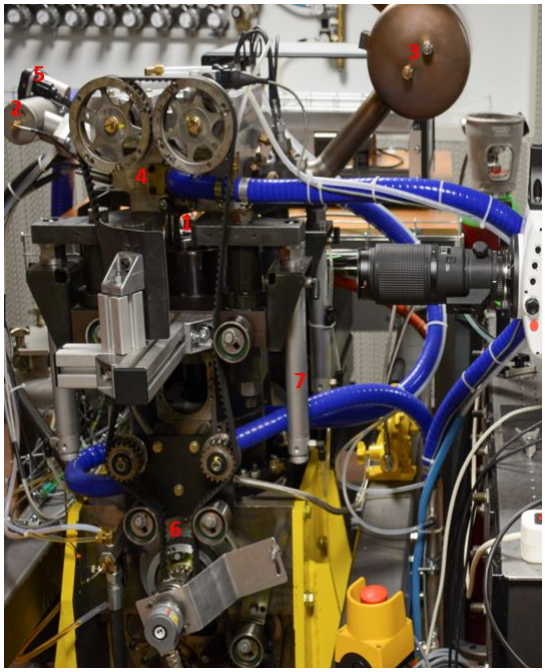

Figure 5.3: Engine test bench and its accessories.

1. Transparent cylinder
2. Intake plenum
3. Exhaust manifold
4. Cylinder head
5. Electronic throttle control
6. Brushless electric motor
7. Pneumatic system to remove cylinder head

Table 5.3

The engine was motored via a 41 kW rotary brushless servo motor (Parker, type: HVA50JER 9000), to be controlled in speed as a function of time by a Compact-RIO FPGA program. The ratio between the torque and the inertial for the total set electric motor and thermal engine was optimized to allow to the acceleration of engine speed from 1000 to 2000 rpm in different periods of time. Engine speed and crank angle information are acquired by using a rotary encoder attached to the crankshaft.

5.2 High and low frequency rate data acquisitions

The in-cylinder pressure is measured by an AVL QH32C quartz pressure transducer (piezo-electric sensor) with a nominal sensitivity of 26.82 pC/bar and pressure range of 200 bar. This sensor is located in the cylinder head and needs to be adjusted by intake pressure to provide absolute in-cylinder pressure. The intake and exhaust pressures are measured by using a piezo-resistive absolute pressure sensor (Kistler 4075A10) with a nominal sensitivity of 10.64 mV/mA.bar and a pressure range of 10 bar. The pressure signals are amplified by a charge amplifier (Kistler-5011).
The acquisition of these data every 0.1 CAD resolution is synchronized with the engine speed, given thanks to a rotary encoder by means of a high-speed digital data acquisition device.

Platinum resistance thermometer (RTDs) are used to control intake air (28°C), cooling (82°C) and engine oil (82°C) temperature. The exhaust temperature was measured by using K-type thermocouple, placed in the exhaust pipe. Absolute pressure sensors are also used to measure the average pressure of the cooling water, engine oil, intake and exhaust air. All of these data are acquired via a PLC data acquisition instrument and transmitted via an Ethernet port to the control computer at the frequency of 10 Hz. In order to guaranty the safety of the installation different alarms are put on every measured data.

5.3 Engine operating

5.3.1 Stationary regime

'Stationary regime' concerns when engine operates at constant speed (revolution per minute, rpm) as 1000, 1200, 1400, 1600, 1800 and 2000 rpm. In the stationary cases, full load condition, i.e. the throttle is fully opened, was used.
To verify statistical convergence criterion, a recording of 600 cycles was done : the difference in average between 600 and 120 consecutive cycles for in-cylinder was obtained less than 1.35% bar and for intake and exhaust pressure less than 0.18% mbar along the cycle and the maximum of difference was obtained for 1000 rpm engine speed.
Therefore, all phase-average of the intake, in-cylinder and exhaust pressures for all regimes presented in Figure 5.4 are based on 120 cycles.

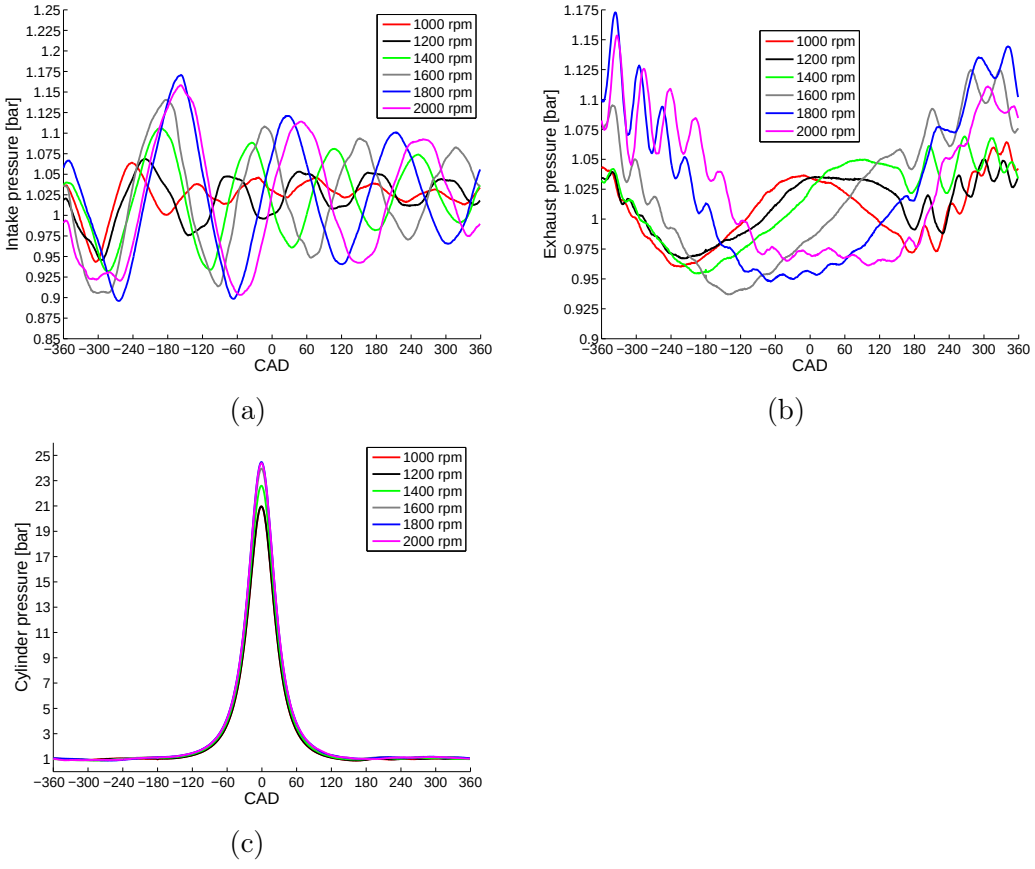

Figure 5.4: (a) Intake pressure, (b) Exhaust pressure and (c) Cylinder pressure as a function of CAD for different engine speeds in stationary condition.

As it can be seen in Figure 5.4a, fluctuations in intake pressure are present even at low regimes. The frequency decreases as function of the increase of regime but with an increase of the amplitudes. One important remark is that same order of fluctuations (frequency and amplitude) is obtained for 1800 and 2000 rpm. The same observation can be done with the exhaust pressure, Figure 5.4b different pressure evolution as function cad for 1800 and 2000 rpm than for the other ones. Exhaust pressure for 1000, 1200, 1400 and 1600 rpm engine speed is almost similar, evidently there are different pressure magnitudes and important offsets in their fluctuations. Therefore, 1800/2000 rpm pressure evolution are

inverse to 1000/1600 rpm during compression and combustion strokes, but these variations around atmospheric pressure are very low: less than 8%.
The evolution of in-cylinder pressure four different engine speeds is presented in Figure 5.4c, It is observed the maximum of in-cylinder pressure increases as function of the engine speed, Table 5.4 but the variations are in the same order that the fluctuations of the exhaust pressure: less than 7% due to the variations in the intake pressure itself. It has to be noted also that for the cases 1000/1200 rpm and 1800/2000 rpm have similar values.

Engine speed	P	Engine speed	P	Engine speed	P
1000	20.96	1400	22.61	1800	24.48
1200	20.98	1600	23.96	2000	24.39

Table 5.4: Cylinder pressure, bar about combustion TDC for different engine speed, rpm.

In Figure 5.5, the relative rms for intake, exhaus and in-cylinder pressure for different engine speeds as a function of CAD are presented.

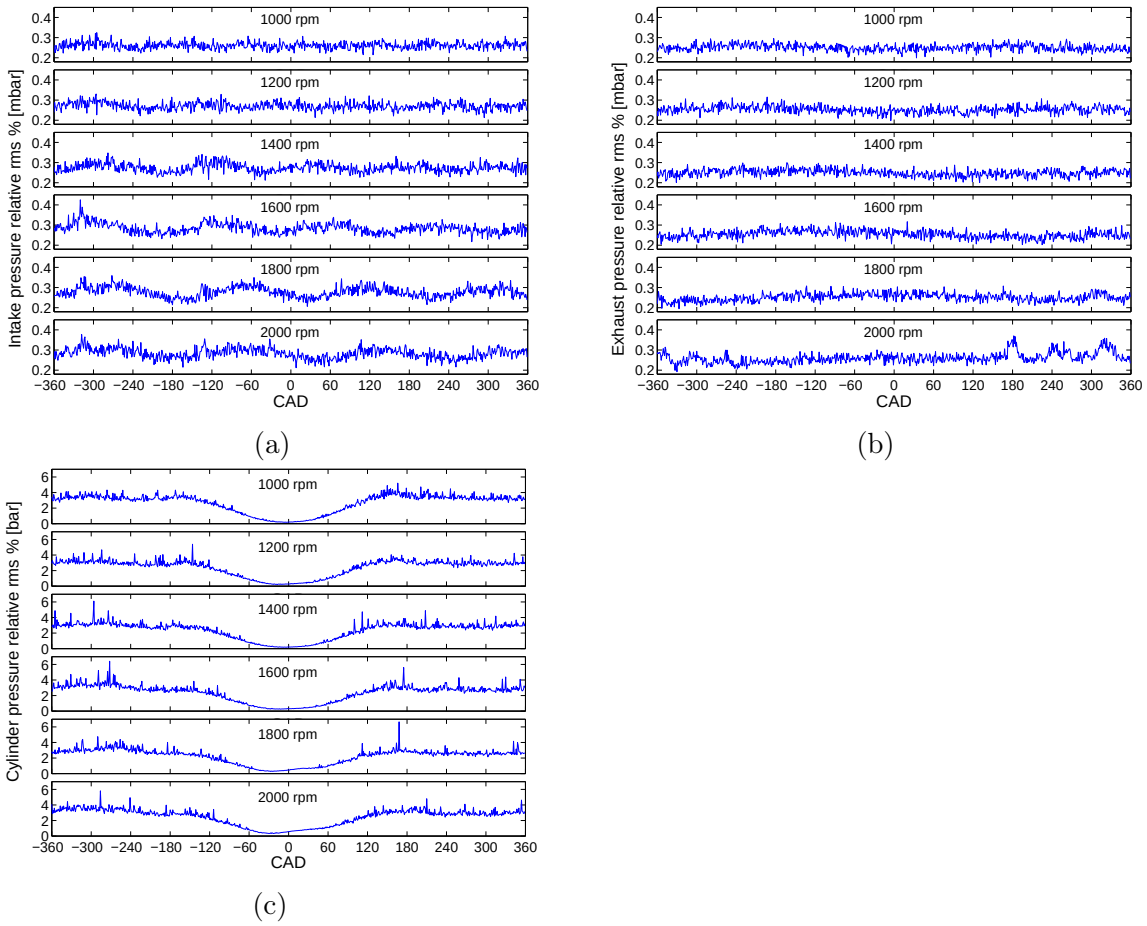

Figure 5.5: Relative standard deviation of intake pressure (a), exhaust pressure (b) and in-cylinder pressure (c) for all regimes.

5.3.2 Transient regime

For the transient conditions, the acceleration ramp of engine speed from 1000 rpm to 2000 rpm in different time periods: during 8 , 12, 16 and 21 cycles are considered, see Figure 5.6. Due to mechanical inertia, there is a delay between the command (called 'Set points') and the engine response ('Measured points'), reduced with the increase of the cycle number during transient regime.

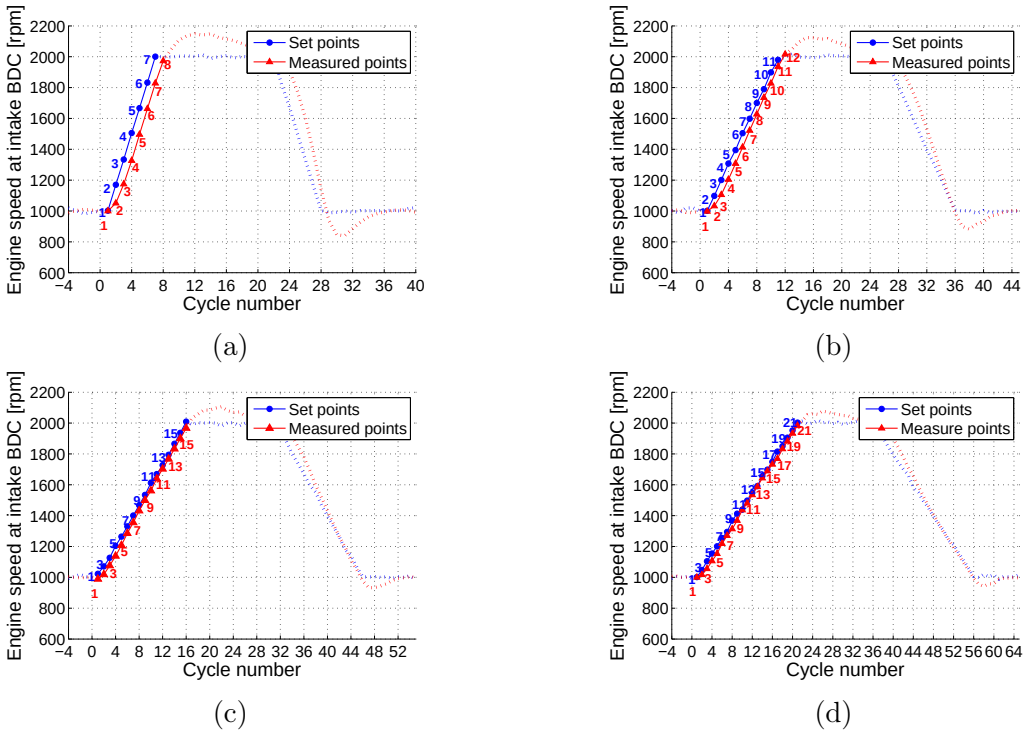

Figure 5.6: Engine speed variation as a function of the regime for transient conditions from 1000 rpm to 2000 rpm in: (a) 8 cycles, (b) 12 cycles, (c) 16 cycles and (d) 21 cycles. The first cycle of acceleration start from the cycle 1.

In Figure 5.7 for different transient conditions, the duration of each cycle is presented and then the entire duration of transient conditions as function of regime numbers are displayed in Table 5.5.

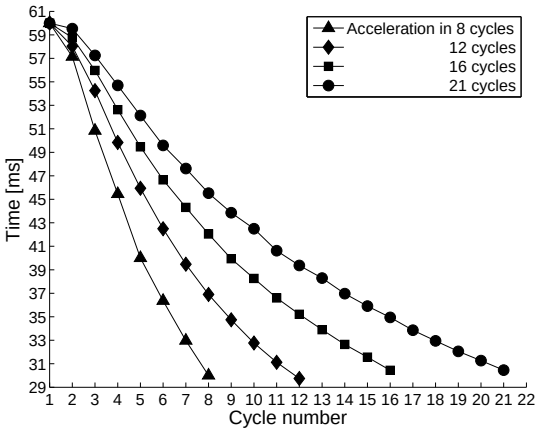

Figure 5.7: The period of each cycle in different transient conditions.

Acceleration	8 cycles	12 cycles	16 cycles	21 cycles
Transient duration [s]	0.352775	0.515298	0.688424	0.899366

Table 5.5: Duration of the acceleration phase.

In Figure 5.8 tevoultin of engine speed during the cycles of different transient conditions are presented. The engine acceleration start from the cycle 1, and the 0 CAD corresponds to combustion TDC. For all transient conditions, the cycle number in which engine speed at intake BDC corresponds to under studied stationary regimes are presented in Table 5.6.
In this study the focus is on the two extreme points, Fast transient condition(FT), engine acceleration from 1000 to 2000 rpm during 8 cycles, and Slow transient condition (ST) the one during 21 cycles. For these two condition the mean (based on 20 realizations) intake,exhaust and cylinder pressure are compared with ones in corresponding stationary regime in Figure 5.9 to Figure 5.11.

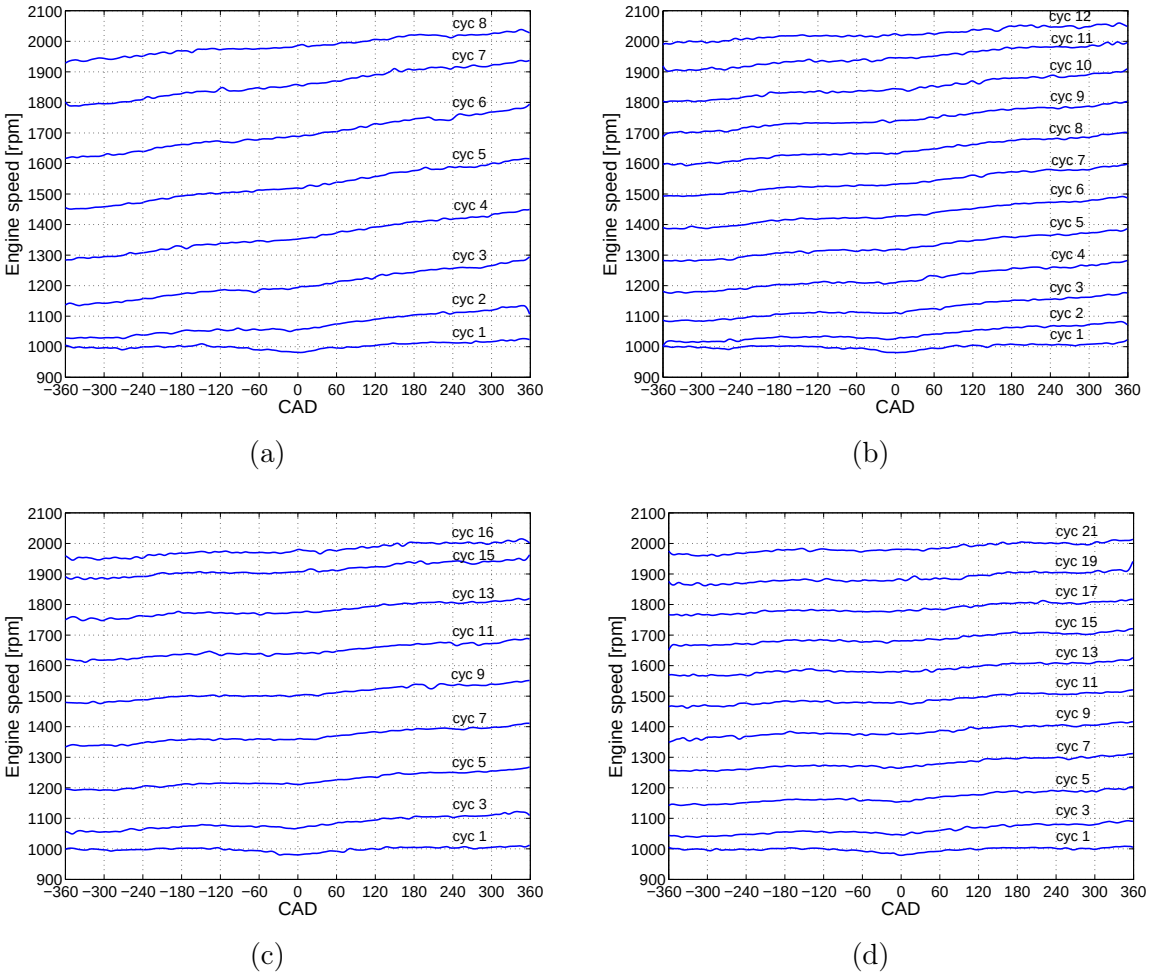

Figure 5.8: Engine speed variation as function of the regime for transient conditions from 1000 rpm to 2000 rpm in: (a) 8 cycles, (b) 12 cycles, (c) 16 cycles and (d) 21 cycles. The first cycle of acceleration start from the cycle 1.

Stationary condition [rpm]	Ramp 8		Ramp 12		Ramp 16		Ramp 21	
	Cycle number	Engine speed [rpm]	Cycle number	Engine speed [rpm]	Cycle number	Engine speed [rpm]	Cycle number	Engine speed [rpm]
1000	1	1000	1	1000	1	1000	1	1000
1200	3	1175	4	1205	5	1211	6	1215
1400	4	1330	6	1410	8	1428	10	1430
1600	6	1662	8	1625	11	1637	14	1630
1800	7	1830	10	1830	14	1837	18	1832
2000	8	1970	12	2015	16	1970	21	1980

Table 5.6: Engine speed at intake BDC of different cycles for transient regimes in comparison to stationary regimes.

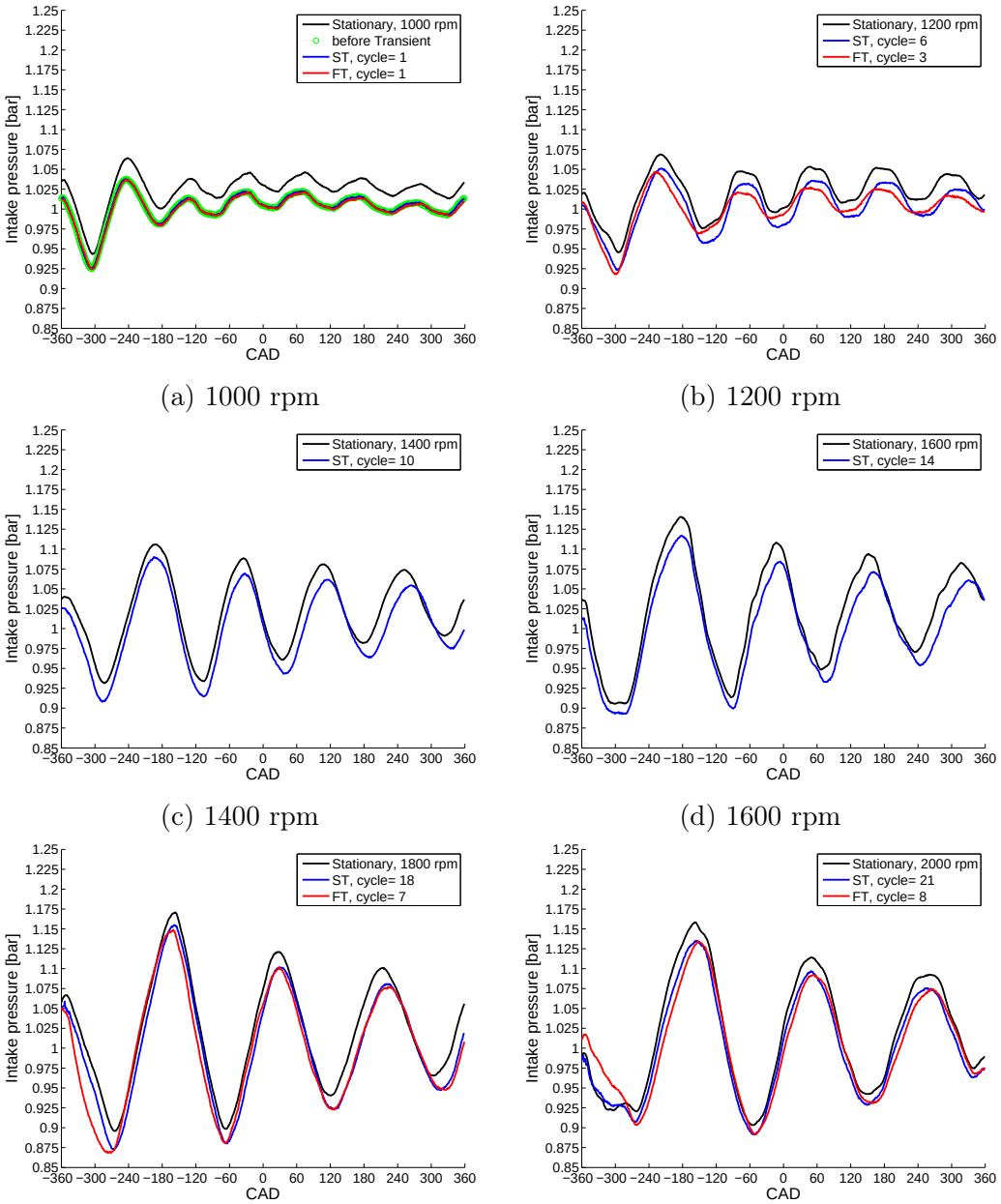

(a) 1000 rpm

(b) 1200 rpm

(c) 1400 rpm

(d) 1600 rpm

(e) 1800 rpm

(f) 2000 rpm

Figure 5.9: The intake pressure for transient conditions versus stationary regime for different engine speeds.

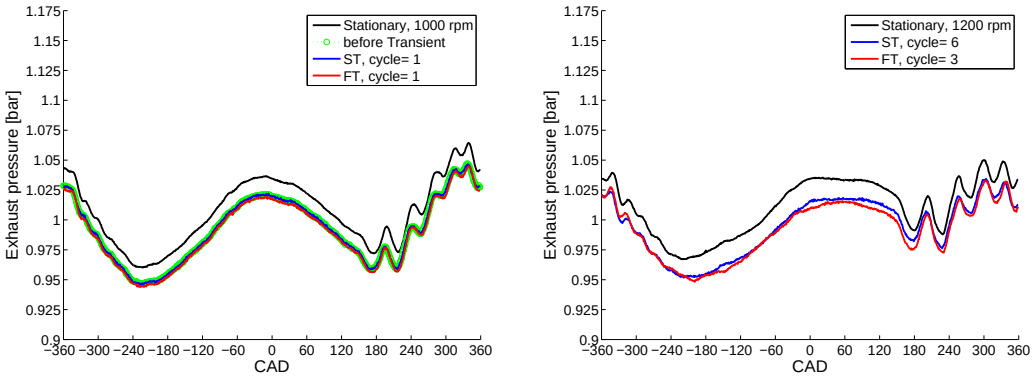

(a) 1000 rpm

(b) 1200 rpm

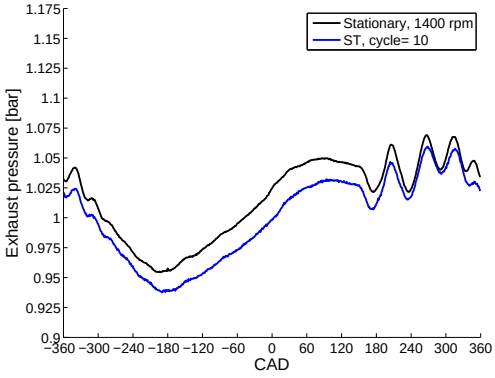

(c) 1400 rpm

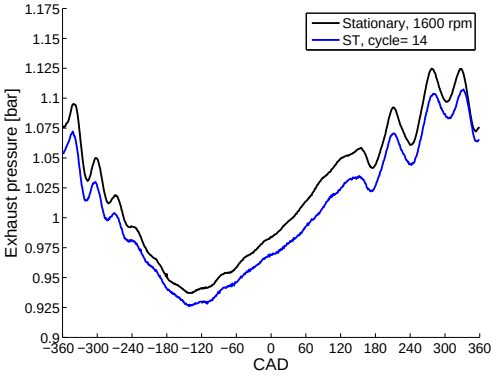

(d) 1600 rpm

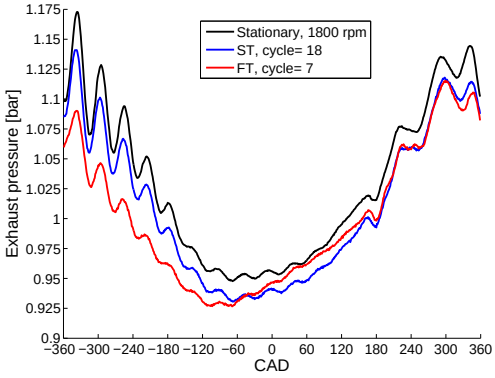

(e) 1800 rpm

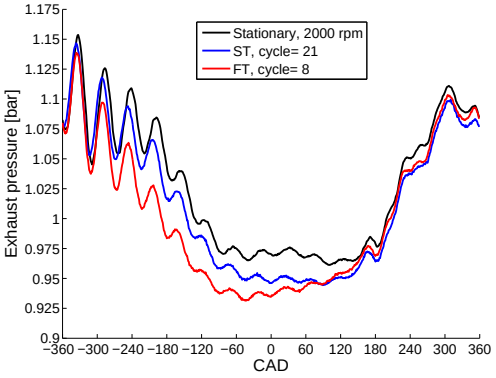

(f) 2000 rpm

Figure 5.10: The exhaust pressure for transient conditions versus stationary regime for different engine speeds.

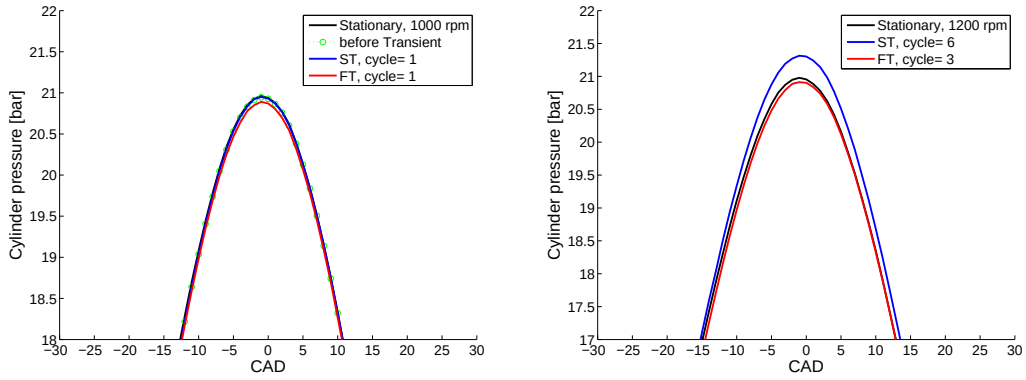

(a) 1000 rpm

(b) 1200 rpm

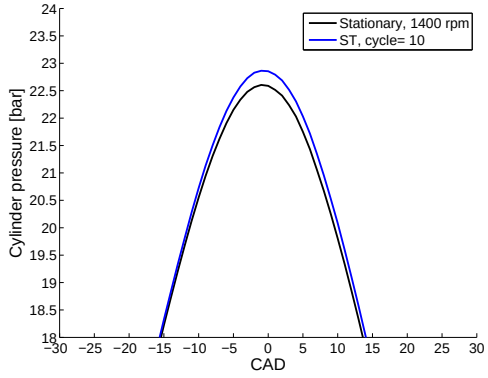

(c) 1400 rpm

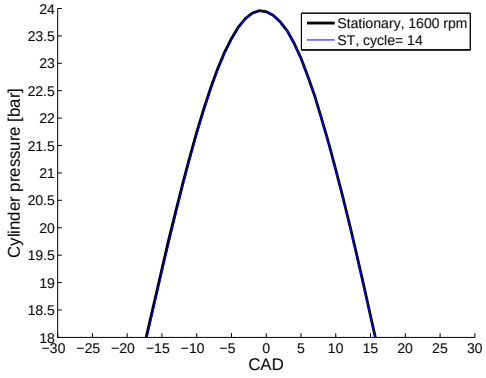

(d) 1600 rpm

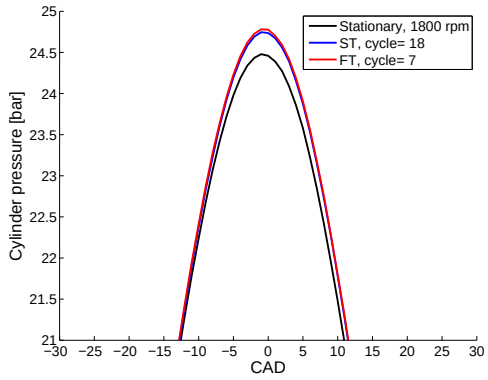

(e) 1800 rpm

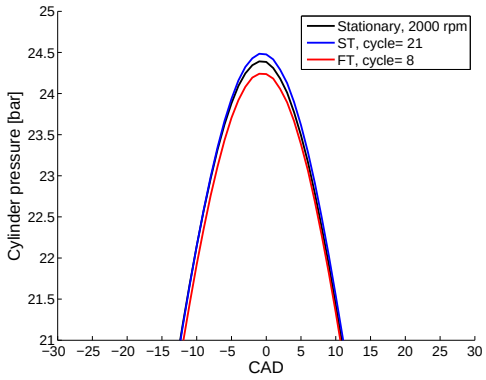

(f) 2000 rpm

Figure 5.11: The in-cylinder pressure for transient conditions versus stationary regime for different engine speeds, for obvious observation the zoom area are presented.

5.4 High speed Particle Image Velocimetry in engine

Particle image velocimetry (PIV) is a non-intrusive technique to measure two components of the velocity in bidimensional space, first introduced by Pickering & Halliwell (1984) [144], and Adrian (1984) [2].
The principle of this method is simple; to measure the displacement $\Delta\overrightarrow{X}$ of a fluid (gas or liquid) during a given time interval, Δt. The position of the fluid is imaged through the light scattered by particles illuminated by a laser light sheet. In most applications, such particles are not naturally present in the flow, so the flow has to be seeded with tracer particles, liquid or solid, by assuming to be sufficiently small and enable to follow the local flow velocity. Each image considered as a sum of small areas windows, so called interrogation windows. The local displacement of particles in each interrogation window between first and second image is computed by a spatial statistical cross-correlation function. Then, from the time interval between two laser pulses, the local flow velocity vector associated at these windows can be calculated by $\overrightarrow{V} = \Delta\overrightarrow{X}/\Delta t$ and attributed to the center of the interrogation window, Raffel et al. (2013) [148], Schröder & Willert (2008) [167], Feldmann & Mayinger (2012) [51].

Reuss et al. (1989) [158] is one of the first that applied PIV for measuring instantaneous in-cylinder flow velocity. Lee & Farrel (1993) [104] and Valentino et al. (1993) [184] employed PIV to study flow pattern around intake valves of CI engines.
Because of low repetition PIV, most of the studies were limited to one exposure per cycle (so result in statistically uncorrelated instantaneous velocity field) and then focused on the cycle to cycle variations of the instantaneous flow fields.
Objectives of several studies are to understand better the large motion in the in-cylinder flow as Reuss et al. (1995) [160], measured high-swirl flow, Brücker et al. (1997) [19] the generation of small-scale structures during compression stroke, by using scanning PIV for in-cylinder swirl motion. Freek et al.(1998) [60]) used film-PIV to examine the cycle-to-cycle variation of swirl flow motion in a five-valve motored engine cylinder. Reuss et al (2000) [157] by means of PIV studied cycle-to-cycle variation in the large-scale velocity structures of high and low-swirl in-cylinder flows. Funk et al.(2002) [63] focused their study on the possibility to measure the Reynolds-decomposed turbulence properties (kinetic energy, length scales, and dissipation rate) of high and low-swirl in-cylinder flow. Deslandes et al. (2003) [40] applied multi-planner PIV in compression ignition (CI) engine to characterize swirl motion. Reeves et al. (1999) [150] used a copper vapor laser with high-speed digital camera to provide high temporal resolution to measure two-component velocity data. Li et al. (2002) [107] used cycle-resolved PIV at swirl plane to study turbulent property and cycle-to-cycle variation of in-cylinder flow. Petersen & Miles (2011) [140] employed PIV in a motored light-duty diesel engine with realistic bowl geometries, for three swirl ratio at three different laser sheet planes during compression and power strokes. They observed the higher swirl ratios reduce the cyclic variability in the same plane of the structure.

Other investigations are more focused in-cylinder tumble flow; Reeves et al. (1994) [149] used PIV to characterize tumble flow during compression stroke, Baby & Floch (1997) [8] applied PIV to study effect of piston shape on tumble distortion, cycle-to-cycle variation and in-cylinder turbulent velocity field, they studied different configurations of curved

pistons in a four-valve engine. Rouland et al. (1997) [165] analyzed in cylinder tumble flow in motored four-valve engine during intake and compression strokes.
Marc et al. (1997) [119] combined LDV and PIV to study compressed tumbling motion and to analyze the characteristics of large and small-scale structures of the turbulent in-cylinder flow. Calendini et al. (2000) [23] used stereoscopic PIV in SI engine for a better understanding of the tumble motion during compression stroke. Pajot & Mounaïm-Rousselle (2000) [136] used PIV measurement to evaluate the influence of mean and instantaneous in-cylinder flow on flame kernel. Konrath et al (2002) [102] employed Holographic PIV to measure three-dimensional in-cylinder flow field with high spatial resolution. Li et al. (2004) [106] studied the large scale motion and turbulent properties of in-cylinder flow field in both tumble and swirl plans by means of digital PIV in a three-valve twin SI engine. Justham et al. (2006) [96] employed simultaneously two individual digital PIV system at the intake and in-cylinder flow fields of a SI engine. They studied the inter-relationship between them to analyze cycle-to-cycle variation phenomenon. Stansfield et al. (2007) [172] provided data on in-cylinder tumble motion at the end of intake stroke in a motored GDI engine for different realistic engine speeds (750, 2000 and 3500 rpm). Keromnes et al. (2010) [100] coupled PIV measurement and POD analysis to study impact of intake port flap on in-cylinder flow at tumble plane.
As well as Baby & Floch (1997) [8], Krishna & Mallikarjuna (2010) [103] used PIV measurement to study effect of piston crown shapes on the in-cylinder tumble flow during intake and compression strokes. As these studies progressed, it became clear that resolution throughout the cycle was necessary to better understand the evolution of in-cylinder flow and also to improve CFD models.

Due to the advancement in high speed camera and laser technology, studies are more and more on detailed flow field description at highest temporal and spatial resolution. Williams et al. (2003) [196] is one of the first to apply Time-Resolved PIV , also called High Speed PIV (HS-PIV), on the flow while interacts with the bluff body.
The crank angle resolved acquisition of PIV images allows the temporal study of in-cylinder flow field and consequently the assessment of the origin of cyclic variation flow field and of the turbulent flow. Tower and Tower (2004) [183] by means of HS-PIV analyzed the cyclic variability of in-cylinder swirl flow in a GDI engine. Druault et al. (2005) [43] combined HS-PIV measurement and POD analysis to study cycle-to-cycle variations of in-cylinder flow field in the tumble plane. Jarvis et al. (2006) [95] used this method, to quantify the velocity field development from tumble motion during the intake and compression stroke at a SI engine. Cosadia et al. (2006) [32] used HS-PIV in a CI engine to study cycle-to-cycle variation of in-cylinder swirl flow, this study focused on the middle and end of compression stroke. Muller et al. (2010) [125] used HS-PIV to measure in-cylinder flow field velocity at the tumble plane over different speed ranges of a direct-injection spray-guided engine. They measured velocity field from middle to end of compression stroke. Voisine et al. (2011) [188] combined PIV and HS-PIV to study in-cylinder flow spatial structure, its temporal evolution during consecutive cycles and also the cyclic variations. Fajardo & Sick (2007) [49] developed the high-speed UV PIV and applied it to a DISI engines in stratified mode to evaluate the instantaneous velocity flow near the spark plug evolution from fuel injection to flame propagation.
Peterson & Sick (2009) [142] also employed HS-PIV and planar laser induced fluorescence simultaneously in spray-guided DISI engine to correlate flow velocity and fuel concentra-

tion near the spark plug during spray and ignition event.

Buschbeck et al. (2012) [22] assessed the influence of in-cylinder aerodynamic on fuel spray development by applying HS-PIV in a SI engine. In other study by using this method, Zegers et al. (2012) [209] investigated the impact of full injection on in-cylinder swirl flow in a heavy-duty diesel engine. Stiehl et al. (2013) [175] used HS-PIV and Mie scattering of fuel droplets in a spray-guided DISI engine in order to study the influence of spray on in-cylinder tumble flow and cycle-to-cycle variation. They reported that spray induces some vortices to the initial in-cylinder air motion, which significantly perturb tumble motion. Stiehl et al. (2016) [174] investigated the impact of intake port geometry variations on in-cylinder flow and flow-spray interaction in a DISI engine that operated in stratified combustion mode.
Peterson et al. (2011) [140] and Mounaïm-Rousselle et al. (2013) [124] studied the flame development during engine combustion stroke by means of HS-PIV. Peterson et al. (2013) [139] applied simultaneously HS-PIV and HS-LIF in a motored SI engine to study the temporal evolution of 2D temperature field during the compression and expansion strokes. Zha et al. (2015) [210] characterized the azimuthal asymmetry of swirl flow during full compression stroke in a light-duty diesel engine with a realistic bowl geometry.

Recently more sophisticated optical diagnostics were performed on in-cylinder flow that provides the information about the volumetric instantaneous velocity flow field as Dannemann et al. (2011) [37]. They measured the three dimensional structure of the in-cylinder velocity field by using multi-planner PIV (eight vertical planar planes within the cylinder) in SI engine. They analyzed spatial distribution of the large and small scale flow structure at several crank angles during intake and compression strokes. Bücker et al. 2012) [20] used stereoscopic-PIV (2D3C) to measure in-cylinder tumble flow in a motored DISI engine, they obtained velocity field within a set of 14 axial planes at 15 crank angles during intake and compression stroke.
Baum et al. (2013) [9] used Topographic-PIV (3D3C) in DISI engine to study the turbulent property and vortical structures of 3D in-cylinder flow. Peterson et al (2012) [143] presented single camera three-dimensional particle tracking velocimetry (SC3D-PTV) that can be used in the configuration with limited optical accesses in order to measure 3-components of velocity field, following this study Chen & Sick (2017) [28] employed plenoptic particle tracking velocimetry to measured three-dimensional and three-component in-cylinder flow 3D3C PTV. Van Overbruggen et al. (2014) [185] applied holographic PIV in engine flow to resolved the complete three-dimensional velocity field. Bode et al. (2017) [14] used dual-plane HS-PIV in a fired spray-guided DISI engine that operated in stratified fuel/air mixture conditions. They studied the influence of three-dimensional in-cylinder tumble flow on spray and combustion cyclic variations.

This study is focused on the in-cylinder non-reactive flow and the velocity fields were measured by HS-PIV (2D2C) in vertical plane for all conditions: stationary and transient regimes.

5.4.1 Set up

HS-PIV 2D2C (Bidimensions-Bicomponents) measurements were performed within the symmetric axial plane (tumble plane), as shown in Figure 5.12. The spark plug is considered as the origin of the coordinate geometry and the distance between the spark plug and the top of the laser sheet is 11.19 mm.
Two second harmonic Laser beams from a Dual-Hawk-HP (Quantronix) laser pass through a set of spherical lenses (Semi cylindrical and Plano-convex lenses), to generate a vertical laser sheet across the middle of optical cylinder. The thickness of laser sheet was adjusted to about 1 mm diameter.
A V1610 Phantom CMOS camera with a 200 mm Nikkor macro lens was used with the aperture f# of 8. The full resolution is 1280×800 $pixels^2$ and the field of view in the tumble plane 55.81×75.65 mm^2 so the magnification ratio was set to 77.52 $\mu/pixel$.

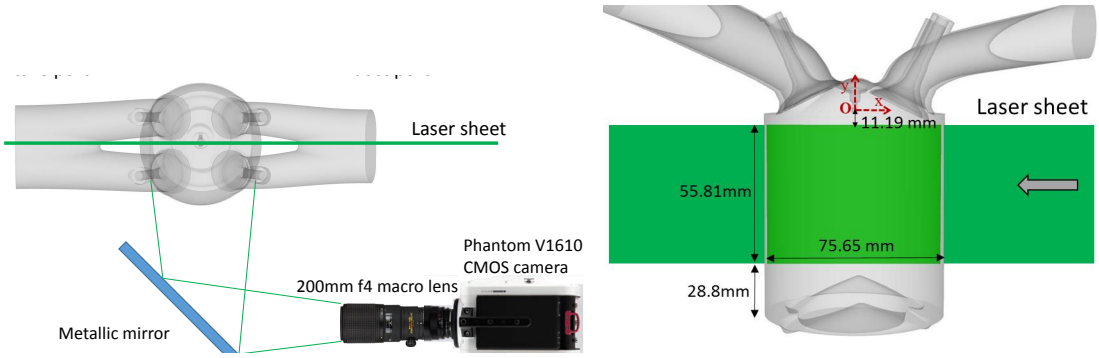

(a) (b)

Figure 5.12: (a) Scheme of PIV set-up, top view, (b) Laser sheet is positioned within the tumble plane at the central axis of the engine cylinder.

The crank-angle encoder (3600 pulses/revolution) was used to synchronize laser and camera to the engine via Lavision High Speed Controller. The inter-pulsed time between both laser pulses was optimized at 10 μs, the laser has a repetition rate up to 8 kHz and a pulse energy of 11 mj.
The temporal resolution of the velocity fields is proportional to the engine speed. So for 1000, 1200 and 1400 rpm engine speed, the instantaneous in-cylinder velocity fields were acquired at each CAD and for 1600, 1800 and 2000 rpm, each 1.5 CAD in the case of stationary or transient modes. 120 consecutive cycles were recorded from 45 CAD ATDC during the intake stroke to 45 CAD BTDC during the compression stroke.

5.4.2 Seeding constraints

Solid microsphere Expancel particles with $d_p = 20\ \mu m$ mean diameter and density of $\rho_p = 70\ kg.m^{-3}$ were used. Similar kinds of seeding particle were previously used by Zegers et al. (2012) [209], Towers and Towers (2004) [183], Nordgren et al. (2003) [128] and Ekenberg et al. (2001) [46]. This type of particles is interesting due to its high temperature resistance and Mie scattering cross section.
The seeding particles were injected directly inside the port before the throttle by means of a cyclone aerosol generator, as Melling (1997) [121]. The pressure drop between the inlet and outlet of cyclone was set to 0.5 bar to optimize seeding density around 10 particles in the final interrogation window.

The particles relaxation time $\tau_p = (\rho_p.d_p^2)/(18\mu_a)$, with μ_a is the air dynamic viscosity, compared with different fluid time scales in order to evaluate how those tracers can follow different scales of in-cylinder fluid motion. The variation of air viscosity during compression stroke was considered by Sutherland's law given as, White (1979) [193]:

$$\frac{\mu_a}{\mu_o} \approx \left(\frac{T_a}{T_o}\right)^{3/2} \left(\frac{T_o + T_s}{T_a + T_s}\right)$$

Where μ_0 is a known viscosity at a known absolute temperature, usually $T_o = 273.15\ K$, $\mu_o = 1.711 \times 10^{-5})\ kg/m.s$ and Sutherland Temperature $T_s = 110.4\ K$. T_a can be calculated by isentropic ideal gas relation.
The Stokes number is defined as $St = \tau_p/\tau_f$ where τ_f is the corresponding fluid time scale. In our experiments, maximum of St would be obtained at 2000 rpm.

- The engine time scale, τ_e, is calculated by $S/\overline{U}_p$, where S is the piston stroke and $\overline{U}_p$ is the mean piston speed.
- $\tau_T = 2/\omega_t$ is the time scale corresponds to the mean tumble turn-over, where $\omega_t = R_t.\omega$, the angular velocity of the equivalent solid body rotation of the instantaneous flow velocity, R_t the tumble ratio and ω the angular velocity of the crankshaft.
- The turbulent turn-over time scale is defined by $\tau_{turb} = L/u'$, where L is the size of most energetic eddies and u', an order of magnitude of the rms of the turbulent velocity fluctuation of these eddies. One estimation can be done from Lumley (1999) [115] as function of CAD as presented in Table 5.7, with b, cylinder bore and h, the clearance height.
- The small eddies turn-over time scale is defined as $\tau_\Delta = \tau_{turb}\left(\frac{\Delta}{L}\right)^{2/3}$, where Δ is the size of the smallest observed turbulent structure which corresponds to the PIV interrogation window, set in this study at 1.24 mm.

These different time scales are compared to particle response times in Table 5.7, at different CAD in the cycle. The particle response time is inferior to the engine, the mean tumble turn-over and the turbulent turn-over time scales of fluid at different CAD. Hence $St \ll 1$ that confirms the seeding particles be able to follow these fluid scales. The fluid time scale for the small eddies has the same order of magnitude as the particle relaxation time at 90 CAD bTDC, it means the particles are not able follow this scale but as mentioned before, this work is not related to that.

CAD	L	u'	τ_p $[s]$	τ_e $[s]$	τ_T $[s]$	τ_{turb} $[s]$	τ_Δ $[s]$
90	$b/6$	$10\overline{U}_p$	8.43×10^{-5}	1.5×10^{-2}	1.5×10^{-5}	2.24×10^{-4}	4.72×10^{-5}
180	$b/6$	$\overline{U}_p$	8.43×10^{-5}	1.5×10^{-2}	1.5×10^{-5}	2.24×10^{-4}	4.72×10^{-4}
270	$b/6$	$\overline{U}_p/2$	7.16×10^{-5}	1.5×10^{-2}	1.5×10^{-5}	4.48×10^{-3}	9.45×10^{-4}
360	$h/6$	$\overline{U}_p/2$	4.43×10^{-5}	1.5×10^{-2}	-	5.82×10^{-3}	-

Table 5.7: Particle relaxation time and characteristic flow time scales for specific CAD bTDC.

5.4.3 PIV Processing

The laser light reflection from cylinder walls is one drastic drawback in the case of optical cylinder use. After crossing the cylinder thickness, some reflections accrue at the outer wall, all of these multiples reflections reduce drastically the PIV image quality. To overcome this problem, an abrasive blasting treatment was done on the inner cylinder wall as well as the outer one. Its benefit can be seen in Figure 5.13. Moreover, a polarizing filter was added front of camera lens.

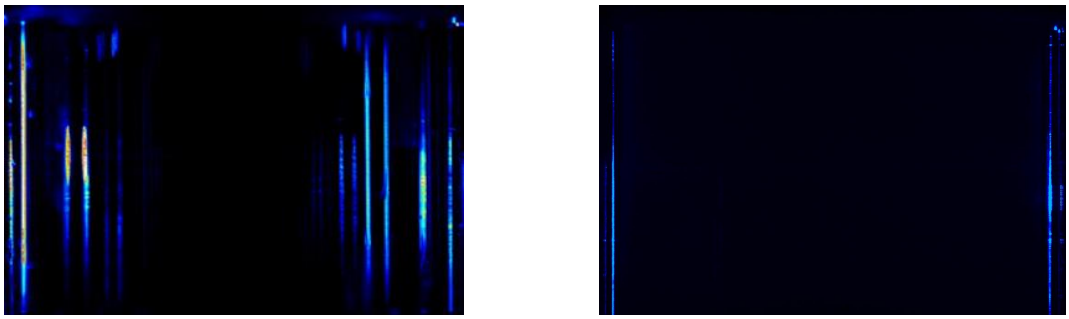

(a) (b)

Figure 5.13: (a) Initial image, (b) Image after abrasive blasting treatment.

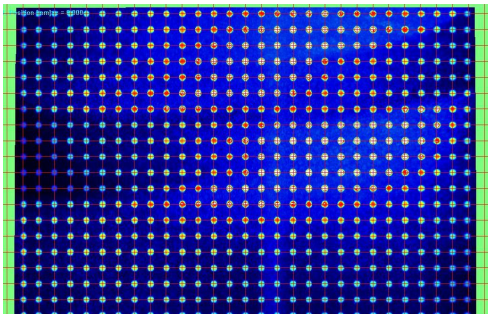

Figure 5.14: Target image used for calibration.

To calibrate the PIV measurement, a spatial target shown in Figure 5.14, of 31 points in horizontal direction and 24 points in vertical direction, with an inter-distance between

the points of 2.53 mm is placed at the center of cylinder systematically before each series of measurements. The calibration root mean score fit error is less than 0.8.
In order to suppress high intensity fluctuations in images and provide homogenous intensity, the images are normalized with a filter of 4 pixels length to remove the background noise.

The velocity vectors are calculated by Cross-correlation with multi-pass iteration decreasing window size, as described Raffel et al. (2007) [36]. The two first passes are of 64×64 pixels and the following two passes of 32×32 pixels with 50% window overlap, so consequently these HS-PIV 2D2C measurements resolved the velocity field within 61×45 vector points with 1.24 mm spatial resolution.
The final pass is calculated adaptively in which the shape and size of interrogation windows change according to the flow gradient and seeding density, that leads to more accurate special resolution in region of high flow gradients, as suggested Wieneke & Pfeiffer (2010) [194] and Theunissen et al. (2010) [180]. In Figure 5.15, as an example, one of the double-frame of the particles image with related calculated velocity vector field before post-processing step are shown.

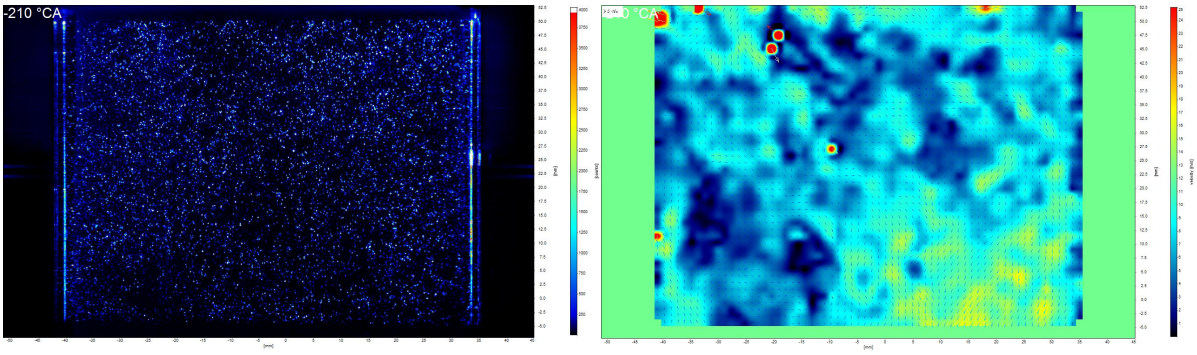

(a) (b)

Figure 5.15: (a) Particles image, (b) Calculated velocity vector field before post-processing.

To remove spurious vectors, the criterion of peak ratio of 1.8 was used. These vectors were replaced by means of median filter operation of 3×3 neighboring pixels as Westerweel et al. (1994) [192]. In order to avoid the modification of flow structure no further vector post-processing was performed. Usually, the synchronization between the laser pulses and camera in stationary regime is simple but in the transient regime considerable effort were carried out for grabbing the correct PIV images while the engine accelerate.

Chapter 6

Results

6.1 Flow pattern observation

In order to assess the influence of engine speed acceleration on the mean flow spatial structure and its temporal evolution during the cycle, the mean flow patterns within the symmetry plane (i.e tumble plane) in transient conditions are compared to the ones in stationary regime. As a reminder, the piston head is a non-symmetrical pent roof shape with a central dish. The coordinate origin $\mathbf{O}(0,0)$ is set at the spark-plug location. The distance between the top of the measurement plane and the origin is 11.19 mm and the distance between bottom of it and physical BDC is 28.8 mm, as presented in Figure 6.1.

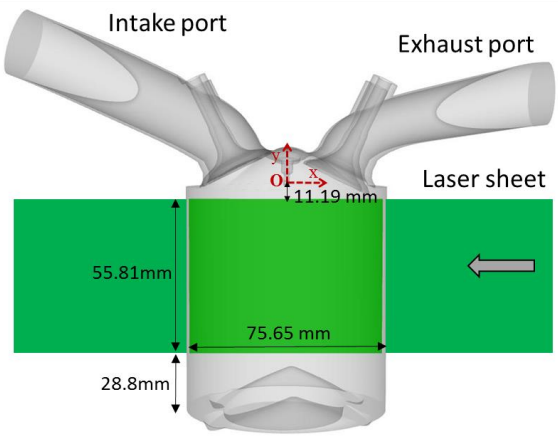

Figure 6.1: Position of velocity measurement plan.

In stationary conditions, the phase-averaged velocity $U_{EA}(\theta) = \frac{1}{N}\sum_{i=1}^{N} U(\theta, i)$ is computed from $N = 120$ instantaneous cycles. In the case of transient conditions, the acceleration is only repeated 20 times and the phase-averaged velocity fields are computed from the similar cycles during acceleration i.e. the phase-averaged velocity for k^{th} cycle during acceleration in K consecutive cycles is defined as $U_{k,EA}(\theta) = \frac{1}{20}\sum_{i=1}^{20} U_k(\theta, i)$. Two engine regime transient conditions are studied : the acceleration from 1000 to 2000 rpm realized during 21 cycles i.e. Slow transient condition (ST) and 8 cycles i.e. Fast

transient condition (FT). In each following figure, the phase-averaged velocity fields for both transient conditions are compared to those of the corresponding flow-fields obtained for stationary conditions corresponding to the same engine regime when it is possible, as shown in Table 6.1.

Stationary condition	Transient in 21 cylces (ST)		Transient in 8 cylces (FT)	
[rpm]	Cycle number	Engine speed [rpm]	Cycle number	Engine speed [rpm]
1000	1	1000	1	1000
1200	6	1215	3	1175
1400	10	1430	-	-
1600	14	1630	-	-
1800	18	1832	7	1830
2000	21	1980	8	1970

Table 6.1: Engine speed at intake BDC of different cycles for transient regimes in comparison to stationary regimes.

6.1.1 Recirculation zone under intake valves

In the early of intake stroke, a small recirculation region located under intake valves develops, both for transient or stationary conditions. To better observe that, only half of the field of view is presented in Figure 6.2. Indeed the outflow from the lowest portion of the intake valves after impacted on the piston head, is redirected toward the cylinder head and results in the generation of a clockwise recirculation zone.
It must be mentioned the inlet valve begins to open from 23 CAD before intake stroke (383 bTDC). Such a recirculation is observed from 316 CAD bTDC in this experimental Field of View (FOV) and while the piston goes down, and at the same time, the inlet valves are more lifted, the ring vortex becomes more stretched and disappears after 300 CAD bTDC for all conditions.
Since the velocity field in the clearance volume is out of FOV, one cannot precisely justify beyond this CAD if the structure of the ring vortex is dissipated or it moves up toward the intake valves. However, due to more lift of the inlet valves, it is expected the inlet jet will break up this vortex structure.

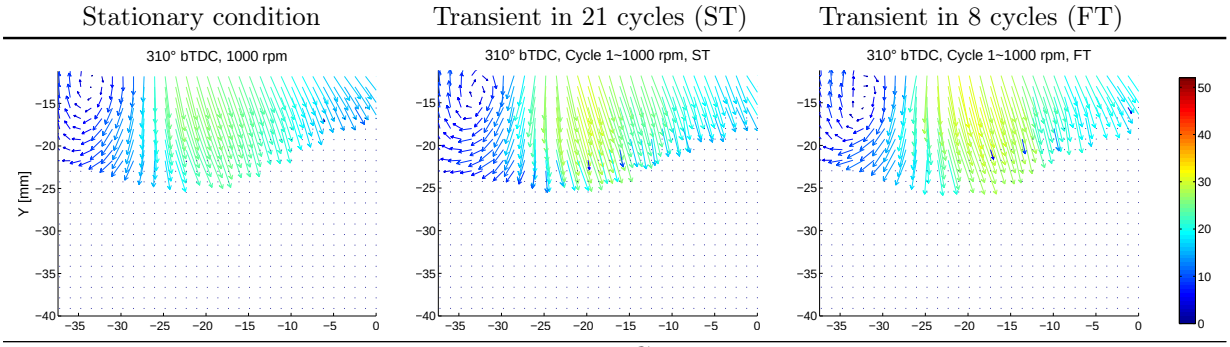

Figure 6.2, *Cont.*

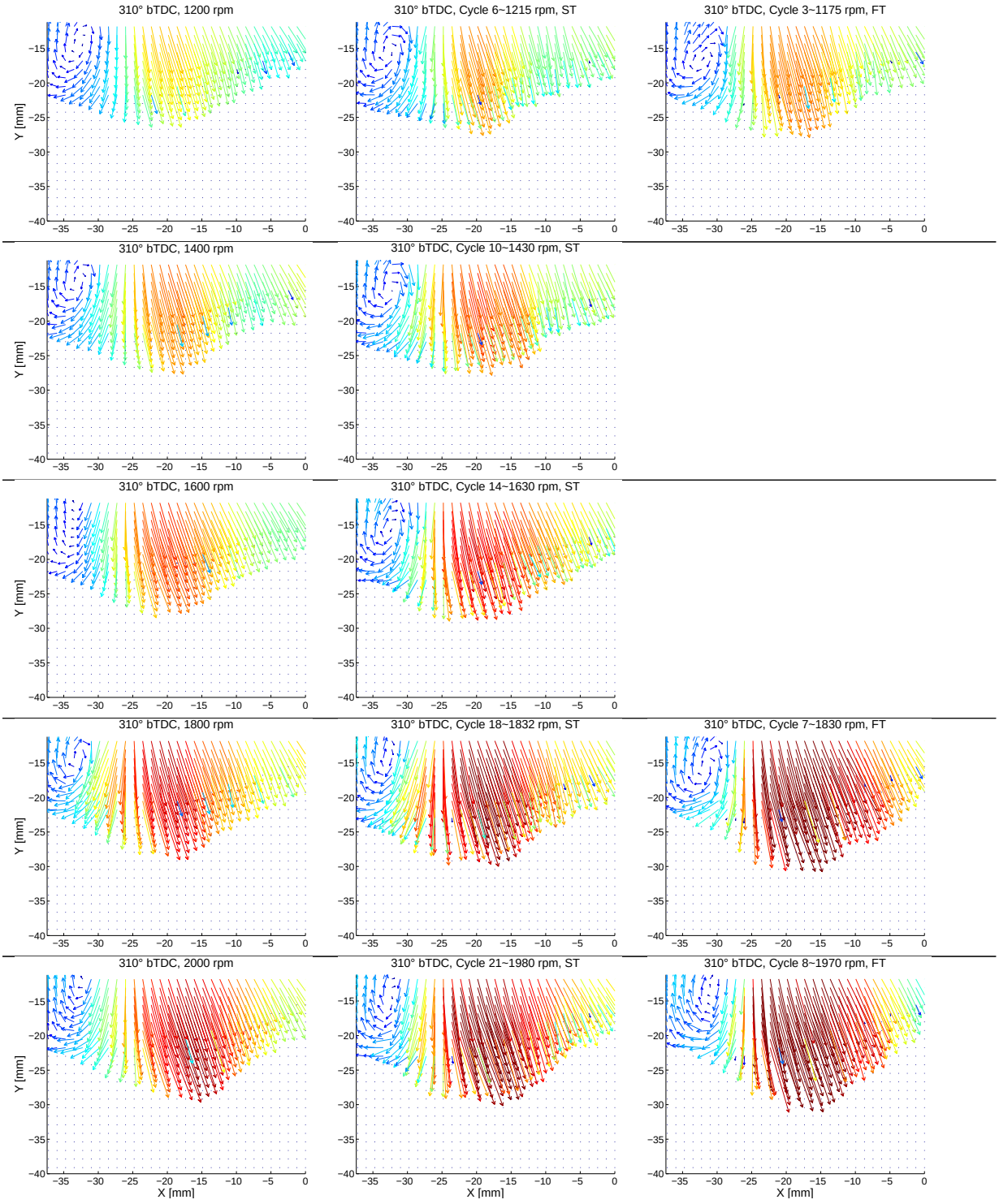

Figure 6.2: Phase-averaged velocity fields for transient conditions at different regimes, compared to stationary conditions at 310 CAD bTDC.

6.1.2 At 290 CAD bTDC

As one can see in Figure 6.3 the increase of the engine speed (controlled in stationary conditions or not in transient ones) accentuates the inlet flow deviation toward the cylinder axis, both in stationary condition as well as transient ones. This deviation is dominated by the intake valves position, their lifting level and engine speed. The intake valves reach their peak lift at 267 CAD bTDC. The edge of flow deviation in transient condition is sharper than the stationary one and the flow deviation itself is more abrupt in fast transient condition (i.e. acceleration in 8 cycles) compared to slow transient ones (in 21 cycles). In the case of higher engine speed, the angle of this deviation seems to be smaller for both stationary and transient conditions.

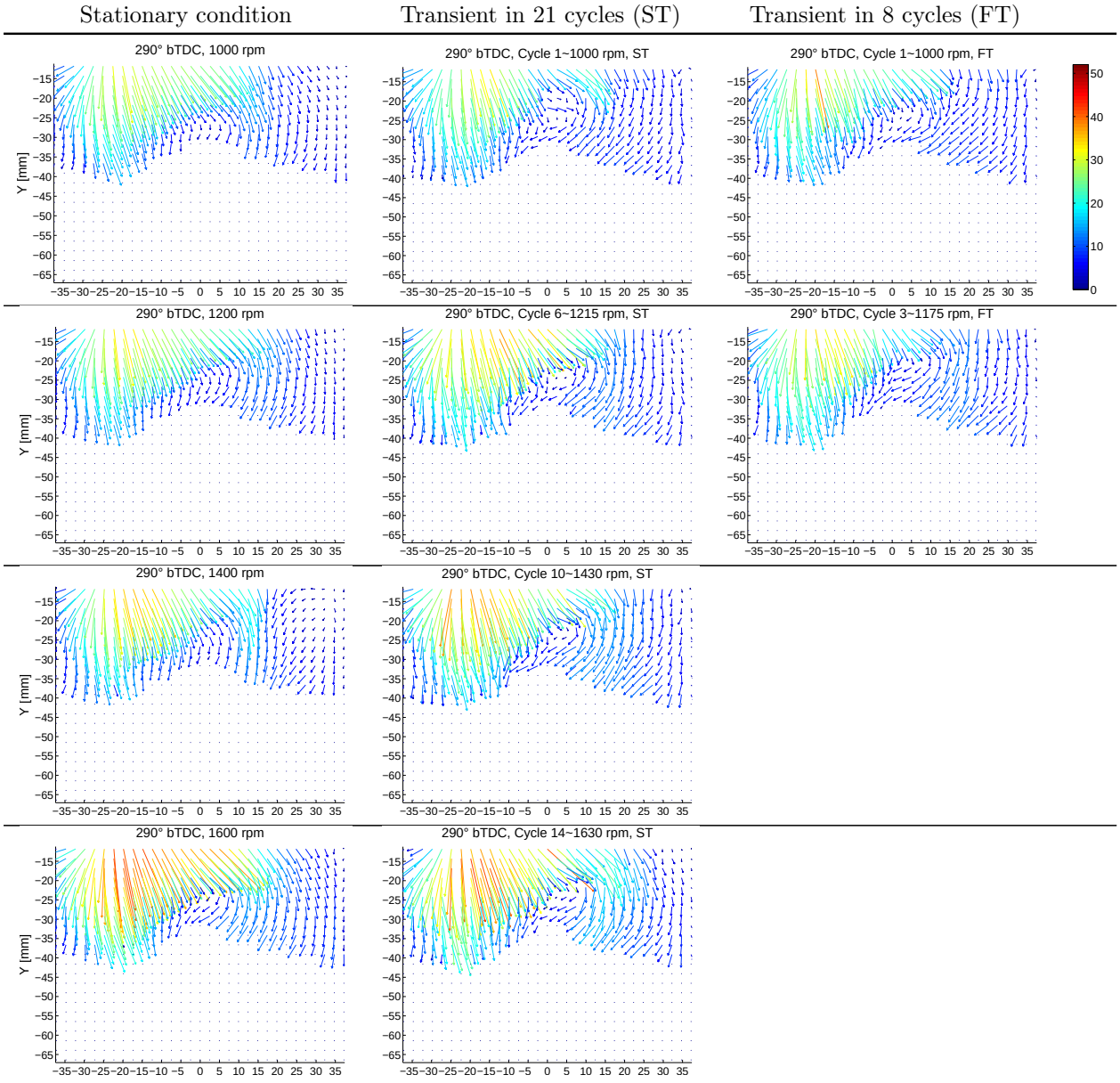

Figure 6.3, *Cont.*

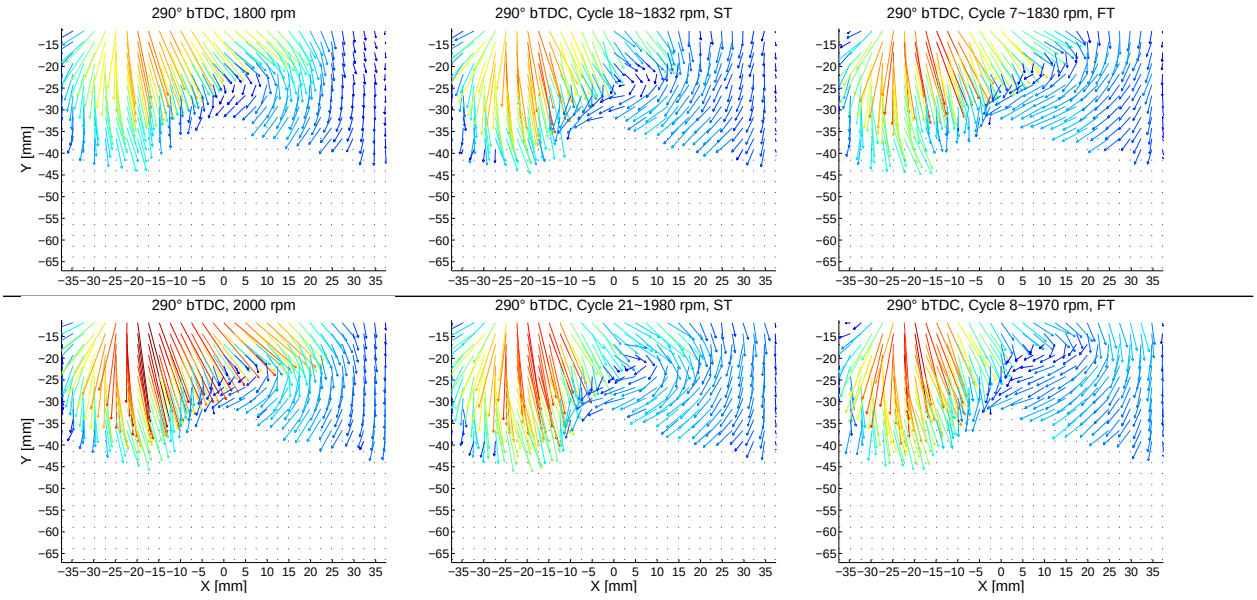

Figure 6.3: Phase-averaged velocity fields for transient conditions at different regimes, compared to stationary conditions at 290 CAD bTDC.

6.1.3 Appearance of the strong tumble motion

In Figure 6.4, the mean velocity fields obtained at the first appearance of the Tumble for each case are plotted. As one can see the flow is guided above the intake valves, at upper-left corner of the measurement plane, and the direction of the in-cylinder mean flow is clockwise. One can notice such a flow recirculation differs from above mentioned rumpled area due to the inlet flow deviation toward the cylinder axis. Globally, at one given engine speed, such a phenomenon take places earlier in transient conditions than in stationary ones, especially in the case of fast acceleration condition. At the highest engine speed, i.e. 2000 rpm, the complete circulation at the vortex core is accomplished almost at the same CAD for stationary and transient conditions.

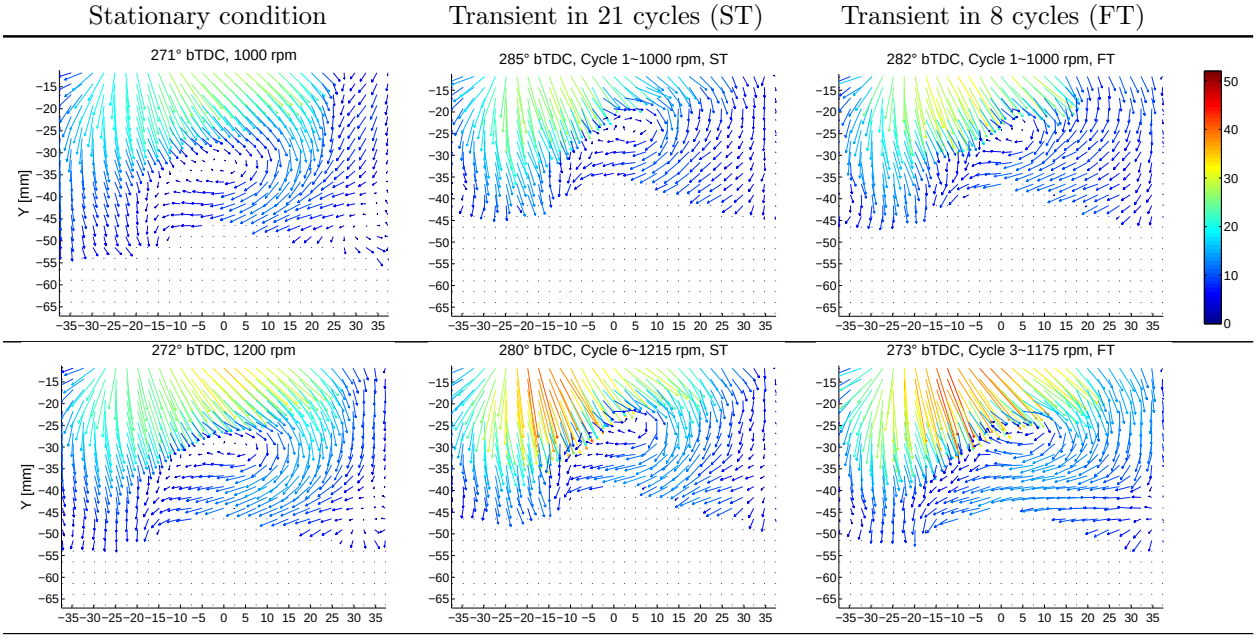

Figure 6.4, *Cont.*

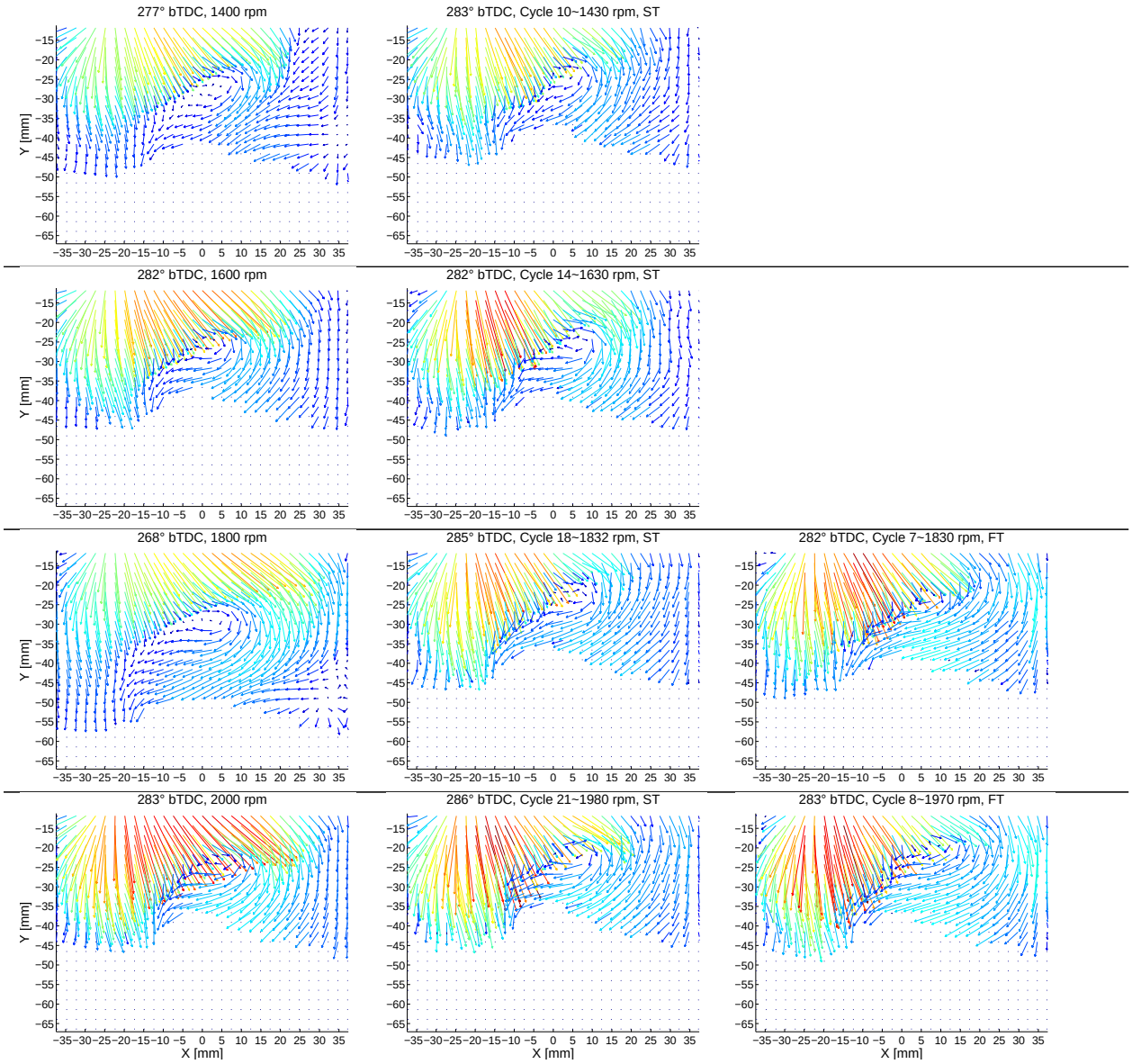

Figure 6.4: Phase-averaged velocity fields for transient conditions at different regimes, compared to stationary conditions at the CAD when the full Tumble motion can be discerned.

In Table 6.5 the CAD when first, a complete recirculation zone in the mean flow velocity field appears is given for different engine speeds in stationary and transient conditions. For this first estimate, only a visual determination of the moment in which the streamlines in the core of the in-cylinder mean flow recirculate entirely was used.

Engine speed [rpm]	Stationary condition	Transient in 21 cycles	Transient in 8 cycles
1000	271	282	285
1200	272	273	280
1400	277	283	-
1600	282	282	-
1800	268	282	285
2000	283	283	286

Table 6.5: Corresponding CAD when Tumble center is discernible for all conditions.

6.1.4 At mid-intake stroke

The global pattern of the in-cylinder mean flow at the mid- intake stroke (270 CAD bTDC) when the intake valves are fully opened, is approximately similar in transient and stationary conditions, as it can be seen in Figure 6.27.

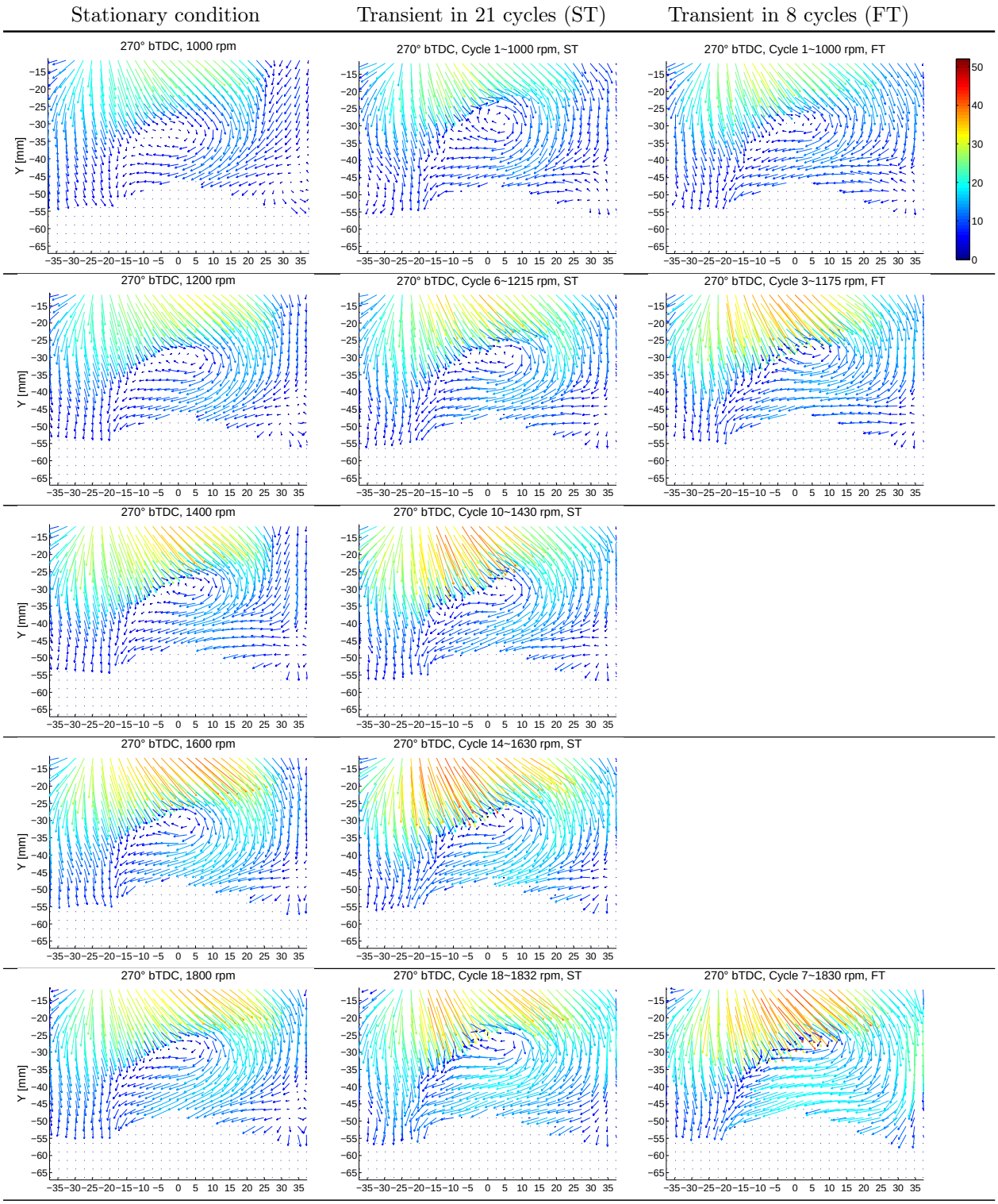

Figure 6.27, *Cont.*

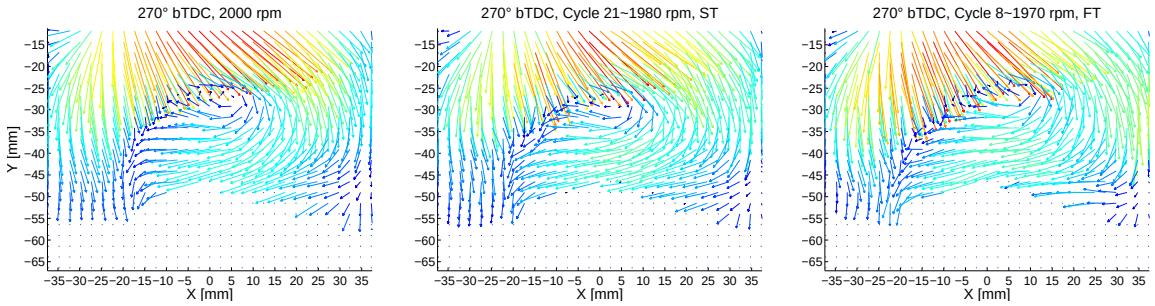

Figure 6.5: Phase-averaged velocity fields for transient conditions at different regimes, compared to stationary conditions at mid-intake stroke.

In this CAD, the flow structure is dominated by the flow due to the intake valves jet and the piston motion. The center of rotational mean flow is obvious in all cases, the jet downward momentum flux, the jet-piston interaction and the piston velocity affect its location.
The center of the tumble seems to be closer to the spark plug when the speed is higher. As an example, the distance between the mean flow center and spark-plug is about 33 mm in 1000 rpm engine speed, whereas it is about 26 mm for 2000 rpm, but it is globally centered in the cylinder bore. The inlet jet flow becomes closer to the right-hand side of the cylinder with the increase of the engine speed and this feature is more prominent in transient conditions.

6.1.5 At BDC - The generation of a second vortex

At compression BDC, 85% of the intake valves are already closed. As can be observed in Figure 6.6, for all conditions, the mean tumble vortex is centered on the lower-left side of the cylinder. A downward flow motion at the right side of the engine cylinder, near the wall in all engines speeds is at this CAD, clearly visible.

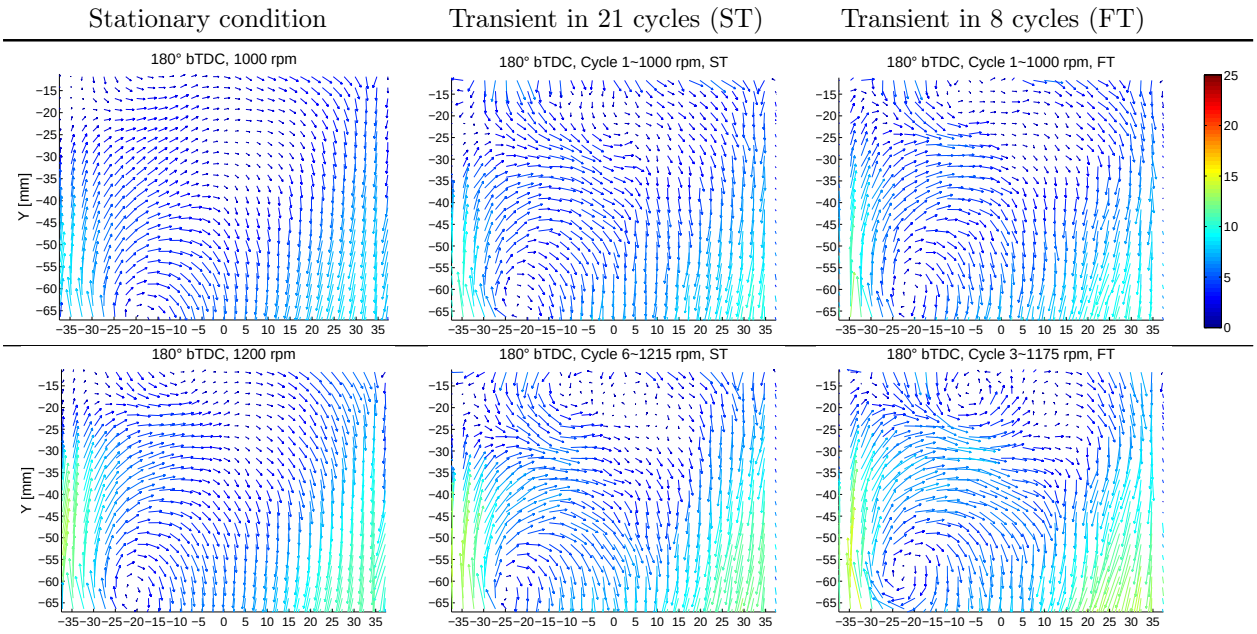

Figure 6.27, *Cont.*

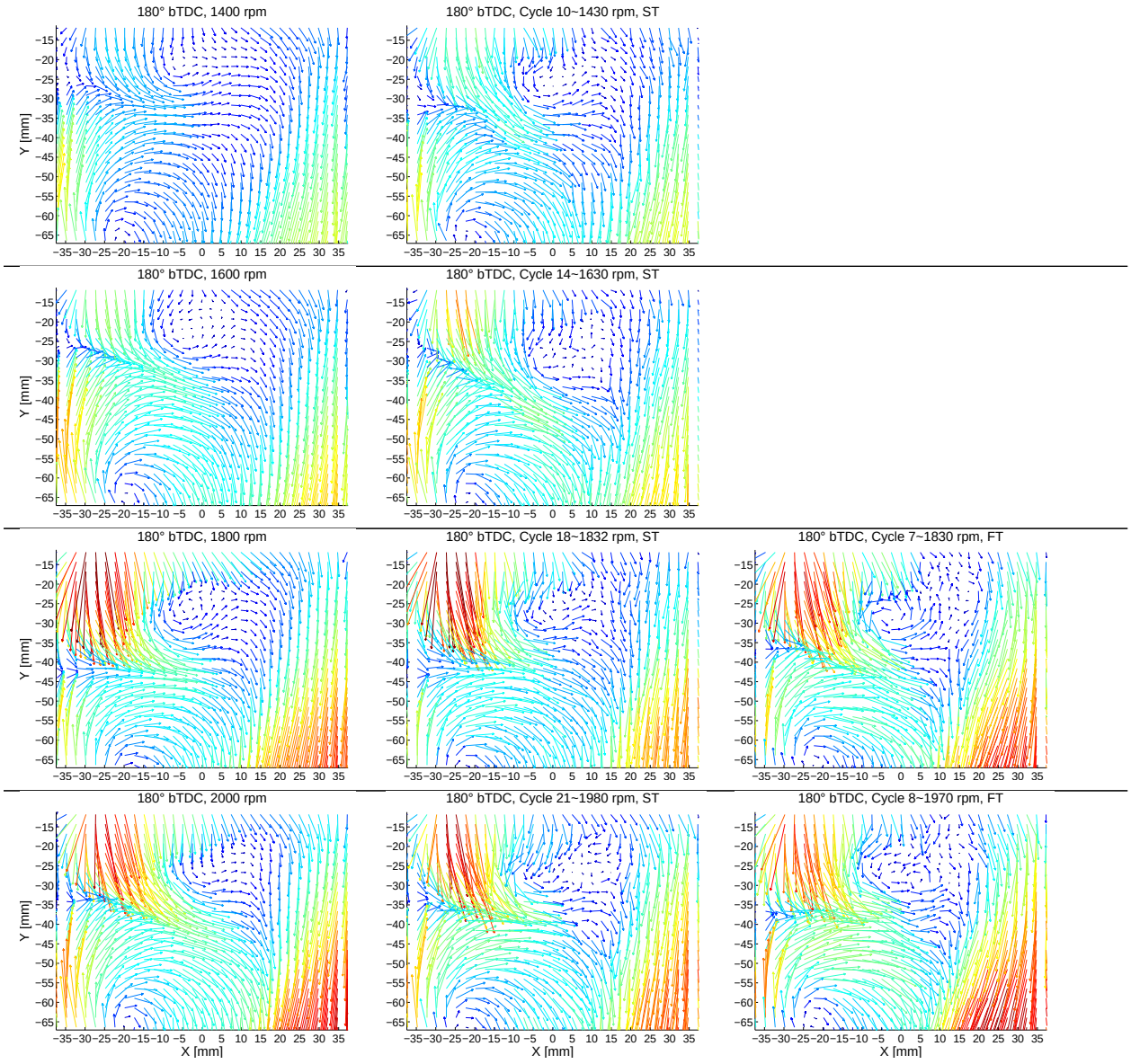

Figure 6.6: Phase-averaged velocity fields for transient conditions at different regimes, compared to stationary conditions at BDC.

The flow streamlines in this region are almost direct up to half of stroke and then start to deviate from the cylinder wall in moderation. Since the distance between bottom of FOV and BDC is about 28 mm, it is not obvious that the up-wash flow at the cylinder left side is due to the flow deflection, resulting from its strikes to the piston head or is a continuation of the upstream deviated flow motion.
Nevertheless, this motion rolls up in the symmetry plane and induces an up-wash motion along the cylinder left wall. Afterwards the mean tumble motion interacts with the descending momentum flux out of the lowest portion of the intake valves, for all conditions (stationary and transient) this interaction is more important at higher engine speed and its position moves away from intake valves. Such a flow interaction results in the generation of a second vortex under intake valves for all conditions, except at lowest rpm in stationary condition.
In addition, it is interesting to point out that the structure of this smaller secondary vortex seems not to be organized at the same CAD in transient or stationary conditions, inducing

different velocity fluctuations in the vortex core. This is illustrated in Figures 6.7 and 6.8 , where 3 velocity fields are plotted at 3 CAD, chosen to represent first the beginning of the second vortex generation, second the second vortex is fully generated and distinguishable, and third, the beginning of its destruction, for respectively 1200 and 2000 rpm.
In this field of view, it is not possible for 1200 rpm, to identify clearly this vortex for the stationary conditions unlike transient conditions and the vortices are more distinguishable for the fast transient mode, due to higher velocity amplitude.

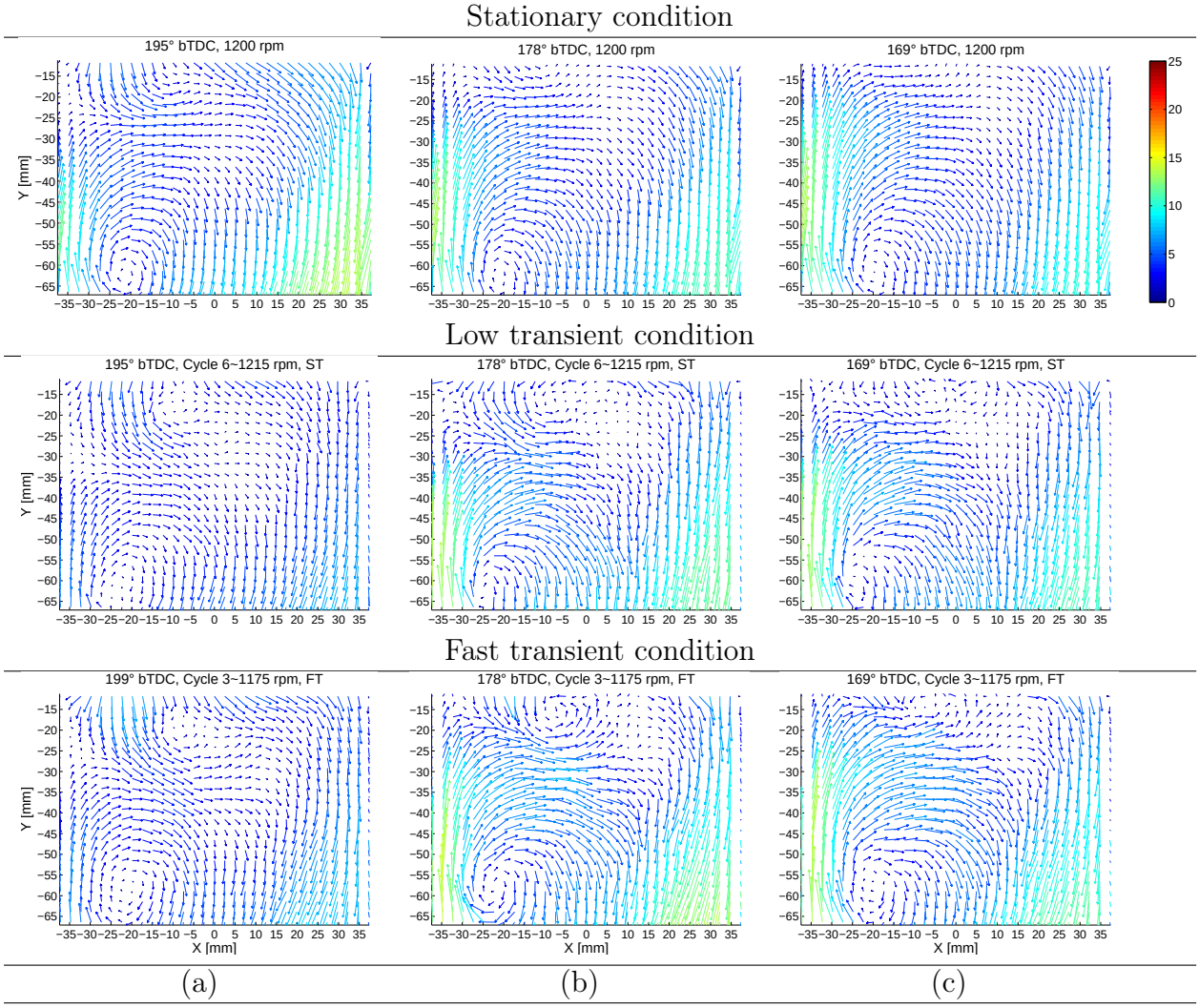

Figure 6.7: Example of velocity fields for stationary and transient conditions to illustrate (a) Generation of the second vortex, (b) fully developed second vortex and (c) Its destruction, 1200 rpm.

For 2000 rpm, both transient conditions, the second vortex is better organized at 183°bTDC. But for the fast transient mode, the second vortex life is longer in time than in slow transient and stationary modes. Moreover, the velocity amplitude is also more important which involves more time to dissipate the vortex. By a visual observation, the CAD corresponding to the generation and the destruction of the second vortex were determined for all engine regimes and all conditions, as in Table 6.8. The moment of birth and destruction of the secondary vortex does not seem to follow a monotone behavior, especially as a function of the regime, but also between different transient conditions and

stationary ones. It seems that in the case of slow transient conditions, the presence of the second vortex is phased as in the stationary regime and in fast transient condition, the duration of the second vortex in CAD is longer.

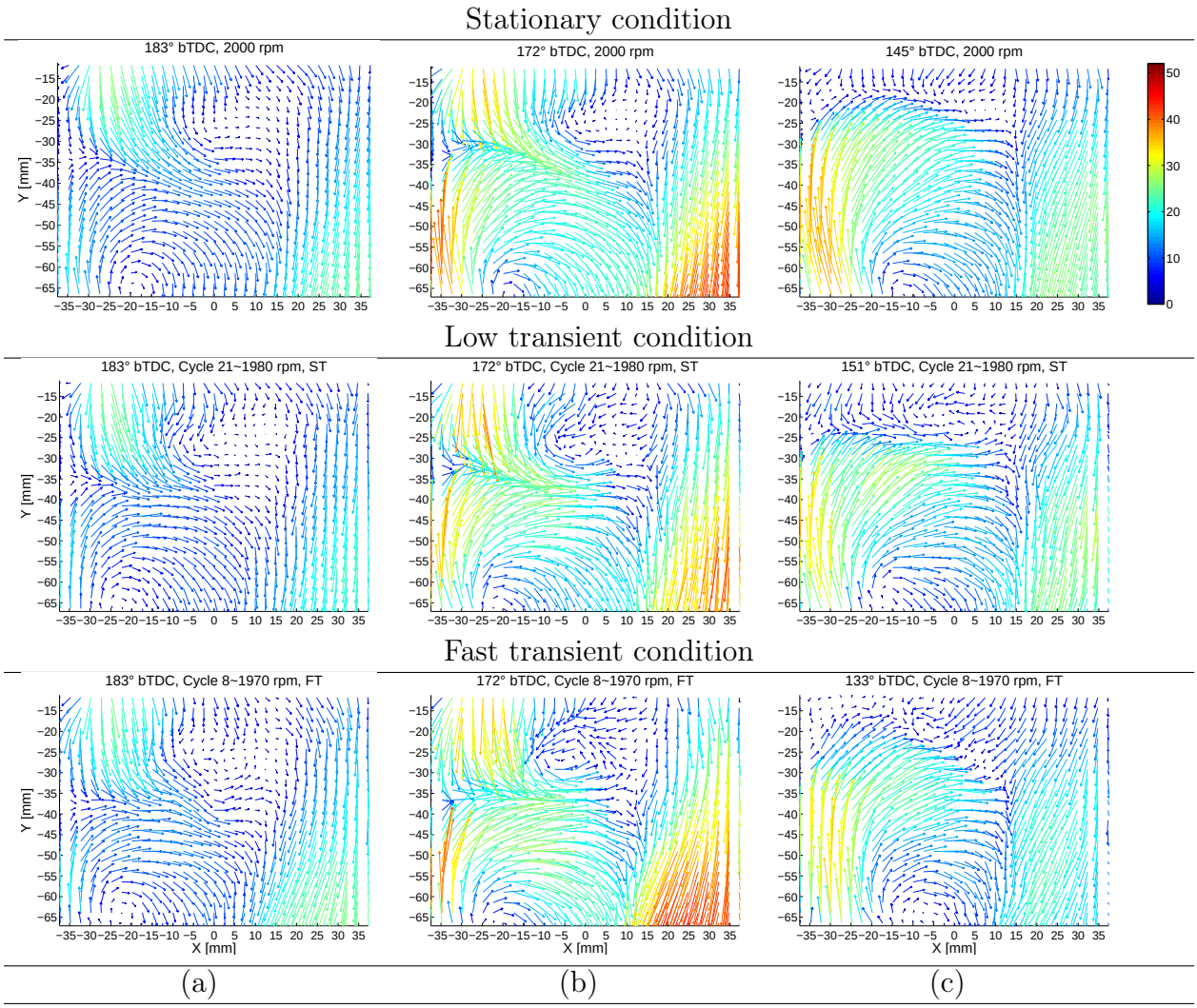

Figure 6.8: Example of velocity fields for stationary and transient conditions to illustrate (a) Generation of the second vortex, (b) Fully developed second vortex and (c) Its destruction, 2000 rpm.

Engine speed	Stationary condition		Transient in 21 cycles		Transient in 8 cycles	
[rpm]	start	end	start	end	start	end
1200	-	-	195	169.5	199.5	174
1400	175	157	178.5	150	-	-
1600	183	154	183	150	-	-
1800	183	132	177	135	184.5	126
2000	172.5	145.5	183	151.5	183	133.5

Table 6.8: CAD corresponding to the generation and destruction of the second vortex for all conditions.

6.1.6 At mid-compression stroke

The mean velocity fields at mid-compression stroke for different engines speed are displayed in Figure 6.9. At this CAD, the second vortex is totally dissipated, only the main tumble structure persists. But it can be seen that the core of mean tumble motion is less organized in transient conditions than in stationary case. Disorders in the vortex core structures seem to be more important in the case of slow acceleration mode, as for 1800 rpm.

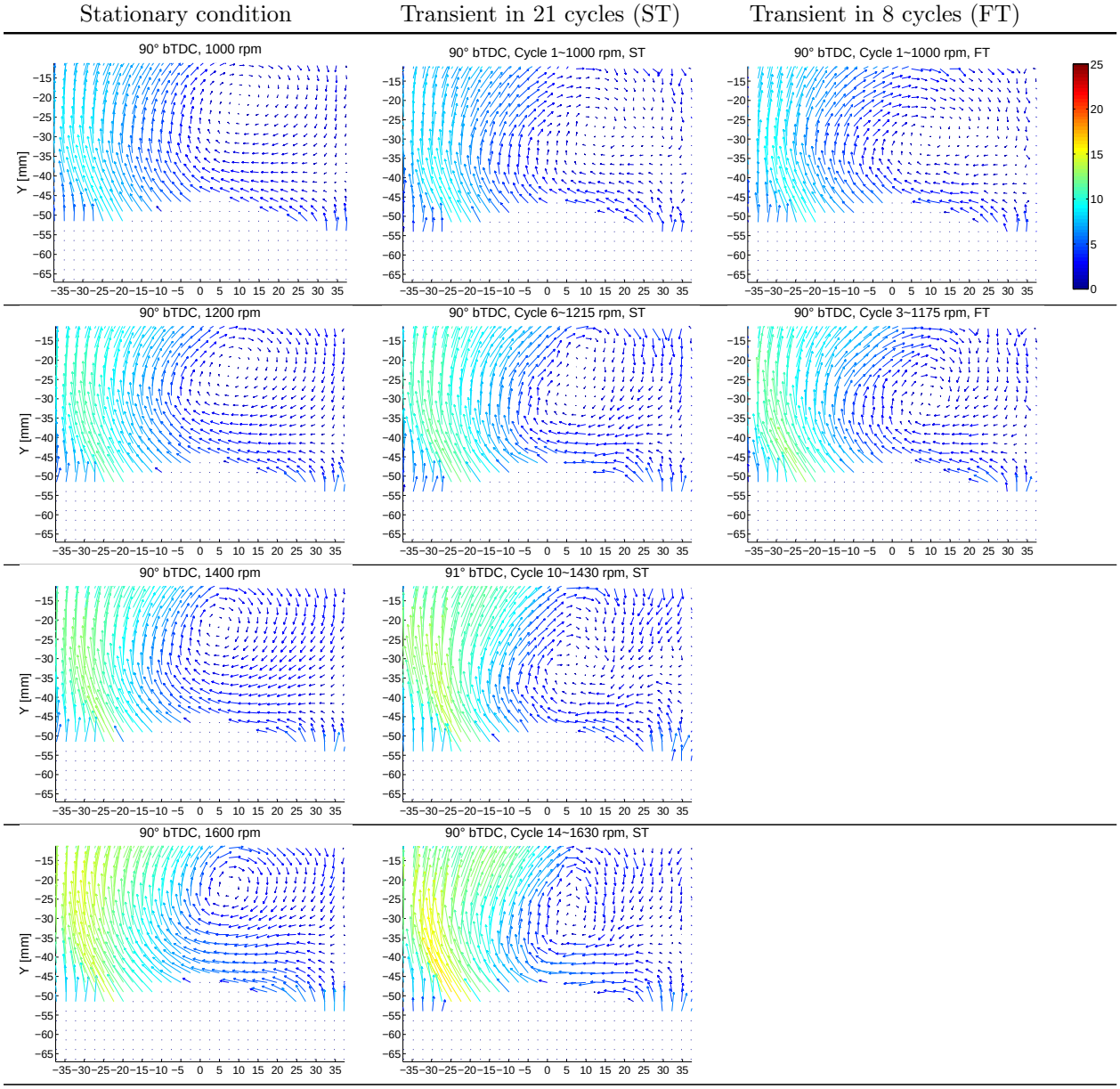

Figure 6.9, *Cont.*

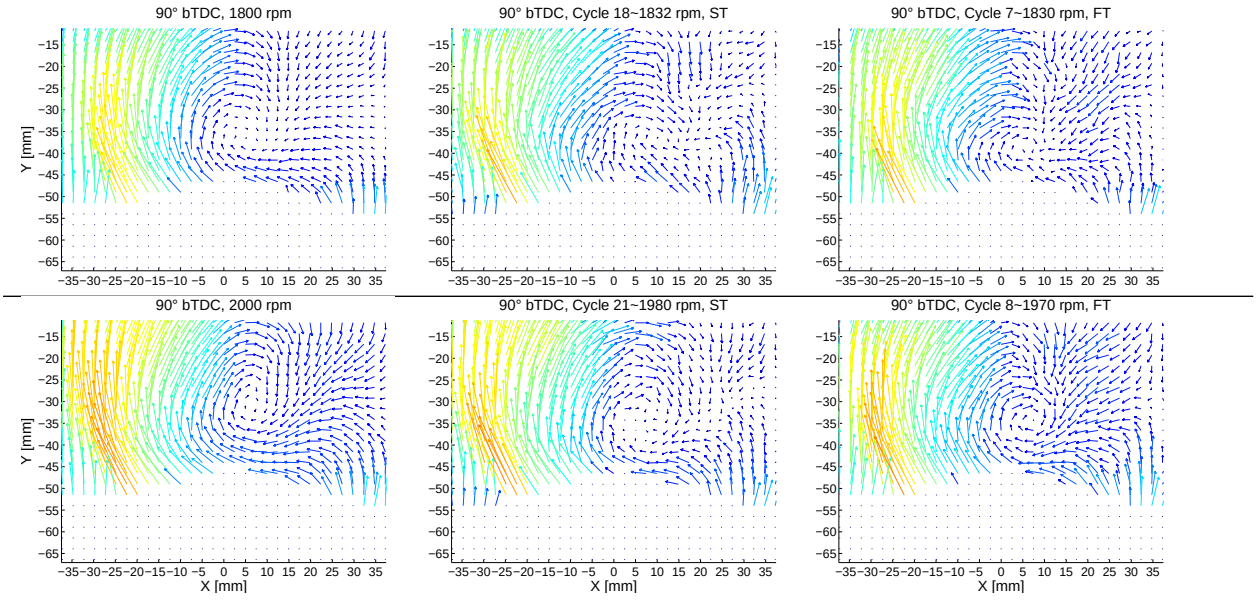

Figure 6.9: Phase-averaged velocity fields for transient conditions at different regimes, compared to stationary conditions at mid-compression stroke.

6.1.7 At 70 CAD bTDC

Figure 6.10 displays the mean flow velocity fields at 70 CAD bTDC: the order of the mean flow velocity magnitude and its spatial structures are almost similar for both transient conditions in comparison to the stationary cases at identical engine regime.
At first glance, the location of the tumble center is not similar for these three conditions, therefore the section 6.2 is devoted to the study of the tumble trajectory and of the tumble ratio in detail.

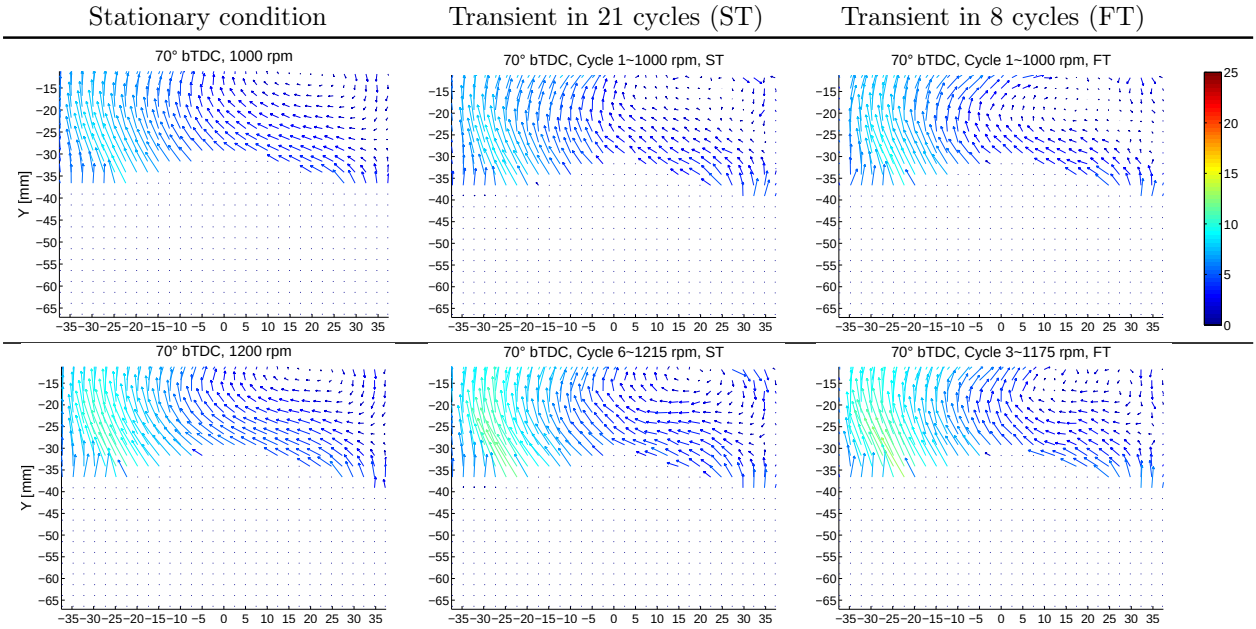

Figure 6.10, *Cont.*

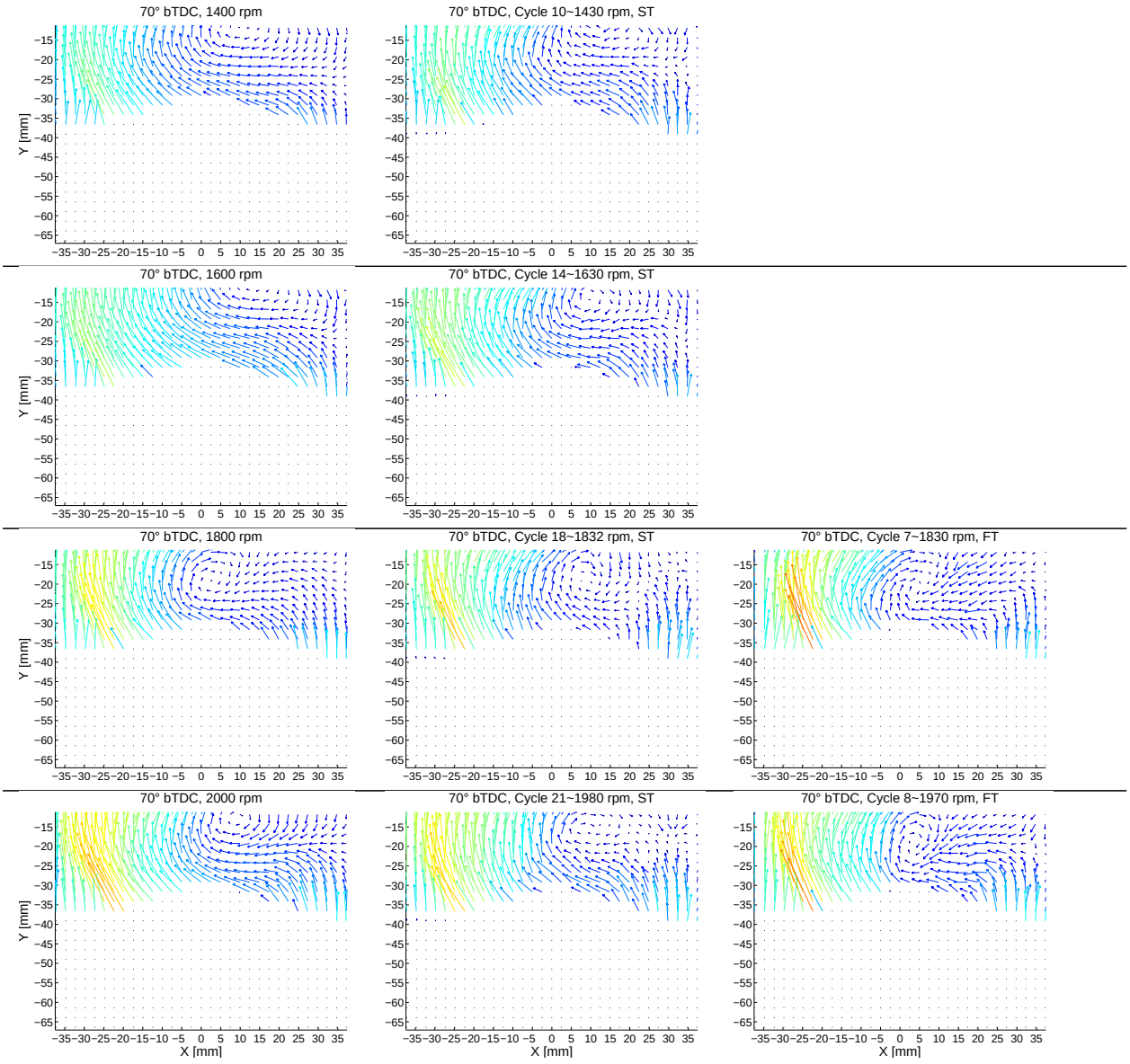

Figure 6.10: mid-intake, Phase-averaged velocity fields for transient conditions at different regimes, compared to stationary conditions at 70 CAD bTDC.

As a conclusion there are several different as well as some similitude in in-cylinder mean flow pattern between transient and stationary regimes that are summarized as follows:
For all engine operation conditions, transient and stationary regimes, at the early of intake stroke (about 310 CAD bTDC) the interaction between inlet jet and piston head generates a recirculation zone under intake valves. It is disappeared after 300 CAD after intake TDC for all conditions.
At 290 CAD the inlet flow deviation from cylinder right side to its center is obvious and at a given engine speed the angle of this deviation is sharper for fast transient condition compared to low transient one as well as stationary regime. In general at a given engine speed, the first complete recirculation zone at the tumble core is observed earlier, during intake stroke, for fast transient condition compared with two other ones. However for higher engine speed of 2000 rpm, it occurs almost at the same CAD for all conditions.

At mid-intake stroke the mean flow spatial structures in all conditions are approximately

similar.
At BDC the tumble center is located at the cylinder lower-left side in all conditions. But the distance between BDC and tumble center changes according to the engine speed in transient conditions as well as stationary one.
The interaction between tumble up-wash flow at the left side of cylinder and downward momentum flux from lower portion of the intake valves generates a second vortex in the opposite direction of the mean tumble motion.
The moments of generation and destruction of this vortex are not similar for different engine speeds but entirely dissipated before mid-compression stroke in all conditions. It seems the presence of this secondary vortex in the case of slow transient condition is phased as in the stationary regimes and in fast transient conditions its structure preserved in time longer than two other conditions. It should be mentioned this vortex is less organized in transient condition compared to stationary regime. Also at mid-compression stroke the core of the mean tumble motion is less organized in transient conditions than that in stationary regime.
At 70 CAD bTDC, for a given engine speed the order of mean flow velocity and its spatial structures are approximately similar for transient and stationary regimes. However the distance between tumble center and TDC is not similar for these different conditions.

6.2 Tumble center trajectory and Tumble ratio

To understand the in-cylinder flow structure and its time-space behavior in S.I. engine, the characterization of the tumble bulk motion and especially the assessment of its in -cycle evolution is of great importance. Moreover, as described previously in Chapter 1, the fluctuations of its intensity and its location affect the air-fuel mixing process and combustion development as Kent et al. (1989) [99], Hill & Zhang (1994) [81] and Hadded & Denbratt (1991) [72].

In this study, the tumble ratio, which represents the strength of the in-cylinder flow motion and the trajectory of the tumble center and tumble ratio, are analyzed for both transient conditions in comparison to stationary cases, from the phase-averaged velocity fields. For that, the tumble center has to be identified in as rigorous a manner as possible. The Eulerian approach based on the flow field topology, introduced by Graftieaux et al. (2001) [67], was used. The velocity field at the point P is sampled along two dimension discrete spatial locations around P, so the dimensionless scalar function Γ can be calculated as defined below:

$$\Gamma(P) = \frac{1}{N} \sum_{S} \frac{\left(\overrightarrow{PM} \wedge \overrightarrow{U_M}\right).z}{\left\|\overrightarrow{PM}\right\| . \left\|\overrightarrow{U_M}\right\|} = \frac{1}{N} \sum_{S} \sin(\theta_M) \tag{6.1}$$

Where S is the two dimensional area centered on P, N the number of points M inside S and z the unit vector, normal to velocity vector. The operator $\|.\|$ represents the Euclidean norm of the vector. The angle between the velocity vector and the radius vector is represented by θ_M. $|\Gamma|$ is bounded by 1 and reaches 1, near the vortex core, if the vortex is axisymmetrical as Lamb-Ossen axisymmetrical vortex.
The angular velocity of vortex is also defined as

$$\omega_s = \frac{\gamma}{I} = \frac{\sum_S \left(\overrightarrow{PM} \wedge \overrightarrow{U_M}\right)}{\sum_S \left(\overrightarrow{PM}.\overrightarrow{PM}\right)} \tag{6.2}$$

Where γ is the angular momentum of fluid and $I$the moment of inertia coefficient. The tumble ratio can be computed as the ratio of the angular velocity to the engine crankshaft angular velocity, $R_t = \omega_t/(2\pi N)$ where N is the engine rotation speed.

The location of the vortex center, computed by this method is highly correlated to the choice of a sub-region S in Eq (6.1). It should be mentioned in the original work of Graftieaux et al. (2001) [67] the effect of the S size was not investigated. In general the vortex center has a low angular velocity compared to its neighboring and its absolute velocity is very low. Stansfield et al. (2007) [172] and Bücker et al. (2012) [21] chose 3×3 grid points as S area for computing Γ at each point P in the velocity field.
Following their suggestion, the values of Γ for two arbitrary velocity fields, which are faced in this study, are displayed in Figure 6.11. For each velocity field, two peaks of Γ with the same order of magnitude are detected, leading to two centers of vortices. A zoom of the zone where the two vortices centers are located is presented in Figure 6.11. To overcome this drawback, a more global S area is selected in this study i.e. half of entire velocity field. The obtained results are presented in Figure 6.11 for each velocity field. Therefore

using this method the center of flow bulk motion is identified that differs of any local recirculation zone.

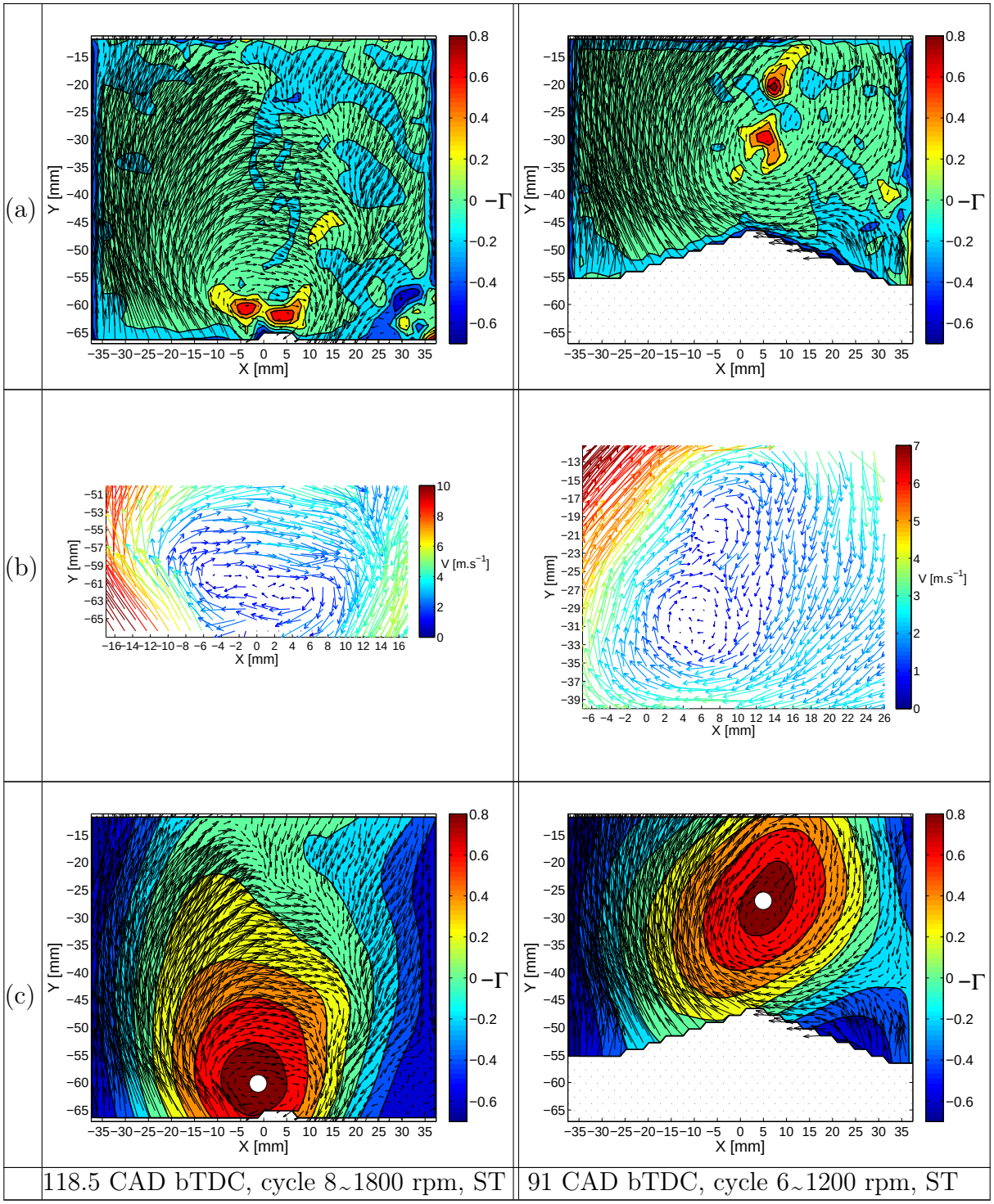

Figure 6.11: Two examples of Γ map computed by 3×3 grid points (a), zoom on the two vortices zone (b), half of entire velocity field as a S sub-region (c). ST: Slow Transient condition.

Since here the sense of flow rotation is clockwise Γ is negative at the vortex center, in the figures the opposite of this value is displayed.

Also using 3×3 grid points as S area can cause the jump of computed tumble center between two consecutive CAD as shown in Figure 6.12. In this example, the vertical displacement of tumble center is 6.2 mm from 108 to 106.5 CAD bTDC because the automatic processing tool identified similar Γ magnitude in two locations.

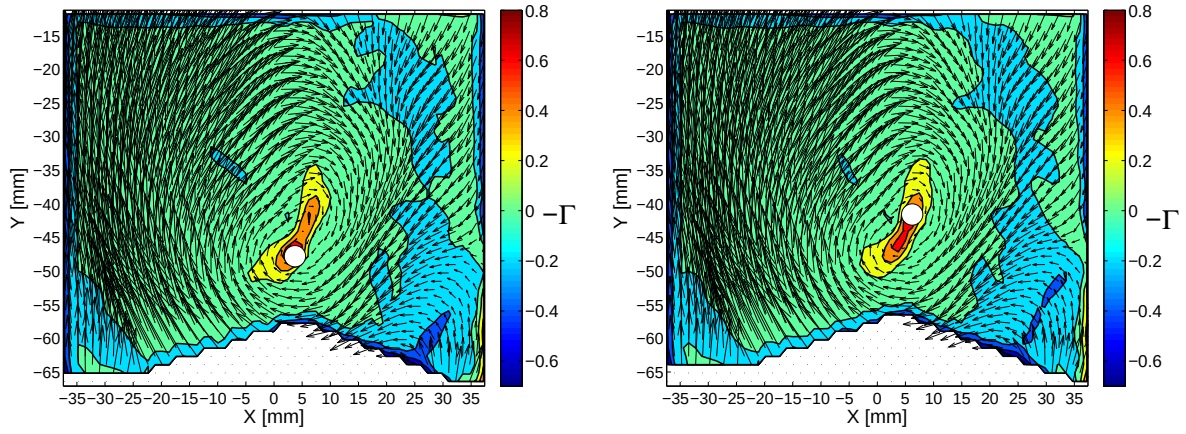

Figure 6.12: Stationary condition, 2000 rpm, (a) 108 CAD bTDC and (b) 106.5 CAD bTDC.

6.2.1 Stationary conditions

The displacement of tumble center in stationary conditions for different engine speeds is presented in Figure 6.13. Globally the trajectory is not strongly affected by the engine regime. During the intake stroke, represented in blue line, the vortex center moves from the bore center downwards the left side, and below the bottom of the FOV, for the BDC CAD (180 bTDC), except at 1200 rpm. During the compression stroke, plotted in red line, the tumble center is located in the FOV but at different CAD according to the engine speeds. At 1200 rpm, the vortex center does not approach to the bottom of the cylinder so during the whole compression stroke, it is located in the FOV. As a reminder the bottom of the FOV is about 28 mm far from BDC. At 1800 and 2000 rpm, during compression stroke, the vortex center appears almost in the same CAD i.e. 133 bTDC, later than for other engine speeds. The center of mean tumble motion is observed until 63 CAD bTDC at 1800 rpm whereas until 77 CAD bTDC for 1000, 1200, 1400 and 1600 rpm engine speed and 72 CAD bTDC for 2000 rpm.
This fact induces that there is a delay in tumble motion toward the TDC for high engine speed, particularly in 1800 rpm that this delay is more significant than that in 2000 rpm engine speed. This issue is related to cylinder pressure that itself correlated to the intake pressure. In Figure 6.14, the pathway of the tumble displacement for different engine speeds in stationary conditions is compared for a common CAD range, i.e. 260 to 201 CAD bTDC during the intake stroke and 132 to 77 CAD bTDC during the compression stroke. The dots represent the vortex center location every 5 CAD for 1000, 1200 and 1400 rpm and 4.5 CAD for 1600, 1800 and 2000 rpm.

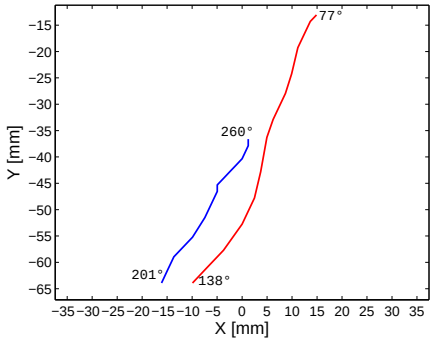

(a) 1000 rpm

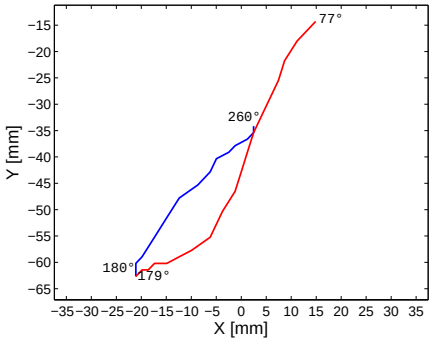

(b) 1200 rpm

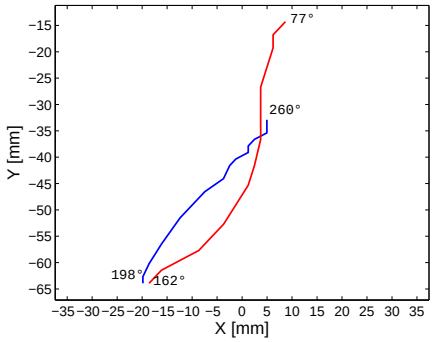

(c) 1400 rpm

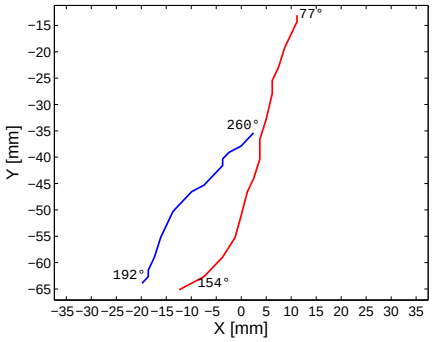

(d) 1600 rpm

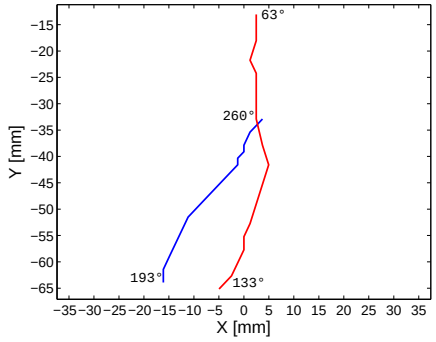

(e) 1800 rpm

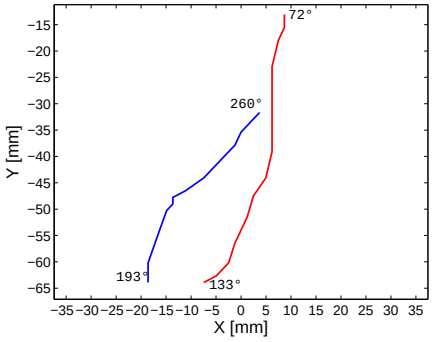

(f) 2000 rpm

Figure 6.13: Trajectory of the tumble center for different engine speeds - stationary condition blue line: intake stroke, red line: compression stroke.

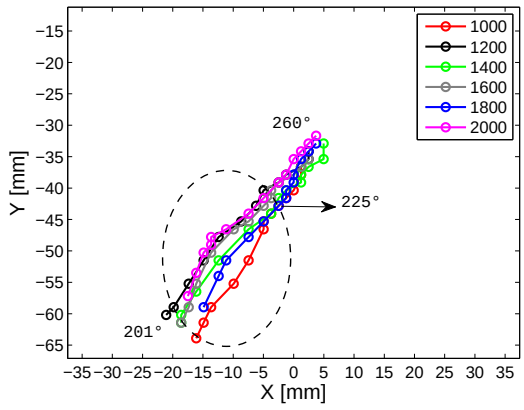

(a)

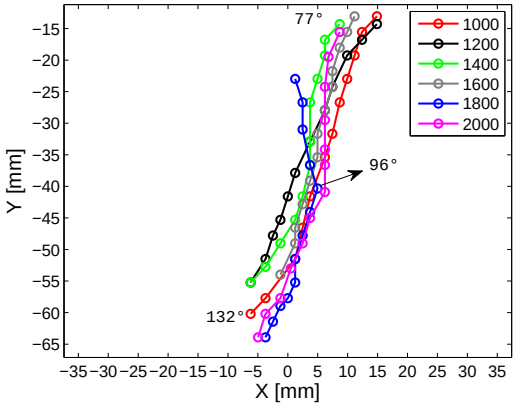

(b)

Figure 6.14: Comparison of the tumble displacement versus engine speeds, Stationary conditions (a) Intake stroke and (b) Compression stroke.

In the first part of the intake stroke, from 260 to 225 CAD bTDC, the displacement of the tumble center can be considered globally similar for different engine regimes. But, from 225 to 201 CAD bTDC, it is accelerated and more dependent to the engine regime. It can be also noticed that for 2000 rpm engine speed, this acceleration is less important. During the compression stroke, the center of mean tumble motion moves from the bottom toward the exhaust valves, located at the top right. As previously observed in Figure 6.13, a difference of behavior can be observed for 1800 rpm: at almost about the mid-compression stroke (96 CAD bTDC), tumble center shifts toward the the cylinder axis. It should be mentioned the intake valves are already fully closed at 147 CAD bTDC, so the total air mass inside the engine cylinder is constant beyond this CAD and the in-cylinder flow is directed by upward movement of the piston. It is interesting to point out at 77 CAD bTDC the center of the tumble is approximately in the same zone, under exhaust valves for all engine speeds except 1800 rpm.

The temporal evolution of tumble ratio as a function of the engine speed is plotted in Figure 6.15. The maximum of the tumble ratio when the intake valves are fully opened is reached between 240-220 CAD bTDC, with an intensity between 2-2.5 and between 120-100 during the compression stroke with an intensity between 0.75-1.5. The organization of the flow that increases tumble intensity during intake stroke, is not directly related to the increase of the engine speed, but during the compression stroke it can be noted that the intensity of the Tumble ratio increases with the increase of the engine speed, induced by the increase of the piston speed itself except for 1800 and 2000 rpm. It could be also noted that after 100 CAD bTDC, the tumble ratio has the same evolution at all engine speeds and reaches the value of 0.25 at 77 CAD bTDC.

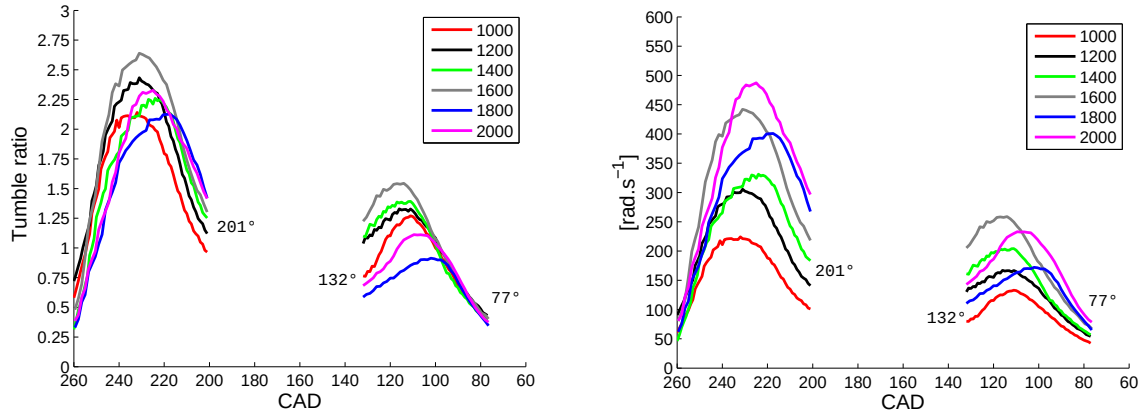

(a) (b)

Figure 6.15: Temporal evolution of the tumble ratio (a) and the tumble angular velocity during intake and compression strokes for different engine speeds, stationary conditions.

To illustrate, the velocity fields at different CAD bTDC are plotted in Figure 6.16 for 1000 rpm engine speed. At 240 CAD bTDC, the flow is entirely expanded in measurement plane contrary to 260 CAD bTDC, moreover the streamlines form a circulation region around the vortex core at its left side whilst such a region is not generated earlier, at 260 CAD bTDC. Afterward the piston motion towards the bot-

tom, the mean flow velocity is more homogeneous in the FOV and its magnitude decreases.

During the compression stroke when the piston goes up toward the mid-stroke, the tumble ratio increases, at 117 CAD bTDC the mean flow traverses below the vortex core in FOV contrary to 132 CAD bTDC, one cause of the raise of tumble ratio at 117 CAD bTDC. During the compression stroke, also due to the piston shape, the circulation region around the vortex is destroyed and the top of the vortex is not in the FOV, as it can be seen in Figure 6.16, that decreases the value of the tumble ratio at the mid-compression, i.e. 90 CAD bTDC.

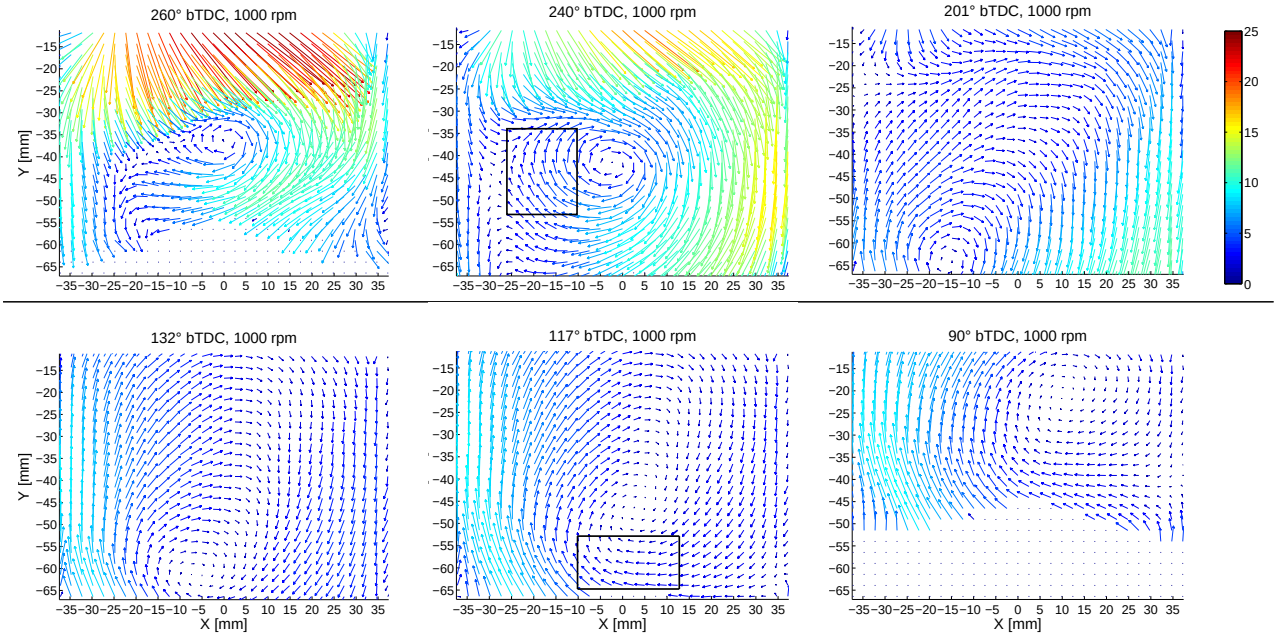

Figure 6.16: Phase-averaged velocity field versus intake and compression strokes, 1000 rpm engine speed, Stationary condition.

As shown in Figure 6.15, the maximum tumble ratio is not reached at the same CAD for every engine speeds, both during intake and compression stroke. As it can be seen in Figure 6.17, where the velocity fields at 230 CAD bTDC are plotted for 1200, 1600 and 2000 rpm, the velocity magnitude is different but the mean bulk motion is fully developed inside the FOV.
At 1600 rpm, the circulation zone to the left side of the vortex core is more significant compared to 2000 or 1200 rpm. And as the circulation area at the left side of the vortex core for 2000 rpm is quite weak, despite the high velocity magnitude top right and left, the order of tumble ratio is less than that for 1200 rpm engine speed. But the signature of the high velocity magnitude at 2000 rpm affects the angular velocity magnitude, plotted Figure 6.5.b. Contrary of the tumble ratio, the mean angular flow angular velocity at 230 CAD bTDC at 2000 rpm is higher compared to 1200 rpm.

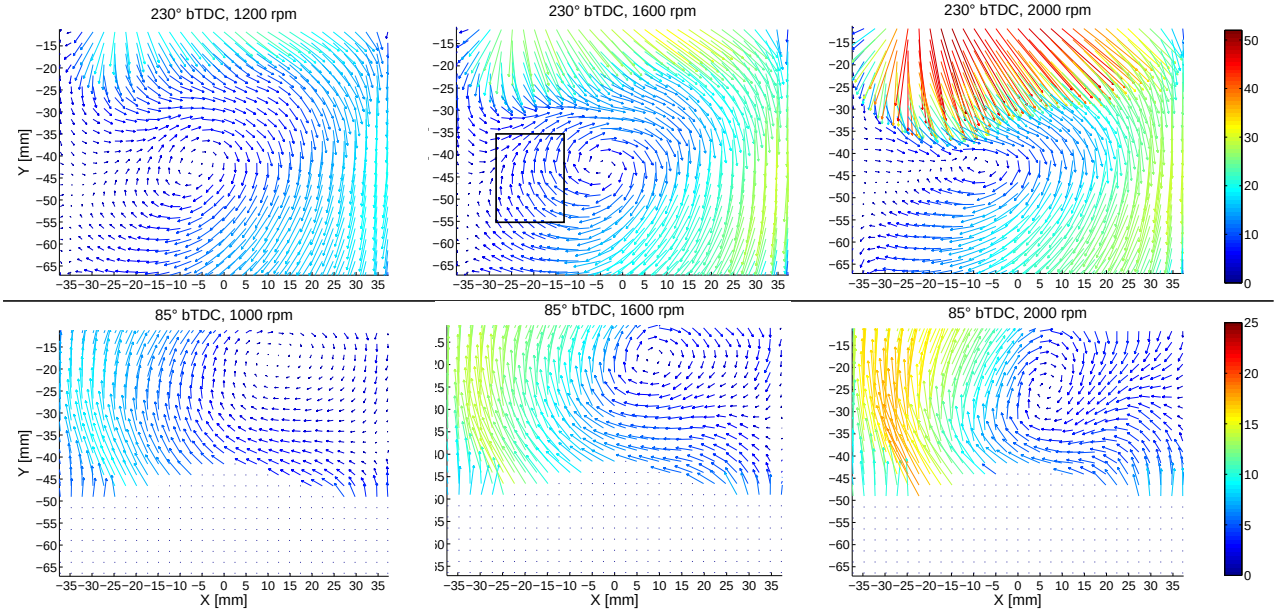

Figure 6.17: Comparison of phase-averaged velocity fields at 230 and 85 CAD bTDC in stationary conditions; 1200, 1600, 2000 rpm.

However during the compression stroke, the flow is very similar after 100 CAD bTDC, (here as in example at 85 CAD bTDC) as it should be expected from the tumble ratio evolution of Figure 6.15. So from these different plots, it is obvious that the velocity magnitude increases as the engine speed increase but this difference is not revealed in the evolution of the tumble ratio (equal to the mean flow angular velocity is normalized by the engine crank shaft angular velocity) but more in the angular tumble velocity profile.

6.2.2 Slow transient condition

The evolution of tumble center estimated from the phase-averaged velocity field in the case of slow transient condition (i.e. a transition from 1000 rpm to 2000 rpm during 21 cycles) is displayed in Figure 6.18, for different engine speeds.
Similar to the trajectory observed in stationary conditions, during the intake stroke (plotted in blue lines) when the piston goes down, the tumble center moves from center to the cylinder the lower left side and during compression stroke (red lines) it approaches approximately to the exhaust valves at the upper-right side. As it was noticed in stationary condition, only at 1200 rpm, the tumble center remains inside the FOV at BDC and for the other engine speeds, when the piston goes toward the BDC, the tumble vortex core is not entirely in the FOV so its center cannot be computed.

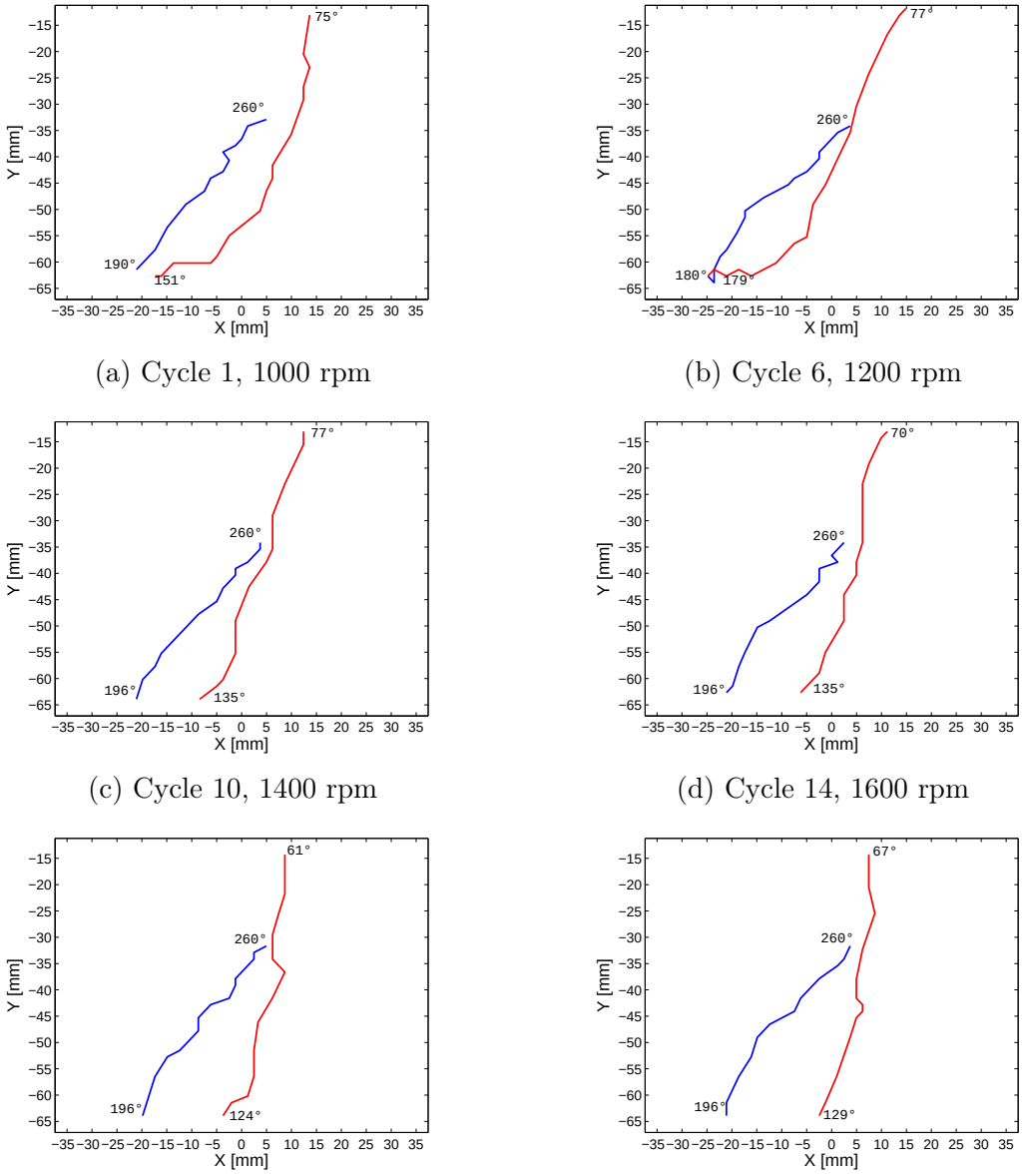

(a) Cycle 1, 1000 rpm

(b) Cycle 6, 1200 rpm

(c) Cycle 10, 1400 rpm

(d) Cycle 14, 1600 rpm

(e) Cycle 18, 1800 rpm

(f) Cycle 21, 2000 rpm

Figure 6.18: Trajectory of the tumble center for different engine speeds, Slow transient condition blue line: intake stroke, red line: compression stroke.

At highest engine speeds, i.e. 1600, 1800 and 2000 rpm, during the compression stroke the center of the bulk motion is entirely located in the FOV up to 70, 61 and 67 CAD bTDC, later than in the lower engine speeds.

In Figure 6.19, the trajectories of the tumble center for different cycles corresponding to engine speeds, during intake and compression strokes are presented, moreover, the trajectory during the cycle just before the start of the acceleration is also plotted during the common CAD range. The vortex center is displayed in every 5 CAD for 1000, 1200 and 1400 rpm engine speeds and 4.5 CAD for the other ones.
During the intake stroke, Figure 6.19a, the tumble center moves from the bore center toward the lower-left side of the cylinder during the piston downward motion. An acceleration between almost about 225 CAD bTDC to approximately 200 CAD bTDC as for stationary condition. A small difference between the tumble center location at 196 CAd bTDC can be distinguished especially at the cycle 6, corresponding to 1200 rpm.

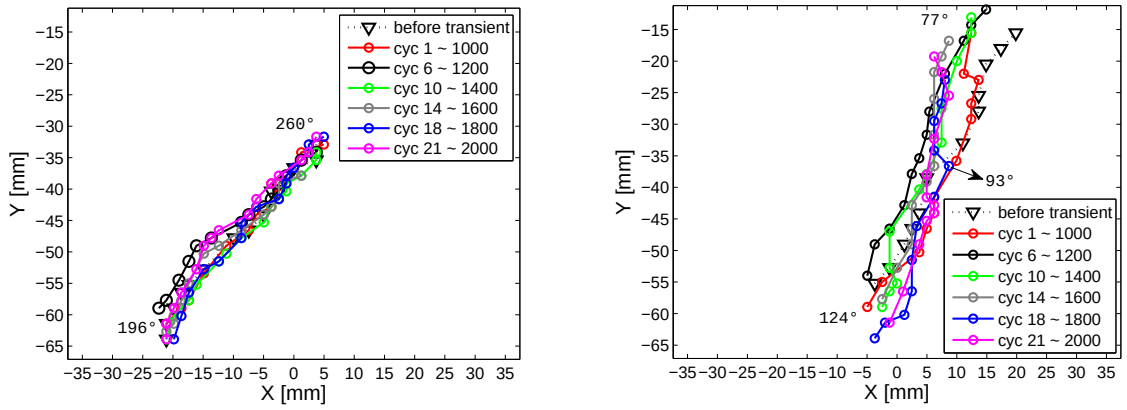

(a) (b)

Figure 6.19: Comparison of the tumble displacement in different cycles of Slow transient condition (a) Intake stroke and (b) Compression stroke.

In compression stroke, Figure 6.19b during the piston ascending motion, the center of the mean flow goes toward the exhaust valves. However the center pathway after mid-stroke is shifted to the cylinder center, in the case of 18^{th} and 21^{th} cycles, corresponding to highest engine speeds.

Temporal evolution of the tumble ratio and the tumble angular velocity for these different cycles are presented in Figure 6.20. The evolution of the Tumble ratio are very similar than those in stationary conditions, with a maximum during the intake stroke, between 2-2.5 around 240-220 CAD bTDC and during the compression stroke 0.75 to 1.25 around 120-100 CAD bTDC. As for stationary conditions, after almost 100 CAD bTDC, the evolution of the tumble ratio is similar for all cycles although the mean angular flow velocity differs. The particularity already observed during the stationary conditions at 1800 rpm is accentuated at slow transition condition, for the 18th cycle. To shed light on the issue, the mean velocity field at 110 CAD bTDC for this cycle is compared to the ones for 6^{th} and 21^{th} cycles respectively corresponding to 1200 and 2000 rpm in Figure 6.21.

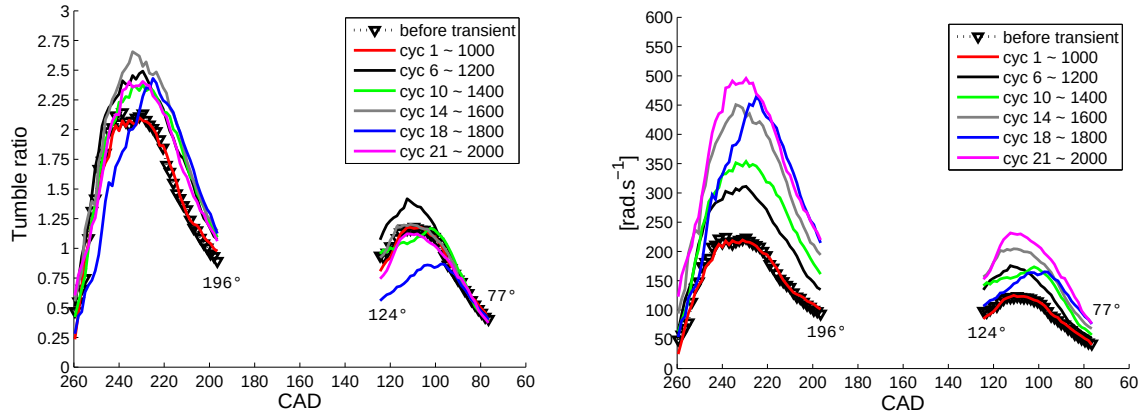

Figure 6.20: Temporal evolution of the tumble ratio (a) and the tumble angular velocity for different cycles, Slow transient condition.

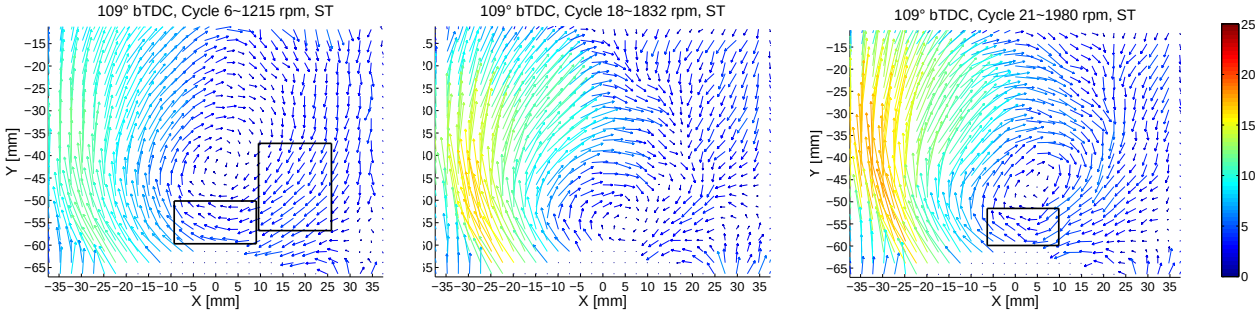

Figure 6.21: MOS-3 Comparison of the mean flow field at 110 CAD bTDC-slow transient condition (a) 1200, (b) 1800 and (c) 2000 rpm.

As one can see there is not any circulation region at the vortex core lower area of in the 18th cycle velocity field at this CAD because the tumble center is very close to the piston head compared to the two other cycles.
For the 6^{th} cycle, corresponding to 1200 rpm, not only such a region is more prominent compared to the 21^{th} cycle but also in the lower-right side of the vortex the velocity vectors generate larger circulation zone

6.2.3 Fast transient condition

The pathway of tumble center displacement for different cycles in fast transition conditions (realized during 8 cycles) is presented in Figure 6.22.

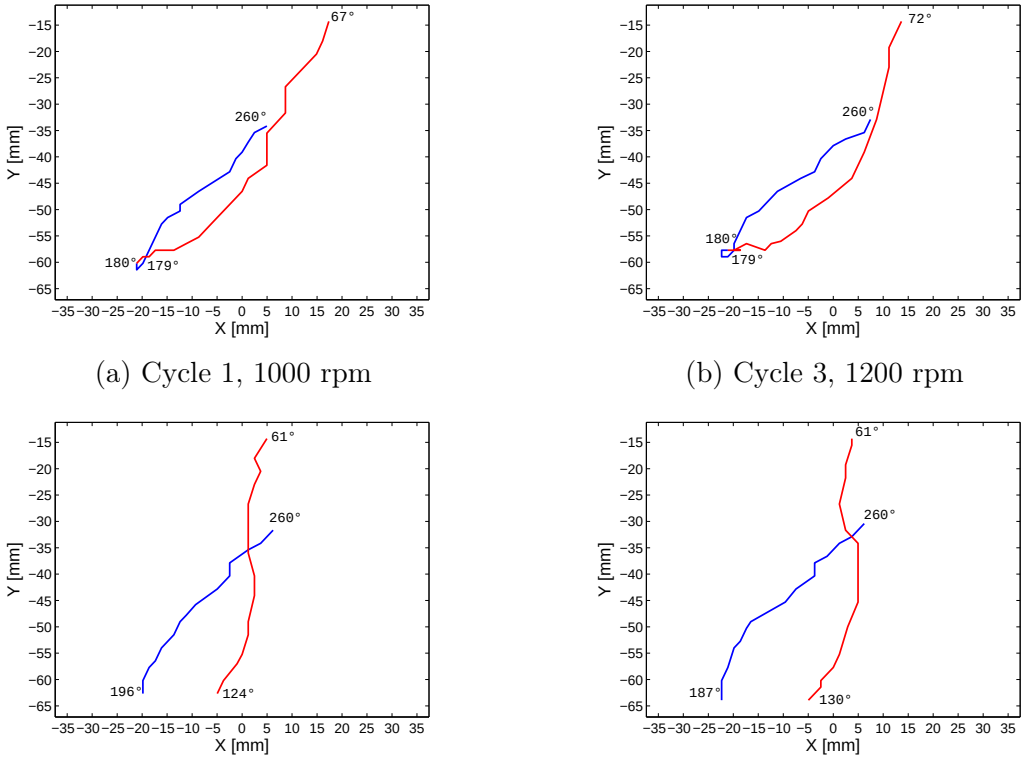

(a) Cycle 1, 1000 rpm

(b) Cycle 3, 1200 rpm

(c) Cycle 7, 1800 rpm

(d) Cycle 8, 2000 rpm

Figure 6.22: Comparison of the tumble displacement in different cycles of Fast transient condition, (a) Intake stroke and (b) Compression stroke.

The general behavior of the trajectory of the tumble center remains identical than previously for stationary and slow transient conditions. However, when the engine speed is about 1000 rpm, the tumble center remains entirely in the FOV at BDC. It means at the beginning of the engine acceleration, i.e. the first cycle, of the fast transient condition, the center of the mean flow at the end of intake stroke has a significant further distance from BDC compared to slow transient condition and stationary condition at 1000 rpm engine speed. Also, during the compression stroke, during this cycle, the vortex center remains in the FOV until 67 CAD bTDC whereas in slow transient condition and stationary regime, it is beyond the FOV. This issue indicates the center of the tumble bulk motion at the beginning of acceleration experiences more downward during compression stroke compared to other above mentioned condition.

For cycles corresponding to highest engine regime (i.e. 1800 and 2000 rpm), during the compression stroke, the mean tumble center remains more time in the FOV up to 61 CAD bTDC. As presented in Figure 6.23a, during the intake stroke, the pathway of the tumble center is similar for the different cycles and also not so different from the slow transient conditions and stationary cases. The difference between cycles corresponding to 1800 and 2000 rpm, compared to 1000 and 1200 rpm especially at the second half of the

compression stroke can be also observed.

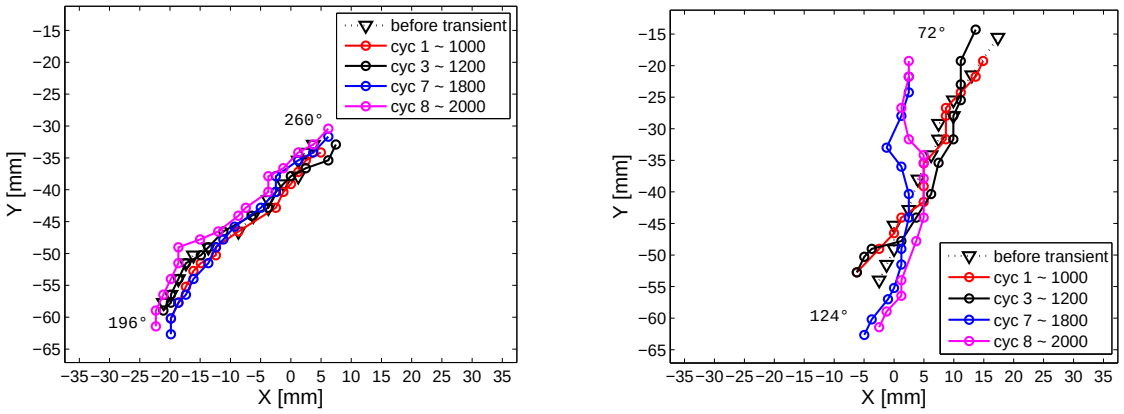

(a) (b)

Figure 6.23: Comparison of the tumble displacement in different cycles of Fast transient condition, (a) Intake stroke and (b) Compression stroke.

In addition the considerable discrepancy in tumble trajectory is observed between the cycles at the begging of transient condition i.e. 1000 and 1200 rpm and the ones at the end of transient condition i.e. 1800 and 2000 rpm: for the highest engine speed, the center of the mean flow is shifted toward the cylinder axis whilst for lower ones it approaches to the upper-right side of the cylinder, under exhaust valves.This feature is related to the in-cylinder flow structures, as an example the mean flow at 85 CAD bTDC for the 3^{th} and the 8^{th} cycles, corresponding to 1200 and 2000 rpm are compared in Figure 6.24.
In the cycle with 2000 rpm engine speed, Figure 6.24b, the mean flow pushes the vortex center to the cylinder axis from two regions. In the lower region the flow acceleration is due to the piston shape and the velocity magnitude in this region is greater than that in the 3^{th} cycle,Figure 6.24a. The upper region is expected to be a continuation of the upstream rotational mean flow from the cylinder head that also has a greater velocity magnitude in 8^{th} cycle.

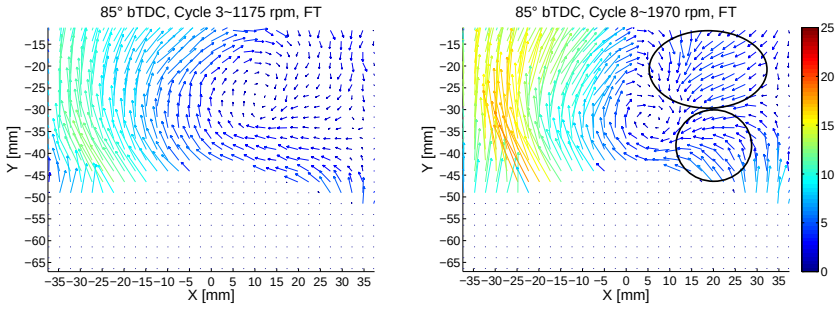

(a) (b)

Figure 6.24: Comparison of the mean flow field at 85 CAD bTDC, Fast transient conditions for two cycles corresponding to (a) 1200 and (b) 1800 rpm.

The profile of the tumble ratio and the mean flow angular velocity for different cycles during engine acceleration are presented in Figure 6.25. As in the case of stationary

regime and slow transient conditions, the global variations of the tumble ratio during different cycles is almost similar therefore the descriptions are not repeated once more. It is interesting to point out unlike slow transient condition, the offset in the peak of tumble ratio during the intake stroke for the cycle corresponding to 1800 rpm is not observed in this transient condition i.e. in all cycles during intake stroke the tumble ratio reaches to its maximum at about 235 CAD bTDC. However the difference remains for the maximum, reached during the compression stroke. Also, during this stroke, as previously observed, after almost 100 CAD bTDC, the evolution of the tumble ratio is similar for the different cycles, even if such similitude is less prominent compared to the slow transient condition and the stationary regimes.

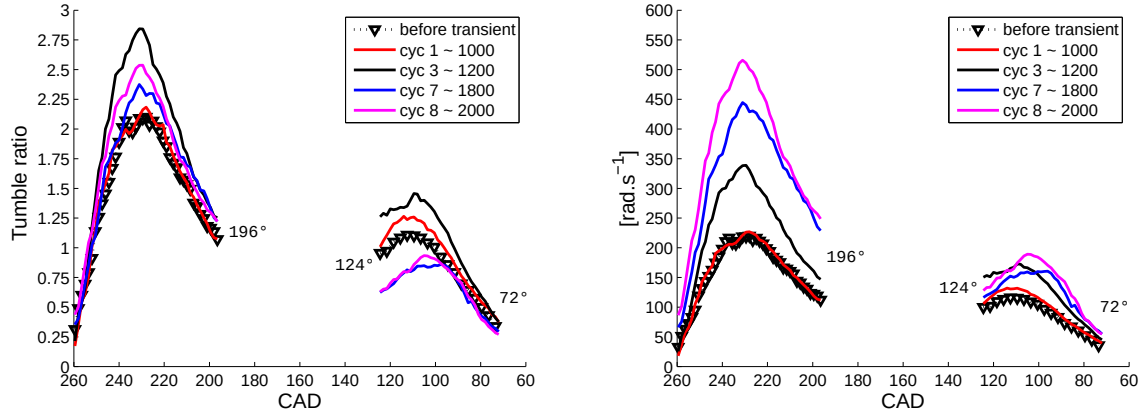

Figure 6.25: Comparison of the tumble trajectory during the intake and compression strokes and the tumble ratio evolution between both transient conditions and stationary regimes.

6.2.4 Comparison between stationary and transient conditions

From the previous results, other plots were done in order to compare the in-cycle evolution of the tumble center trajectory and its ratio in the case of transient conditions to stationary regimes. It should be mentioned the common CAD range in which the vortex core is entirely in the FOV is considered and the tumble center is displayed in every 3 CAD in order to have more detail information.

As previously observed, the trajectory of the tumble center and the tumble ratio have the same evolution during the cycle for transient conditions versus stationary regime. However, some differences can be noted and are discussed below.

In the case of 1000 rpm, presented in the first row of Figure 6.26, the tumble center is the case of transient conditions is located above that generated at stationary regime during the intake stroke and the first part of the compression stroke, but at 77 CAD bTDC, it can be considered that the tumble has the same location. For 1200 rpm, the trajectory of the Tumble center remains inside the FOV: during the intake stroke the trajectory is identical, and in the case of fast regime acceleration, the center is offset to the right before reach the same location at 77 CAD bTDC. The comparison at 1400 and 1600 rpm, only between the slow transient condition and the stationary regime confirms that the

low transient condition does not affect a lot the life of the tumble motion.

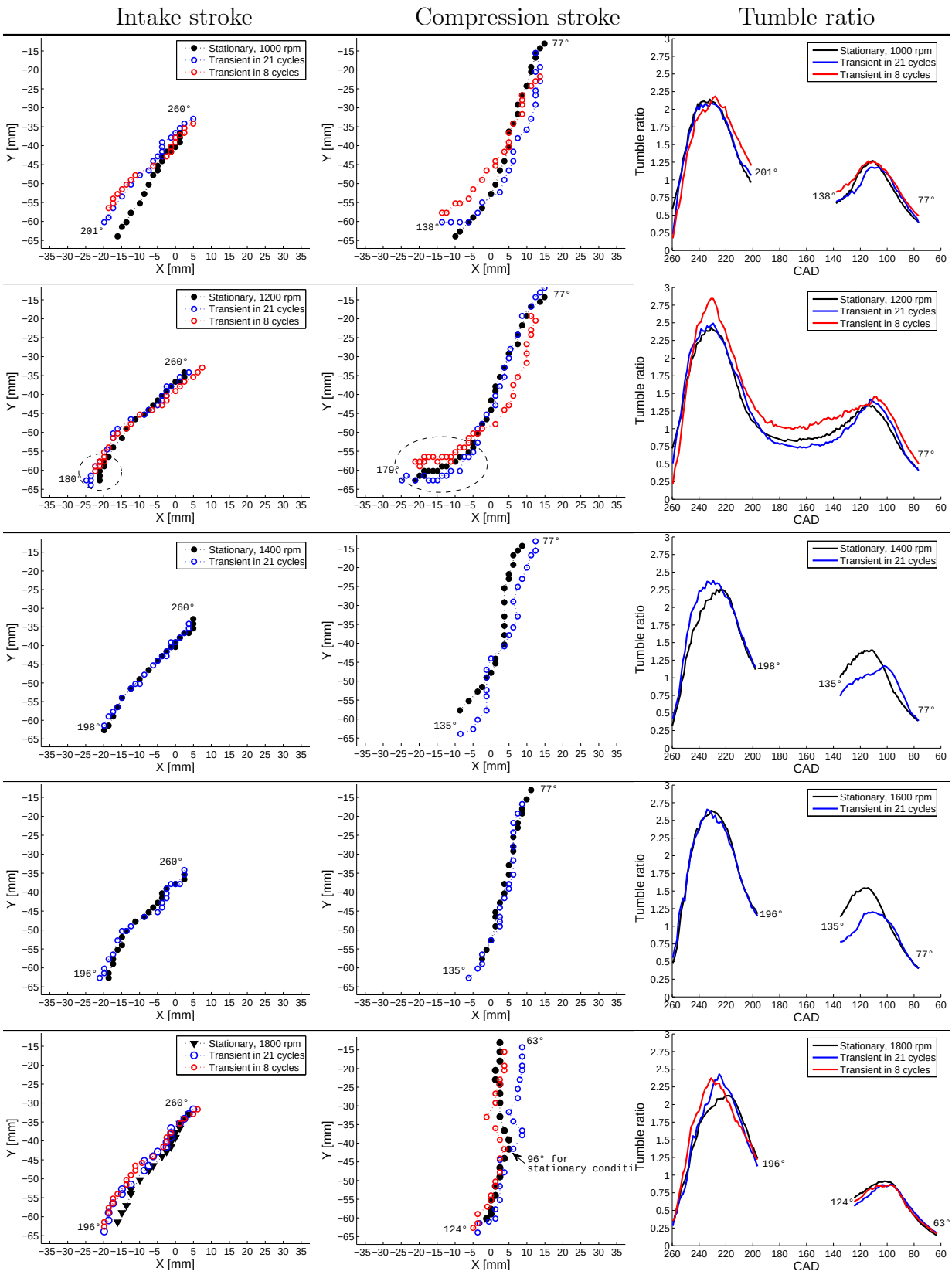

Figure 6.26, *Cont.*

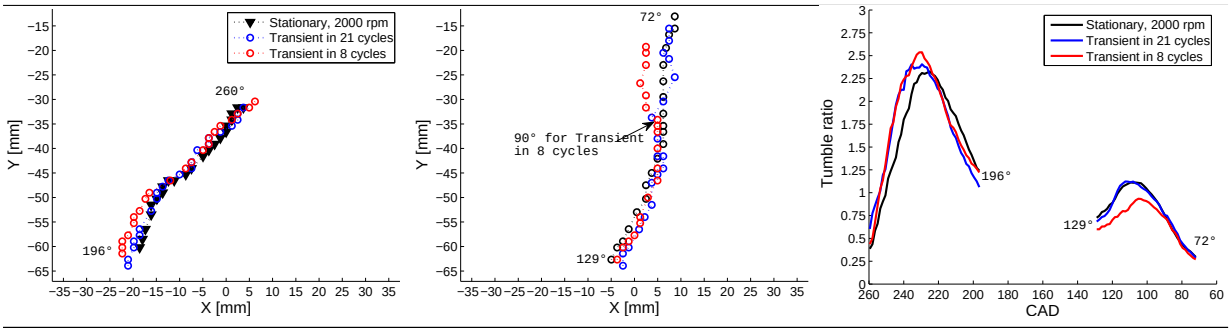

Figure 6.26: Comparison of the tumble trajectory during the intake and compression strokes and the tumble ratio evolution between both transient conditions and stationary regime.

The intensity of the tumble ratio evolves in a very similar way and especially the maximums during the intake stroke are reached at the same CAD for all conditions with a variation of the maximum value around 10%. More differences can be observed during the compression stroke for the angle when the maximum is reached and especially for the regimes (i.e. 1400 and 1600 rpm) where only slow transient condition can be plotted. But from 90 CAD bTDC until the last CAD, the values are identical: the tumble starts to be dissipate in smaller structures, not affected by the acceleration.
Examples of the velocity field are presented in Figure 6.27, for cycle 10 in slow transient conditions corresponding to the regime of 1400 rpm, during the compression stroke. At 135 CAD bTDC the mean flow center in transient condition is closer to the bottom of the FOV compared to the stationary regime, but at 77 CAD bTDC, the difference is less obvious.

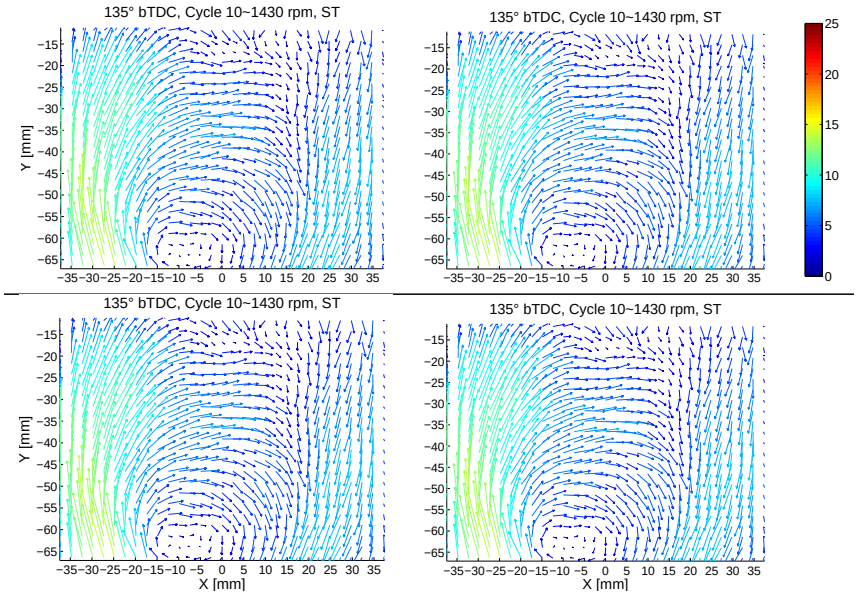

Figure 6.27: The phase-averaged velocity field at 135 CAD bTDC and 77 CAD bTDC for Slow transient and stationary condition, 1400 rpm.

In conclusion knowledge of the tumble during the last part of the compression stroke is the most important as this motion will generate the turbulence useful for the flame development. Therefore, the position of the tumble center and of the piston head are plotted in Figure 6.28, to facilitate the comparison during the last part of the compression stroke, which can be observed with the FOV. First, it has to be concluded that for all engine speeds, the tumble center in the case of transient acceleration is below that generated during stationary conditions.
Second, the fast transient acceleration induces a displacement of the tumble center below that in low transient condition.
During the second part of the compression stroke, it has to be noticed that the tumble center is not out of the FOV at the same CAD for the different conditions; it is out of the FOV is 61 and 67 CAD bTDC for respectively fast and slow transient conditions, later that in stationary regime, i.e 72 CAD bTDC. Therefore, the acceleration of the regimes slightly slows down the motion of the tumble without affect its intensity and its dissipation.

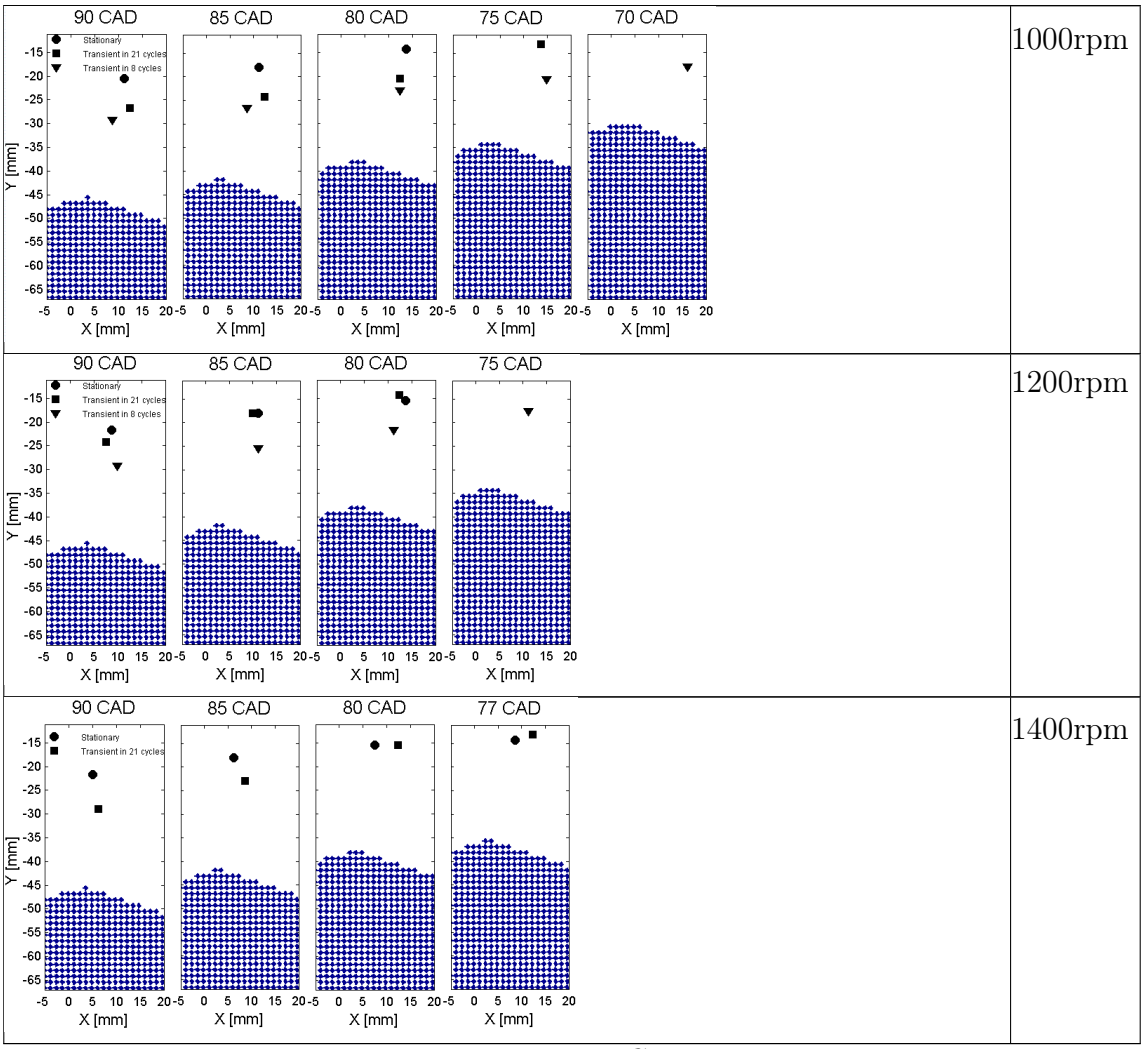

Figure 6.28, *Cont.*

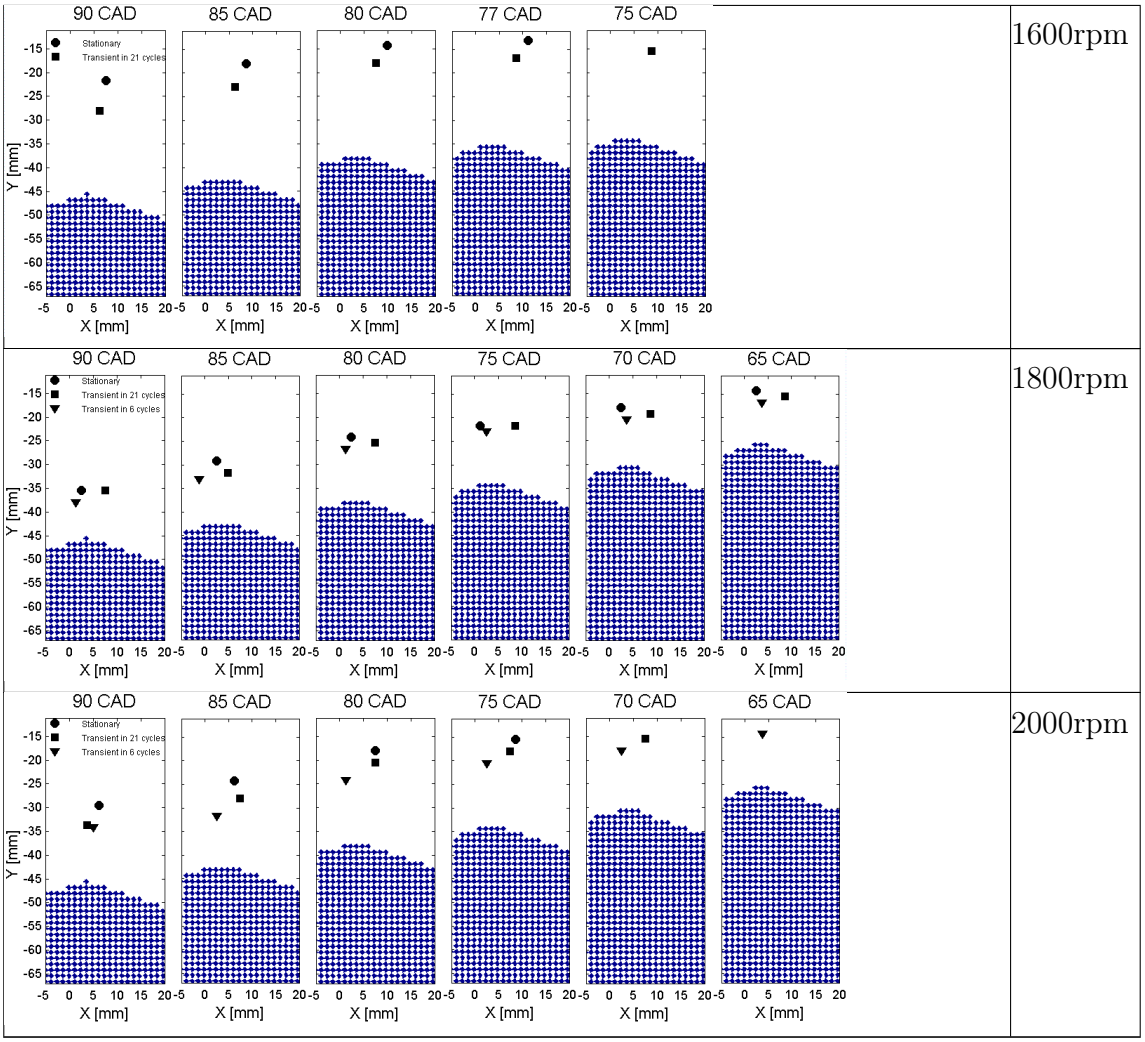

Figure 6.28: Position of the tumble center relative to the piston position for all transient and stationary conditions.

6.3 Application of Bivariate 2D-EMD

As previously explained in Chapter 1, the in-cylinder instantaneous velocity can be decomposed to three parts: mean flow, coherent fluctuations associated with cycle-to-cycle fluctuations of the mean flow and random turbulent fluctuations. Several studies used POD to distinguish different parts of in-cylinder velocity field as (Baby et al. (2002) [7], Fogleman et al. (2004) [56], Druault et al. (2005) [43], Roudnitzky et al. (2006) [164], Foucher et al. (2008) [57], Voisine et al. (2011) [188], Chen et al. (2012) [27]).
POD is a statistical approach deal with convergence criteria that restricts its interest for inherently unsteady conditions. Another difficulty in POD analysis is determination of the cutoff modes to separate the mean flow field, large-scale energetic structure, and high frequency turbulent fluctuations.
EMD is an intuitive, direct, and adaptive with a posteriori-defined basis function derived from the data themselves so it is quite adapted to analyze both nonlinear and nonstationary dynamics. When a given instantaneous velocity field is decomposed by EMD, the feature of the flow large-scale structure appears in the last modes i.e. low frequency part and causes "sudden" jump (and no progressive evolution) in the modes energy contents profile. Hence the flow large-structure can be separated from random turbulent fluctuations i.e. high frequency part.

In this part of study the proposed Bivariate 2D-EMD, validated in section 4.3, is applied on experimental in-cylinder velocity fields, in order to assess the potential of this approach in separation of turbulent fluctuations from flow large-scale organized motion. Due to a lack of time and the long CPU time to calculate EMD (about 7 hours CPU time for a velocity field of 127×127 data points), the decomposition requires 7 hours CPU time), Only the results from EMD analysis of the 1400 rpm case is presented for both stationary and transient conditions and compare to the ones obtained by POD analysis according to 120 consecutive cycles, for the stationary conditions.
As remind, the size of velocity fields is $55.81 \times 75.65\ mm^2$ within 61×45 vector points with $1.24\ mm$ spatial resolution.

In Bivariate 2D-EMD analysis, two adjacent white Gaussian noise channels are used. The noises have a same power and in each sifting process their variance is equal to the mean variance of the two principal input signals i.e. $U$and V velocity components. To compute the mean envelope, input multi-components signal is projected on 64 directions with the projection density defined by $\alpha = 0.3$. For Sifting process the Mean-value stoppage criterion with $(0.05, 0.5, 0.05)$ is used and the number of ensemble realizations NE is set to 100.

6.3.1 Comparison between EMD and POD

To compare the results obtained by EMD and POD, the in-cylinder velocity fields obtained for 6 CAD: at mid-compression stroke, 215 CAD bTDC, BDC, 125 CAD bTDC, mid-compression stroke and 70 CAD bTDC were chosen.
In EMD flow decomposition, the separation between turbulent fluctuations and organized motion is done by using the energy criterion described in Eq (4.9). The Figure 6.29 present the Energy contents as function of the EMD mode for the instantaneous

velocity field obtained at the 6 previously defined CAD. The number of modes is not constant but for all cases, that the last mode has the most energy content, considered as the large-scale organized motion. It should be also noticed that the energy content for the last mode is more important during the intake stroke than during the compression.

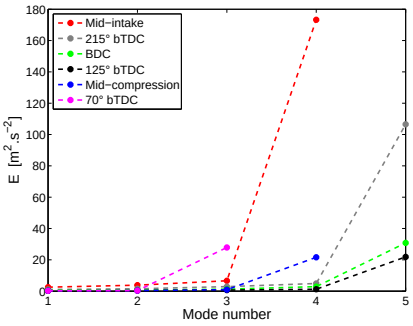

Figure 6.29: Energy contents as function of the EMD mode for the 6 instantaneous velocity fields

The POD analysis is performed by Davis software (LaVision) and the first modes that contained the most part of the energy, were considered as in-cylinder large-scale organized motion. In Figure 6.30 to 6.35, the low frequency and the high frequency velocity fields resulting from Bivariate 2D-EMD and POD analysis are presented for the 6 CADs.

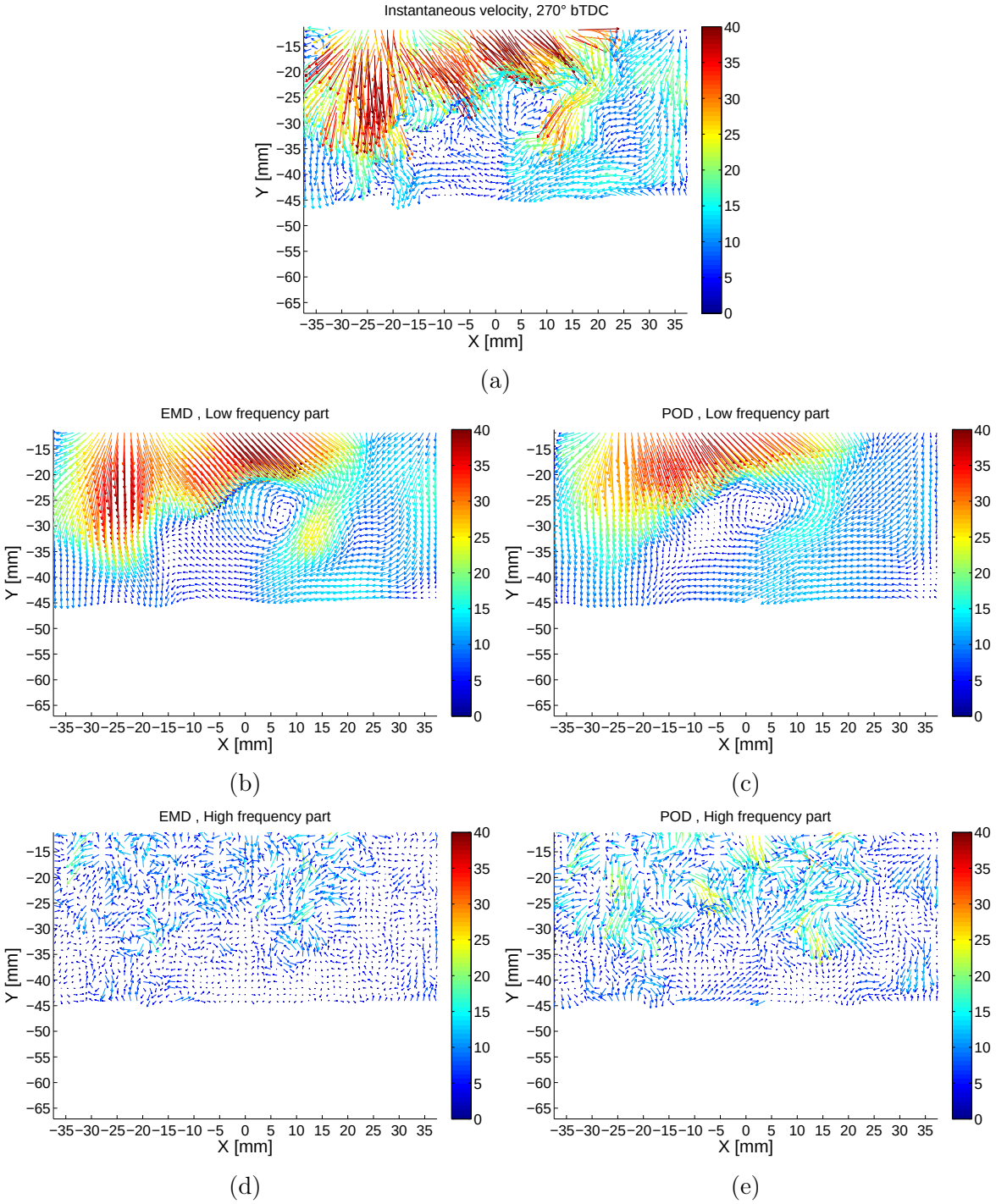

Figure 6.30: Low and high frequency velocity fields resulted from EMD and POD analysis at mid-intake stroke, stationary condition, 1400 rpm engine speed.

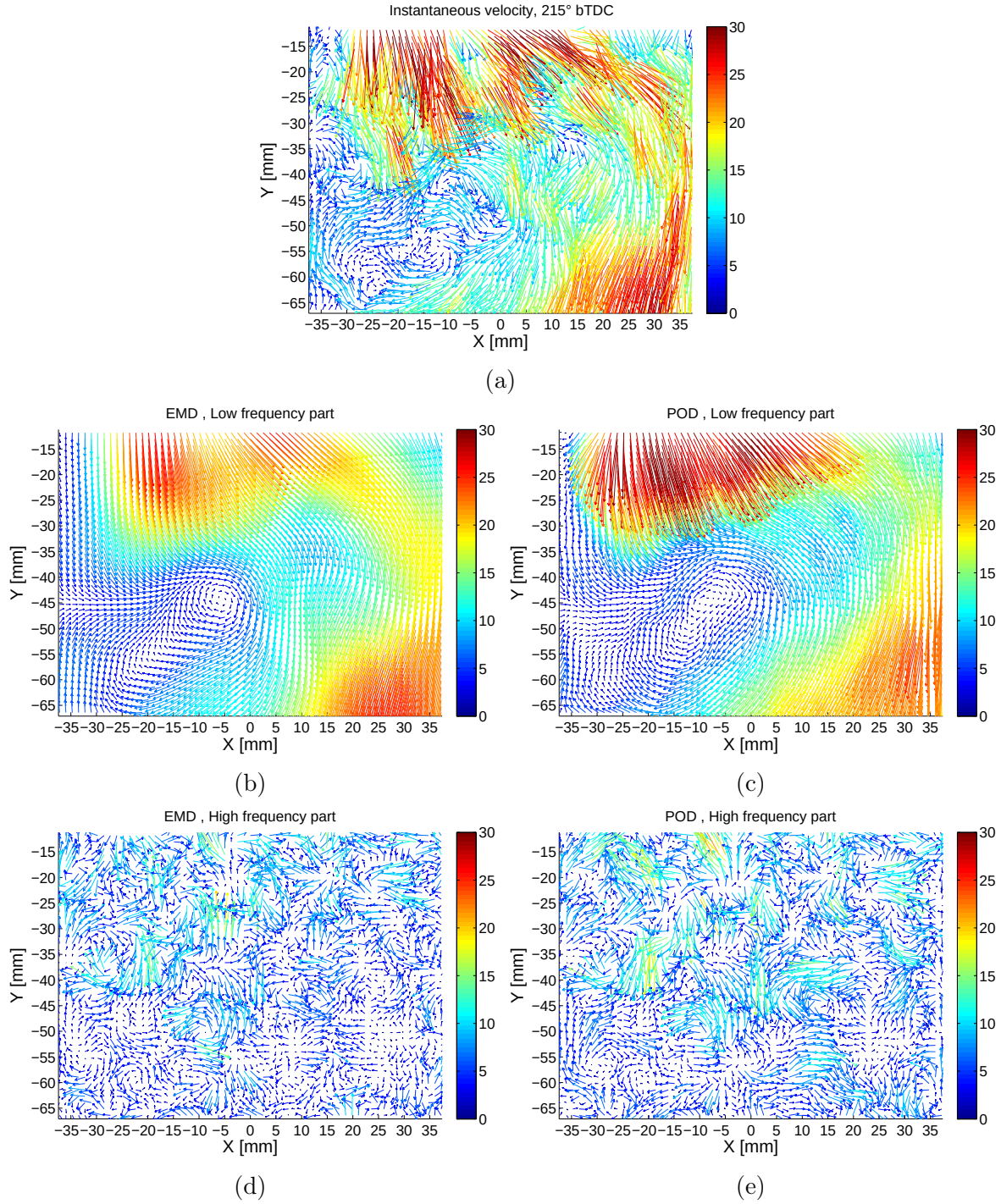

Figure 6.31: Low and high frequency velocity fields resulted from EMD and POD analysis at 215 CAD bTDC, stationary condition, 1400 rpm engine speed.

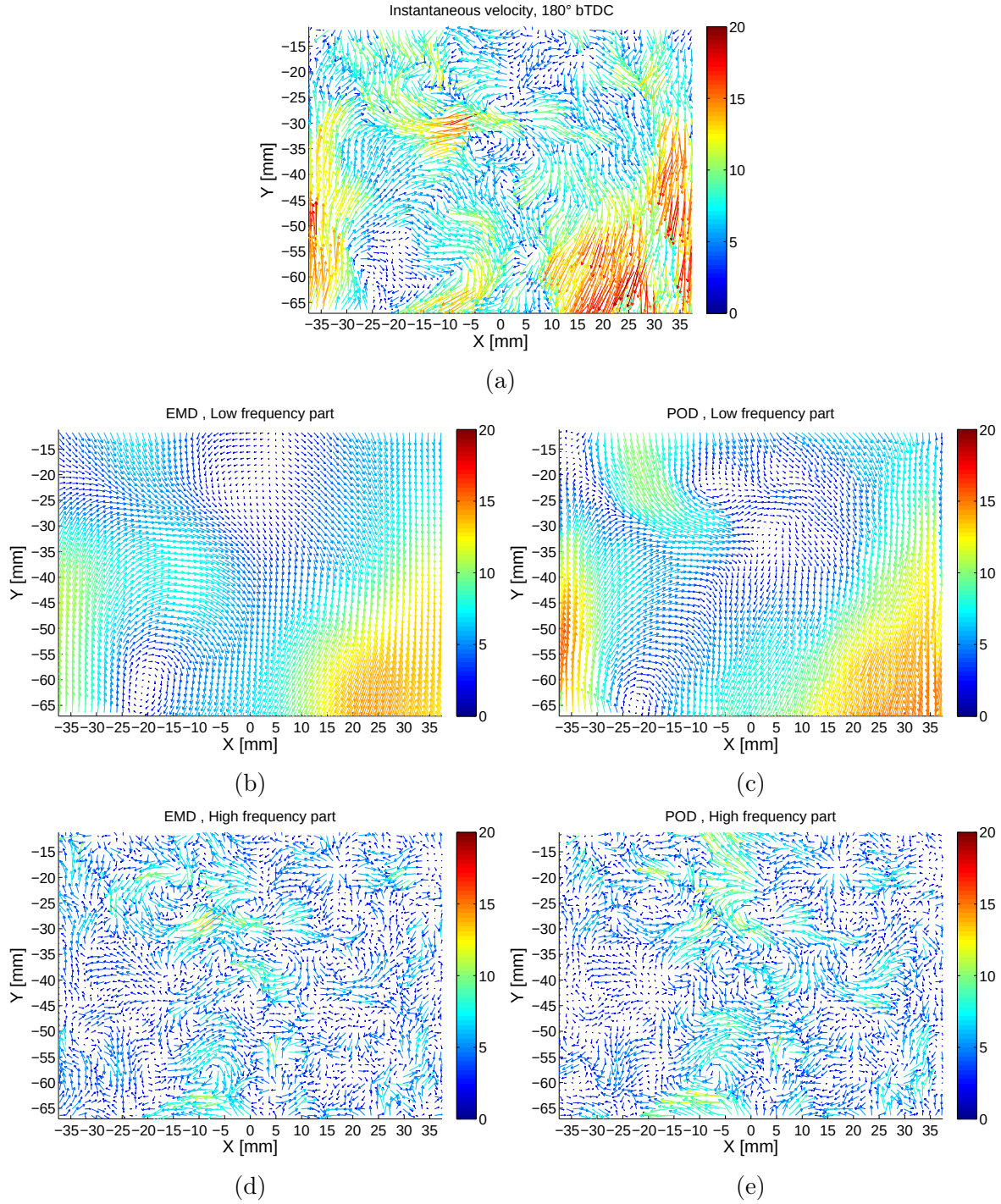

Figure 6.32: Low and high frequency velocity fields resulted from EMD and POD analysis at BDC, stationary condition, 1400 rpm engine speed.

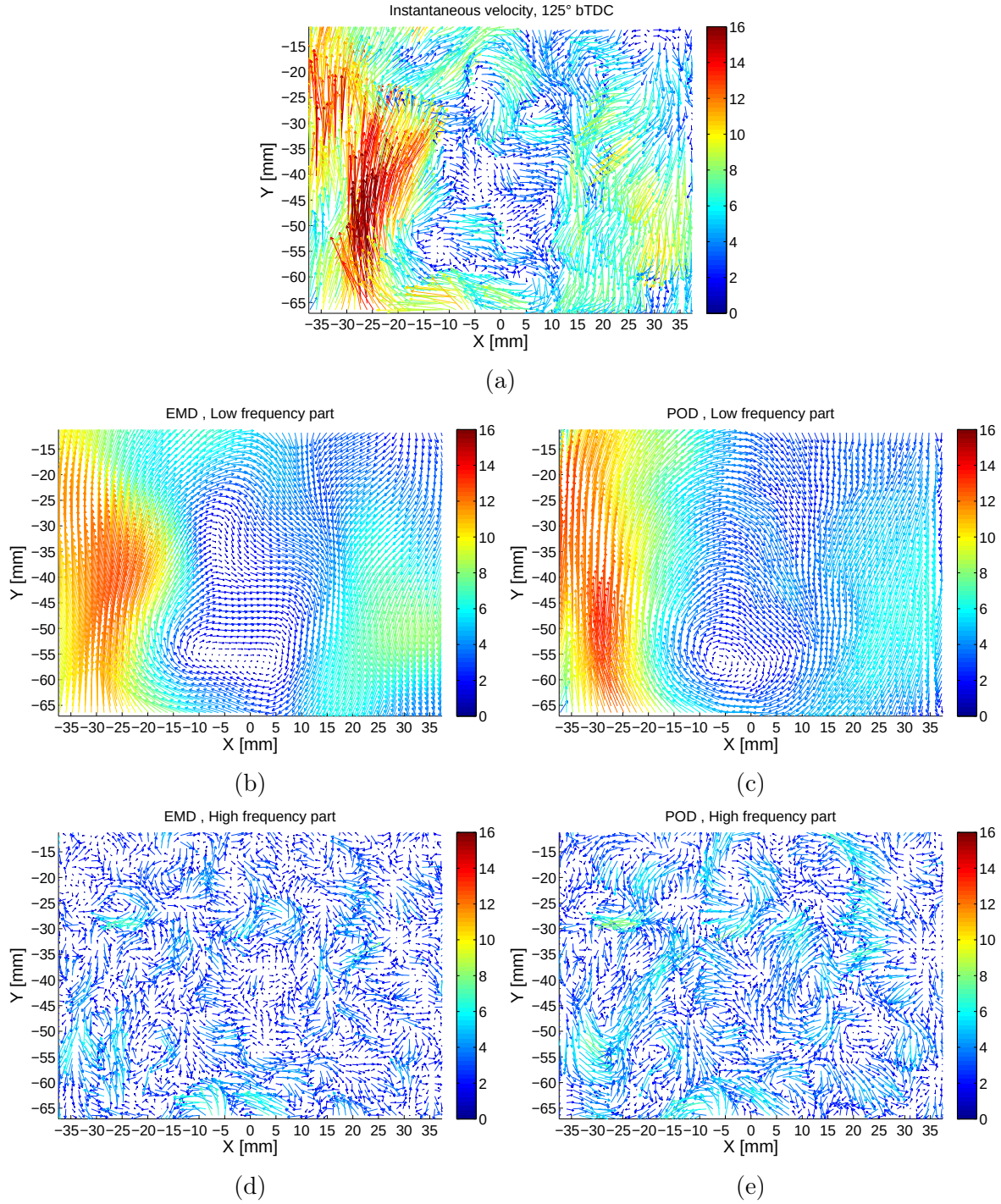

Figure 6.33: Low and high frequency velocity fields resulted from EMD and POD analysis at 125 CAD bTDC, stationary condition, 1400 rpm engine speed.

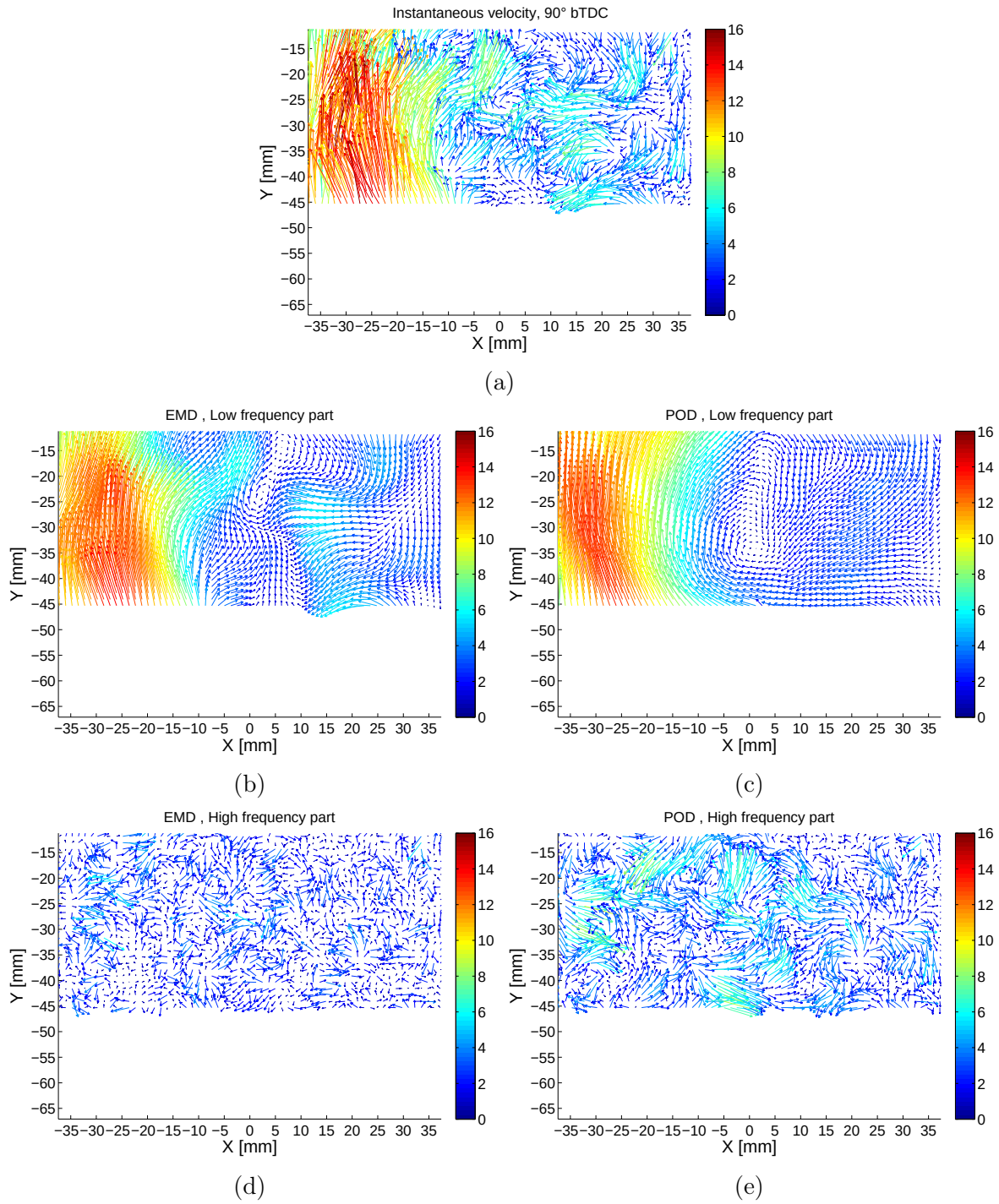

Figure 6.34: Low and high frequency velocity fields resulted from EMD and POD analysis at mid-compression stroke, stationary condition, 1400 rpm engine speed.

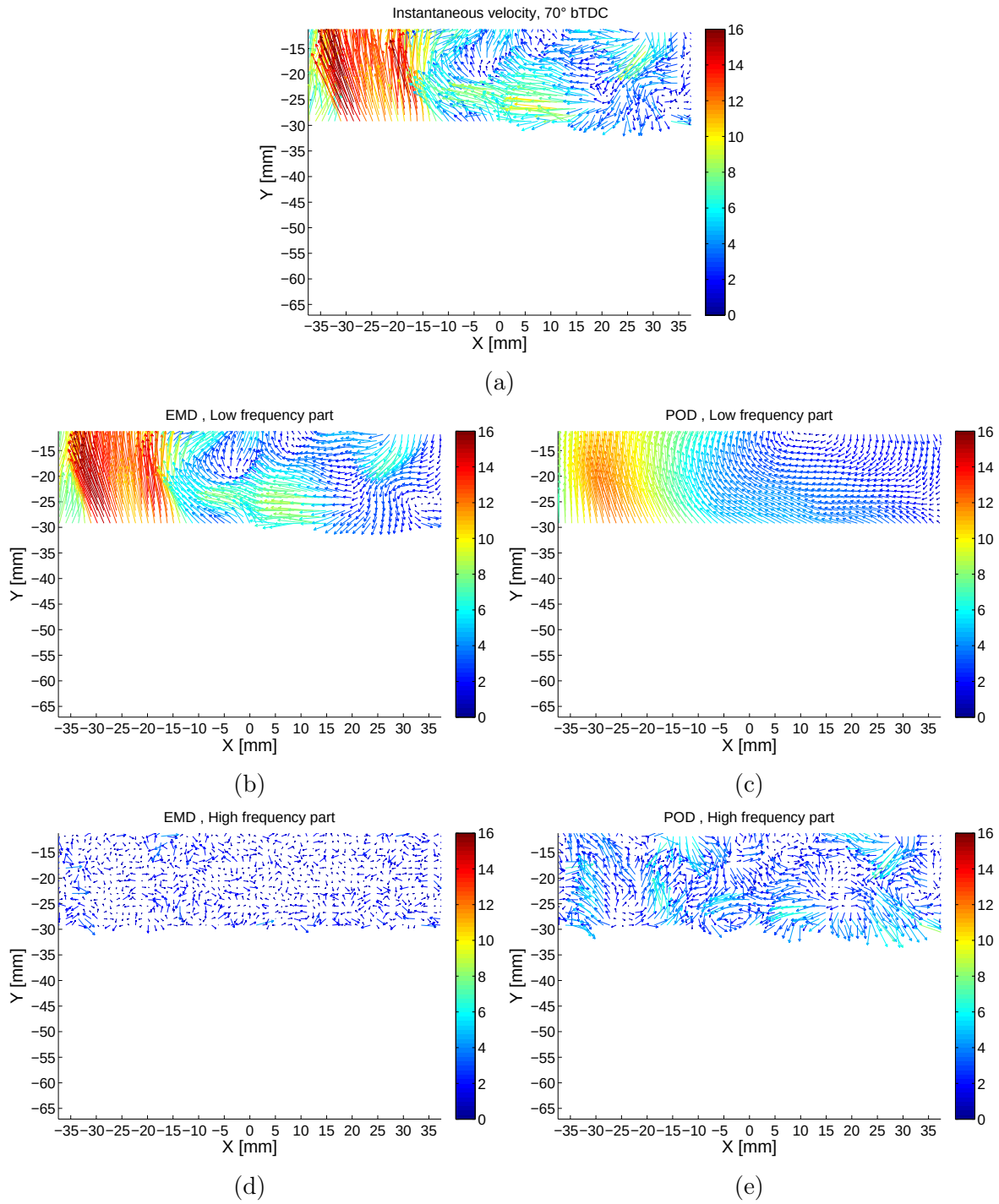

Figure 6.35: Low and high frequency velocity fields resulted from EMD and POD analysis at 70 CAD bTDC, stationary condition, 1400 rpm engine speed.

By assuming that the results of in-cylinder velocity field decomposition obtained by POD analysis are the real ones, the relative mean square error can be computed to evaluate the relative accuracy of the EMD results, as follow:

$$\sigma = \frac{\sum_{i=1}^{n_x}\sum_{j=1}^{n_y}\left|\mathrm{U}_{POD}(x_i,y_j)-\mathrm{U}_{EMD}(x_i,y_j)\right|^2}{\sum_{i=1}^{n_x}\sum_{j=1}^{n_y}\left|\mathrm{U}_{POD}(x_i,y_j)\right|^2} \tag{6.3}$$

Where n_x and n_y are the total numbers of the points in 2D velocity field in x and y directions and symbol $|.|$ denotes absolute value. U_{POD} and U_{EMD} represent the velocity obtained by POD and EMD analysis respectively. This relative difference computed for both high and low frequency parts of the different velocity fields are presented in Table 6.17.

CAD	High frequency part	High frequency part
270	25	9.1
215	17	3.4
180	14	4.2
125	15	3
90	29	5
70	50	10

Table 6.17: Relative mean square difference (%) for different parts of flow estimated by EMD approach, with supposing the results of POD analysis are the reality.

For all cases, the relative difference for the high frequency part is higher than that for low frequency part, i.e. the global organized motion. The maximum is reached at the mid-intake and mid-compression CAD, this is mainly due to the low velocity magnitude in high frequency part that a small difference leads to large error, indeed a small value in denominator of Eq (6.3).

In Figure 6.36 the power spectra of the high frequency flow obtained by Bivariate 2D-EMD and POD, at different CADs, are presented. They are computed by using Welch's method with 50% overlapping segments and Hann window function. The FFT is computed by considering the entire velocity fields, i.e. 61 points for U components that correspond to the cylinder bore but for V components it varies as a piston position.
For all cases, in the highest wave number regions, corresponding to the dissipation and Kolmogorov scales (the scale below which the dissipation becomes important) and also in the turbulence inertial subrange, the energy spectra of velocity fields are globally superimposed to each other for both U and V components.
Whereas in the range of small wavenumber associated to turbulent integral scale, the energy spectra of the velocity field obtained by Bivariate 2D-EMD is for all cases, below that computed by POD as well as directly from initial velocity fields.

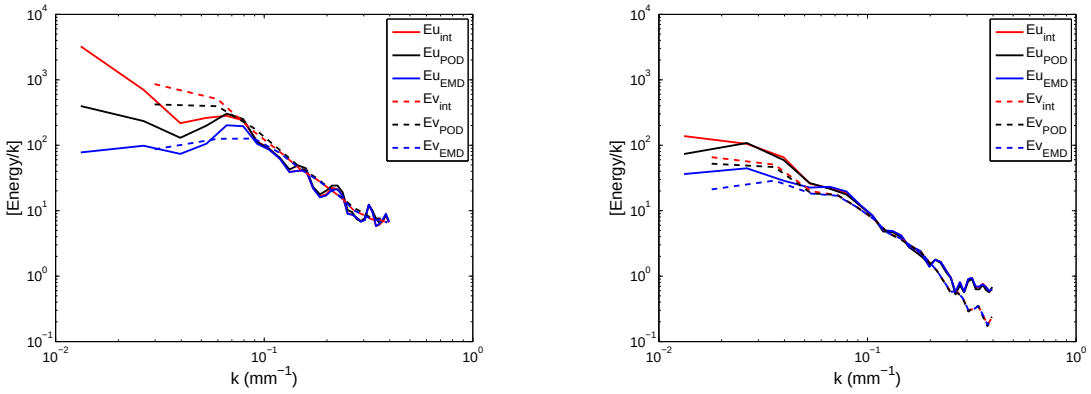

(a) Mid-intake

(b) 125 CAD

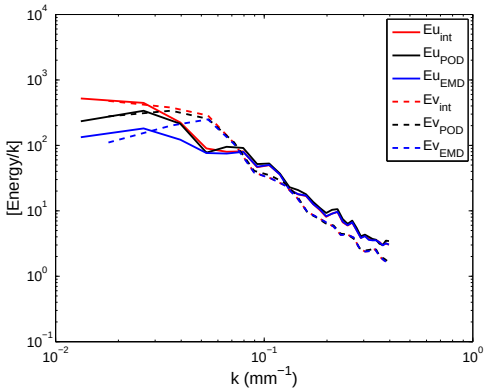

(c) 215 CAD

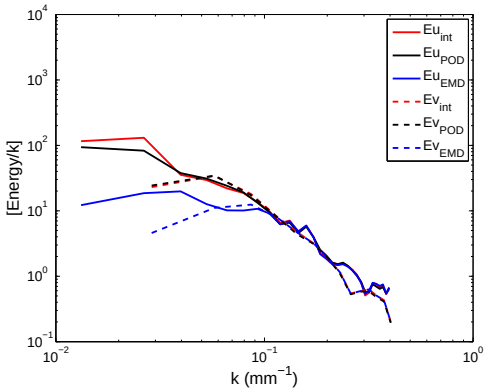

(d) Mid-compression

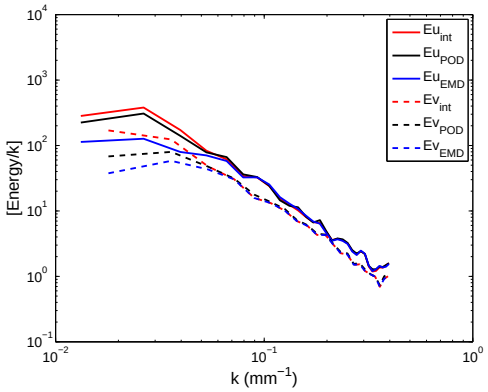

(e) BDC

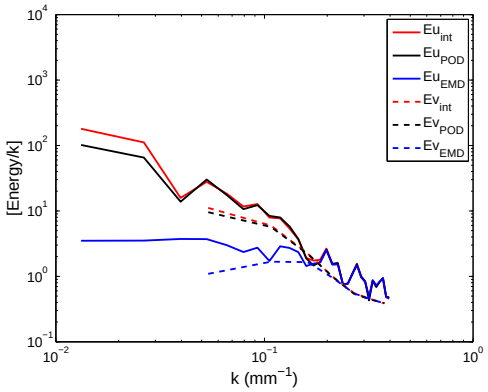

(f) 70 CAD

Figure 6.36: Power spectrum of high frequency part obtained by EMD and POD at different CAD for both U and V components, the ones of instantaneous velocity fields are also plotted.

It is interesting to notice in mid-compression stroke and 70 CAD bTDC, Figures 6.36d and 6.36f respectively, the difference between power spectrum of the velocity field obtained by Bivariate 2D-EMD and that captured by POD analysis become more important compared to other CAD and the spectra of turbulent velocity captured by POD is very close to that for instantaneous velocity field.
The two components U and V of the low frequency part of the velocity field at BDC, determined from Bivariate 2D-EMD and POD are compared in Figure 6.37.

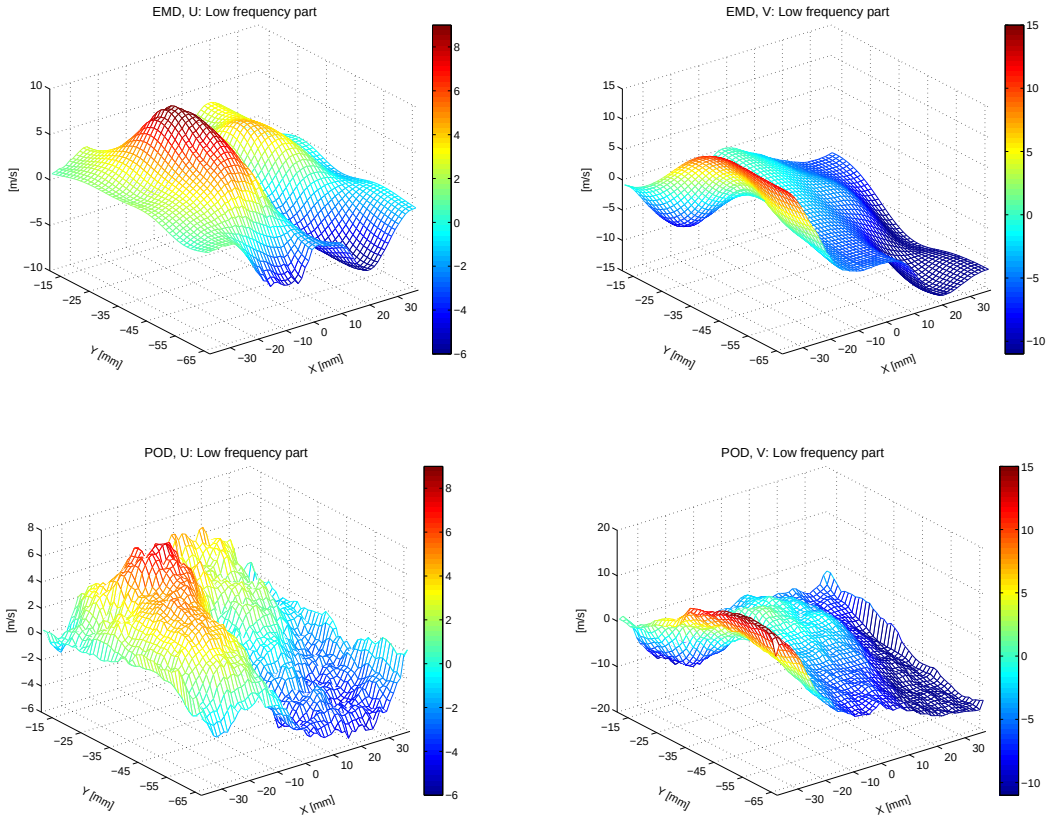

Figure 6.37: Low frequency part of velocity field at BDC, for U and V components, from Bivariate 2D-EMD and POD analysis.

The global evolution in 2D space is quite similar between two approaches, for both U and V components but some small fluctuations are present in case of POD analysis. It is important to notice in Bivariate 2D-EMD approach the feature of flow large-scale organized motion is appeared in one IMF mode of the decomposition, the last one, but in POD analysis, the energy of this motion is distributed in different modes. As mentioned by Chen et al. (2012) [27], " the flow pattern of every structures from every velocity fields (background and vortex) is contained in every modes. The modes are not themselves individual coherent structures as some times implied by verbal descriptions in the literature ".

6.3.2 Application of Bivariate 2D-EMD on transient in-cylinder velocity fields

In this part, the Bivariate 2D-EMD is used to separate high frequency flow fluctuations from the in-cylinder flow organized motion when the engine operates in transient condition i.e. acceleration from 1000 to 2000 rpm in 21 cycles. Due to a lack of time, only the cycle in which the mean engine speed correspond to 1400 rpm is presented.
Similar to stationary regime the velocity fields at mid-compression stroke, 215 CAD bTDC, BDC, 125 CAD bTDC, mid-compression stroke and 70 CAD bTDC are analyzed. Each of these velocity field are decomposed by Bivariate 2D-EMD then the energy criterion for each field are computed, see Figure 6.38.

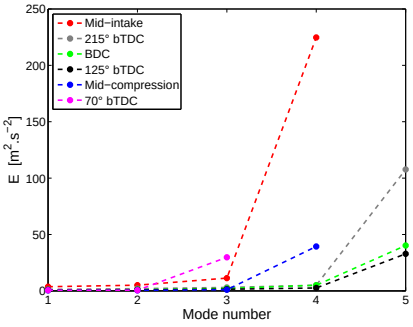

Figure 6.38: Energy contents as function of the EMD mode for the 6 instantaneous velocity fields.

It is observed for all cases, the energy of the last mode increases abruptly compared to the first ones hence it is considered as an organized motion and the remained first modes construct turbulent part of the instantaneous velocity field. This separation for different velocity field is presented in Figure 6.39 to 6.44. Also the power spectra for two components U and V of estimated turbulent parts (high frequency part) are compared to ones determined from instantaneous velocity field.

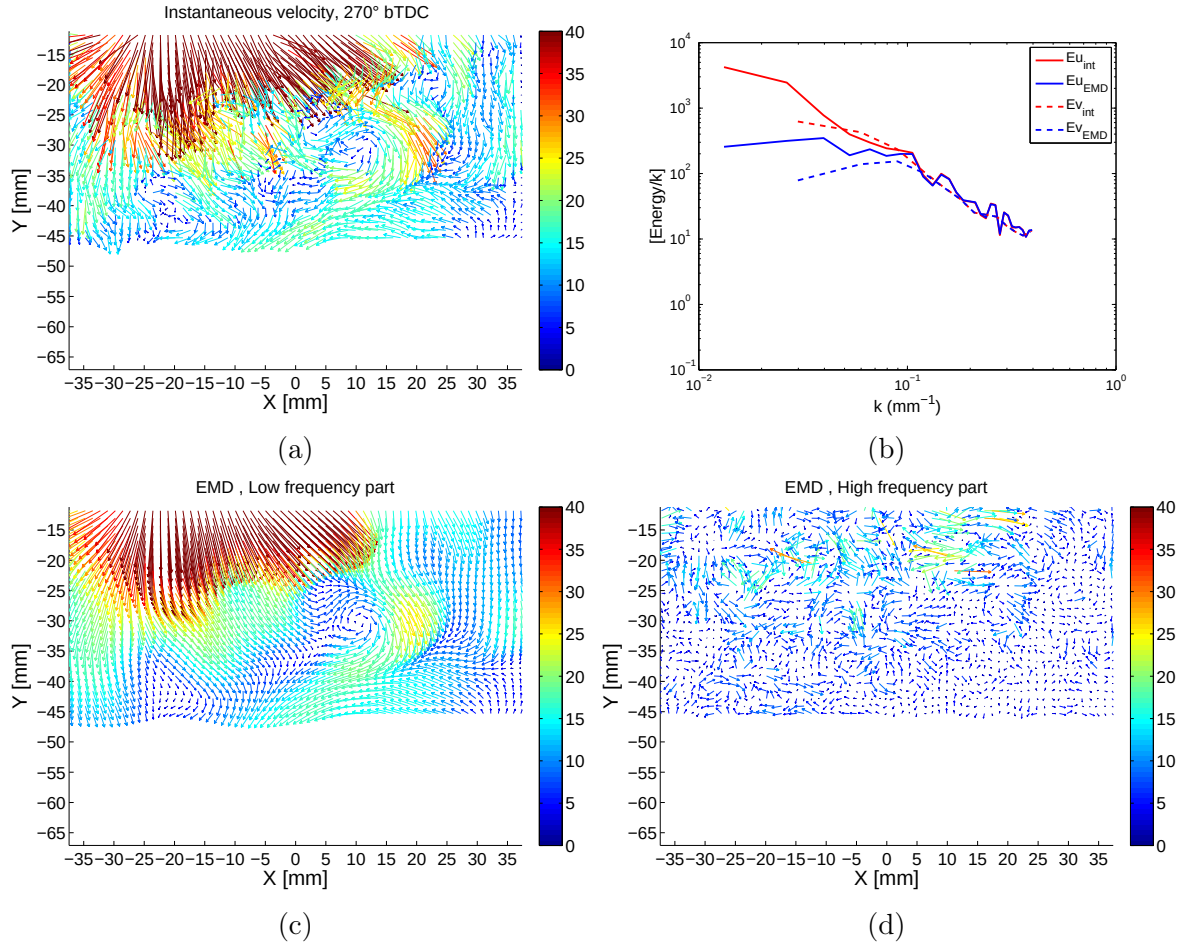

Figure 6.39: Results of EMD analysis, Mid-intake stroke, Cycle 10 (1400 rpm), Slow transient condition.

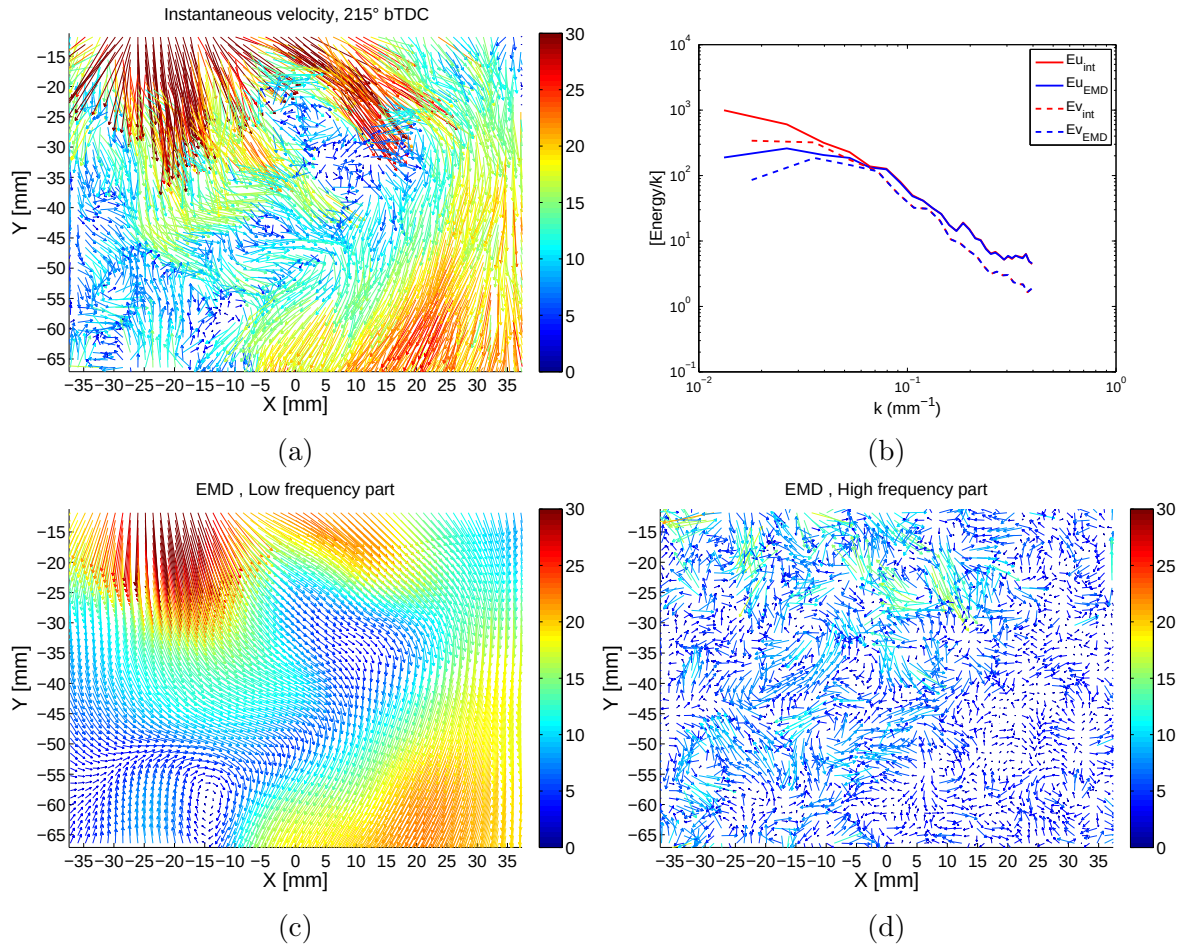

Figure 6.40: Results of EMD analysis, 215 CAD bTDC, Cycle 10 (1400 rpm), Slow transient condition.

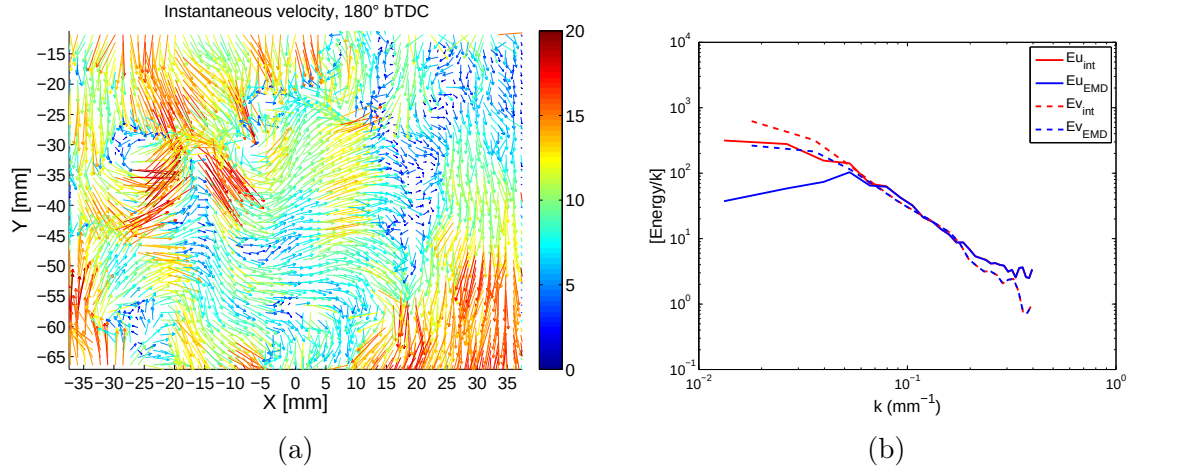

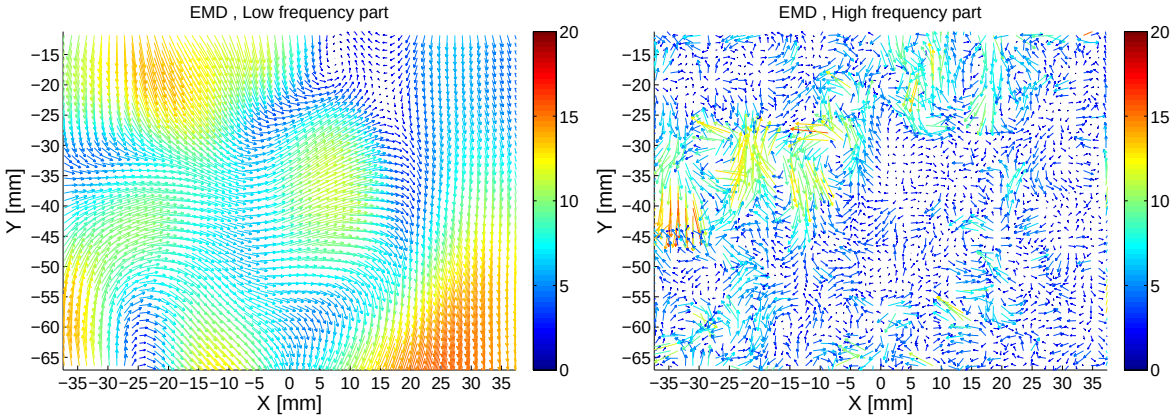

(c) (d)

Figure 6.41: Results of EMD analysis, BDC, Cycle 10 (1400 rpm), Slow transient condition.

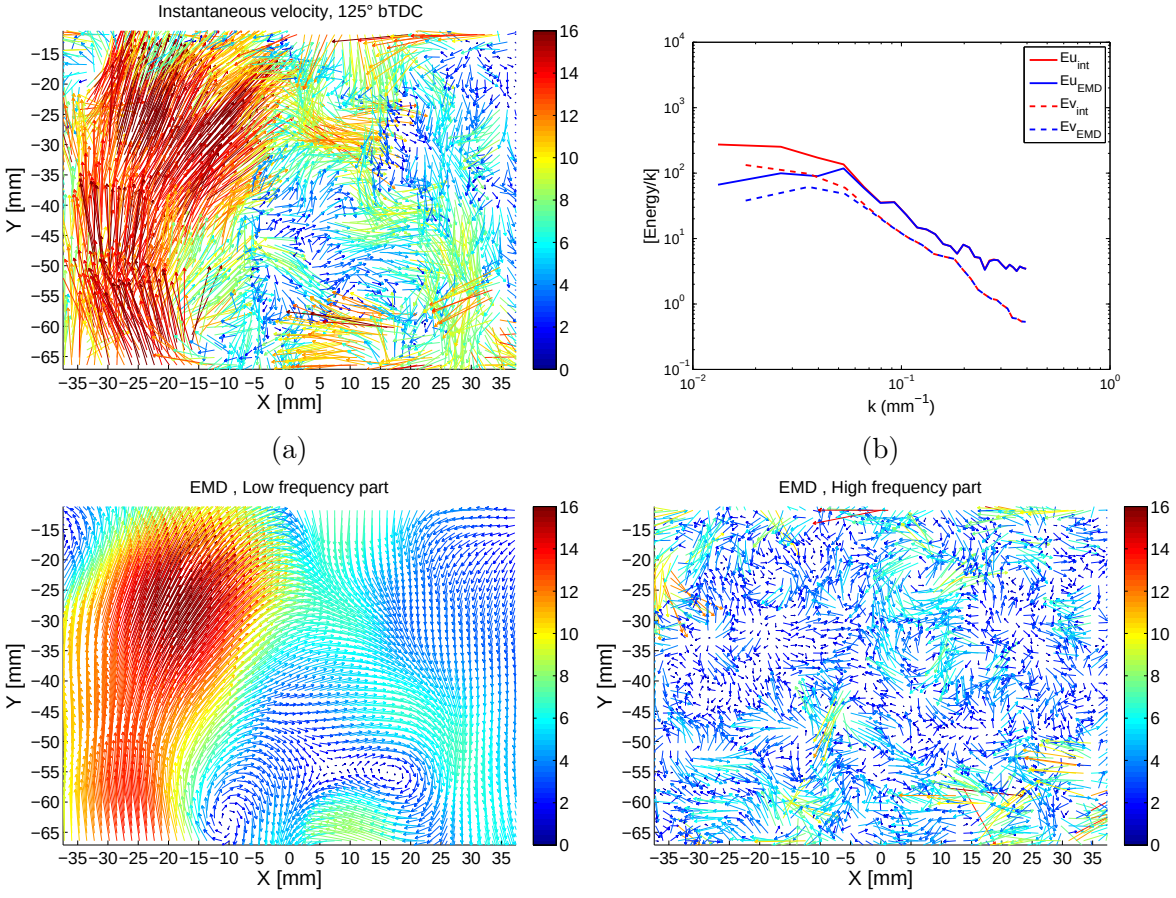

(a) (b)

(c) (d)

Figure 6.42: Results of EMD analysis, 125 CAD bTDC, Cycle 10 (1400 rpm), Slow transient condition.

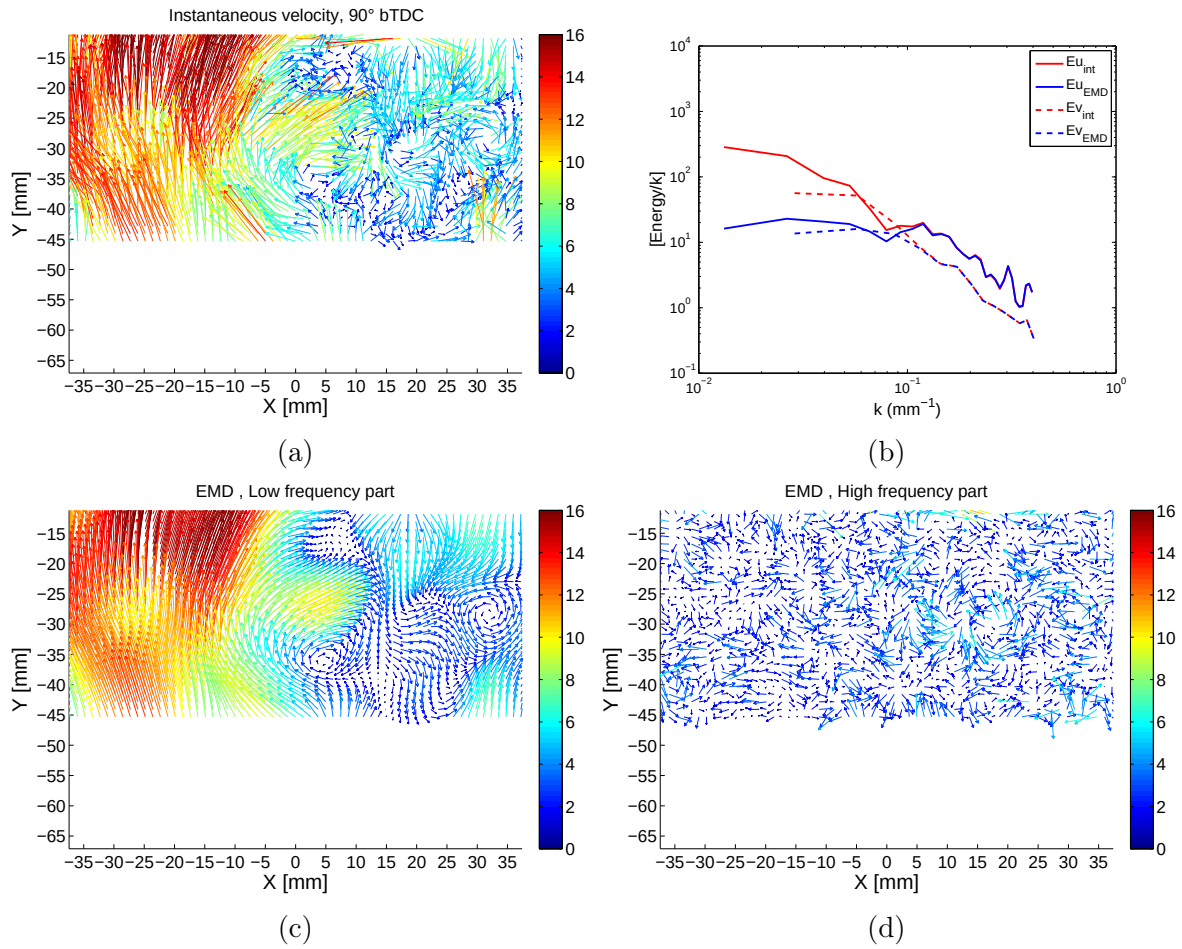

Figure 6.43: Results of EMD analysis, Mid-compression stroke, Cycle 10 (1400 rpm), Slow transient condition.

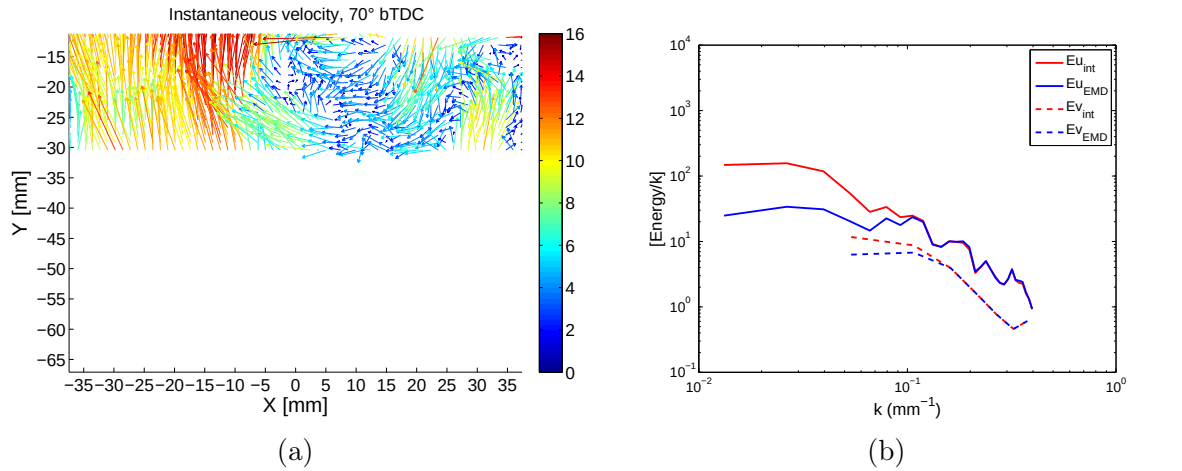

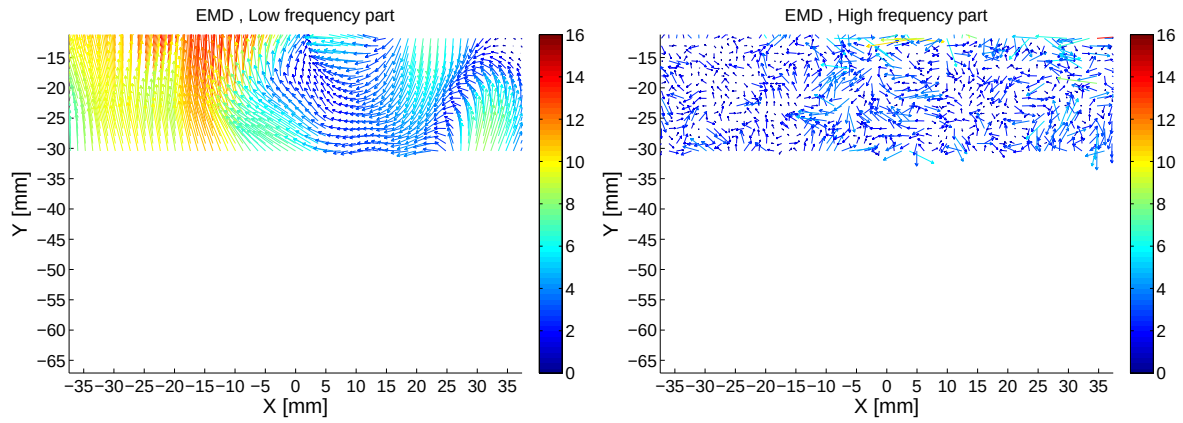

(c) (d)

Figure 6.44: Results of EMD analysis, 70 CAD bTDC, Cycle 10 (1400 rpm), Slow transient condition.

From the latest results, by visual inspection one can notice how the separation between low and high frequency parts of the velocity fields is well done, by applying Bivariate 2D-EMD on an instantaneous velocity field and allows the extraction of the in-cylinder organized motion.
There is a good similarity between the flow high and low frequency parts identified by Bivariate 2D-EMD and the ones obtain by POD analysis, however it is obvious for profound analysis such a comparison between two approaches should be performed by means of synthetic signals.

General conclusion and perspectives

The main purpose of this phd thesis is to assess the performance of Empirical Mode Decomposition (EMD) for analyzing unsteady flow in order to separate turbulent fluctuations from in-cylinder large-scale organized motion. The great interest of such distinction is to estimate turbulent intensity that has a great influence on flame propagation and combustion development in SIDI engines but also to help for a better understanding of cycle-to-cycle variation of in-cylinder mean flow that highly affects the performance of IC engines. The EMD is quite suitable for analyzing both nonlinear and non-stationary data, however this approach has not yet developed by signal processing community to decompose bivariate (or trivariate) 2D data.
In this study, we proposed Bivariate 2D-EMD for decomposition of two dimensional velocities field in which the velocity vector has two components i.e. vertical and horizontal one. To validate this approach, first it was applied on an experimental homogeneous and isotropic turbulent flow (HIT), perturbed by a synthetic Lamb-Ossen vortex to simulate the feature of in-cylinder organized motion. Through different test cases, the scale, the amplitude and the position of synthetic vortex were changed according to turbulent velocity field. By applying an energy criterion on the modes results from decomposition process, the initial HIT flow was separated from synthetic perturbation. Based on this investigation the Bivariate 2D-EMD hold great promise as a new tool to separate large-scale organized motion i.e. flow low frequency part from random turbulent fluctuations i.e. high frequency part in an instantaneous two dimensional velocity field.
The fundamental point is that by Bivariate 2D-EMD approach, the turbulent part of a given instantaneous velocity field is separated from organized motion just based on the instantaneous velocity field itself however using POD approach this separation is performed based on several cycles. Hence, the POD needs a number of cycles to represent statistical average and the obtained results can be under influence of the events that are occurred in others realization. This feature of EMD made it as a powerful tool for analyzing the phenomena that are intrinsically transient. The proposed method could be used for analyzing 2D velocity fields with two or three components obtained in different configurations as channel flows, flow motion around a circular cylinder and above the airfoils.

In this thesis the Bivariate EMD was used to separate coherent structure from homogeneous isotropic turbulence. The velocity field under analysis was a two-component turbulence time series i.e. temporal evolution of a correlated horizontal and axial velocity at a given point in flow. The coherent structure was simulated by a sinusoidal wave that its amplitude and frequency got varied. This investigation proved in the case where the frequency of coherent structure is in a range lower than the frequency of integral scale of turbulent flow, the HIT flow can be perfectly separated from coherent structures

otherwise just the fast dynamic of HIT is detectable.
In addition in this work, the performance of different type of EMD (standard EMD, EEMD, CEEMD and CEEMDAN) and the effects of stopping criterion for sifting process in the decomposition quality of a mono-component turbulence time series were compared. The velocity field under analysis contained a homogeneous and isotropic turbulence that is perturbed by a synthetic Lamb-Ossen vortex that simulate in-cylinder organized motion. The results show applying modified versions of standard EMD cannot improved the quality of decomposition in such a perturbed turbulent flow and even leads to mode-mixing in the results of decomposition. Using standard EMD with Fixed sifting time stoppage criterion for this type of signal is quite appropriate.

In the second part of this thesis, for the first time the evolution of in-cylinder flow during transient engine operation was measured by means of High speed 2D-2C PIV. The velocity fields are obtained within tumble plane in a transparent mono-cylinder DISI engine. The transient regime consists of engine acceleration from 1000 to 2000 rpm during 8, 12, 16 and 21 consecutive cycles. Flow-fields are also obtained in the case of stable regime, 1000, 1200, 1400, 1600, 1800 and 2000 rpm, in order to provide some comparisons. This part of study has two principal objectives, first comparing the evolution of the Tumble motion and its intensity, during the intake and the compression stroke, in transient conditions to stable regime and second, providing a data base to validate CFD results.

The analysis of the results was focused on extreme conditionss: Fast transient condition, i.e. engine acceleration during 8 cycles and slow transient condition i.e. acceleration during 21 cycles. The results showed the global evolution of tumble center trajectory and tumble ratio in transient conditions are similar to ones in stable regime but some difference were observed. It was observed for all engine speeds the tumble center after mid-compression stroke in transient conditions is below that in stable regimes and this feature is more prominent in fast transient condition compared with lower one. Also the acceleration of the engine speed slightly slow down the motion of tumble toward TDC however it has no influence on its intensity and dissipation.
In addition in one given engine speed, the in-cylinder mean flow pattern (phase-averaged velocity field) in transient conditions was compared in details with corresponding ones in stable regimes and several difference and some similitudes were reported.
In the last part, Bivariate 2D-EMD was first applied on real data i.e. in-cylinder flow when engine operated in stationary condition as well as transient regimes, for one case. The results obtained in stationary condition were compared with ones from POD analysis.

Future works:

To resolve turbulent integral length scales of in-cylinder flow the PIV measurements with higher spatial resolution than that in this study are required for future investigations. In addition to study the effects of in-cylinder flow in transient regime on flame propagation and to estimate turbulence intensity in its vicinity, the velocity field should be measured within the cylinder clearance volume and near the spark plugs.
In-cylinder flow is quite complex and three-dimensional hence for better understanding its evolution during transient regimes and to study its influence on combustion process, the third components of velocity vector has to be considered so for perspective Stereoscopic

PIV (2D-3C) or multi-planner PIV within the axe parallel and perpendicular to tumble plane could be interesting to be done.

The obtained results by Bivariate 2D-EMD analysis are encouraging as different steps for validation were done. To confirm its ability to analyze different types of flow in fluid mechanics, it should be compared with other appropriates methods for analyzing non-stationary phenomena as wavelet analysis. The proposed Bivariate 2D-EMD needs to be optimized and its algorithm should be parallelized in order to reduce computation time. Indeed for a given velocity field that contains 127×127 data points, the decomposition requires 7 hours CPU time. Last and next step, the Bivariate 2D-EMD will be implemented for LES results analysis to help the interpretation of the results and to compare more easily them with the experimental results.

Conclusion générale et perspectives

(Version Française)

L'objective principal de cette thèse est d'évaluer la performance du la décomposition modale empirique (EMD) pour analyser l'écoulement instationnaire afin de séparer les fluctuations turbulente du mouvement organisé à grande échelle dans le cylindre du moteur. Le grand intérêt d'une telle séparation est d'estimer l'intensité turbulente qui affecte fortement la propagation de la flamme et le développement de la combustion dans les moteurs á allumage commandé, mais aussi de mieux comprendre la variation cyclique d'écoulement moyen dans le cylindre qui affecte fortement les performances des moteurs à combustion interne. L'EMD est tout à fait approprié pour analyser des données instationnaires et non-linéaires, cependant cette approche n'a pas encore été développée par la communauté de traitement du signal pour décomposer des données bidimensionnelles bivariées (ou trivariables).
Dans cette étude, nous avons développé et adapté Bivariate 2D-EMD pour décomposer des champs de vitesses (2D) dans lequel le vecteur de vitesse a deux composantes, vertical et horizontal. Pour valider cette approche, il a d'abord été appliqué et validé sur un écoulement turbulent homogène et isotrope (THI) expérimental, perturbé par un tourbillon synthétique de type Lamb-Ossen qui simule la caractéristique du mouvement organisé dans le cylindre. Par différents cas tests, l'échelle, l'amplitude et la position du tourbillon synthétique ont été modifiées en fonction du champ de vitesse turbulente. En appliquant un critère d'énergie sur les résultats des modes issus du processus de décomposition, l'écoulement THI initial a été séparé de la perturbation synthétique. Basé sur cette étude, le Bivariate 2D-EMD est très prometteur en tant que nouvel outil pour séparer un mouvement organisé à grande échelle (la partie basse fréquence d'écoulement) de la fluctuation turbulente aléatoire (la partie haute fréquence) dans un champ de vitesse bidimensionnel instantané. Le point fondamental est que par cette approche, la partie turbulente d'un champ de vitesse instantané est séparé du mouvement organisé juste basé sur le champ de vitesse instantanée lui-même, alors que la décomposition en modes propres orthogonaux (POD) nécessite plusieurs cycles pour représenter la moyenne statistique. Cette caractéristique de l'EMD en fait un outil puissant pour analyser les phénomènes intrinsèquement transitoires. La méthode proposée pourrait être utilisée pour analyser le champ de vitesse 2D avec deux ou trois composantes obtenus dans différentes configurations comme des écoulements de canal, l'écoulement autour d'un cylindre circulaire et au-dessus des hydrofoils.

Dans cette thèse, l'EMD bivariate a été utilisée pour séparer la structure cohérente de la turbulence homogène et isotrope. Le champ de vitesse analysé était une série temporelle de turbulence à deux composantes, c'est-à-dire l'évolution temporelle d'une vitesse hor-

izontale et axiale corrélée à un point donné d'écoulement. La structure cohérente a été simulée par une onde sinusoïdale dont l'amplitude et la fréquence ont été variée. Cette investigation s'est prouvée dans le cas où la fréquence de la structure cohérente est inférieure à la fréquence de l'échelle intégrale d'écoulement turbulent, le THI peut être parfaitement séparé des structures cohérentes sinon seule la dynamique rapide du THI est détectable. En outre, dans ce travail, la performance de différents types d'EMD (standard EMD, EEMD, CEEMD et CEEMDAN) et les effets du critère d'arrêt pour le procédé de tamisage (Sifting process) sur la qualité de décomposition d'une série temporelle de turbulence mono-composant ont été comparés. Le champ de vitesse analysé contenait une turbulence homogène et isotrope, perturbée par un tourbillon synthétique de type Lamb-Ossen simulant mouvement organisé dans le cylindre. Les résultats montrent que l'application de versions modifiées de standard EMD ne peuvent pas améliorer la qualité de la décomposition dans un tel écoulement turbulent perturbé et conduisent même à un mélange de modes (Mode-mixing) dans les résultats de la décomposition. L'utilisation d'un standard EMD avec un critère d'arrêt de temps de tamisage fixe (Fixed sifting time stoppage criterion) pour ce type de signal est parfaitement pertinente.

Dans la deuxième partie de cette thèse, pour la première fois, l'évolution de l'écoulement dans le cylindre pendant les régimes transitoire a été mesurée en utilisant de PIV 2D-2C haute cadence. Les champs de vitesse sont obtenus dans le plan symétrique (tumble plan) dans un moteur GDI mono-cylindre transparent. Le régime transitoire consiste en une accélération du moteur de 1000 à 2000 tr/min pendant 8, 12, 16 et 21 cycles consécutifs. Des champs d'écoulement sont également obtenus dans le cas d'un régime stable, 1000, 1200, 1400, 1600, 1800 et 2000 tr/min, afin de fournir quelques comparaisons. Cette partie de l'étude a deux objectifs principaux, le premier est de comparer l'évolution du mouvement tumble et son intensité, pendant les phases d'admission et compression, dans des conditions transitoires à régime stable et la deuxième objective est de fournir une base de données pour valider les résultats de simulation numérique dans le cadre d'un projet ANR ASTRIDE.

Pour analyse des résultats des conditions extrêmes sont considérés: transitoire rapide, c'est-à-dire accélération du moteur pendant 8 cycles et condition transitoire lente, c'est-à-dire accélération pendant 21 cycles. Les résultats ont montré que l'évolution globale de la trajectoire du centre de tumble et son intensité (tumble ratio) dans des conditions transitoires sont similaires à celles du régime stable, mais des différences ont été observées. Pour toutes les vitesses du moteur, le centre de tumble après mi-course de compression dans des conditions transitoires est inférieur à celui dans les régimes stables et cela est plus remarquable dans le cas de transitoire rapide comparé à une transition lente. De plus, l'accélération du régime moteur ralentit légèrement le mouvement de tumble vers le PMH mais n'a aucune influence sur son intensité ainsi que son taux de dissipation.

En plus, dans un régime moteur donné, la configuration d'écoulement moyen dans le cylindre (la moyenne de phase) dans des conditions transitoires a été comparée en détail avec les régimes correspondants dans des conditions stables et plusieurs différences et quelques similitudes ont été rapportées. Dans la dernière partie, Bivariate 2D-EMD a été appliqué pour la première fois sur des données réelles, c'est-à-dire sur l'écoulement dans un cylindre lorsque le moteur fonctionne à l'état stationnaire ainsi que dans les régimes transitoires et

les résultats obtenus en condition stationnaire ont été comparés à ceux de l'analyse POD.

Perspectives:

Pour résoudre les échelles de longueur intégrale d'écoulement turbulence dans le cylindre, les mesures PIV avec une résolution spatiale plus élevée que celle de cette étude sont nécessaires pour les investigations futures. En plus d'étudier les effets d'écoulement dans le cylindre en régime transitoire sur la propagation de la flamme et d'estimer l'intensité de la turbulence dans son voisinage, le champ de vitesse doit être mesuré dans le chambre de combustion plus proches du site d'allumage.
L'écoulement dans le cylindre est assez complexe et tridimensionnel donc pour mieux comprendre son évolution pendant les régimes transitoires et pour étudier son influence sur le processus de combustion, la troisième composante du vecteur de vitesse doit être considérée donc pour la perspective PIV stéréoscopique (2D-3C) ou PIV multi-plans dans les plans parallèle et perpendiculaire au plan de tumble pourrait être intéressant à faire.

S'appuyant sur différentes étapes de validation, les résultats obtenus par Bivariate 2D-EMD sont encourageants, pour confirmer son potentiel à analyser différents types d'écoulement en mécanique des fluides, il convient de la comparer à d'autres méthodes appropriées pour analyser des phénomènes instationnaires comme la transformée en ondelettes. L'EMD 2D bivariate proposé doit être encore optimisé et son algorithme devrait être parallélisé afin de réduire le temps de calcul. En effet pour un champ de vitesse donné qui contient 127×127 points de données, la décomposition nécessite 7 heures de temps CPU. La dernière et prochaine étape sera d'appliquer l'EMD pour analyser des résultats LES afin d'aider à l'interprétation des résultats et de les comparer plus facilement aux résultats expérimentaux.

Bibliography

[1] Abraham, P., Liu, K., Haworth, D., Reuss, D., and Sick, V. Evaluating large-eddy simulation (LES) and high-speed particle image velocimetry (PIV) with phase-invariant proper orthogonal decomposition (POD). *Oil & Gas Science and Technology-Revue d'IFP Energies nouvelles 69(1)* (2014), 41–59.

[2] Adrian, R. J. Scattering particle characteristics and their effect on pulsed laser measurements of fluid flow: speckle velocimetry vs particle image velocimetry. *Applied optics 23(11)* (1984), 1690–1691.

[3] Ahrabian, A., Rehman, N. U., and Mandic, D. Bivariate empirical mode decomposition for unbalanced real-world signals. *IEEE Signal Processing Letters 20(3)* (2013), 245–248.

[4] Altaf, M. U. B., Gautama, T., Tanaka, T., and Mandic, D. P. Rotation invariant complex empirical mode decomposition. In *In Acoustics, Speech and Signal Processing. ICASSP 2007. IEEE International Conference on* (2007), vol. 3, IEEE, pp. III–1009.

[5] Arcoumanis, C., Godwin, S. N., and Kim, J. W. Effect of tumble strength on combustion and exhaust emissions in a single-cylinder, four-valve, spark-ignition engine. *SAE Technical Paper*, 981044 (1998).

[6] Arcoumanis, C., Hu, Z., Vafidis, C., and Whitelaw, J. H. Tumbling motion: a mechanism for turbulence enhancement in sparkignition engines. *SAE Paper 900060* (1990).

[7] Baby, X., Dupont, A., Ahmed, A., Deslandes, W., Charnay, G., and Michard, M. A new methodology to analyze cycle-to-cycle aerodynamic variations. *SAE Technical Paper*, 2002-01-2837 (2002).

[8] Baby, X., and Floch, A. Investigation of the in-cylinder tumble motion in a multi-valve engine: effect of the piston shape. *SAE Technical Paper*, 971643 (1997).

[9] Baum, E., Peterson, B., Surmann, C., Michaelis, D., Böhm, B., and Dreizler, A. Investigation of the 3D flow field in an IC engine using tomographic PIV. In *Proceedings of the Combustion Institute* (2013), vol. 34(2), pp. 2903–2910.

[10] Baumgarten, C. *Mixture formation in internal combustion engines.* Springer Science & Business Media, 2006.

[11] Benramdane, S., Astolfi, J. A., Cexus, J. C., and Boudraa, A. O. Experimental investigation of wall-pressure fluctuations on a transiently moving hydrofoil by empirical mode decomposition. In *The Seventeenth International Offshore and Polar Engineering Conference* (January 2007), International Society of Offshore and Polar Engineers.

[12] Bhuiyan, S. M., Adhami, R., and Khan, J. F. Fast and adaptive bidimensional empirical mode decomposition using order-statistics filter based envelope estimation. *EURASIP Journal on Advances in Signal Processing 2008(1)* (2008), 1–18.

[13] Bhuiyan, S. M., Khan, J. F., and Adhami, R. A novel approach of edge detection via a fast and adaptive bidimensional empirical mode decomposition method. *Advances in Adaptive Data Analysis 2(02)* (2010), 171–192.

[14] Bode, J., Schorr, J., Krüger, C., Dreizler, A., and Böhm, B. Influence of three-dimensional in-cylinder flows on cycle-to-cycle variations in a fired stratified disi engine measured by time-resolved dual-plane PIV. In *Proceedings of the Combustion Institute* (2017), vol. 36(3), pp. 3477–3485.

[15] Bojanov, B. D., Hakopian, H., and Sahakian, B. *Spline Functions and Multivariate Interpolations (Mathematics and Its Applications)*. KLuwer Academic Publicher, 1993.

[16] Bookstein, F. L. Principal warps: Thin-plate splines and the decompositions of deformations,. *IEEE Transactions on Pattern Analysis and Machine Intelligence 11(6)* (1989), 567–585.

[17] Borée, J., Maurel, S., and Bazile, R. Disruption of a compressed vortex. *Physics of Fluids 14(7)* (2002), 2543–2556.

[18] Borée, J., and Miles, P. C. In-Cylinder Flow. Encyclopedia of automotive engineering, 2014.

[19] Brücker, C. 3D scanning PIV applied to an air flow in a motored engine using digital high-speed video. *Measurement Science and Technology 8(12)* (1997), 1480.

[20] Bücker, I., Karhoff, D. C., Klaas, M., and Schröder, W. Stereoscopic multi-planar PIV measurements of in-cylinder tumbling flow. *Experiments in fluids 53(6)* (2012), 1993–2009.

[21] Bücker, I., Karhoff, D. C., Klaas, M., and Schröder, W. Stereoscopic multi-planar PIV measurements of in-cylinder tumbling flow. *Experiments in fluids 53(6)* (2012), 1993–2009.

[22] Buschbeck, M., Bittner, N., Halfmann, T., and Arndt, S. Dependence of combustion dynamics in a gasoline engine upon the in-cylinder flow field, determined by high-speed PIV. *Experiments in fluids 53(6)* (2012), 1701–1712.

[23] Calendini, P. O., Duverger, T., Lecerf, A., and Trinite, M. In-cylinder velocity measurements with stereoscopic particle image velocimetry in a SI engine. *SAE Technical Paper*, 2000-01-1798 (2000).

[24] Cao, Y., Kaiser, E., Borée, J., Noack, B. R., Thomas, L., and Guilain, S. Cluster-based analysis of cycle-to-cycle variations: application to internal combustion engines. *Experiments in fluids, 55(11)* (2014), 1837.

[25] Catania, A. E., and Mittica, A. Extraction techniques and analysis of turbulence quantities from in-cylinder velocity data. *ASME J. Eng. Gas Turbines Power 111* (1989), 466–478.

[26] Chen, C. Y., Guo, S. M., Chang, W. S., Tsai, J. S. H., and Cheng, K. S. An improved bidimensional empirical mode decomposition: A mean approach for fast decomposition. *Signal Processing 98* (2014), 344–358.

[27] Chen, H., Reuss, D. L., and Sick, V. On the use and interpretation of proper orthogonal decomposition of in-cylinder engine flows. *Measurement Science and Technology 23(8)* (2012), 085302.

[28] Chen, H., and Sick, V. Three-dimensional three-component air flow visualization in a steady-state engine flow bench using a plenoptic camera. *SAE International Journal of Engines 10*, 2017-01-0614 (2017).

[29] Chen, M., Zhang, W., Zhang, X., and Ding, N. In-cylinder cfd simulation of a new 2.0 l turbocharged gdi engine. *SAE Technical Paper*, 2011-01-0826 (2011).

[30] Chen, Q., Huang, N. E., Riemenschneider, S., and Xu, Y. A b-spline approach for empirical mode decomposition. *Adv. Comput. Math 24* (2006), 171–195.

[31] Chen, X., Wu, Z., and Huang, N. E. The time-dependent intrinsic correlation based on the empirical mode decomposition. *Advances in Adaptive Data Analysis 2(02)* (2010), 233–265.

[32] Cosadia, I., Borée, J., Charnay, G., and Dumont, P. Cyclic variations of the swirling flow in a diesel transparent engine. *Experiments in Fluid 41 (1)* (2006), 115–134.

[33] Cui, J., and Freeden, W. Equidistribution on the sphere. *SIAM J. Sci. Comput 18* (1997), 595–609.

[34] Dam, E., Koch, M., and Lillholm, M. Quaternions, interpolation and animation, univ. *Copenhegan, Denmark* (1998).

[35] Damerval, C., Meignen, S., and Perrier, V. A fast algorithm for bidimensional emd. *IEEE Sig. Process. Lett 12* (2005), 701–704.

[36] Damerval, C., Meignen, S., and Perrier, V. A new formulation for empirical mode decomposition based on constrained optimization. *IEEE Signal Process. Lett 14(12)* (2007), 932–935.

[37] Dannemann, J., Pielhop, K., Klaas, M., and Schröder, W. Cycle resolved multi-planar flow measurements in a four-valve combustion engine. *Experiments in fluids 50(4)* (2011), 961–976.

[38] Daubechies, I. *Ten Lectures on Wavelets*, vol. 61. SIAM CBMS-NSF Series in Applied Mathematics, 1992.

[39] Daubechies, I., Lu, J., and Wu, H. T. Synchrosqueezed wavelet transforms: An empirical mode decomposition-like tool. *Applied and computational harmonic analysis 30(2)* (2011), 243–261.

[40] Deslandes, W., Dupont, A., Baby, X., Charnay, G., and Borée, J. Piv measurements of internal aerodynamic of diesel combustion chamber. *SAE Technical Paper*, 2003-01-3083 (2003).

[41] Diks, C. *Nonlinear Time Series Analysis: Methods and Applications.* World Scientific Press, 1999.

[42] Druault, P., Bouhoubeiny, E., and Germain, G. POD investigation of the unsteady turbulent boundary layer developing over porous moving flexible fishing net structure. *Experiments in fluids 53(1)* (2012), 277–292.

[43] Druault, P., Guibert, P., and Alizon, F. Use of proper orthogonal decomposition for time interpolation from PIV data. *Experiments in Fluids 39(6)* (2005), 1009–1023.

[44] Ducoin, A., Astolfi, J. A., Deniset, F., and Sigrist, J. F. Computational and experimental investigation of flow over a transient pitching hydrofoil. *European Journal of Mechanics-B/Fluids 28(6)* (2009), 728–743.

[45] Ekchian, A., and Hoult, D. Flow visualization study of the intake process of an internal combustion engine. *SAE Technical Paper*, 790095 (1979).

[46] Ekenberg, M., Reinmann, R., Olofsson, E., Gillet, B., and Johansson, B. The influence of a late in-cylinder air injection on in-cylinder flow measured with particle image velocimetry (PIV). *SAE Technical Paper*, 2001-01-3492 (2001).

[47] Enaux, B., Granet, V., Vermorel, O., Lacour, C., Pera, C., Angelberger, C., and Poinsot, T. LES study of cycle-to-cycle variations in a spark ignition engine. In *Proceedings of the combustion Institute* (2011), vol. 33(2), pp. 3115–3122.

[48] Enotiadis, A. C., Vafidis, C., and Whitelaw, J. H. Interpretation of cyclic flow variations in motored internal combustion engines. *Experiments in Fluids 10(2)* (1990), 77–86.

[49] Fajardo, C., and Sick, V. Flow field assessment in a fired spray-guided spark-ignition direct-injection engine based on UV particle image velocimetry with sub crank angle resolution. In *Proceedings of the combustion institute* (2007), vol. 31(2), pp. 3023–3031.

[50] Fansler, T., and French, D. Cycle resolved laser velocimetry measurements in a reentrant-bowl-in-piston engine. *SAE Technical Paper*, 880377 (1988).

[51] Feldmann, O., and Mayinger, F. *Optical measurements: techniques and applications. Springer Science & Business Media.* Springer Science & Business Media, 2012.

[52] Feynman, J., and Ruzmaikin, A. The Centennial Gleissberg Cycle and its association with extended minima. *Journal of Geophysical Research: Space Physics 119(8)* (2014), 6027–6041.

[53] Flandrin, P. *Time-frequency/time-scale analysis*, vol. 10. Academic press., 1998.

[54] Flandrin, P., and Goncalves, P. Empirical mode decompositions as data-driven wavelet-like expansions. *International Journal of Wavelets, Multiresolution and Information Processing 2(04)* (2004), 477–496.

[55] Flandrin, P., Rilling, G., and Goncalves, P. Empirical mode decomposition as a filter bank. *Signal Processing Letters, IEEE 11(2)* (2004), 112–114.

[56] Fogleman, M., Lumley, J., Rempfer, D., and Haworth, D. Application of the proper orthogonal decomposition to datasets of internal combustion engine flows. *Journal of Turbulence 5(23)* (2004), 1–3.

[57] Foucher, F., Landry, L., Halter, F., and Mounaïm-Rousselle, C. Turbulent flow fields analysis of a spark-ignition engine as function of the boosted pressure. In *14th International Symposium on Laser Techniques to Fluid Mechanics.* (July 2008).

[58] Foucher, F., and Ravier, P. Determination of turbulence properties by using empirical mode decomposition on periodic and random perturbed flows. *Experiments in fluids 49(2)* (2010), 379–390.

[59] Franzke, C. L. Warming trends: nonlinear climate change. *Nature Climate Change 4(6)* (2014), 423.

[60] Freek, C., Hentschel, W., and Merzkich, W. High Speed PIV-A Diagnostic Tool for IC-Engines. In *Proceedings of the Eighth International Symposium on Flow Visualization* (1998).

[61] Freudenhammer, D., Peterson, B., Ding, C. P., Boehm, B., and Grundmann, S. The influence of cylinder head geometry variations on the volumetric intake flow captured by magnetic resonance velocimetry. *SAE International Journal of Engines 8(2015-01-1697)* (2015), 1826–1836.

[62] Fujimoto, M., Iwai, K., Kataoka, M., and Tabata, M. Effect of combustion chamber shape on tumble flow, squish-generated flow and burn rate. *JSAE review 23(3)* (2002), 291–296.

[63] Funk, C., Sick, V., Reuss, D. L., and Dahm, W. J. Turbulence properties of high and low swirl in-cylinder flows. *SAE Paper*, 2002-01-2841 (2002).

[64] Galmiche, B., Mazellier, N., Halter, F., and Foucher, F. Turbulence characterization of a high-pressure high-temperature fan-stirred combustion vessel using LDV, PIV and TR-PIV measurements. *Experiments in fluids 55(1)* (2014), 1636.

[65] Gledzer, E. B., and Ponomarev, V. M. Instability of bounded flows with elliptical streamlines. *Journal of Fluid Mechanics 240* (1992), 1–30.

[66] Goryntsev, D., Sadiki, A., Klein, M., and Janicka, J. Large eddy simulation based analysis of the effects of cycle-to-cycle variations on air-fuel mixing in realistic DISI IC-engines. In *Proceedings of the Combustion Institute* (2009), vol. 32(2), pp. 2759–2766.

[67] Graftieaux, L., Michard, M., Grosjean, N. Rilling, G., Flandrin, P., Goncalves, P., and Lilly, J. M. Combining PIV, POD and vortex identification algorithms for the study of unsteady turbulent swirling flows. *Measurement Science and technology, 12(9)* (2001), 1422–1429.

[68] Granet, V., Vermorel, O., Lacour, C., Enaux, B., Dugué, V., and Poinsot, T. Large-Eddy Simulation and experimental study of cycle-to-cycle variations of stable and unstable operating points in a spark ignition engine. *Combustion and Flame 159(4)* (2012), 1562–1575.

[69] Gröchenig, K. *Foundations of Time-Frequency Analysis.* Birkhauser, 359 pp, 2001.

[70] Guanlei, X., Xiaotong, W., and Xiaogang, X. Improved bi-dimensional EMD and Hilbert spectrum for the analysis of textures. *Pattern Recognition 42(5)* (2009), 718–734.

[71] Haar, A. Zur theorie der orthogonalen funktionen-systeme. *Math. Ann 69* (1910), 971–977.

[72] Hadded, O., and Denbratt, I. Turbulence characteristics of tumbling air motion in four-valve si engines and their correlation with combustion parameters. *SAE Technical Paper*, 910478 (1991).

[73] Haller, G. Lagrangian coherent structures from approximate velocity data. *Physics of fluids 14(6)* (2002), 1851–1861.

[74] Hasse, C., Sohm, V., and Durst, B. Numerical investigation of cyclic variations in gasoline engines using a hybrid urans/les modeling approach. *Computers & Fluids 39(1)* (2010), 25–48.

[75] Haworth, D., El Tahry, S. H., Huebler, M. S., and Chang, S. Multi-dimensional port-and-cylinder flow calculation for two-and-four-valves-percylinder engines: Influence of intake configuration on flow structure,. *SAE Paper*, 900257 (1990).

[76] Haworth, D. C. Large-eddy simulation of in-cylinder flows. *Oil & Gas Science and Technology 54(2)* (1999), 175–185.

[77] hekmati, A., Ricot, D., and Druault, P. About the convergence of pod and epod modes computed from cfd simulation. *Computers & Fluids 50(1)* (2011), 60–71.

[78] Hemakom, A., Ahrabian, A., Looney, D., ur Rehman, N., and Mandic, D. P. Nonuniformly sampled trivariate empirical mode decomposition. In *Acoustics, Speech and Signal Processing (ICASSP) , 2015 IEEE International Conference on* (April 2015), IEEE, pp. 3691–3695.

[79] Hemakom, A., Goverdovsky, V., Looney, D., and Mandic, D. P. Adaptive-projection intrinsically transformed multivariate empirical mode decomposition in cooperative brain-computer interface applications. *Phil. Trans. R. Soc. A 374*, 2065 (2016), 20150199.

[80] Heywood, J. *Internal Combustion Engines Fundamentals.* McGraw Hill Company, New York, 1988.

[81] Hill, P. G., and Zhang, D. The effects of swirl and tumble on combustion in spark-ignition engines. *Progress in energy and combustion science 20(5)* (1994), 373–429.

[82] Hotelling, H. Analysis of a complex of statistical variables into principal components. *Journal of educational psychology 24(6)* (1933), 417.

[83] Hou, T. Y., and Shi, Z. Adaptive data analysis via sparse time-frequency representation. *Advances in Adaptive Data Analysis 3(01n02)* (2011), 1–28.

[84] Hou, T. Y., and Shi, Z. Data-driven time-frequency analysis. *Applied and Computational Harmonic Analysis 35(2)* (2013), 284–308.

[85] Hu, Z., Whitelaw, J. H., and Vafidis, C. Flame propagation studies in a four-valve pentroof-chamber spark ignition engine. *SAE Technical Paper*, 922321 (1992).

[86] Huang, N. E. Computer implemented empirical mode decomposition apparatus, method and article of manufacture for two-dimensional signals. *US Patent*, 6,311,130 B1 (Granted Oct. 30 2001).

[87] Huang, N. E. *Hilbert-Huang Transform and Its Applications.* World Sci., Singapore, 2005.

[88] Huang, N. E., and Attoh-Okine, N. O. *The Hilbert-Huang transform in engineering.* CRC Press, 2005.

[89] Huang, N. E., Long, S. R., and Shen, Z. The mechanism for frequency downshift in nonlinear wave evolution. *Adv. Appl. Mech 32* (1996), 59–111.

[90] Huang, N. E., Shen, Z., and Long, S. R. A new view of nonlinear water waves: the Hilbert spectrum. *Annual review of fluid mechanics 31(1)* (1999), 417–457.

[91] Huang, N. E., Shen, Z., Long, S. R., Wu, M. C., Shih, H. H., and Zheng, Q. and. Liu, H. H. The empirical mode decomposition and the hilbert spectrum for nonlinear and non-stationary time series analysis. in proceedings of the royal society of london a: Mathematical, physical and engineering sciences. *The Royal Society 454(1971)*, 1971 (1998), 903–995.

[92] Huang, N. E., Wu, M. L. C., Long, S. R., Shen, S. S., Qu, W., Gloersen, P., and Fan, K. L. A confidence limit for the empirical mode decomposition and hilbert spectral analysis. in proceedings of the royal society of london a: Mathematical, physical and engineering sciences. *The Royal Society 459*, 2037 (September 2003), 2317–2345.

[93] Huang, Y. X., Schmitt, F. G., Lu, Z. M., and Liu, Y. L. An amplitude-frequency study of turbulent scaling intermittency using empirical mode decomposition and Hilbert spectral analysis. *EPL (Europhysics Letters) 84(4)* (2008), 40010.

[94] Jager, G., Koch, R., Kunoth, A., and Pabel, R. Fast Empirical Mode Decompositions of Multivariate Data Based on Adaptive Spline-Wavelets and a Generalization of the Hilbert-Huang-Transformation (HHT) to Arbitrary Space Dimensions. *Advances in Adaptive Data Analysis* (2010).

[95] Jarvis, S., Justham, T., Clarke, A., Garner, C. P., Hargrave, G. K., and Halliwell, N. A. Time resolved digital PIV measurements of flow field cyclic variation in an optical IC engine. In *In Journal of Physics: Conference Series* (2006), vol. 45(1), IOP Publishing, p. 38.

[96] Justham, T., Jarvis, S., Clarke, A., Garner, C. P., Hargrave, G. K., and Halliwell, N. A. Simultaneous study of intake and in-cylinder IC engine flow fields to provide an insight into intake induced cyclic variations. In *Journal of Physics: Conference Series* (2006), vol. 45(1), IOP Publishing, p. 146.

[97] Kantz, H., and Schreiber, T. *Nonlinear Time Series Analysis*. Cambridge University Press, 1999.

[98] Kapitza, L., Imberdis, O., Bensler, H. P., Willand, J., and Thévenin, D. An experimental analysis of the turbulent structures generated by the intake port of a DISI-engine. *Experiments in fluids 48(2)* (2010), 265–280.

[99] Kent, J. C., Mikulec, A., Rimal, L., Adamczyk, A. A., Mueller, S. R., Stein, R. A., and Warren, C. C. Observations on the effects of intake-generated swirl and tumble on combustion duration. *SAE Technical Paper*, 892096 (1989).

[100] Keromnes, A., Dujol, C., and Guibert, P. Aerodynamic control inside an internal combustion engine. *Measurement Science and Technology 21(12)* (2010), 125404.

[101] Khalighi, B. Study of the intake tumble motion by flow visualization and particle tracking velocimetry. *Experiments in Fluids 10(4)* (1991), 230–236.

[102] Konrath, R., Schröder, W., and Limberg, W. Holographic particle image velocimetry applied to the flow within the cylinder of a four-valve internal combustion engine. *Experiments in fluids 33(6)* (2002), 781–793.

[103] Krishna, B. M., and Mallikarjuna, J. M. Comparative study of in-cylinder tumble flows in an internal combustion engine using different piston shapes-an insight using particle image velocimetry. *Experiments in fluids 48(5)* (2010), 863–874.

[104] Lee, J., and Farrell, P. V. Intake valve flow measurements of an IC engine using particle image velocimetry. *SAE Technical Paper*, 930480 (1993).

[105] Lee, K., Bae, C., and Kang, K. The effects of tumble and swirl flows on flame propagation in a four-valve SI engine. *Applied thermal engineering 27(11)* (2007), 2122–2130.

[106] Li, Y., Zhao, H., Leach, B., Ma, T., and Ladommatos, N. Characterization of an in-cylinder flow structure in a high-tumble spark ignition engine. *International Journal of Engine Research 5(5)* (2004), 375–400.

[107] Li, Y., Zhao, H., Peng, Z., and Ladommatos, N. Particle image velocimetry measurement of in-cylinder flow in internal combustion engines-experiment and flow structure analysis. In *Proceedings of the Institution of Mechanical Engineers, Part D: Journal of Automobile Engineering* (2002), vol. 216(1), pp. 65–81.

[108] Liang, H., Lin, Q. H., and Chen, J. D. Z. Application of the empirical mode decomposition to the analysis of esophageal manometric data in gastroesophageal reflux disease. *IEEE Transactions on biomedical engineering 52(10)* (2005), 1692–1701.

[109] Linderhed, A. Variable sampling of the empirical mode decomposition of twodimensional signals. *Int. J. Wavelets Multresolution Inform. Process. 3* (2005), 435–452.

[110] Linderhed, A. Image empirical mode decomposition: A new tool for image processing. *Advances in Adaptive Data Analysis, World Scientific Publishing Company 1* (2009), 265–294.

[111] Long, S. R. *Hilbert-Huang Transform and Its Applcations*. eds. N. E. Huang and S. S. P. Shen (World Scientific, Singapore), 2005, ch. Applications of HHT in image analysis, pp. 289–305.

[112] Looney, D., Hemakom, A., and Mandic, D. P. Intrinsic multi-scale analysis: a multi-variate empirical mode decomposition framework. In *Proc. R. Soc. A* (January 2015), vol. 471 of *2173*, The Royal Society, p. 20140709.

[113] Looney, D., and Mandic, D. P. Multiscale image fusion using complex extensions of emd. *IEEE Transactions on Signal Processing 57(4)* (2009), 1626–1630.

[114] Lumley, J. L. The structure of inhomogeneous turbulent flows. *Atmospheric turbulence and radio wave propagation* (1967), 166–178.

[115] Lumley, J. L. *Engines: an introduction*. Cambridge University Press, 1999.

[116] Lumley, J. L. Early work on fluid mechanics in the IC engine. *Annual review of fluid mechanics 33(1)* (2001), 319–338.

[117] Lundgren, T. S., and Mansour, N. N. Transition to turbulence in an elliptic vortex. *Journal of Fluid Mechanics 307* (1996), 43–62.

[118] Mandic, D. P., ur Rehman, N., Wu, Z., Huang, N. E. Niang, O., Thioune, A., El Gueirea, M. C., Deléchelle, E., and Lemoine, J. Empirical mode decomposition-based time-frequency analysis of multivariate signals: The power of adaptive data analysis. *IEEE signal processing magazine 30(6)* (2013), 74–86.

[119] Marc, D., Borée, J., Bazile, R., and Charnay, G. Tumbling vortex flow in a model square piston compression machine: Piv and ldv measurements. *SAE Technical Paper*, 972834 (1997).

[120] Mazellier, N., and Foucher, F. Separation between coherent and turbulent fluctuations: what can we learn from the empirical mode decomposition? *Experiments in fluids 51(2)* (2011), 527–541.

[121] Melling, A. Tracer particles and seeding for particle image velocimetry. *Measurement Science and Technology 8(12)* (1997), 1406.

[122] Mock, P., Kühlwein, J., Tietge, U., Franco, V., Bandivadekar, A., and German, J. The WLTP: How a new test procedure for cars will affect fuel consumption values in the EU. *International Council on Clean Transportation 9* (2014), 35–47.

[123] Moreau, J., Borée, J., Bazile, R., and Charnay, G. Destabilisation of a compressed vortex by a round jet. *Experiments in Fluids 37* (2004), 856–871.

[124] Mounaïm-Rousselle, C., Landry, L., Halter, F., and Foucher, F. Experimental characteristics of turbulent premixed flame in a boosted Spark-Ignition engine. In *Proceedings of the Combustion Institute* (2013), vol. 34(2), pp. 2941–2949.

[125] Müller, S. H. R., Böhm, B., Gleisner, M., Grzeszik, R., Arndt, S., and Dreizler, A. Flow field measurements in an optically accessible, direct-injection spray-guided internal combustion engine using high-speed PIV. *Experiments in fluids 48(2)* (2010), 281–290.

[126] Niang, O., Thioune, A., El Gueirea, M. C., Deléchelle, E., and Lemoine, J. Partial differential equation-based approach for empirical mode decomposition: application on image analysis. *IEEE Transactions on Image Processing 21(9)* (2012), 3991–4001.

[127] Niederreiter, H. *Random number generation and quasi-Monte Carlo methods.* SIAM, 1992.

[128] Nordgren, H., Hildingsson, L., Johansson, B., Dahlén, L., and Konstanzer, D. Comparison between in-cylinder PIV measurements, CFD simulations and steady-flow impulse torque swirl meter measurements. *SAE Technical Paper*, 2003-01-3147 (2003).

[129] Nunes, J. C., Bouaoune, Y., Delechelle, E., Niang, O., and Bunel, P. Image analysis by bidmensional empirical mode decomposition. *Image Vision Comput 21* (2003), 1019–1026.

[130] Nunes, J. C., and Delechelle, E. Empirical mode decomposition: Applications on signal and image processing. *Advances in Adaptive Data Analysis 01:01* (2009), 125–175.

[131] Nunes, J. C., Guyot, Y., and Delechelle, E. Texture analysis based on local analysis of the bidimensional empirical mode decomposition. *Machine Vision Appl 16* (2005), 177–188.

[132] Obukhov, A. Turbulence and Atmospheric Dynamics. English transl. ed. JL Lumley, CTR Monogr. Palo Alto. In *CA: The Cent.* Turbul. Res, 2000.

[133] Obukhov, A. M. Three-mode interaction in an incompressible fluid. *Radiophysics and Quantum Electronics 19(6)* (1976), 614–620.

[134] Ozdor, N., Dulger, M., and Sher, E. Cyclic variability in spark ignition engines a literature survey. *SAE Technical Paper*, 940987 (1994).

[135] Pajot, O. *Etude Expérimentale de l'Influence de l'Aérodynamique sur le Comportement et la Structure du Front de Flamme dans les Conditions d'un Moteur à Allumage Commandé*. PhD thesis, UNIVERSITE D'ORLEANS, 2000.

[136] Pajot, O., and Mounaïm-Rousselle, C. Instantaneous flow field effects on the flame kernel in SI engine by simultaneous optical diagnostics. *SAE Technical Paper*, 2000-01-1796 (2000).

[137] Pearson, K. LIII.On lines and planes of closest fit to systems of points in space. *The London, Edinburgh, and Dublin Philosophical Magazine and Journal of Science 2(11)* (1901), 559–572.

[138] Petersen, B., and Miles, P. C. PIV measurements in the swirl-plane of a motored light-duty diesel engine. *SAE International Journal of Engines 4*, 2011-01-1285 (2011), 1623–1641.

[139] Peterson, B., Baum, E., Böhm, B., Sick, V., and Dreizler, A. High-speed PIV and LIF imaging of temperature stratification in an internal combustion engine. In *Proceedings of the combustion institute* (2013), vol. 34(2), pp. 3653–3660.

[140] Peterson, B., Reuss, D. L., and Sick, V. High-speed imaging analysis of misfires in a spray-guided direct injection engine. In *Proceedings of the Combustion Institute* (2011), vol. 33(2), pp. 3089–3096.

[141] Peterson, B., Reuss, D. L., and Sick, V. On the ignition and flame development in a spray-guided direct-injection spark-ignition engine. *Combustion and Flame 161(1)* (2014), 240–255.

[142] Peterson, B., and Sick, V. Simultaneous flow field and fuel concentration imaging at 4.8 khz in an operating engine. *Applied Physics B: Lasers and Optics 97(4)* (2009), 887–895.

[143] Peterson, K., Regaard, B., Heinemann, S., and Sick, V. Single-camera, three-dimensional particle tracking velocimetry. *Optics express 20(8)* (2012), 9031–9037.

[144] Pickering, C. J., and Halliwell, N. A. Laser speckle photography and particle image velocimetry: photographic film noise. *Applied optics 23(17)* (1984), 2961–2969.

[145] Plancherel, M. Sur les formules de rťeciprocitťe du type de fourier. *J. London Math. Soc., Ser. 1(8)* (1933), 220–226.

[146] Qian, C., Wu, Z., Fu, C., and Wang, D. On changing El Niño: A view from time-varying annual cycle, interannual variability, and mean state. *Journal of Climate 24(24)* (2011), 6486–6500.

[147] Queiroz, C., and Tomanik, E. Gasoline direct injection engines-a bibliographical review. *SAE Technical Paper*, 973113 (December 1997).

[148] Raffel, M., Willert, C. E., Wereley, S., and Kompenhans, J. *Particle image velocimetry: a practical guide*. Springer, 2013.

[149] Reeves, M., Garner, C. P., Dent, J. C., and Halliwell, N. A. Study of barrel swirl in a four-valve optical IC engine using particle image velocimetry. In *International Symposium COMODIA* (1994), vol. 94, p. 29.

[150] Reeves, M., Towers, D. P., Tavender, B., and Buckberry, C. H. A high-speed all-digital technique for cycle-resolved 2-Dflow measurement and flow visualisation within SI engine cylinders. *Optics and lasers in engineering 31(4)* (1999), 247–261.

[151] Rehman, N., Looney, D., and Rutkowski, T. M.and Mandic, D. P. Bivariate emd-based image fusion. In *Statistical Signal Processing, 2009. SSP'09. IEEE/SP 15th Workshop on*. IEEE, August 2009, pp. 57–60.

[152] Rehman, N., and Mandic, D. P. Multivariate empirical mode decomposition. *In Proceedings of The Royal Society of London A: Mathematical, Physical and Engineering Science.The Royal Society* (December 2009).

[153] Rehman, N., and Mandic, D. P. Empirical mode decomposition for trivariate signals. *IEEE Transactions on signal processing 58(3)* (2010), 1059–1068.

[154] Rehman, N., and Mandic, D. P. Filter bank property of multivariate empirical mode decomposition. *IEEE Transactions on Signal Processing 59(5)* (2011), 2421–2426.

[155] Rehman, N., Park, C., Huang, N. E., and Mandic, D. P. EMD via MEMD: multivariate noise-aided computation of standard EMD. *Advances in Adaptive Data Analysis 5(02)* (2013).

[156] Rehman, N. u., Ehsan, S., Abdullah, S. M. U., Akhtar, M. J., Mandic, D. P., and McDonald-Maier, K. D. Multi-scale pixel-based image fusion using multivariate empirical mode decomposition. *Sensors 15(5)* (2015), 10923–1094.

[157] Reuss, D. L. Cyclic variability of large-scale turbulent structures in directed and undirected IC engine flows. *SAE Technical Paper*, 2000-01-0246 (2000).

[158] Reuss, D. L., Adrian, R. J., Landreth, C. C., French, D. T., and Fansler, T. D. Instantaneous planar measurements of velocity and large-scale vorticity and strain rate in an engine using particle mage velocimetry. *SAE technical papers*, 890616 (1989).

[159] Reuss, D. L., Bardsley, M., Felton, P. G., Landreth, C. C., and Adrian, R. J. Velocity, vorticity, and strain-rate ahead of a flame measured in an engine using particle image velocimetry. *SAE Technical Paper*, 900053 (1990).

[160] Reuss, D. L., Kuo, T. W., Khalighi, B., Haworth, D., and Rosalik, M. Particle image velocimetry measurements in a high-swirl engine used for evaluation of computational fluid dynamics calculations. *SAE Technical Paper*, 952381 (1995).

[161] Rilling, G., Flandrin, P., and Goncalves, P. On empirical mode decomposition and its algorithms. In *IEEE-EURASIP workshop on nonlinear signal and image processing* (June 2003), IEEER, Grado, Italy, pp. 8–11.

[162] Rilling, G., Flandrin, P., Goncalves, P., and Lilly, J. M. Bivariate empirical mode decomposition. *IEEE Signal Process. Lett 14* (2007), 936–939.

[163] Rothrock, M. A., and Spencer, R. C. The influence of directed air flow on combustion in a spark-ignition engine. Tech. Rep. 657, NACA, Langley, VA, 1939. (Prof. J. Lumley 70th birthday Symposium Papers).

[164] Roudnitzky, S., Druault, P., and Guibert, P. Proper orthogonal decomposition of in-cylinder engine flow into mean component, coherent structures and random Gaussian fluctuations. *Journal of Turbulence 7(70)* (2006).

[165] Rouland, E., Trinite, M., Dionnet, F., Floch, A., and Ahmed, A. Particle image velocimetry measurements in a high tumble engine for in-cylinder flow structure analysis. *SAE Technical Paper*, 972831 (1997).

[166] Ruiz, T., Borée, J., Tran, T., Sicot, C., and Brizzi, L. E. Finite time lagrangian analysis of an unsteady separation using high speed particle image velocimetry. *Physics of Fluids 22(075103)* (2010), 1–9.

[167] Schröder, A., and Willert, C. E. *Particle image velocimetry: new developments and recent applications*, vol. 112. Springer Science & Business Media, 2008.

[168] Shadden, S., Dabiri, J., and Marsden, J. Lagrangian analysis of fluid transport in empirical vortex ring flows. *Physics of Fluids 18 (4)* (2006), 1–11.

[169] Shen, S. P., Shu, T., Huang, N. E., Wu, Z., North, G. R., Karl, T. R., and Easterling, D. R. *Hilbert-Huang Transform and its Applications*. World scientific, Singapor, 2005, ch. HHT analysis of the nonlinear and non-stationary annual cycle of daily surface air temperature data, pp. 187–210.

[170] Söderberg, F., Johansson, B., and Lindoff, B. Wavelet analysis of in-cylinder ldv measurements and correlation against heat-release. *SAE Technical Paper*, 980483 (1998).

[171] Song, P., and Zhang, J. On the application of two-dimensional empirical mode decomposition in the information separation of oceanic remote sensing image. *High Technol.Lett 11* (2001), 62–67.

[172] Stansfield, P., Wigley, G., Justham, T., Catto, J., and Pitcher, G. Piv analysis of in-cylinder flow structures over a range of realistic engine speeds. *Experiments in fluids 43(1)* (2007), 135–146.

[173] Stefan, S. Optical diagnostics on FSI transparent engine. In *FISITA World Automotive Congress, Barcelona* (2004), pp. 23–27.

[174] Stiehl, R., Bode, J., Schorr, J., Krüger, C., Dreizler, A., and Böhm, B. Influence of intake geometry variations on in-cylinder flow and flow-spray interactions in a stratified direct-injection spark-ignition engine captured by time-resolved particle image velocimetry. *International Journal of Engine Research 17(9)* (2016), 983–997.

[175] Stiehl, R., Schorr, J., Krüger, C., Dreizler, A., and Böhm, B. In-cylinder flow and fuel spray interactions in a stratified spray-guided gasoline engine investigated by high-speed laser imaging techniques. *Flow, turbulence and combustion 91(3)* (2013), 431–450.

[176] Strang, G. Wavelets and dilation equations: A brief introduction. *SIAM review 31(4)* (1989), 614–627.

[177] Sullivan, P., Ancimer, R., Dziedzic, M., and Wallace, J. Analysis of single-point nonstationary data with application to SI engines. In *CSME forum on Thermal and Fluids Engineering.* (May 1996).

[178] Sullivan, P., Ancimer, R., and Wallace, J. Turbulence averaging within spark ignition engines. *Experiments in Fluids 27(1)* (1999), 92–101.

[179] Tanaka, T., and Mandic, D. P. Complex empirical mode decomposition. *IEEE Signal Process.Lett 14(2)* (2006), 101–104.

[180] Theunissen, R., Scarano, F., and Riethmuller, M. L. Spatially adaptive piv interrogation based on data ensemble. *Experiments in Fluids 48(5)* (2010), 875–887.

[181] Tong, H. *Nonlinear Time Series Analysis.* Oxford University Press, 1990.

[182] Torres, M. E., Colominas, M. A., Schlotthauer, G., and Flandrin, P. A complete ensemble empirical mode decomposition with adaptive noise. In *Acoustics, speech and signal processing (ICASSP), 2011 IEEE international conference on* (May 2011), IEEE, pp. 4144–4147.

[183] Towers, D. P., and Towers, C. E. Cyclic variability measurements of in-cylinder engine flows using high-speed particle image velocimetry. *Measurement Science and Technology 15(9)* (2004), 1917.

[184] Valentino, G., Kaufman, D., and Farrell, P. Intake valve flow measurements using PIV. *SAE Technical Paper*, 932700 (1993).

[185] van Overbrüggen, T., Dannemann, J., Klaas, M., and Schröder, W. Holographic particle image velocimetry measurements in a four-valve combustion engine. *Experiments in fluids 55(1)* (2014), 1634.

[186] Vermorel, O., Richard, S., Colin, O., Angelberger, C., Benkenida, A., and Veynante, D. Towards the understanding of cyclic variability in a spark ignited engine using multi-cycle LES. *Combustion and Flame 156(8)* (2009), 1525–1541.

[187] Voisine, M. *Etude expérimentale de l'aérodynamique interne des moteurs: mise en œuvre de diagnostics d'analyses spatio-temporels pour un écoulement de rouleau compressé.* PhD thesis, ENSMA, 2010.

[188] Voisine, M., Thomas, L., Borée, J., and Rey, P. Spatio-temporal structure and cycle to cycle variations of an in-cylinder tumbling flow. *Experiments in Fluids 50(5)* (2011), 1393–1407.

[189] Wang, Y. H., Yeh, C. H., Young, H. W. V., Hu, K., and Lo, M. T. On the computational complexity of the empirical mode decomposition algorithm. *Physica A: Statistical Mechanics and its Applications 400* (2014), 159–167.

[190] Wanga, H., Zhixun, S., Cao, J., Wang, Y., and Zhang, H. Empirical mode decomposition on surfaces. *Graphical Models 74(4)* (July 2012), 83.

[191] Welch, P. The use of fast fourier transform for the estimation of power spectra: a method based on time averaging over short, modified periodograms. *IEEE Transactions on audio and electroacoustics 15(2)* (1967), 70–73.

[192] Westerweel, J. Efficient detection of spurious vectors in particle image velocimetry data. *Experiments in Fluids 16(3)* (1994), 236–247.

[193] White, F. M. *Fluid mechanics, 1999.* McGraw-Hill, New York, NY, USA, 3-225, 1979.

[194] Wieneke, B., and Pfeiffer, K. Adaptive piv with variable interrogation window size and shape. In *15th Int Symp on Applications of Laser Techniques to Fluid Mechanics Lisbon, Portugal* (2010).

[195] Wiktorsson, M., Lindoff, B., Johansson, B., and Soderberg, F. Wavelet analysis of in-cylinder LDV velocity measurements. *SAE Technical Paper*, 961921 (1996).

[196] Williams, T. C., Hargrave, G. K., and Halliwell, N. A. The development of high-speed particle image velocimetry (20 khz) for large eddy simulation code refinement in bluff body flows. *Experiments in fluids 35(1)* (2003), 85–91.

[197] Windrows, B., and Stearns, S. D. *Adaptive Signal Processing.* Prentice Hall, 1985.

[198] Wu, C. H., Chang, H. C., Lee, P. L., Li, K. S., Sie, J. J., Sun, C. W., Yang, C., Li, P. H., Deng, H. T., and Shyu, K. K. Frequency recognition in an SSVEP-based brain computer interface using empirical mode decomposition and

refined generalized zero-crossing. *Journal of neuroscience methods 196(1)* (2011), 170–181.

[199] Wu, Z., and Huang, N. E. A study of the characteristics of white noise using the empirical mode decomposition method. In *Royal Society of London A: Mathematical, Physical and Engineering Sciences* (June 2004), vol. 460, The Royal Society, pp. 1597–1611.

[200] Wu, Z., and Huang, N. E. *Hilbert-Huang Transform: Introduction and Applications*. World Scientific, Singapore, 2005, ch. Statistical significant test of intrinsic mode functions, pp. 125–148.

[201] Wu, Z., and Huang, N. E. Ensemble empirical mode decomposition: a noise-assisted data analysis method. *Advances in adaptive data analysis 1(01)* (2009), 1–41.

[202] WU, Z., Huang, N. E., and Chen, X. The multi-dimensional ensemble empirical mode decomposition method. *Advances in Adaptive Data Analysis* (2009).

[203] Wu, Z., Huang, N. E., and Hou, T. Y. On the relations of empirical mode decomposition to the fourier transform and wavelet analysis. *Appl Comput Harmon Anal* (2010).

[204] Xu, Y., Liu, B., Liu, J., and Riemenschneider, S. Two-dimensional empirical mode decomposition by finite elements. *Proc. Roy. Soc. London A 462* (2006), 3081–3096.

[205] Yamakawa, M., Youso, T., Fujikawa, T., Nishimoto, T., Wada, Y., Sato, K., and H., Y. Combustion technology development for a high compression ratio SI engine. *SAE International Journal of Fuels and Lubricants 5*, 2011-01-1871 (2011), 98–105.

[206] Yang, T. Y. *Finite Element Structural Analysis*. Prentice-Hall, 1986. pp.446-449.

[207] Yeh, J. R., Shieh, J. S., and Huang, N. E. Complementary ensemble empirical mode decomposition: A novel noise enhanced data analysis method. *Advances in Adaptive Data Analysis 2(02)* (2010), 135–156.

[208] Yuan, Y., Jin, M., Song, P., and Zhang, J. Empirical and dynamical detection of the sea bottom topography from synthetic aperture radar image. *Adv. Adapt. Data Anal 1* (2009), 243–263.

[209] Zegers, R. P. C., Luijten, C. C. M., Dam, N. J., and de Goey, L. P. H. Pre-and post-injection flow characterization in a heavy-duty diesel engine using high-speed PIV. *Experiments in fluids 53(3)* (2012), 731–746.

[210] Zha, K., Busch, S., Miles, P. C., Wijeyakulasuriya, S., Mitra, S., and Senecal, P. K. Characterization of flow asymmetry during the compression stroke using swirl-plane piv in a light-duty optical diesel engine with the re-entrant piston bowl geometry. *SAE International Journal of Engines 8*, 2015-01-1699 (2015), 1837–1855.

[211] Zhao, F., Lai, M. C., and Harrington, D. L. Automotive spark-ignited direct-injection gasoline engines. *Progress in energy and combustion science 25(5)* (1999), 437–562.

[212] Zhou, Y., Chen, W., Gao, J., and He, Y. Application of Hilbert-Huang transform based instantaneous frequency to seismic reflection data. *Journal of Applied Geophysics 82* (2012), 68–74.

Potential of the Empirical Mode Decomposition to analyze instantaneous flow fields in Direct Injection Spark Ignition engine: Effect of transient regimes

Abstract

This study introduces a new approach called Bivariate 2D-EMD to separate large-scale organized motion i.e., flow low frequency component from random turbulent fluctuations i.e., high frequency one in a given in-cylinder instantaneous 2D velocity field. This signal processing method needs only one instantaneous velocity field contrary to the other methods commonly used in fluid mechanics, as POD. The proposed method is quite appropriate to analyze the flows intrinsically both unsteady and nonlinear flows as in in-cylinder. The Bivariate 2D-EMD is validated through different test cases, by optimize it and apply it on an experimental homogeneous and isotropic turbulent flow (HIT), perturbed by a synthetic Lamb-Ossen vortex, to simulate the feature of in-cylinder flows. Furthermore, it applies on experimental in-cylinder flows. The results obtained by EMD and POD analysis are compared. The evolution of in-cylinder flow during transient engine working mode, i.e., engine speed acceleration from 1000 to 2000 rpm with different time periods, was obtained by High speed PIV 2D-2C. The velocity fields are obtained within tumble plane in a transparent mono-cylinder DISI engine and provide a data base to validate CFD.

Keywords: Organized motion, Turbulence, Separation, Bivariate 2D-EMD, Transient regime, DISI engine, HS-PIV.

Potentiel de la décomposition modal empirique pour analyser les champs d'écoulement instantanés dans le moteur à allumage commandé par injection direct : Effet des régimes transitoires

Résumé

Cette étude introduit une nouvelle approche appelée Bivariate 2D-EMD pour séparer le mouvement organisé à grande échelle, soit la composante basse fréquence de l'écoulement des fluctuations turbulentes, soit la composante haute fréquence dans un champ de vitesse instantané bidimensionnel. Cette séparation nécessite un seul champ de vitesse instantané contrairement aux autres méthodes plus couramment utilisées en mécanique des fluides, comme le POD. La méthode proposée durant cette thèse est tout à fait appropriée à l'analyse des écoulements qui sont intrinsèquement instationnaires et non linéaires comme l'écoulement dans le cylindre lorsque le moteur fonctionne dans des conditions transitoires. Bivariate 2D-EMD est validé à travers différents cas test, sur un écoulement turbulent homogène et isotrope (THI) expérimental, qui a été perturbé par un tourbillon synthétique de type Lamb-Ossen, qui simule le mouvement organisé dans le cylindre. Enfin, Il est appliqué sur un écoulement expérimental obtenu dans un cylindre et les résultats de la séparation d'écoulement sont comparés à ceux basés sur l'analyse POD. L'évolution d'écoulement dans le cylindre pendant le fonctionnement du moteur transitoire, c'est à dire une accélération du régime moteur de 1000 à 2000 tr/min en différentes rampes, sont mesurée en utilisant de PIV 2D-2C haute cadence. Les champs de vitesse sont obtenus dans le plan de tumble dans un moteur un moteur GDI mono-cylindre transparent et forment une base de données nécessaire pour valider les résultats de simulation numérique.

Mots clés: Mouvement organisé, Turbulence, Séparation, Bivariate 2D-EMD, Régime transitoire, GDI moteur, HS-PIV.

UNIVERSITE D'ORLEANS

Laboratoire PRISME
8 rue Léonard de Vinci
45072 Orléans cedex
FRANCE

Agence Nationale de la Recherche
ANR